ABSTRACT

Title of dissertation: RF PHOTONIC VECTOR MODULATION AND DEMODULATION TECHNIQUES FOR MILLIMETER-WAVE COMMUNICATIONS

Vincent R. Pagán, Doctor of Philosophy, 2015

Dissertation directed by: Professor Thomas E. Murphy
Department of Electrical and Computer Engineering

RF photonic techniques for modulating and demodulating microwave and millimeter-wave signals on RF carriers are theoretically analyzed and experimentally demonstrated. The two demodulating configurations utilize cascaded electrooptic phase-modulation followed by optical filtering. The spurious free dynamic ranges of these configurations are measured and a technique to intrinsically linearize the latter system to fifth-order is experimentally confirmed. Measurements are then performed at frequencies between 7 and 70 GHz that verify RF photonic based down-conversion using a harmonic of the electrical local oscillator (LO). Furthermore, this architecture is extended to allow for vector demodulation of digitally-encoded signals. Results of RF photonic demodulation of 4-quadrature amplitude modulation (QAM) and 16-QAM RF encoded millimeter-wave signals are presented.

Two RF photonic techniques for generating and encoding millimeter-wave RF signals are analyzed and experimentally demonstrated. The first uses phase-modulation and optical filtering in an interferometric configuration. Phase-shift

keyed encoded microwave and millimeter-wave signals are electrooptically synthesized using a harmonic of the electrical LO at data-rates of up to 6 Gbps and frequencies of up to 40 GHz. A second RF photonic scheme is developed to allow for vector modulation and upconversion using dual-drive Mach-Zehnder modulators. Vector modulation and upconversion are then shown at harmonics of the LO up to the fourth-order and at frequencies up to 60 GHz. Moreover, generation of 2.488 Gbps 4-QAM signals on a 36 GHz carrier using the second harmonic of the LO are demonstrated with this approach. Wired and wireless microwave and millimeter-wave transmission experiments are successfully conducted with the RF photonic systems detailed above in a laboratory environment.

RF PHOTONIC VECTOR MODULATION AND DEMODULATION TECHNIQUES FOR MILLIMETER-WAVE COMMUNICATIONS

by

Vincent Richard Pagán

Dissertation submitted to the Faculty of the Graduate School of the
University of Maryland, College Park in partial fulfillment
of the requirements for the degree of
Doctor of Philosophy
2015

Advisory Committee:
Prof. Thomas E. Murphy, Chair
Prof. Mario Dagenais
Prof. Julius Goldhar
Prof. Maio Yu, Dean's Representative
Dr. Bryan M. Haas

Dedication

I dedicate this dissertation to my family, especially to my wife, Briana, for her unconditional support and to my parents, Richard and Patricia, for instilling in me the importance of hard work.

Acknowledgments

First and foremost I would like to thank my advisor, Professor Thomas Murphy, for his guidance and tutelage throughout my time at UMD. He gave me the freedom to explore and conduct research on my own while making himself available to assist and encourage me whenever I needed help or advice. It has truly been a pleasure to work under the guidance of such a gifted, professional, and supportive individual.

I would also express my appreciation to the leadership at the Laboratory for Physical Sciences (LPS). In particular, I would like to thank Mr. William Klomparens, Ms. Catherine Bracey-Tynes, Dr. Kenneth Ritter, and Dr. Douglas Ketchum for their support and understanding throughout the course of my work. Under their leadership, I have always had the opportunity to work on interesting academic problems with real-world applications.

I would like to thank Prof. Mario Dagenais, Prof. Julius Goldhar, Prof. Miao Yu, and Dr. Bryan Haas for agreeing to serve on my committee. I would particularly like to express my appreciation to Dr. Bryan Haas for his encouragement to join the LPS team and his advice and guidance over the years.

I am very fortunate to have the opportunity to work with and learn from many talented scientists and researchers at LPS including Dr. Warren Herman, Dr. Dong Park, Dr. Paul Petruzzi, Dr. John Mack, Dr. Jeremiah Wathen, Dr. Yongzhang Leng, and Mr. Victor Yun. Thank you so much for your help.

I would also like to thank my colleagues in the Photonics Research Laboratory

at UMD. I've learned a lot from you at the lab meetings by watching you encounter and solve tough technical problems. I hope that you have been as fortunate to learn from me as I have from you.

I would also like to thank Dr. John Rodgers at the UMD Institute for Research in Electronics and Applied Physics (IREAP) for his idea to use vector network analysis to characterize the photonic transmitter and for allowing me to use the equipment in his lab to conduct the measurements.

To my many colleagues and friends who have made my time at LPS rewarding and enjoyable, thank you. In particular, I would like to thank Mr. Paul Swanson, Mr. Joseph Duperre, Mr. George de la Vergne, Dr. Paveen Apiratikul, Mr. Daniel Hinkel, Dr. Charles Krafft, Dr. Vincent Ballarotto, Dr. Mihaela Ballarotto, Dr. Timothy Horton, and Dr. Christopher Richardson for their comradery, helpful discussions, and encouragement, work related or otherwise.

It is truly impossible to remember all whose contributions have been instrumental to the completion of this work and I am certain that I have inadvertently left out some. However, I would like to express my sincere gratitude.

Last but not least, I would like to thank my family and friends for their support, encouragement, and understanding - I couldn't have finished this without you.

Thank you all!

Table of Contents

List of Tables

List of Figures

List of Abbreviations

ΦM	Phase-Modulation (-Modulator)
AC:	Alternating Current
ADC:	Analog-to-Digital Converter
APD:	Avalanche PD
ASE:	Amplified Spontaneous Emission
ASK:	Amplitude-Shift Keyed
AWG:	Arbitrary Waveform Generator
AWGN:	Additive White Gaussian Noise
BB:	BaseBand
BER:	Bit Error Ratio
BERT:	BER Tester
BOSA:	Brillouin OSA
BPF:	BandPass Filter
BPSK:	Binary PSK
BS:	Base Station
BSC:	Base Station Controller
BW:	BandWidth
CΦM:	Cascaded Phase-Modulation (-Modulator)
CATV:	CAble TeleVision
CIM:	Cascaded Intensity-Modulation (-Modulator)
CohD:	Coherent Detection
COTS:	Commercial Off-The-Shelf
CSR:	Carrier-to-Sideband Ratio
CW:	Continuous-Wave
DAC:	Digital-to-Analog Converter
DC:	Direct Current
DCM:	Directional Coupler Modulator
DD:	Direct Detection
DD-MZM:	Dual-Drive MZM
DFB:	Distributed Feedback
DM:	Direct-Modulation
DOC:	Directional Optical Coupler
DP-MZM:	Dual-Parallel MZM
DR:	Dynamic Range
DSB:	Double-SideBand
DSO:	Digital Sampling Oscilloscope
DSP:	Digital Signal Processing
DUT:	Device Under Test
EAM:	Electro-Absorption Modulator

EB:	ExaByte
E/O:	Electrical-to-Optical
EO:	ElectroOptic
EDFA:	Erbium-Doped Fiber Amplifier
EIRP:	Equivalent Isotropic Radiated Power
EMI:	ElectroMagnetic Interference
ESA:	Electrical Spectrum Analyzer
FBG:	Fiber Bragg Grating
FCC:	Federal Communications Commission
FEC:	Forward Error Correction
FFT:	Fast Fourier Transform
FIR:	Finite Impulse Response
FSK:	Frequency-Shift Keyed
FSPL:	Free-Space Path Loss
FSO:	Free-Space Optical
FSR:	Free Spectral Range
FWHM:	Full Width at Half Maximum
GbE:	Gigabit Ethernet
HPF:	High-Pass Filter
HWHM:	Half Width at Half Maximum
ID:	Interferometric Detection
IEEE:	Institute of Electrical and Electronics Engineers
IF:	Intermediate Frequency
IFFT:	Inverse FFT
IIP3:	Input IP3
IM:	Intensity-Modulation (-Modulator)
IMD:	Intermodulation Distortion
IMD3:	Third-Order IMD
InGaAs:	Indium Gallium Arsenide
InP:	Indium Phosphide
IP:	Internet Protocol
IP3:	Third-Order Intercept Point
I/Q:	In-phase/Quadrature
IR:	InfraRed
IREAP:	Institute for Research in Electronics and Applied Physics
LCOS:	Liquid Crystal On Silicon
LD:	Laser Diode
LDPC:	Low-Density Parity-Check
$LiNbO_3$:	Lithium Niobate
LPS:	Laboratory for Physical Sciences

LO: Local Oscillator
LOS: Line-Of-Sight
MLL: Mode-Locked Laser
mmW: millimeter-Wave
MS: Mobile Station
MSN: Mobile Switching Node
MSSC: Mobile Service Switching Center
MZI: Mach-Zehnder Interferometer
MZM: Mach-Zehnder Modulator
NF: Noise Figure
NLOS: Non-LOS
NRZ: Non-Return-to-Zero
NTIA: National Telecommunications and Information Administration
OC: Optical Circulator
OCS: Optical Carrier Suppression
ODL: Optical Delay Line
O/E: Optical-to-Electrical
OF: Optical Filtering
OIP3: Output IP3
OLO: Optical LO
OOK: On-Off-Keyed
OSA: Optical Spectrum Analyzer
PΦM: Parallel Phase-Modulation (-Modulator)
PC: Polarization Controller
PCS: Personal Communications Service
PD: PhotoDetector
PDL: Polarization Dependent Loss
PIN: P-doped/ Intrinsic/ N-doped
PM: Polarization Maintaining
PMD: Polarization Mode Dispersion
PMF: PM Fiber
POF: Plastic Optical Fiber
PPLL: Photonic Phase Locked Loop
PRBS: Pseudorandom Binary Sequence
PSD: Power Spectral Density
PSK: Phase-Shift Keyed
QAM: Quadrature Amplitude Modulation
RAN: Radio Access Network
Rb: Rubidium
RBW: Resolution BW

RF:	Radio Frequency
RIN:	Relative Intensity Noise
RNC:	Radio Network Controller
RoF:	Radio-over-Fiber
RR:	Repetition Rate
RS:	Reed-Solomon
RTO:	Real-Time Oscilloscope
RX:	Receiver
SFDR:	Spurious Free DR
SINR:	Signal-to-Interference-plus-Noise
SOA:	Semiconductor Optical Amplifier
SOP:	State of Polarization
SMF:	Single-Mode Fiber
SNR:	Signal-to-Noise Ratio
SSB:	Single-SideBand
SWaP:	Size, Weight, and Power
TE:	Transverse Electric
TFPS:	Thin Film Polymer on Silicon
TM:	Transverse Magnetic
TOD:	Third-Order Distortion
TX:	Transmitter
UHF:	Ultra High Frequency
UTC:	Uni-Traveling-Carrier
VNA:	Vector Network Analyzer
WDM:	Wavelength-Division Multiplexing
WSS:	Wavelength Selective Switch

Chapter 1

Introduction

1.1 Motivation

Next generation wireless communication systems will likely require millimeter-wave (mmW) carrier frequencies and complex in-phase/ quadrature (I/Q) modulation formats in order to support ever increasing consumer demands for higher bandwidths [15–17]. Globally, mobile internet protocol (IP) traffic is expected to be the highest growth IP segment with forecasted rates of 24.3 exabytes (EB = 10^{18} B) per month in 2019, an increase of about 10 times from 2014 [18]. Although traffic growth from internet and managed IP segments is expected to be slower than that of the mobile segment, their combined traffic is still forecasted to reach rates of 132 EB per month in 2018, an increase of 2.1 times from 2014 [1]. The projected global

Table 1.1: Projected global traffic demand in 2018 in EB per month [1].

	Consumer	**Business**	**Total**
Internet	70	16	86
Managed IP	25	5	29
Mobile Data	13	3	16
Total	108	24	132

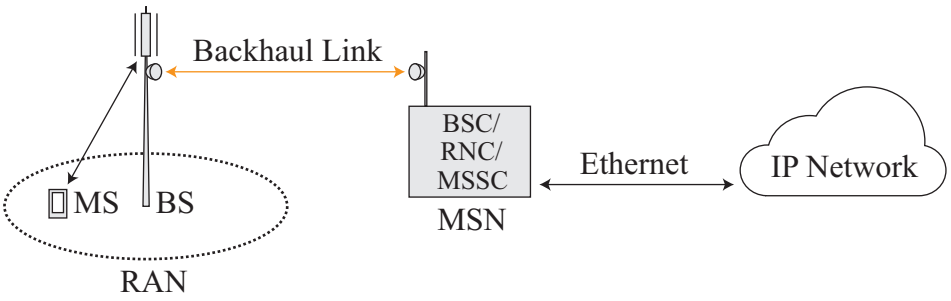

Figure 1.1: Diagram of a simplified mobile network. After [4].

traffic demand for the internet, managed IP, and mobile data segments in 2018 are provided in Table 1.1.

From a high-level viewpoint, the mobile network infrastructure consists of radio access networks (RANs) connected to mobile switching nodes (MSNs) through backhaul links as shown in Fig. 1.1. RANs include mobile stations (MSs) and base stations (BSs) while the MSNs are composed of base station controllers (BSCs), radio network controllers (RNCs), and mobile service switching centers (MSSCs). The BSCs, RNCs, and MSSCs could be co-located or distributed. The MSNs connect the RANs to the core network that provides access to other switching and gateway nodes [4].

Much work has been performed on establishing a set of standards and specifications for communication utilizing the unlicensed 60 GHz spectrum, which is shown for a few regions in Fig. 1.2. The WiGig Alliance released a tri-band specification adopting existing 2.4 GHz and 5.8 GHz technologies (802.11a,b,g,n,ac) while introducing a new short-range, multi-gigabit wireless specification at 60 GHz

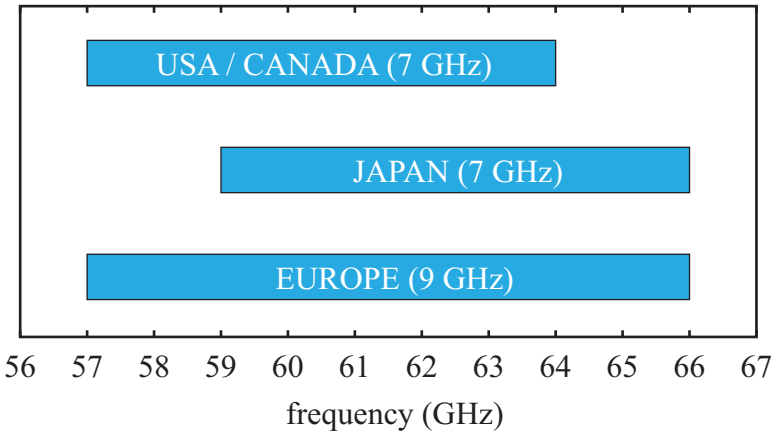

Figure 1.2: 60 GHz spectrum by region.

(802.11ad) [19]. In March 2013, WiGig merged with Wi-Fi to further unify the specification and decrease the time-to-market. Shipments of 1.8 billion Wi-Fi/ WiGig devices annually is forecasted by 2016 [20]. Although WiGig is posed to enable faster wireless connectivity, it will further exacerbate existing backhaul capacity issues [4].

To support increasing traffic from the RANs and the proliferation of connected mobile devices, higher capacity backhaul links become necessary [21]. Backhaul is typically facilitated with copper wiring, optical fiber, microwave links, or free-space optical (FSO) links. Although optical fiber solutions presently support the highest data-rates of the available options, wireless links are often employed due to the high cost of installing or leasing fiber. FSO links typically operate in the unregulated infrared (IR) spectral region and thus can support, in principle, a virtually unlimited bandwidth [22]. However, clouds, fog, and precipitation degrade the performance of FSO links [23]. For example, dense advection fog results in attenuation on the order

of 100 dB/km at an eye-safe wavelength of $\lambda = 1550$ nm [24]. Thus, hybrid FSO links employing a redundant RF link have been investigated for high-availability links [21, 25].

In 2003, the Federal Communications Commission (FCC) announced lightly licensed mmW spectrum for high-speed communications [26]. The spectrum is split between bands at 71-76 GHz, 81-86 GHz, 92-94 GHz, and 94.1-95 GHz. This is in addition to the 7 GHz of unlicensed spectrum available in the 60 GHz band, which spans from 57 to 64 GHz in the USA. Thus, a total of 19.9 GHz of allocated RF spectrum is potentially available for wireless backhaul as shown in Fig. 1.3. To put this in perspective, the total global spectral allocation for all cellular technologies combined does not exceed 780 MHz [27].

Solutions to address multi-gigabit wireless backhaul need to be developed in the near-term in order to support the successful roll-out of next-generation wireless

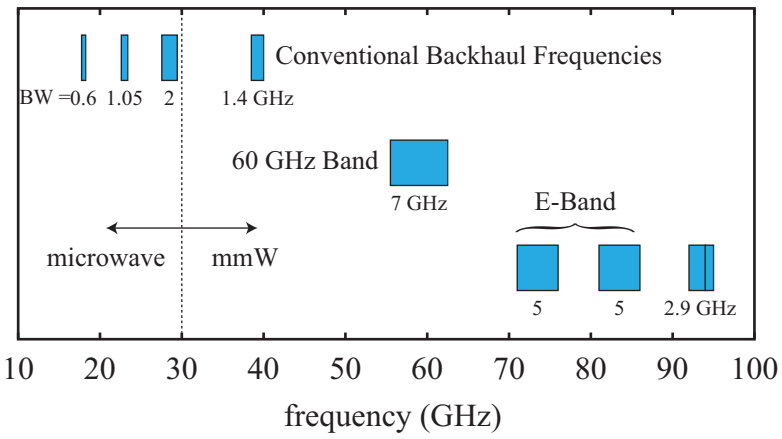

Figure 1.3: Conventional backhaul frequencies and 60 GHz and 70/80/90 GHz backhaul frequencies.

technologies such as WiGig. At mmW frequencies, traditional coaxial cables are inefficient and prohibitively lossy for transmission over distances longer than tens of meters. Radio-over-fiber (RoF) has emerged as a promising technology to support mmW backhaul of next-generation, multi-gigabit wireless access [28] due to the wide bandwidth of photonic components and the low-loss of optical fiber.

As mobile infrastructures continue to evolve, more of the network is employing packet-switching technologies. Thus, there is an increasing interest in seamless integration of packet-switched networks with wireless transmission systems, and in particular, the support of 10-Gigabit Ethernet (GbE) wireless links [29]. Such links are expected to meet the current demand of bridging broadband networks [30].

The widest consecutive bandwidth in 60/70/80/90 bands is the 7 GHz of bandwidth at 60 GHz. Although wide by wireless standards, this band cannot support 10-GbE data-rates with simple on-off-keyed (OOK) modulation [31]. More spectrally efficient modulation schemes such as M-ary phase-shift keying (PSK) or

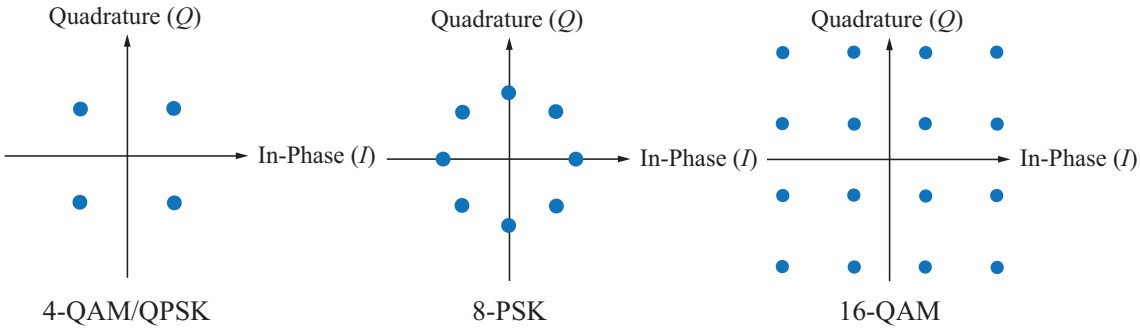

Figure 1.4: Example vector signal constellations.

M-ary quadrature amplitude modulation (QAM) could be employed to provide an $(\log_2 M)$-fold increase in the data-rate for a given bandwidth, making it possible, in principle, to relay 10-GbE data-rates and above within the allocated bands [29,32]. Example vector modulated signal constellations are shown in Fig. 1.4.

RF photonics describes the field where optical technologies are applied to RF communication and signal processing systems. Applications of RF photonics include the optical relay of analog signals [33–35], phased array control [36–38], reconfigurable and tunable RF filters [37, 39–41], and wide-bandwidth frequency converters [37, 42, 43], among others [44–46].

Much work has been reported in the literature on RF photonic techniques for electrooptic mmW generation and modulation [15, 23, 29, 30, 32, 42, 47–54]. Of this set, only [32, 50, 54] utilize RF photonics to generate a vector modulated mmW signal.

Furthermore, all of these works employed a completely electrical receiver rather than an RF photonic based receiver for downconversion and demodulation. To the author's knowledge, little work has been done on RF photonic receivers capable of vector demodulation beside that reported by [55, 56]. The goal of this dissertation is to explore RF photonic techniques, both on the transmit and receive ends, for wireless relay of spectrally efficient modulation formats at mmW frequencies.

1.2 Organization of this Work

This dissertation is organized as follows: Chapter 2 provides a brief overview of RF photonic technologies germane to this work. Chapter 3 provides a concise primer on photonic components used in this work, primarily from a system designer point of view. This chapter can be skipped by those familiar with RF photonic technologies. Chapter 4 provides the theoretical framework for the two RF photonic receiver technologies explored during this research project. Both of these receiver technologies are based on electrooptic phase-modulation and support electrooptic downconversion. Chapter 5 provides the experimental results obtained based on the proposed RF photonic receivers. Chapter 6 provides the theoretical framework for the two RF photonic transmitter architectures investigated and Chapter 7 provides the corresponding experimental results. The first transmitter is based on electrooptic phase-modulation and the second on electrooptic intensity-modulation. Both of the RF photonic transmitters support harmonic upconversion. Chapter 8 presents some fundamentals on designing mmW RF wireless links. In Chapter 9, wireless system demonstrations based on the RF photonic receivers and transmitters are shown. Chapter 10 provides a summary of this work and recommendations for future work.

Chapter 2

RF Photonics

RF photonics is the field where photonic technologies are applied to generate, transport, process, frequency convert, and control RF signals. The availability of spectrally pure optical sources, frequency combs, high-speed optical modulators, tunable/ reconfigurable optical filters, fast photodetectors, and low-loss optical fiber has enabled the development of advanced microwave and millimeter-wave (mmW) communication systems [45, 57]. It is a promising technology for applications such as cable television (CATV) distribution, cellular communications backhaul, and RF beamforming/ steering [58–60]. Some of the main advantages of RF photonic systems over their all-electronic counterparts are their lower transmission losses at microwave and mmW frequencies, immunity from electromagnetic interference (EMI), wide-bandwidth operation, tunability and reconfigurability, and wavelength-division multiplexing (WDM) expansion capability [45, 61].

2.1 Block Diagram

Since RF photonics encompasses many technologies, it is difficult to formulate a generic block diagram that can be broadly applied to all scenarios while still being useful. In the most general sense, an RF photonic system has an RF input and an RF output and photonic elements in between. A block diagram of a RF photonic

system is shown in Fig. 2.1. This diagram is similar to the one proposed by Clark and Waterhouse for a generic RF front end [61]. It should be noted that the ordering of the blocks is not necessarily fixed. Furthermore, it is often the case that a single element or a combination of elements provides the functionality described by more than one block.

The electrical conditioning blocks typically consist of RF amplifiers and filters. Pre-amplifiers are commonly used before an RF photonic system in order to lower the overall system noise figure (NF). It can be shown that the composite system NF is dominated by the gain and noise figure of the first stage (see Appendix C). Furthermore, post-amplification can be used at the output of the RF photonic system in order to achieve appropriate output power levels for follow-on systems. However, high-power photodetectors are being developed and may alleviate the requirement for post-amplification when used in conjunction with high incident optical pow-

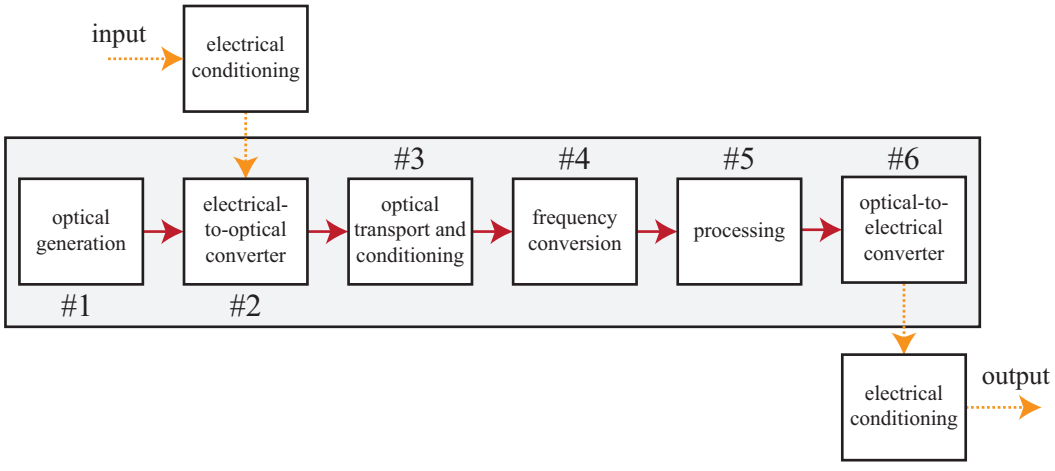

Figure 2.1: Block diagram of a generic RF photonic system.

ers [62,63]. Other components that are typically found in the electrical conditioning blocks include RF filters, circulators, power splitters, hybrids, and phase-shifters. For more information on RF components, the reader is referred to [3].

2.1.1 Optical Generation

Typically, optical generation is performed with a simple continuous-wave (CW) laser diode (LD). The laser diode may be followed by optical amplification stages, optical filters, and polarization controllers. In some cases, more complex optical generators such as optical comb sources or optical pulse generators are employed [41,64,65]. Mode-locked lasers (MLLs) are also utilized for frequency [66] or analog-to-digital conversion [67].

2.1.2 Electrical-to-Optical Conversion

Electrical-to-optical (E/O) conversion describes the process of imparting an RF signal onto an optical carrier. There are two general categories for performing this task, namely, direct-modulation and external-modulation [34]. Direct-modulation (DM) is the process of directly modulating the laser while external-modulation utilizes a device other than the laser to modulate the optical signal. One of the main advantages of direct-modulation is that the optical generator and the E/O converter is combined into a small and compact device [68]. However, directly modulated lasers have limited bandwidths and modulation depth when compared with those achievable utilizing external-modulators [68]. Furthermore,

direct-modulation produces a chirped waveform [69].

External-modulation is often used in high-performance links due to the additional degree of freedom in selecting the laser and the modulator separately [70]. In practice the lowest noise lasers do not have the highest modulation bandwidths. So, if a high-performance mmW link is required, a low-noise laser and a high-speed modulator can be individually selected and then combined to meet the design specifications. Low-noise, narrow-linewidth ($<$ 2 kHz) fiber lasers with 200 mW of output power at at 1550 nm are available [71]. Thin film polymer on silicon (TFPS) intensity-modulators having 3 dB bandwidths of 65 GHz and 7 dB bandwidths of 110 GHz are also now commercially available [72]. Furthermore, phase-modulators based on lithium niobate ($LiNbO_3$) with an electrooptic (EO) response up to 300 GHz have been reported [73].

While DM principally encodes the intensity of the optical carrier, external-modulation provides access to additional degrees of freedom. Modulators are available to encode the intensity, phase, or polarization of the incoming optical signal. The most commonly utilized modulators are electrooptic and in some case require biasing. For example, intensity-modulators (IMs) based on a Mach-Zehnder interferometer (MZI) are typically paired with active bias control electronics to maintain their set point. An alternative is phase-modulation (ΦM) which has two main advantages for RF photonics: 1) phase-modulation is an inherently linear process and 2) phase-modulators do not require active bias control electronics [74].

In most radio-over-fiber (RoF) systems, the primary goal is to transport an analog signal from one location to another with low loss and high fidelity. For these

applications, performance metrics such as the noise figure and spurious free dynamic range (SDFR) are very important. Much work has been done to lower the NF and increase the SFDR of RoF links as these are the two main performance limitations of RoF links [44]. Detailed discussions on the performance limitations of analog links are considered in [34, 35, 75].

RoF systems can also used to transport digitally encoded RF signals, where the digital signal has been encoded on the phase, amplitude, or frequency of an RF carrier. With electronic transmitters, the encoding is typically performed at an intermediate frequency (IF) that is lower than the carrier frequency, and then the signal is upconverted prior to wireless transmission [3]. At the receive end, the signal is downconverted to an IF and then demodulated. One of the main limitations of this approach is that the maximum bandwidth of the signal cannot exceed the carrier frequency. Thus, even if a mmW carrier is utilized, the system bandwidth will still be limited by the IF frequency.

One approach for alleviating this issue is to take advantage of the wide-bandwidth of RF photonic components. Rather than encoding the signal and then relaying the IF or upconverted RF signal, the baseband (BB) signal can be 'upconverted' to an optical IF, which has a much greater frequency than the RF signal, and then 'downconverted' to the desired RF frequency for transmission. In this case, the parenthesized terms 'upconverted' and 'downconverted' are meant to imply electrical-to-optical (E/O) conversion and optical-to-electrical (O/E), respectively, and thus have a unique connotation in this context that should not be confused with the use of these terms in the conventional RF engineering sense.

At the receive end, RF photonics can be used to downconvert and demodulate the information signal to baseband. Furthermore, RF photonics baseband-to-RF modulation can be extended to perform vector modulation, where the amplitude and/ or phase of the generated RF signal can be simultaneously encoded. This makes it possible to generate spectrally efficient vector modulated signals, such as M-ary phase-shift keying (PSK) and M-ary quadrature amplitude modulation (QAM). The spectral efficiency of M-ary signaling is $\log_2 M$ times higher than a two-state encoding scheme such as on-off-keying (OOK), permitting higher data-rates to be relayed within a given bandwidth.

2.1.3 Optical Transport and Conditioning

One of the primary advantages of RF photonics is the ability to relay microwave and mmW signals over significant distances with lower loss than copper cables. Although coaxial cables are the most widely used transmission line for routing RF signals, they are inadequate at microwave/ mmW frequencies. Even low-loss coaxial cables for communication systems have losses on the order of 100 dB/km at microwave frequencies. Amplifiers can be used to compensate for these losses, however, the amplifiers must be placed at strategic places along the length of the link in order to maintain a satisfactory signal-to-noise ratio (SNR) at the receive end. Since electrical amplifiers are active devices, electrical power needs to be available at these locations. The use of in-line amplifiers also necessitates that environmental protection and thermal management be considered at each amplification stage. In-

practice, noise and distortion levels increase after each amplifier in the chain leading to signal degradation.

In addition to being considerably less lossy than coaxial cables at microwave/ mmW frequencies, optical fibers have lower size, weight and power (SWaP) considerations, offer uniform attenuation in the RF frequency bands, and do not suffer from electromagnetic interference (EMI) [34, 45, 46, 76]. Furthermore, optical fibers have an almost limitless RF bandwidth; thus, they can be used at mmW frequencies above 67 GHz where coaxial cables are not readily available and rigid waveguides are the only metallic transmission line alternative [30].

In the most basic RoF configuration, an RF signal is modulated onto an optical carrier via a modulation device, relayed over a length of optical fiber, and converted back to an RF signal via a photodetection device [34]. Typically the optical wavelengths used fall in the 1.3 or 1.55 μm bands as standard optical fiber has near-zero dispersion and lowest-loss in these bands, respectively [59]. Once the signal has been converted to the optical domain, it can be relayed over considerable distances with optical fiber owing to the low propagation losses of standard optical fibers (i.e. $\alpha_F \approx 0.2$ dB/km at $\lambda = 1550$ nm).

However, the advantages of RoF over coaxial cable do not come without a tradeoff. As an example, consider a short RF link. In the limit that the propagation length approaches zero, the losses associated with relay over coaxial cable also approach zero, neglecting connector losses and impedance mismatches. The zero span insertion loss of a RoF link represents the inefficiencies of converting from the electrical domain to the optical domain, and then back again [34, 59].

Often the optical transport and conditioning block of the RF photonics system simply describes the relay of the optical carrier over fiber. However, it can also encompass amplification stages, filtering, and dispersion compensation.

2.1.4 Frequency Conversion

As discussed in Section 2.1.2, most RF communication systems encode baseband information onto an intermediate frequency and then upconvert the IF to the desired RF frequency prior to RF relay. The converse is performed at the receive end. In practice, the encoded information bandwidth is less than or equal to 10 % of the carrier frequency [49]. Since only fractional bandwidths are utilized, it is frugal to reduce the total system cost by utilizing the lowest frequency components available that meet the performance requirements as the price of components increases dramatically with frequency. Furthermore, in modern day communication systems, the source and destination signals are typically digital, making analog-to-digital converters (ADCs) and digital-to-analog converters (DACs) integral parts of the complete system design. According to the Nyquist-Shannon criterion [77], the minimum sample rate should be twice the highest frequency component. Thus, in cases where ADCs or DACs are to be used, it is cost effective to convert the RF signal to the lowest intermediate frequency possible prior to converting between domains.

To perform frequency conversion, a nonlinear element such as a diode is required. Nonlinearities are necessary to generate frequency components at the output

that are not present at the input. Generally, many frequency components will be produced through the mixing process. Thus, filtering is commonly used in conjunction with frequency converters to suppress the spurious terms [78]. In addition to generating frequency converted components (i.e. desired distortion products), mixing also produces undesired distortion products. Furthermore, there is typically a conversion loss penalty incurred with the mixing process.

Frequency conversion can be implemented optically using either heterodyne detection [79, 80] or electrooptic mixing [81–84], altogether eliminating the need for an electrical mixer. In instances where RF photonics are already being utilized to transport a signal, it often makes sense to utilize the existing nonlinearities in the system to perform frequency conversion rather than introducing additional nonlinear elements external to the RF photonic system. The tradeoff is that higher frequency components are needed at the modulator and/ or detector ends relative to the case where an IF is transported over optical fiber.

Optical heterodyne detection methods have the advantage that they inherently produce a frequency converted signal. The output signal frequency can be selected by adjusting the frequency difference between the optical carrier and an optical local oscillator (OLO). However, if the laser and OLO are free-running, then even small changes in the center frequencies of the lasers can result in large RF frequency shifts. For example, a relative difference in wavelength between the carriers of just 8 pm at an optical wavelength near 1550 nm (i.e. 0.0005 %) results in a frequency shift of 10 GHz, which is clearly significant at microwave frequencies. Thus, it is essential that the laser and OLO be frequency locked in order to prevent drift of the IF. This

can be difficult to achieve when the transmitter and receiver are separated by any significant distance. In addition, the phase noise of the lasers is imparted on the generated RF signal.

Electrooptic mixers typically utilize a secondary modulator that is driven by a microwave/ mmW LO, thereby providing the benefit of electrical heterodyne detection while eliminating the need for a stable and synchronized optical sources. EO mixing has been widely explored using IM [83, 85]. Configurations using cascaded intensity-modulators with direct-detection (CIM-DD) [81] are the most popular, particularly of the Mach-Zehnder modulator (MZM) variety. Parallel MZMs [86], dual-drive MZMs (DD-MZMs) [87], and dual-parallel MZMs (DP-MZMs) [88] have also been reported. In a similar fashion, phase-modulators can be combined in parallel or series to perform frequency conversion; however, they have been investigated to a lesser extent due to the more complex O/E conversion process.

2.1.5 Processing

RF photonics offers significant advantageous for processing including wide-bandwidth, EMI immunity, tunability, and reconfigurability [40]. Performing signal processing in the photonic domain can overcome the sampling speed bottleneck encountered with conventional all-electrical approaches [89]. Finite impulse response (FIR) filters [39,90], true-time delays [36,60], and phase-shifters [91], among others, have been demonstrated using RF photonic-based systems.

Unlike passive coaxial cable links, RoF links are active and thus require four

parameters to specify their performance. In addition to the shared link parameters of loss and bandwidth, the NF and dynamic range (DR) parameters need to be specified in order to fully specify the performance of an analog optical link [34]. In some wide-bandwidth applications, the SFDR precludes the use of RoF links. Although not signal processing in the traditional sense, certain RoF architectures can be intrinsically linearized to suppress some of the generated distortion. Rather than add a separate block to Fig. 2.1, linearization is considered to be part of the processing block. The topic of linearization is briefly discussed in Appendix D.3.

2.1.6 Optical-to-Electrical Conversion

In this section, three methods for O/E conversion will be described; namely, direct-detection, coherent-detection, and phase-modulation to intensity-modulation conversion followed by direct-detection.

2.1.6.1 Direct-Detection

Optical direct-detection (DD) is the non-coherent process of converting the optical signal energy to electrical signal energy. Since the optical signal energy is independent of the phase of an optical signal, direct-detection cannot be used to detect phase-encoded signals such as PSK signals. DD can be used to detect amplitude-shift keyed signals (ASK) or frequency shift keyed signals (FSK) [92]. Although direct-detection allows for simple detection (only a photodiode is needed), it precludes the use of M-PSK or M-QAM formats, for $M > 2$.

2.1.6.2 Coherent-Detection

Conventionally, phase-modulated signals are recovered through optical coherent-detection (CohD), which requires an OLO [93]. With CohD, the amplitude- and/ or phase-encoded optical signal is mixed with an OLO [94]. At the photodetector, the signal encoded on the phase of the optical carrier is converted to an electrical signal on an RF carrier at the IF, which is the frequency difference between the laser and the OLO. If the laser and the OLO have the same frequency, then the IF is zero and the detection method is said to be homodyne. Otherwise, the IF will be non-zero and the detection method is said to be heterodyne.

One of the main advantages of CohD is the increased receiver sensitivity when compared to DD. Furthermore, in principle, any IF can be achieved by tuning the frequency difference between the laser and the OLO. Finally, balanced detection can be used, resulting in a 3 dB increase in power at the IF and a reduction of common-mode noise.

One of the main disadvantages of coherent-detection is the relative complexity of the receive end configuration, especially when compared with simple direct-detection, which requires only a square-law photodetector. In addition, the laser and the OLO need to be stabilized with each other in order to prevent frequency drift of the IF. The laser and OLO should also be co-polarized to obtain the highest conversion efficiency. Furthermore, the phase-noise of the laser and the OLO will be transferred to the IF signal. Finally, since coherent-detection is based on interferometry, it is inherently nonlinear with a sinusoidal transfer function.

2.1.6.3 ΦM-to-IM Conversion

It is well know that ΦM-to-IM conversion can be achieved in a dispersive element [95–98]. Dispersion describes the phase-velocity frequency dependence of a wave as it propagates through a medium. A qualitative example will be provided here. Suppose that an optical carrier is phase-modulated by a pure RF tone. For 'small' modulation depths ($m \ll 1$), the optical power spectrum will resemble that of an amplitude modulated signal (i.e. the carrier, a lower sideband, and an upper sideband will be present in the optical spectrum). Although the power spectrum should in principle be symmetric, the upper and lower sidebands will be anti-phased. Thus, the beat product between the upper sideband and the carrier and the lower sideband and the carrier will cancel if the signal is non-coherently detected.

At the output of a dispersive medium, the net phase incurred by each frequency will in general not be equal. If the dispersion is tuned such that the relative phase-shift between the upper and lower sidebands is 0°, the sidebands at the output of the dispersive medium will now be in-phase resulting in a signal that can be directly detected. Optical fiber can be used as a dispersive medium in the C-band. Thus, the ΦM-to-IM conversion can be performed using a length of optical fiber [99]. In systems where the modulation frequencies are known, an appropriately chosen dispersion medium inserted after phase-modulation can be used to achieve electrooptic frequency mixing [84, 100, 101].

From the qualitative example above, it can be concluded that the only real requirement to detecting a phase-modulated signal is to implement a scheme that

breaks the phase or amplitude relationships between the optical sidebands. This can be done by changing the relative phase between the optical sidebands as in the fiber example or by changing the relative amplitudes of the optical sidebands. Several methods forΦM-to-IM conversion have been reported including selective selective sideband amplification [102], optical filtering [9, 103, 104], and interferometry [5]. After ΦM-to-IM conversion, direct-detection can be employed.

2.2 Standard Architectures

In this section, four standard link architectures are discussed; namely, direct-modulation with direct-detection (DM-DD), intensity-modulation with direct-detection (IM-DD), intensity- or phase-modulation with coherent-detection (IM/ΦM-CohD), and phase-modulation with direct-detection (ΦM-DD) after phase-modulation to intensity-modulation (ΦM-to-IM) conversion.

2.2.1 DM-DD Link

Traditionally RoF links have utilized intensity-modulation (IM) to impart an electrical signal onto an optical carrier at the transmitter (TX) and direct-detection (DD) to convert the optical signal back to the electrical domain at the receiver (RX) [33, 34, 45, 57, 85, 105]. Intensity-modulation can be performed by either directly modulating laser injection current (i.e. 'direct-modulation') or by modulating the optical signal produced by the laser (i.e. 'external-modulation') [34]. Direct-modulation is the simplest approach, however, it places additional requirements on

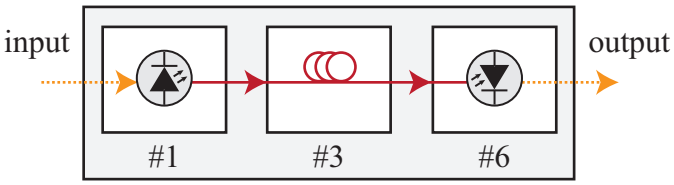

Figure 2.2: Block diagram of a DM-DD link.

the laser such as meeting the minimum modulation bandwidth and minimum modulation slope efficiency for a given design. DM-DD and IM-DD RoF links are analyzed in detail in [34]. A block diagram of a simple DM-DD link is shown in Fig. 2.2. The numbers following the '#' signs are referenced to the blocks in Fig. 2.1.

2.2.2 IM-DD Link

Externally-modulated links often offer improved performance over direct-modulation links, especially for broadband operation, as low-noise lasers can be employed without consideration of their modulation bandwidth [70]. Thus, the highest performing modulators and lasers available can be individually selected and combined to build high-performance links. A block diagram of an externally-modulated IM-DD RoF

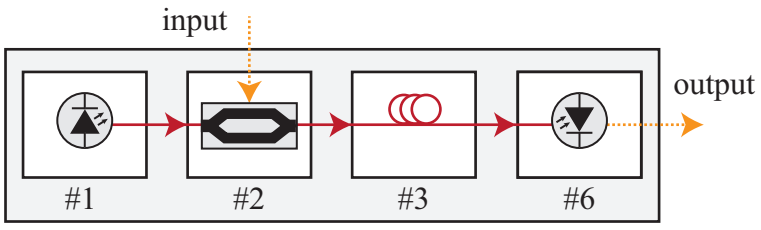

Figure 2.3: Block diagram of an IM-DD link.

link is shown in Fig. 2.3.

One of the main advantages of IM-DD links is their relative simplicity, particularly at the receive end, which can consist of as little as a photodetector (PD). The photodetector, which is typically a PIN diode structure in most RF photonic communication systems, converts incident photons to electrons via square-law detection of the optical field [59]. IM-DD RoF links have been studied extensively in the literature. The mathematical derivation of link gain is derived in Appendix A. The interested reader is referred to [106] for more details.

Electrooptic frequency conversion can be performed using IM-DD and this has been the subject of much research [33, 81, 82, 85, 86, 105, 107]. Typically, a pair of cascaded MZMs is used as shown in Fig. 2.4. The analysis of cascaded intensity modulators (CIMs) is more involved than that of the single modulator case due to the additional beat products generated. The theory provided in Appendix A can be extended to account for frequency mixing by applying the transfer function for the MZM twice and then solving for the gain for the IF of interest.

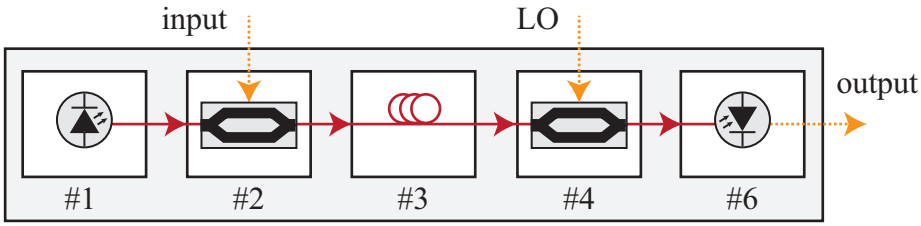

Figure 2.4: Block diagram of a downconverting CIM-DD link.

2.2.3 (IM/ΦM)-CohD Link

The conventional method for detecting phase-encoded signals is with coherent-detection. Coherent-detection can also be used to detect intensity-modulated signals with improved sensitivity relative to the direct-detection case. However, with the advent of the Erbium-doped fiber amplifier (EDFA), CohD has not typically been used in IM systems due to the additional complexity and expense associated with coherent receivers.

In the most basic coherent optical system, two optical waves are mixed to produce a photocurrent at the difference frequency. The mixing can be with a simple coupler or a more sophisticated device such as six port 90° optical hybrid [108]. In the simple block diagram shown in Fig. 2.5, phase-modulation and intensity-modulation will both result in amplitude variations in the photocurrent rendering it difficult to distinguish between amplitude and phase variations. Six port optical hybrids have four output ports allowing the phase and amplitude to be individually resolved with two sets of balanced detectors. The mathematical derivation of a

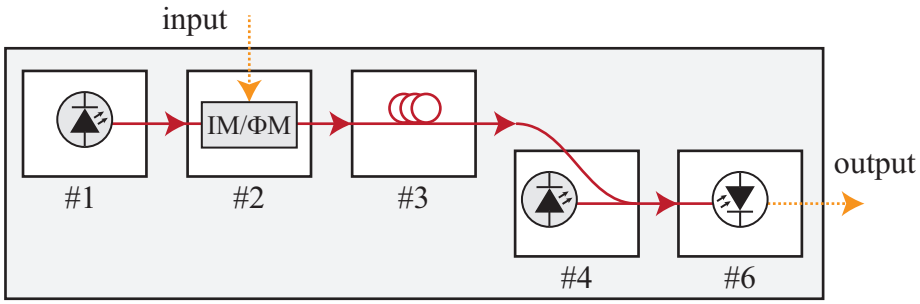

Figure 2.5: Block diagram of an externally-modulated link (IM/ΦM) with CohD.

simple ΦM-CohD system similar to that shown in Fig. 2.5 is provided in Appendix B. Optical coherent detection of phase-encoded signals are analyzed in more detail in [109].

2.2.4 ΦM-DD Link with ΦM-to-IM Conversion

As mentioned in Section 2.1.6.3, phase-modulation can be converted to intensity-modulation prior to direct-detection using a dispersive element [101], an asymmetric Mach-Zehnder interferometer (MZI) [5], or an optical filter [9, 103, 104]. In this dissertation, the work of Urick et al. on interferometric detection is extended to allow for electrooptic downconversion. In addition, the work of Haas and Murphy [9, 110] was used as the basis for developing a mmW vector demodulator with harmonic downconversion. These methods allow DD rather then CohD, to be implemented at the receive end, simplifying the receiver design. A generic ΦM-DD link with ΦM-to-IM conversion is shown in Fig. 2.6.

Of these approaches, ΦM-to-IM conversion using passive optical filtering (ΦM-OF) has the advantage of being both compact and inexpensive, while altogether

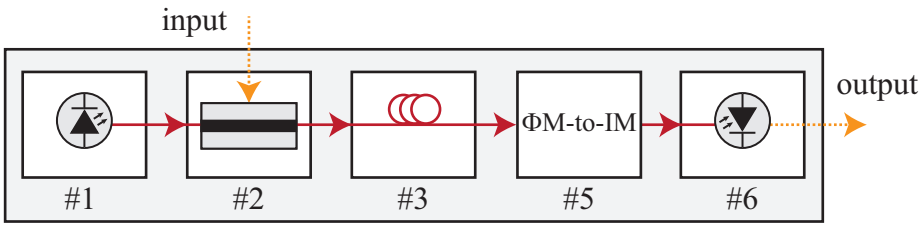

Figure 2.6: Block diagram of a ΦM-DD link with ΦM-to-IM conversion.

eliminating the need for an OLO and bias control electronics while ΦM-to-IM conversion using interferometric detection (ΦM-ID) allows for relatively high downconversion gains to be achieved.

2.3 Wireless Links

Wireless systems for microwave/ mmW wireless backhaul have become the topic of much research due to the advantages of RF photonics. In particular, high data-rate RF photonic transmitters have been developed to upconvert baseband or data-encode RF signals. Clever techniques for optical reuse and multi-band distribution have been considered [111]. Dispersion tolerant schemes have also been reported [47,51]. Bandwidth efficiencies of 3.86 b/s/Hz have been achieved at aggregate bit-rates of 27.04 Gbps in the 60 GHz band alone [15] and record data-rates of 100 Gbps have been demonstrated at a millimeter-wave frequency of 237.5 GHz [112].

As the main goal of this dissertation is to consider techniques to relay baseband digital signals through moderate spans of optical fiber at the transmitter and the receiver ends and over a mmW link between the TX and the RX antennas, only techniques reported in the literature that support upconversion of baseband digital signals will be considered in this section. Although not exhaustive by any means, a representative subset of works reporting baseband upconversion and modulation of a microwave/ mmW signal is provided in Fig. 2.7.

To understand Fig. 2.7, consider one of the data points, for example [113]. In this case, the generated RF signal had the same frequency as the electrical LO

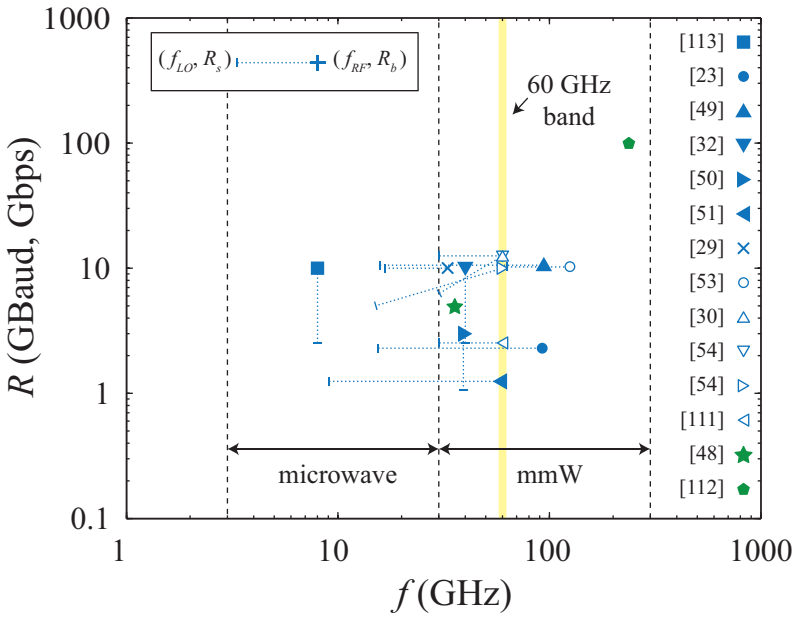

Figure 2.7: Frequencies and data-rates of a representative subset of microwave/ mmW transmitters reported in the literature.

($f_{RF} = f_{LO} = 8$ GHz). Furthermore, a spectrally efficient modulation scheme (16-QAM) was used to photonically produce a vector modulated signal having a symbol rate of $R_s = 2.5$ GBaud, which is equivalent to an aggregate bit-rate of $R_b = \log_2(16)R_s = 10$ Gbps. Since no harmonic upconversion was performed and the bit-rate was higher than the Baud-rate, the line is vertical. Diagonal lines in the plot correspond to cases where more efficient modulation schemes were used in conjunction with electrooptic upconversion. Symbols without dashed lines correspond to techniques that employ optical heterodyne mixing rather than electrooptic mixing (i.e. [48] and [112]).

Although much work has been performed on developing RF photonic trans-

mitters for wireless backhaul, not as much work has been done in developing vector demodulating RF photonic receivers. Vector demodulation refers to the process of resolving the in-phase and quadrature components. Two works in particular have addressed this topic to some extent. The first was a two-channel downconverter for phase-detection reported by Biernacki et al. [56]. The system used a CW laser followed by a MZM to impart the LO on the optical carrier. After LO modulation and amplification, the optical signal was divided and fed into two nominally identical branches, each containing a MZM and balanced photodetector. The input RF signal was split using a 90° hybrid and applied to the MZMs in the two branches. The system was demonstrated at RF frequencies of f_{RF} = 2 - 18 GHz.

A similar system was reported by Sambaraju et al. [55]. In this configuration, an optical delay line rather than a 90° electrical hybrid was used to achieve the quadrature condition between the two branches of the RF photonic demodulator. The optical signals were then bandpass filtered using a pair of FBGs (one in each branch) centered at the RF frequency. Error-free demodulation of a 2.5 Gbps 4-QAM signal was achieved at an RF frequency of f_{RF} = 20 GHz.

To the author's knowledge, there have been no reports of wireless system that employ a RF photonic transmitter and RF photonic receiver to encode and decode vector modulated RF signals. In this dissertation, techniques for RF modulation and demodulation are explored. Two techniques for downconverting RF photonic receivers are demonstrated based on electrooptic phase-modulation. The first was an extension of the work performed by Urick et al. [5] and the second an extension on the work perform by Haas and Murphy [9]. Based on of the latter results, a technique

for vector demodulation using phase-modulation is developed and demonstrated.

A technique to implement BPSK and a technique to implement vector modulated formats are then considered. The first is based on phase-modulation and optical filtering and is similar to a frequency conversion technique reported by Mast et al. [43]. However, due to instabilities in the experimental setup, a configuration based on two parallel DD-MZMs was investigated. Conceptually, this technique is similar to the simulated design reported by Al-Shareefi et al. [114], with the exception that two lasers were used to increase the stability of the system.

Chapter 3

Key Component Models

In this chapter, simple mathematical models for key components are presented. The purpose is not to provide a comprehensive mathematical treatise of the components, but rather it is to present a concise primer of the requisite details necessary to understand the RF photonic techniques described in this dissertation.

3.1 Laser

The optical sources for RF photonic systems are lasers. Laser, which is an acronym for light amplification by stimulated emission of radiation, is the name for a coherent optical source. Lasers come in many varieties, ranging from gas lasers to semiconductor laser diodes. Most lasers used in RF photonics work are of the semiconductor variety although fiber-based lasers are also employed due to their narrow linewidths. The schematic representation of a continuous-wave (CW) laser diode having output power, P_L, and angular frequency, ω_L, is shown in Fig. 3.1.

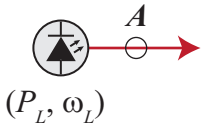

Figure 3.1: Schematic representation of a CW laser diode.

An ideal CW laser emits a single-frequency sinusoidal waveform at a constant optical power. However, in practice, lasers also emits spurious tones and generate noise. For example, phase noise broadens the linewidth of the laser into a Lorentzian shape [115]. Laser nonidealities that are of particular importance for RF photonic system design are the linewidth, spectral purity, and relative intensity noise (RIN). The physics and engineering of lasers are very rich areas of study, and are not the subject of this dissertation. Interested readers should refer to the many references on this topic, which include [116, 117].

In the frequency domain, the signal produced by an ideal CW laser can be represented by a Dirac-delta function centered at its carrier frequency. Using phasor notation, the optical signal generated by a CW laser having wavelength λ_L and average power P_L can be represented as

$$u_A(t) = \sqrt{P_L}\, e^{j\omega_L t} \tag{3.1}$$

where $\omega_L = 2\pi c/\lambda_L$ its angular frequency and c is the speed of light in vacuo.

3.2 Photodetector

Photodetectors (PDs) are used to convert optical signals to electrical signals. In this dissertation, the terms photodetector and photodiode will be used interchangeably. The most frequently encountered type of photodetector used in RF photonic systems are PIN photodiodes, which consist of p-doped, intrinsic, and n-doped semiconductor regions. Avalanche photodiodes (APDs) are sometimes used at microwave frequencies and below due to their high gain. Another type

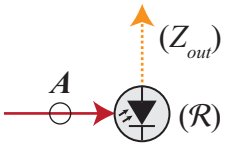

Figure 3.2: Schematic representation of a PIN photodetector.

of photodiode that is becoming more common in mmW RF photonics work is the uni-traveling-carrier photodiode (UTC-PD), in which hole transport is blocked via quantum confinement, increasing the net carrier mobility. The schematic representation of a photodetector having responsivity, $\mathcal{R}$, and output impedance, Z_{out}, is shown in Fig. 3.2.

An ideal photodetector can be modeled as a current source with infinite internal resistance that produces a photocurrent in direct proportion to the incident optical power. Furthermore, an ideal photodetector has infinite bandwidth and no polarization dependent loss (PDL). The ratio of the photocurrent produced by the photodetector to the power incident on the photodetector is given by its responsivity, $\mathcal{R}$. Mathematically, the responsivity can be expressed as

$$\mathcal{R} = \eta \frac{e\lambda}{hc} \tag{3.2}$$

where η is the quantum efficiency (ideally $\eta = 1$), e is the elementary charge, λ is the wavelength of the incident optical signal, h is Planck's constant, and c is the speed of light in vacuo. At C-band wavelengths (λ = 1530-1565 nm), the highest achievable responsivities possible with perfect quantum efficiency are $\mathcal{R}$ = 1.23-1.26 A/W. Typical values of $\mathcal{R}$ at λ = 1550 nm are around $\mathcal{R}$ = 0.6-0.9 A/W.

Mathematically, square-law photodetection can be expressed as

$$i(t) = \mathcal{R}|u_A(t)|^2 \tag{3.3}$$

where $\mathcal{R}$ is the responsivity of the photodetector given by Eq. (3.2)and $u_A(t)$ is the incident optical field, which can be assumed is normalized such that $|u_A(t)|^2$ represents the optical power.

Many photodetectors have an internal terminating resistor to reduce the reflections due to the impedance mismatch between the intrinsic high-impedance of the photodetector and the low-impedance of the majority of commercial off-the-shelf (COTS) RF components. The schematic for a photodetector with an internal terminating resistor, Z_{int} connected to an output impedance Z_{out} is shown in Fig. 3.3. Typically, $Z_{int} = Z_{out} = 50\ \Omega$. In this case, half of the photocurrent flows through the internal terminating resistor resulting in an effective responsivity that is half of that predicted by Eq. (3.2). The half-fold reduction in photocurrent corresponds to a 6 dB penalty in the output RF power relative to the case without an internal terminating resistor. In the expressions derived in this dissertation, the internal terminating resistor is not explicitly included. To account for this, the responsivity used can simply be halved.

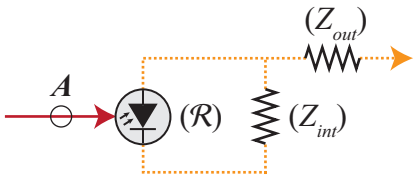

Figure 3.3: Circuit diagram of a PD containing an internal terminating resistor.

In practice, photodetectors are fairly linear, especially for CW optical signals at low optical powers. However, as the photocurrent is increased, the photodetector transfer function will become nonlinear [118]. The effects of photodetector nonlinearities are not considered in this dissertation.

3.3 Optical Coupler

Optical couplers are used to split or combine optical signals. Generically, most optical couplers are directional four-port devices. Directional optical couplers (DOCs) come in several varieties including fused biconically tapered, offset, butt-joint, beamsplitting, and wavefront-dividing, among others [119]. In this work, fused biconically tapered and beamsplitting DOCs are used.

Optical couplers are often characterized by their power splitting ratio and excess optical loss. In addition, they can be non-polarization maintaining or polarization maintaining (PM). A schematic representation of a fused biconically tapered directional coupler with power splitting ratio, ϵ, and excess optical insertion loss, α_{DOC}, is shown in Fig. 3.4.

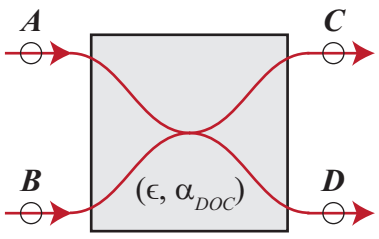

Figure 3.4: Schematic representation of an optical coupler.

The output optical fields can be related to the input optical fields by

$$\begin{bmatrix} u_C(t) \\ u_D(t) \end{bmatrix} = \left(\sqrt{\alpha_{DOC}} \begin{bmatrix} \sqrt{1-\epsilon} & j\sqrt{\epsilon} \\ j\sqrt{\epsilon} & \sqrt{1-\epsilon} \end{bmatrix} \right) \begin{bmatrix} u_A(t) \\ u_B(t) \end{bmatrix} \tag{3.4}$$

where α_{DOC} is the excess optical loss and ϵ is the power splitting ratio of the directional optical coupler. For the case where $\epsilon = 1/2$, Eq. (3.4) simplifies to

$$\begin{bmatrix} u_C(t) \\ u_D(t) \end{bmatrix} = \left(\sqrt{\frac{\alpha_{DOC}}{2}} \begin{bmatrix} 1 & j \\ j & 1 \end{bmatrix} \right) \begin{bmatrix} u_A(t) \\ u_B(t) \end{bmatrix}. \tag{3.5}$$

3.4 Optical Delay Line

Optical delay lines (ODLs) are used to add delay to an optical signal. Variable optical delay lines are typically implemented by varying the length of a path in free space. If the optical field to be delayed exists in an optical fiber, a pair of collimators is often used to convert the guided wave to free-space and back again. Fiber-coupled variable optical delay lines typically have a delay range of a fraction of a ns.

Static optical delay lines can be made by sending the optical field through a length of optical fiber. Since the light travels at the speed of light in vacuo, c, divided by the effective refractive index, n_{eff}, the fiber delay, τ, can simply be given by

$$\tau = L\frac{n_{eff}}{c} \tag{3.6}$$

where L is the fiber length. Standard single-mode optical fiber has an effective refractive index of $n_{eff} \approx 1.47$ at an optical wavelength of $\lambda = 1550$ nm. Thus, each meter of optical fiber adds a delay of approximately $\tau \approx 5$ ns. The primary

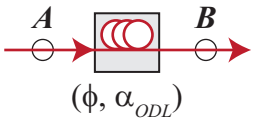

Figure 3.5: Schematic representation of an optical delay line.

consideration that must be taken into account when implementing a long temporal delay using optical fiber is chromatic dispersion in the fiber, particularly in cases where double-sideband (DSB) optical signals are relayed. Chromatic dispersion will be discussed in more detail in Section 3.12.1. Of secondary importance, is the fiber optical insertion loss incurred in the optical delay line. For standard single-mode fiber, the loss is typically $\alpha_F \approx 0.2$ dB/km at $\lambda = 1550$ nm.

The schematic representation of an optical delay line with phase, ϕ, and optical insertion loss, α_{ODL}, is shown in Fig. 3.5. The phase-shift, ϕ, can be expressed in terms of the physical properties of the ODL as

$$\phi = \frac{2\pi n_{eff}}{\lambda} L \tag{3.7}$$

where n_{eff} is the effective refractive index and L is the length of the fiber delay line.

The output field can be related to the input field by

$$u_B(t) = \sqrt{\alpha_{ODL}}\, e^{-j\phi} u_A(t) \tag{3.8}$$

where α_{ODL} is the insertion loss and ϕ is the phase-shift produced by the optical delay line.

3.5 Mach-Zehnder Interferometer

A Mach-Zehnder interferometer (MZI) consists of two optical couplers, one at the input and one at the output, and a relative difference in optical delay in the upper and lower arms [106]. A mathematical model for a fiber-based MZI is shown in Fig. 3.6.

Assuming that the input optical signals are given by $u_A(t)$ and $u_B(t)$ and that the output optical signals are given by $u_E(t)$ and $u_F(t)$, the output signals are related to the input signals by

$$\begin{aligned}\begin{bmatrix} u_E(t) \\ u_F(t) \end{bmatrix} &= \left(\sqrt{\alpha_{DOC2}} \begin{bmatrix} \sqrt{1-\epsilon_2} & j\sqrt{\epsilon_2} \\ j\sqrt{\epsilon_2} & \sqrt{1-\epsilon_2} \end{bmatrix} \right) \\ &\times \begin{bmatrix} \sqrt{\alpha_{ODL1}} e^{-j\phi_1} & 0 \\ 0 & \sqrt{\alpha_{ODL2}} e^{-j\phi_2} \end{bmatrix} \\ &\times \left(\sqrt{\alpha_{DOC1}} \begin{bmatrix} \sqrt{1-\epsilon_1} & j\sqrt{\epsilon_1} \\ j\sqrt{\epsilon_1} & \sqrt{1-\epsilon_1} \end{bmatrix} \right) \begin{bmatrix} u_A(t) \\ u_B(t) \end{bmatrix} \end{aligned} \tag{3.9}$$

where α_{DOCi} is the excess loss of the i^{th} directional optical coupler, ϵ_i is the power

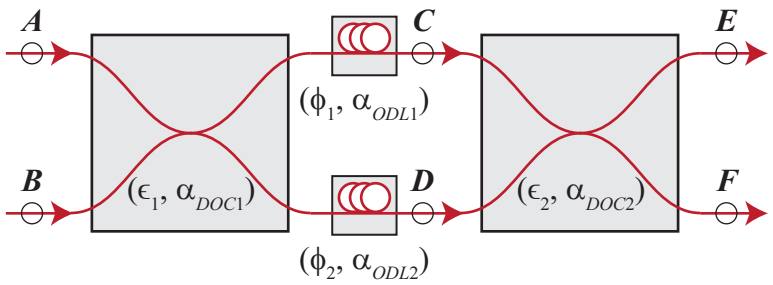

Figure 3.6: Schematic representation of a fiber-based MZI.

coupling coefficient of the i^{th} optical coupler, and α_{ODLi} is the insertion loss of the i^{th} optical delay line. Performing the matrix multiplication operations and rearranging, the output fields can be written as

$$\begin{aligned} u_E(t) &= 2j\sqrt{\alpha_{DOC1}}\sqrt{\alpha_{DOC2}}\, e^{-j\Sigma\phi/2} \\ &\times \left\{ \left[\frac{\sqrt{\alpha_{ODL1}}\sqrt{1-\epsilon_1}\sqrt{1-\epsilon_2}\, e^{-j\Delta\phi/2} - \sqrt{\alpha_{ODL2}}\sqrt{\epsilon_1}\sqrt{\epsilon_2}\, e^{j\Delta\phi/2}}{2j} \right] u_A(t) \right. \\ &+ \left. \left[\frac{\sqrt{\alpha_{ODL1}}\sqrt{1-\epsilon_1}\sqrt{\epsilon_2}\, e^{-j\Delta\phi/2} + \sqrt{\alpha_{ODL2}}\sqrt{\epsilon_1}\sqrt{1-\epsilon_2}\, e^{j\Delta\phi/2}}{2} \right] u_B(t) \right\} \end{aligned} \tag{3.10}$$

$$\begin{aligned} u_F(t) &= 2j\sqrt{\alpha_{DOC1}}\sqrt{\alpha_{DOC2}}\, e^{-j\Sigma\phi/2} \\ &\times \left\{ \left[\frac{\sqrt{\alpha_{ODL1}}\sqrt{\epsilon_1}\sqrt{1-\epsilon_2}\, e^{-j\Delta\phi/2} + \sqrt{\alpha_{ODL2}}\sqrt{1-\epsilon_1}\sqrt{\epsilon_2}\, e^{j\Delta\phi/2}}{2} \right] u_A(t) \right. \\ &+ \left. \left[\frac{-\sqrt{\alpha_{ODL1}}\sqrt{\epsilon_1}\sqrt{\epsilon_2}\, e^{-j\Delta\phi/2} + \sqrt{\alpha_{ODL2}}\sqrt{1-\epsilon_1}\sqrt{1-\epsilon_2}\, e^{j\Delta\phi/2}}{2j} \right] u_B(t) \right\} \end{aligned} \tag{3.11}$$

where the common phase, $\Sigma\phi$, is defined as $\Sigma\phi \equiv \phi_1 + \phi_2$ and the differential phase, $\Delta\phi$, is defined as $\Delta\phi \equiv \phi_1 - \phi_2$. For the maximum extinction ratio case, $\alpha_{DOC1} = \alpha_{DOC2} = \alpha_{DOC}$, $\alpha_{ODL1} = \alpha_{ODL2} = \alpha_{ODL}$, and $\epsilon_1 = \epsilon_2 = 1/2$. In this case, Eqs. (3.5)-(3.6) reduce to

$$u_E(t) = -j\sqrt{\alpha_{MZI}}\, e^{-j\Sigma\phi/2} \left[(\sin\Delta\phi/2)\, u_A(t) - (\cos\Delta\phi/2)\, u_B(t) \right] \tag{3.12}$$

$$u_F(t) = +j\sqrt{\alpha_{MZI}}\, e^{-j\Sigma\phi/2} \left[(\cos\Delta\phi/2)\, u_A(t) + (\sin\Delta\phi/2)\, u_B(t) \right] \tag{3.13}$$

where $\sqrt{\alpha_{MZI}} = \sqrt{\alpha_{DOC}^2 \alpha_{ODL}}$ is the total insertion loss of the MZI.

For the case that only one input signal is applied to the MZI (i.e. $u_B(t) = 0$),

the output fields given by Eq. (3.12)-(3.13) further simplify to

$$u_E(t) = -j\sqrt{\alpha_{MZI}}\, e^{-j\Sigma\phi/2} \sin(\Delta\phi/2) u_A(t) \tag{3.14}$$

$$= t_1(\Delta\phi) u_A(t)$$

$$u_F(t) = j\sqrt{\alpha_{MZI}}\, e^{-j\Sigma\phi/2} \cos(\Delta\phi/2) u_A(t) \tag{3.15}$$

$$= t_2(\Delta\phi) u_A(t)$$

where $t_i(\Delta\phi)$ is the MZI transfer function between the input and the i^{th} port. For the case where the MZM has only one output, the functional form for optical field at the output of the MZM can be taken as either Eq. (3.14) or Eq. (3.15). Additional information on MZIs is discussed in [120].

3.6 Electrooptic Modulator

Here simple models for electrooptic phase-modulators and intensity modulators based on a MZI, are presented.

3.6.1 Phase-Modulator

The simplest electrooptic (EO) modulator geometry is the phase-modulator. A phase-modulator (ΦM) consists of an optical waveguide made in an EO material and a set of electrical contacts to apply the input signal. If an electrical signal is applied to a material exhibiting the Pockels effect, then the optical phase will be delayed or advanced in proportion to the strength of the electrical signal. Most commercially available phase-modulators are fabricated in a lithium niobate ($LiNbO_3$) waveguide

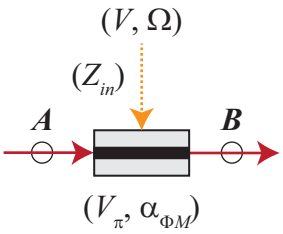

Figure 3.7: Schematic representation of an electrooptic ΦM driven by an RF signal.

[121] although phase-modulators based on electrooptic polymers [122] and indium phosphide (InP) [123] can also be realized.

Assuming that the direction normal to the top surface of the phase-modulator is defined as the z-direction and that the light is propagating in the y-direction, the electrooptic coefficient along the x-axis, or transverse electric (TE) direction, is approximately 1/3 of the electrooptic coefficient along the z-axis, or transverse magnetic (TM) direction, for a z-cut $LiNbO_3$ or a z-poled phase-modulator. In the simple mathematical model presented here, it is assumed that the state-of-polarization (SOP) at the input of the phase-modulator is such that V_π has been minimized. The results presented here can be extended to account for arbitrary SOPs by writing the expressions in terms of Jones vectors.

The schematic representation of an electrooptic phase-modulator driven by an RF signal is shown in Fig. 3.7. Assuming that the field generated by the laser is given by Eq. (3.1), the optical field at the output of the phase-modulator is given

by

$$\begin{aligned} u_B(t) &= \sqrt{\alpha_{\Phi M}}\, e^{jm\sin\Omega t} u_A(t) \\ &= \sqrt{P_L}\sqrt{\alpha_{\Phi M}}\, e^{j\omega_L t}\, e^{jm\sin\Omega t} \end{aligned} \tag{3.16}$$

where $\alpha_{\Phi M}$ is the insertion loss of the phase-modulator and m is the modulation depth expressed in radians as

$$m = \frac{\pi V}{V_\pi}. \tag{3.17}$$

Often, it is convenient to express Eq. (3.16) as a weighted sum of harmonics of the RF tone using the well-known Jacobi-Anger identity

$$e^{jz\sin\theta} = \sum_{p=-\infty}^{\infty} J_p(z) e^{jp\theta}. \tag{3.18}$$

Rewriting Eq. (3.16) using Eq. (3.18) yields

$$u_B(t) = \sqrt{P_L}\sqrt{\alpha_{\Phi M}}\, e^{j\omega_L t} \sum_{p=-\infty}^{\infty} J_p(m) e^{jp\Omega t}. \tag{3.19}$$

Based on Eq. (3.19), the optical spectral components generated via phase-modulation with a pure RF tone are illustrated in Fig. 3.8.

Since the field given by Eq. (3.16) is phase-modulated, only a DC photocurrent would result if the signal were incident on a square-law photodetector. The amplitude of the DC photocurrent produced by square-law detection of the field given by Eq. (3.16) is

$$\begin{aligned} i(t) &= \mathcal{R} P_L \alpha_{\Phi M} \\ &= I_{DC}. \end{aligned} \tag{3.20}$$

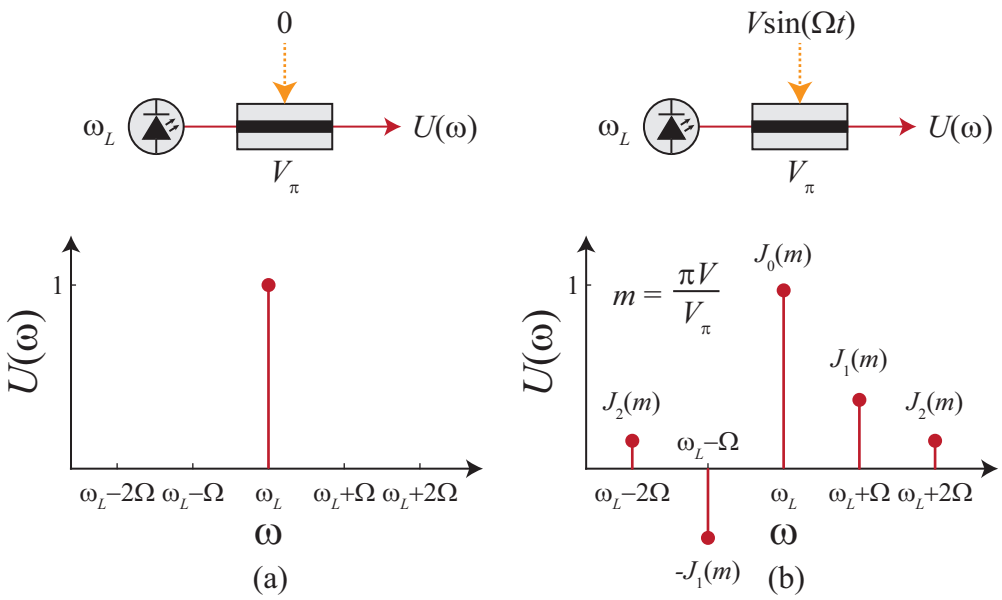

Figure 3.8: Normalized optical spectra of a phase-modulated signal. (a) RF sinusoidal excitation 'off' and (b) RF sinusoidal excitation 'on'.

3.6.2 Intensity-Modulator

The most commonly studied type of external modulation is intensity-modulation (IM). For this type of modulation, the laser output power is held constant and the information is encoded onto the intensity profile [34]. The main advantage of intensity-modulation is the simple method for detection, which can consist of as little as a square-law photodetector. Devices used for external intensity-modulation include the Mach-Zehnder modulator (MZM), the directional coupler modulator (DCM), and the electro-absorption modulator (EAM). Of these devices, the MZM is by far the most commonly utilized in telecommunications and RF photonics.

The mathematical model for intensity-modulation using a MZM device is

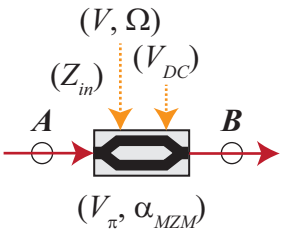

Figure 3.9: Schematic representation of an electrooptic MZM with RF sinusoidal excitation.

based on the MZI shown analyzed in Section 3.5. A MZM is a MZI having phase-modulators embedded in the interferometer arms rather than optical delay lines. At the electrooptic intensity-modulator, the optical field is encoded with a sinusoidal RF signal with amplitude V and angular frequency Ω. The optical signal emerging from a single optical input, single optical output MZM follows from Eqs. (3.9)-(3.16) and is given by

$$\begin{aligned} u_B(t) &= \begin{bmatrix} \sqrt{\alpha_{MZM}} & 0 \end{bmatrix} \left(\frac{1}{\sqrt{2}} \begin{bmatrix} 1 & j \\ j & 1 \end{bmatrix} \right) \begin{bmatrix} e^{j\phi_1(t)} & 0 \\ 0 & e^{j\phi_2(t)} \end{bmatrix} \\ &\times \left(\frac{1}{\sqrt{2}} \begin{bmatrix} 1 & j \\ j & 1 \end{bmatrix} \right) \begin{bmatrix} u_A(t) \\ 0 \end{bmatrix} \end{aligned} \tag{3.21}$$

where α_{MZM} is the insertion loss of the MZM. Single-drive MZMs are most commonly found. In the push-pull configuration, $\phi_1(t) = \phi(t)/2$ and $\phi_2(t) = -\phi(t)/2$ and

$$\begin{aligned} \phi(t) &= \frac{\pi}{V_\pi} (V_{DC} + V \sin \Omega t) \\ &= M_{DC} + m \sin \Omega t. \end{aligned} \tag{3.22}$$

Performing the matrix multiplication operations in Eq. (3.21), the optical signal emerging from the MZM is

$$u_B(t) = j\sqrt{\alpha_{MZM}}\sin\left[\phi(t)/2\right]u_A(t). \tag{3.23}$$

In Eq. (3.22), V_π is the half-wave voltage of the MZM, which is the amount of voltage that must be applied to the modulator input to achieve a π radian phase-shift. Generally, the DC and RF inputs are internally connected to separate sets of electrodes, resulting in different DC and RF V_π s. In addition, the RF V_π is typically frequency dependent. However, for simplicity, it is assumed that the DC and RF V_π s are nominally identical and frequency independent in Eq. (3.22). Furthermore, it is assumed that the modulation results in a symmetric optical spectrum. A more general analysis allowing for asymmetric optical sidebands is presented in [124].

In this derivation, a single-drive MZM was assumed. However, DD-MZMs are also available where the phase in each arm can be independently controlled through separate RF inputs. An electrical 180° hybrid can be used prior to the DD-MZM to split a signal RF signal into two out-of-phase RF signals. This configuration is commonly used for optical carrier suppression (OCS) if the DD-MZM is null biased as shown in Fig. 3.10(a) [125]. If an electrical 90° hybrid is used instead, a single-sideband (SSB) optical signal can be produced with a DD-MZM biased at quadrature as shown in Fig. 3.10(b) [125]. In this this dissertation, DD-MZMs are used to separately apply two different signals to the two arms of the MZM. More details will be discussed in Chapters 6-7.

In this previous analysis of a MZM, two nonidealities that could affect system

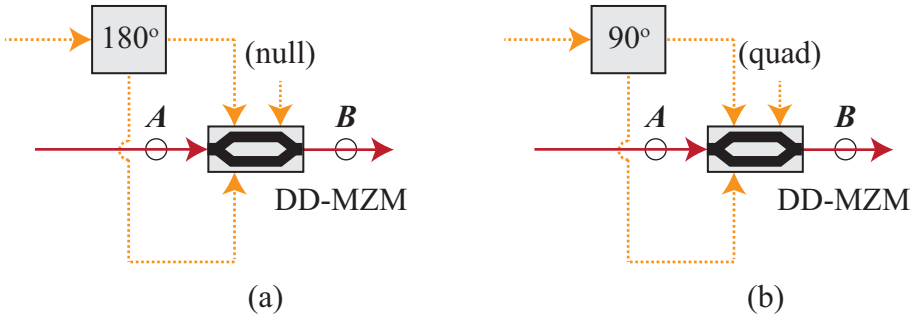

Figure 3.10: Schematic representation of (a) OCS generation and (b) SSB generation using a DD-MZM.

performance were not considered. Although not derived here, they are mentioned for completeness. An ideal MZM exhibits zero chirp, which is defined as the ratio of intensity-modulation to phase-modulation. However, due to unbalanced optical power splitting ratios and/or unbalanced RF modulation efficiencies, z-cut MZMs exhibit chirp [126]. These imbalances also contribute to the finite DC extinction ratio in practical MZM devices. A model for characterizing chirp of a DD-MZM having a finite DC extinction ratio is reported in [127].

3.7 Fiber Bragg Grating

A fiber Bragg grating (FBG) is a periodic disturbance of the refractive index over the length of a section of optical fiber. When the wavelength of the optical signal into the FBG satisfies the Bragg condition, it is reflected. In principle, all other wavelengths are transmitted. The Bragg condition is given by

$$\lambda_B = 2n_{eff}\Lambda \tag{3.24}$$

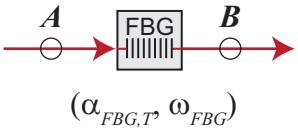

Figure 3.11: Schematic representation of a FBG.

where λ_B is the Bragg wavelength, n_{eff} is the effective refractive index of the fiber, and Λ is the grating period. The characteristics of FBGs are best modeled using coupled-mode theory [128], which is not presented in this dissertation. FBGs have a uniform or a chirped pitch depending on their intended application. In addition, the refractive index profile can be uniform or apodized.

FBGs can be used for add/ drop multiplexing in wavelength division multiplex (WDM) systems [129] or dispersion compensation [130]. In RoF links, optical carrier suppression implemented with FBGs has been shown to improve the optical receiver sensitivity by increasing the effective modulation depth [104, 131].

In this dissertation, FBGs will be modeled as perfect rectangular filters scaled only by their insertion losses. A schematic representation of a uniform fiber Bragg grating is shown in Fig. 3.11 where $\alpha_{FBG,T}$ is the insertion loss in transmission and ω_{FBG} is the center wavelength of the FBG.

FBGs can be used as to perform optical notch filtering as shown in Fig. 3.12. In this simplified example, an optical field is applied to port A of the FBG and the transmitted optical signal emerging from port B and the reflected optical signal emerging from port A are shown as referenced to Fig. 3.11. Since the reflected signal propagates in the opposite direction as the applied signal, it is designated with a

prime symbol. The FBG transfer function is denoted as $H_{FBG}(\omega)$.

In this example, the signals shown in Fig. 3.12 are the frequency-domain representations of the time-domain waveforms given by $u_A(t)$ and $u_B(t)$. The frequency- and time-domain representations are related to each other through the Fourier transform. For reference, the Fourier transform convention that will be used is

$$U(\omega) = \int_{-\infty}^{\infty} u(t)\, e^{-j\omega t} dt. \tag{3.25}$$

Based on Eq. (3.25), the corresponding inversion relation is

$$u(t) = \frac{1}{2\pi} \int_{-\infty}^{\infty} U(\omega)\, e^{j\omega t} d\omega. \tag{3.26}$$

3.8 Optical Circulator

Optical circulators (OCs) are non-reciprocal devices that can be used for separating a reflected or backward traveling signal. The schematic representation of an optical circulator is shown in Fig. 3.13. In general, each of the ports on an optical circulator is an input for optical fields directed into the circulator and an output for optical fields directed out of the circulator. However, in practice many circulators have only one port that is intended for bi-directional operation. In Fig. 3.13, port

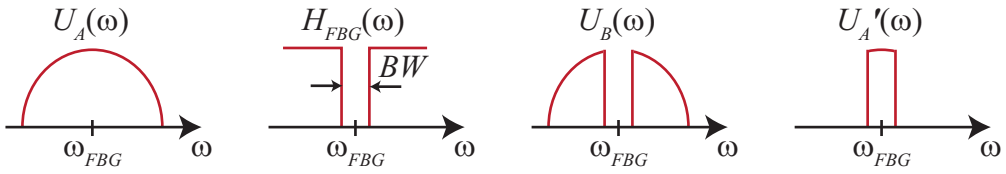

Figure 3.12: Diagram illustrating optical notch filtering with a FBG.

A is shown as an input and ports B and C are shown as outputs. Mathematically, the transfer function of a generalized optical circulator is given by

$$\begin{bmatrix} u'_A(t) \\ u'_B(t) \\ u'_C(t) \end{bmatrix} = \left(\sqrt{\alpha_{OC}} \begin{bmatrix} 0 & 0 & 1 \\ 1 & 0 & 0 \\ 0 & 1 & 0 \end{bmatrix} \right) \begin{bmatrix} u_A(t) \\ u_B(t) \\ u_C(t) \end{bmatrix} \tag{3.27}$$

where $u'_i(t)$ represents the output field from the i^{th} port, $u_i(t)$ represents the input field from the i^{th} port, and α_{OC} is the insertion loss optical circulator.

An optical isolator can be formed by sinking one of the ports. For example, if port C is connected to an optical sink and the input signal is applied to port A, then the output signal will be routed to port B. Conversely, if a signal is applied to port B, it will be directed to the sink at port C, isolating port A from port B in the reverse direction.

Circulators are often used in RoF links for optical reuse [51,132,133]. Optical circulators can be combined with FBGs to implement a narrow bandwidth optical BPF as shown in Fig. 3.14. In this configuration, the total optical circulator loss is doubled since the light is routed through the circulator twice. Furthermore, the loss of the FBG is the loss due to imperfect reflection loss ($\alpha_{FBG,R}$) rather than

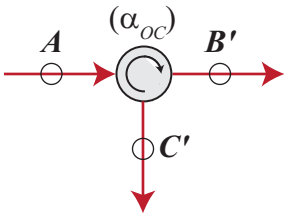

Figure 3.13: Schematic representation of an optical circulator.

transmission loss ($\alpha_{FBG,T}$).

3.9 EDFA

C-band optical amplifiers come in two main flavors, namely, Erbium-doped fiber amplifiers (EDFAs) and semiconductor optical amplifiers (SOAs). Of these, EDFAs are more commonly used in RF photonics work due to their better performance, which include higher gains and lower noise figures (NFs). However, SOAs can be advantageous in scenarios where size, weight, and power (SWaP) considerations are restrictive.

An EDFA works by exciting Erbium atoms in a doped optical fiber with an optical pump, most commonly around 980 nm although 1480 nm can also be used. The C-band optical signal is coupled with the pump light and propagated through a length of Erbium-doped fiber. The C-band optical signal is amplified by the excited ions through stimulated emission.

In addition to amplifying the input signal, EDFAs also produce noise due to amplified spontaneous emission (ASE). From quantum theory, it can be shown that

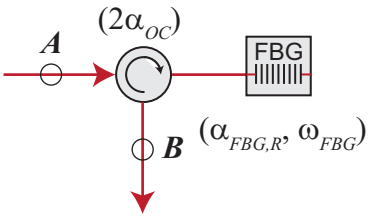

Figure 3.14: Diagram illustrating the implementation of a FBG-based optical BPF.

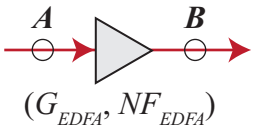

Figure 3.15: Schematic representation of an EDFA.

the theoretical minimum NF of an EDFA is 3 dB. That is, the signal-to-noise ratio (SNR) at the EDFA output is 3 dB lower than the SNR at the input [134, 135].

EDFAs can be operated in the linear regime or in compression. In some cases, it is desirable to operate the amplifier in saturation to reduce the noise figure and increase the gain of an analog link. The tradeoffs of using a highly compressed EDFA in analog links is analyzed in [136].

The schematic representation of an EDFA is shown in Fig. 3.15. This symbol could also be used to represent a SOA, however, in this dissertation EDFAs are exclusively utilized.

3.10 Optical Bandpass Filter

An ideal optical bandpass filter (BPF) completely transmits light within the bandwidth (BW) of the filter and completely extinguishes light outside the BW of the filter. In the frequency domain, a BPF can be represented by a boxcar function. Practical BPFs introduce non-zero insertion losses and do not completely suppress frequency components outside of the bandwidth of the filter. Tunable optical BPFs are also available and are often used after optical amplification to suppress out-of-

band noise (i.e. ASE suppression). A schematic representation of an optical BPF is shown in Fig. 3.16.

3.11 Polarization Controller

One of the parameters describing a transverse electromagnetic wave is its state of polarization (SOP). A transverse electromagnetic wave can be described in terms of two orthogonal polarization components. If the propagation direction of the wave is defined as the y-direction, then it can be polarized in the x-direction, the z-direction, or a superposition of the two. In fiber optic communications, light polarized in the z-direction is labeled transverse magnetic (TM) and light polarized in the x direction is labeled transverse electric (TE).

As standard optical fiber is radially symmetric, it can support TE and TM light equally as well. However, lasers typically emit linearly polarized light and the efficiency of electrooptic modulators is a function of the SOP. Thus, in many scenarios, it is important to be able to control the polarization at certain points in the RF photonic system.

In a laboratory environment, manual polarization controllers (PCs) are often

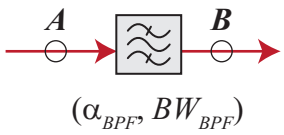

Figure 3.16: Schematic representation of an optical BPF.

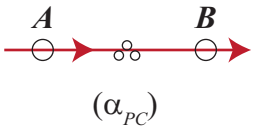

Figure 3.17: Schematic representation of a polarization controller.

used to adjust the SOP. However, as the SOP in a standard optical fiber is typically a random function of time, manual polarization controllers have limited utility in deployed systems. Automatic polarization trackers are available to maintain a constant SOP at the output port. The generic symbol for a polarization controller having insertion loss α_{PC} is shown in Fig. 3.17.

In this dissertation, the models assume that the SOP has been adjusted to achieve maximum electrooptic conversion efficiency.

3.12 Optical Fiber

Optical fiber is a cylindrical dielectric waveguide that supports the propagation of light. The two main components of a simple fiber are its core and its cladding. If the refractive index of the core is selected to be higher than that of the cladding, then light can be confined in the core through total internal reflection. In principle, the cladding of a dielectric core fiber could be air; however, as some of the optical mode propagates in the cladding, any lossy material in contact with the core will result in optical losses [119]. The number of optical modes supported by the fiber at a given wavelength can be engineered by designing the index difference between

the core and the cladding and core diameter.

Commercially available optical fibers are made out of silica, plastic, or a combination of the two. Silica fibers offer considerably lower losses than plastic optical fibers (POFs) are the choice for most telecommunication applications. The phase velocity of light propagating through the fiber depends on the wavelength. This phenomenon is termed chromatic dispersion and is characterized by the dispersion parameter, D. Additional sources of dispersion include modal dispersion and polarization mode dispersion.

In theory, the SOP of the light at the input of the fiber is maintained over the length of the fiber. However, static and time-varying stresses along the length of the fiber will cause the SOP to vary along the length of the fiber in a random manner. Stress rods can be incorporated in the fiber to break the radial symmetry of the fiber and preserve the polarization state of light propagating in the fiber. Such fibers are called polarization-maintaining fibers (PMFs).

For RF photonic applications, single-mode fibers (SMFs) are typically employed due the lack of modal dispersion. PMFs can also be used but they are more expensive and are more difficult to splice as the stress rods need to be aligned. The electrical-to-optical conversion efficiency of most commercial modulators is a function of the SOP of the light into the modulator. Thus, PMF is often used between the laser and modulator and between cascaded modulators.

The schematic representation of an optical fiber of length L with loss per unit length, α_F, and dispersion parameter, D, is shown in Fig. 3.18.

Another important topic that should be considered for high-power and/ or

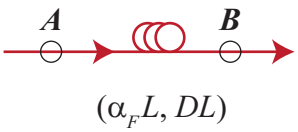

Figure 3.18: Schematic representation of an optical fiber.

long-haul optical transmission is fiber nonlinearities. Excellent references on this topic are available such as [99, 137].

3.12.1 Chromatic Dispersion

In an optical fiber, the propagation constant, β, is in general frequency dependent. Taylor expanding $\beta(\omega)$ around ω_0 yields

$$\beta(\omega) = \sum_{p=0}^{\infty} \frac{\beta^{(p)}(\omega_0)}{p!} (\omega - \omega_0)^p \tag{3.28}$$

where $\beta^{(p)}$ denotes the p^{th} derivative of $\beta(\omega)$ evaluated at ω_0 and $p!$ is the p^{th} factorial. Typically, Eq. (3.28) is written as

$$\beta(\omega) = \beta_0 + \beta_1(\omega - \omega_0) + \frac{\beta_2}{2}(\omega - \omega_0)^2 + ... \tag{3.29}$$

where β_0 is the phase delay, β_1 is the group delay, and β_2 is the group delay dispersion per unit length. The dispersion parameter can be related to the group delay dispersion through

$$D = -\frac{2\pi c \beta_2}{\lambda^2} \tag{3.30}$$

where λ is the optical wavelength and c is the speed of light in vacuo.

Chromatic dispersion causes the spectral components of an optical signal to propagate at different velocities, changing their phase-relation. Although generally

considered an impairment [98], dispersion can be used to convert ΦM-to-IM or vice versa. In 1986, Chraplyvy et al. demonstrated ΦM-to-IM conversion in a dispersive optical fiber [95].

In many RF photonic applications such as analog relay, the dispersion can cause RF signal fading, increased even-order distortion, and phase-to-intensity noise conversion [35]. The transfer function for optical fiber with dispersion and loss can be modeled as [97]

$$H(f) = \sqrt{\alpha_F L}\, e^{j2\pi^2 \beta_2 L f^2}. \tag{3.31}$$

For standard single-mode optical fiber near $\lambda = 1550$ nm, $\alpha_F \approx 0.2$ dB/km and $\beta_2 \approx 21.7 \times 10^{-27}$ s^2/m.

Chi et al. presented analytical models for phase-modulation based systems with ΦM-to-IM conversion. Assuming that $\alpha_F \approx 0$, the fiber length, L, should be selected to satisfy

$$L = \frac{(2n+1)}{4\pi} \frac{1}{\beta_2 f^2} \tag{3.32}$$

for efficient ΦM-to-IM conversion where f is the RF frequency and n is a positive integer [101].

Chapter 4

RF Photonic Receiver Theory

In this chapter, the theory behind two downconverting RF photonic receiver architectures is presented and analyzed. The two receivers utilize phase-modulation to encode the input signal onto an optical carrier. The first receiver is an extension of the work performed by Urick et al. on interferometric detection of phase-encoded optical signals. The second receiver is a continuation of the work performed by Haas et al. on phase-modulation to intensity-modulation (ΦM-to-IM) conversion with optical carrier suppression (OCS) using a fiber Bragg grating (FBG).

If a phase-modulated signal is incident on a square-law detector, only a DC photocurrent will result as proved in Eq. (3.20). This is because square-law detection, by definition, produces a signal that is proportional to the magnitude-square of the incoming signal. However, if the symmetry of the phase-modulated signal is altered by selectively attenuating or amplifying certain spectral components, then the resulting signal can no longer be represented as the product of the optical carrier and a complex exponential.

4.1 Phase-Detection Using a MZI

Urick et al. demonstrated that a phase-modulated signal can be detected using a thermally tuned asymmetric-delay Mach-Zehnder interferometer (MZI) as

shown in Fig. 4.1 [5]. Since MZIs typically have two complementary outputs, balanced detection can be employed increasing the system gain and suppressing the common-mode noise. The phase-modulation, interferometric detection (ΦM-ID) technique offers improved performance over the traditional intensity-modulation, direct-detection (IM-DD) approach, including higher RF gain, lower noise figure (NF), and improved dynamic range (DR). However, unlike the IM-DD system, the enhanced performance is over a limited bandwidth due to the sinusoidal transfer function of the MZI [5].

In this dissertation, electrooptic (EO) downconversion is demonstrated based on cascaded phase-modulation with interferometric detection (CΦM-ID) [6]. The CΦM-ID link is an extension of the ΦM-ID architecture. The mathematical model is shown in Fig. 4.2.

Denoting the power and angular frequency of the optical carrier by P_L and ω_L, respectively, the optical signal at point A can be expressed as

$$u_A(t) = \sqrt{P_L}\, e^{j\omega_L t}. \tag{4.1}$$

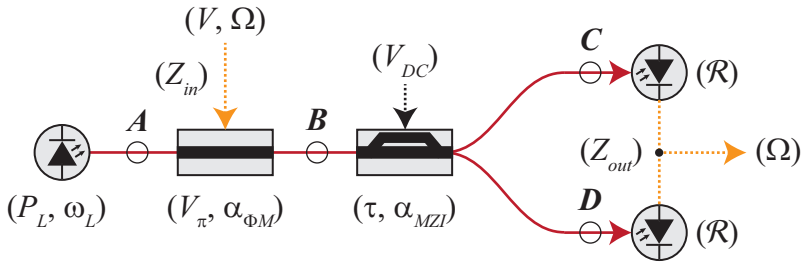

Figure 4.1: Mathematical model of the ΦM-ID link. After [5].

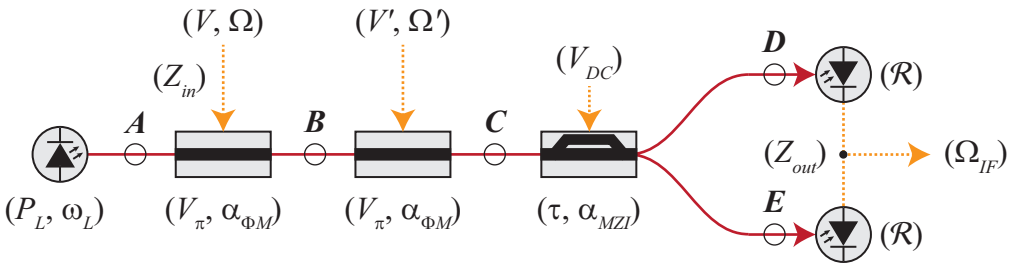

Figure 4.2: Mathematical model of the downconverting CΦM-ID link. After [6].

For simplicity, the case where the input and the LO signals are pure RF tones having angular frequencies Ω and Ω' is analyzed. Under this condition, the time-varying voltages applied to the two phase-modulators can be written as

$$v(t) = V \sin \Omega t \tag{4.2}$$

$$v'(t) = V' \sin \Omega' t. \tag{4.3}$$

Thus, the optical signal at point B is

$$u_B(t) = \sqrt{P_L}\sqrt{\alpha_{\Phi M}}\, e^{j\omega_L t} e^{jm \sin \Omega t} \tag{4.4}$$

where m is the modulation depth of the input signal defined in radians by

$$m \equiv \pi \frac{V}{V_\pi} \tag{4.5}$$

and V_π is the half-wave voltage of the phase-modulator. Likewise, the optical signal at point C is

$$u_C(t) = \sqrt{P_L}\alpha_{\Phi M}\, e^{j\omega_L t} e^{jm \sin \Omega t} e^{jm' \sin \Omega' t} \tag{4.6}$$

where m' is defined analogously as that given by Eq. (4.5) for m. The exponentiated sinusoids in Eq. (4.6) can be rewritten using the Jacobi-Anger expansion given by

Eq. (3.18), which is reproduced below as

$$e^{jz\sin\theta} = \sum_{p=-\infty}^{\infty} J_p(z)\, e^{jp\theta} \tag{4.7}$$

where $J_p(z)$ is the Bessel function of the first kind of order p and argument z as

$$u_C = \sqrt{P_L}\alpha_{\Phi M}\, e^{j\omega_L t} \sum_{p=-\infty}^{\infty}\sum_{q=-\infty}^{\infty} J_p(m)J_q(m')\, e^{j(p\Omega+q\Omega')t}. \tag{4.8}$$

The asymmetric MZI is an optical delay-line filter that produces two complementary output signals. In the frequency domain, the optical transfer functions relating the input to the complementary outputs of the MZI are

$$t_1(\omega) = \sin\left[\frac{(\omega-\omega_L)\,\tau+\theta}{2}\right] \tag{4.9}$$

$$t_2(\omega) = \cos\left[\frac{(\omega-\omega_L)\,\tau+\theta}{2}\right] \tag{4.10}$$

where t_1 corresponds to the transfer function relating the input to the upper output, t_2 corresponds to the transfer function relating the input to the lower output, τ is the group delay difference between the arms of the MZI, and θ is the bias phase offset. The free-spectral range (FSR) of the filter can be related to the group delay difference by $FSR = 1/\tau$. The filtered optical signal emerging from the upper arm of the asymmetric MZI can be expressed as

$$\begin{aligned} u_D &= \sqrt{P_L}\alpha_{\Phi M}\sqrt{\alpha_{MZI}}\, e^{j\omega_L t} \\ &\times \sum_{p=-\infty}^{\infty}\sum_{q=-\infty}^{\infty} J_p(m)J_q(m')\, e^{j(p\Omega+q\Omega')t} \sin\left[\frac{(p\Omega+q\Omega')\,\tau+\theta}{2}\right] \end{aligned} \tag{4.11}$$

with a similar expression for $u_E(t)$. The intermediate frequency (IF) of the down-converting CΦM-ID link is defined as

$$\Omega_{IF} = |\Omega - \Omega'|. \tag{4.12}$$

Choosing Ω' to be in the vicinity of Ω, the group delay of the MZI should be chosen to satisfy

$$\tau^{(opt)} = \frac{\pi}{\Omega'} \tag{4.13}$$

to achieve the highest downconversion gain and widest operational bandwidth. Furthermore, the bias should be adjusted to satisfy

$$\theta^{(opt)} = n\frac{\pi}{2} \tag{4.14}$$

where n is odd. Selecting $\theta = 0$, the optical carrier and odd-order sidebands of $u_C(t)$ are routed to the upper output port, while the carrier and the even-order sidebands are routed to the lower output port.

The calculated optical spectrum of the twice phase-modulated optical signal and the complementary asymmetric MZI filter transmittance curves are plotted in Fig. 4.3 for the upper (sine function) and lower (cosine function) outputs of the interferometer for the case where $\theta = 0$ and $\tau = \pi/\Omega'$.

Since the LO was chosen to be close to the RF input signal frequency, Eq. (4.11) can be approximated as

$$\begin{aligned} u_D &= \sqrt{P_L}\alpha_{\Phi M}\sqrt{\alpha_{MZI}}\, e^{j\omega_L t} \\ &\times \sum_{\substack{p=-\infty \\ (p+q)\text{odd}}}^{\infty} \sum_{q=-\infty}^{\infty} (-1)^{(p+q-1)/2} J_p(m) J_q(m')\, e^{j(p\Omega+q\Omega')t}. \end{aligned} \tag{4.15}$$

The photocurrent generated in the upper square-law photodetector is given by

$$\begin{aligned} i_D(t) &= \mathcal{R}|u_D(t)|^2 \\ &= -\mathcal{R}P_L\alpha_{\Phi M}^2\alpha_{MZI} \sum_{\substack{p=-\infty \\ (p+q)\text{odd}}}^{\infty} \sum_{q=-\infty}^{\infty} \sum_{\substack{r=-\infty \\ (r+s)\text{odd}}}^{\infty} \sum_{s=-\infty}^{\infty} (-1)^{(p+q+r+s)/2} \\ &\times J_p(m) J_q(m') J_r(m) J_s(m')\, e^{j[(p-r)\Omega+(q-s)\Omega']t}. \end{aligned} \tag{4.16}$$

The Bessel functions can be expanded in an infinite power series for p a positive integer as

$$J_p(z) = \frac{z^p}{2^p\, p!}\left[1 - \frac{z^2}{(2)(2p+2)} + \frac{z^4}{(2)(4)(2p+2)(2p+4)} - \ldots\right] \tag{4.17}$$

where p is the order of the Bessel function of argument z [138]. For Bessel functions of integer order $p < 0$, the following mapping can be used

$$J_p(z) = (-1)^p J_{-p}(z). \tag{4.18}$$

In practice, the modulation depth produced by the input signal is generally small. For the case where $z \ll 1$, Eq. (4.17) can be approximated as

$$J_p(z) \approx \frac{z^p}{2^p\, p!}. \tag{4.19}$$

For small input signals ($m \ll 1$), the photocurrent in Eq. (4.16) can be Taylor

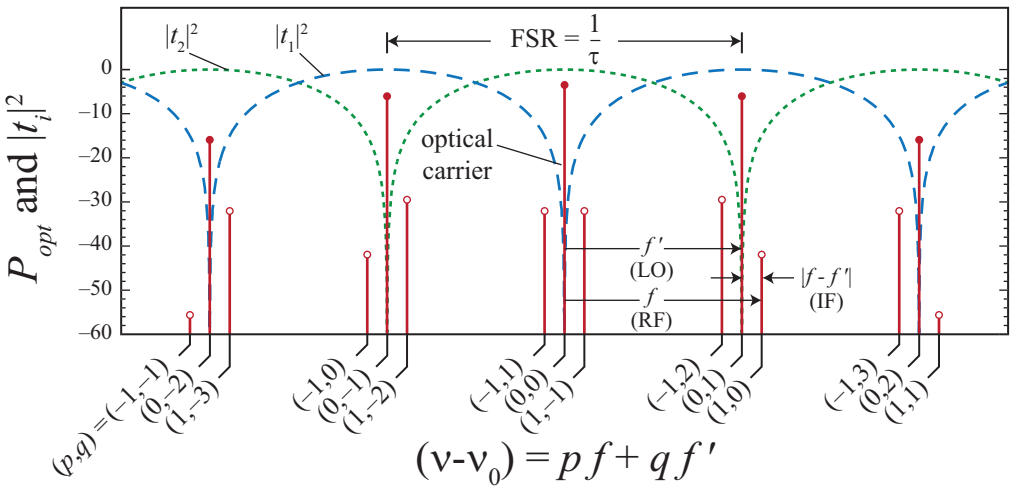

Figure 4.3: Calculated optical spectrum and complementary asymmetric MZI filter transmittance curves. After [6].

expanded to first-order in m using Eqs. (4.18)-(4.19). Performing the required algebraic steps and simplifying yields

$$i_D(t) = \mathcal{R}P_L \left\{ \frac{1}{2}\left[1 - J_0(2m')\right] + mJ_1(2m')\cos\Omega_{IF}t \right\}. \tag{4.20}$$

Assuming that the optical losses between the input and the two output ports of the MZI are nominally identical and subsequently invoking power conservation, it can be shown that

$$|u_D(t)|^2 + |u_E(t)|^2 = P_L\alpha_{\Phi M}^2\alpha_{MZI}. \tag{4.21}$$

This implies that the currents produced by the two photodetectors are complementary. Thus,

$$i_E(t) = \mathcal{R}P_L\alpha_{\Phi M}^2\alpha_{MZI} \left\{ \frac{1}{2}\left[1 + J_0(2m')\right] - mJ_1(2m')\cos\Omega_{IF}t \right\}. \tag{4.22}$$

The differential photocurrent produced by the balanced detector is

$$\begin{aligned} \Delta i(t) &= i_D(t) - i_E(t) \\ &= \mathcal{R}P_L\alpha_{\Phi M}^2\alpha_{MZI}\left[-J_0(2m') + 2mJ_1(2m')\cos\Omega_{IF}t\right]. \end{aligned} \tag{4.23}$$

If the differential photocurrent $\Delta i(t)$ drives a load with impedance Z_{out}, then the time-averaged downconverted power at the IF is given by

$$P_{IF} = 2\left[\mathcal{R}P_L\alpha_{\Phi M}^2\alpha_{MZI}mJ_1(2m')\right]^2 Z_{out}. \tag{4.24}$$

The time-averaged RF input power through an input impedance, Z_{in}, is

$$P_{RF} = \frac{1}{2}\frac{1}{Z_{in}}\left(\frac{mV_\pi}{\pi}\right)^2. \tag{4.25}$$

Taking the ratio of Eq. (4.24) to Eq. (4.25), the small-signal RF-to-IF downconversion gain of the link is

$$G_{RF-IF,C\Phi M-ID} = \left[\frac{2\pi\mathcal{R}P_L\alpha_{\Phi M}^2\alpha_{MZI}J_1(2m')}{V_\pi}\right]^2 Z_{out}Z_{in}. \tag{4.26}$$

The gain of a non-downconverting, quadrature-biased MZM IM-DD link can be shown to be (see Appendix A)

$$G_{RF,IM-DD} = \left(\frac{\pi\mathcal{R}P_L\alpha_{MZM}}{2V_\pi}\right)^2 Z_{out}Z_{in} \tag{4.27}$$

where α_{MZM} is the insertion loss of the MZM. The downconverting CΦM-ID gain in Eq. (4.26) can be expressed in terms of the IM-DD gain in Eq. (4.27) as

$$G_{RF-IF,C\Phi M-ID} = 16J_1^2(2m')\left(\frac{\alpha_{MZM}}{\alpha_{\Phi M}^2\alpha_{MZI}}\right)G_{RF,IM-DD}. \tag{4.28}$$

The maximum downconversion gain of the CΦM-ID link is achieved by choosing the LO modulation depth to maximize the factor $J_1(2m')$. This occurs at a LO modulation depth of $m' = 0.9206$ and corresponds to a link gain that is 7.34 dB higher than that of a comparable MZM link, if the losses in the modulators and the losses in the MZI are ignored. Assuming typical values for modulator and MZI insertion losses (i.e. $10\log_{10}\alpha_{\Phi M} = 10\log_{10}\alpha_{MZM} = 3$ dB and $10\log_{10}\alpha_{MZI} = 2$ dB), the gain of the downconverting CΦM-ID link is 2.34 dB higher than that of a comparable non-downconverting, quadrature-biased MZM IM-DD link.

Alternatively, the common-mode relative intensity noise (RIN) can be minimized by maximizing the current through one of the photodetectors and then setting the LO modulation depth at $m' = 1.202$. Relative to the maximum gain case, the common-mode noise suppression case results in approximately 1 dB lower gain.

If a two-tone RF signal consisting of two closely spaced tones at Ω_1 and Ω_2 is applied to the first phase-modulator, then the output will included third-order intermodulation distortion (IMD3) products at $|2\Omega_1 - \Omega_2 - \Omega'|$ and $|2\Omega_2 - \Omega_1 - \Omega'|$ in addition to the downconverted terms at $|\Omega_1 - \Omega'|$ and $|\Omega_2 - \Omega'|$. Extending the results of the preceding analysis, it can be shown that the downconverted difference photocurrent can be expanded to third-order as

$$\begin{aligned} \Delta i(t) &= \mathcal{R} P_L \alpha_{\Phi M}^2 \alpha_{MZI} \\ &\times \left[J_0(2m') + 2m_1 J_1(2m') \cos\left(\Omega_1 - \Omega'\right) t \right. \\ &- \left. m_1^2 m_2 J_1(2m') \cos\left(2\Omega_1 - \Omega_2 - \Omega_0\right) t \right] \\ &+ \text{similar terms at } (\Omega_2 - \Omega') \text{ and } (2\Omega_2 - \Omega_1 - \Omega') \end{aligned} \tag{4.29}$$

where m_i is the modulation depth corresponding to the tone at Ω_i where $i \in \{1, 2\}$ and only the leading contributions to each frequency component in Eq. (4.29) have been retained.

4.2 Phase-Detection with Optical Filtering

Haas and Murphy demonstrated that a phase-modulated signal can be down-converted and detected by cascaded phase-modulation and optical filtering (CΦM-OF). An optical fiber Bragg grating (FBG) can be used in transmission mode as a notch filter to suppress the optical carrier [9] or in reflection mode (with an optical circulator) as an optical bandpass filter (BPF) to transmit only certain optical sidebands [110]. With both these approaches, the optical carrier is suppressed prior to photodetection. The mathematical model for the notch filter configuration is shown

in Fig. 4.4.

One of the main disadvantages of using a FBG is that its bandwidth can limit the frequency response. In the notch filter configuration, the bandwidth of the FBG will attenuate low frequency components. To maximize the system bandwidth, the FBG should be centered on the optical carrier. This results in a lower cutoff frequency approximately equal to the half width at half maximum (HWHM) bandwidth of the FBG.

In this dissertation, the optical notch filter configuration is studied and extended to allow for harmonic downconversion. Furthermore, a technique to electrooptically linearize the link is presented [8, 139]. Although not the main focus of this dissertation, linearization is an important topic for high-fidelity analog transport. Finally, a method for vector demodulation based on this technique is presented based on the work reported in [7, 10].

Following Eqs. (4.1)-(4.7), the optical signal at point C can again be expressed

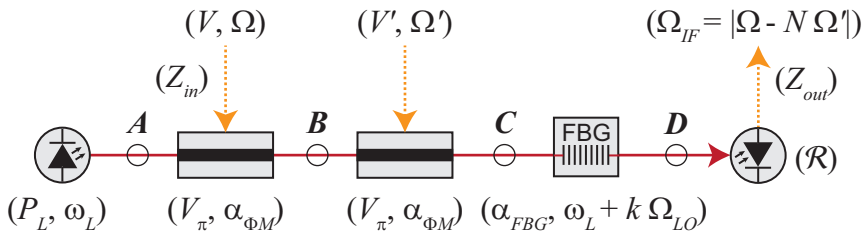

Figure 4.4: Mathematical model of the CΦM-OF link with harmonic downconversion.

as Eq. (4.8), which for convenience is reproduced below

$$u_C = \sqrt{P_L}\alpha_{\Phi M} \sum_{p=-\infty}^{\infty} \sum_{q=-\infty}^{\infty} J_p(m) J_q(m')\, e^{j(p\Omega+q\Omega')t}. \tag{4.30}$$

In general, the optical notch filter can be positioned to block the k^{th} optical sideband. For the OCS case, $k = 0$. The optical notch filter can be mathematically modeled by excluding those terms in Eq. (4.30) for which $Np + q = k$ where N is defined here as the electrooptic harmonic downconversion number. Applying this constraint to Eq. (4.30) yields

$$u_D(t) = \sqrt{P_L}\alpha_{\Phi M}\sqrt{\alpha_{FBG,T}}\, e^{j\omega_L t} \sum_{\substack{p \\ (Np+q\neq k)}} \sum_{q} J_p(m) J_q(m')\, e^{j(p\Omega+q\Omega')} \tag{4.31}$$

where $\alpha_{FBG,T}$ is the out-of-band insertion loss of the FBG in transmission mode. Following the FBG, the optical field is detected by a square-law photodetector having responsivity $\mathcal{R}$ to produce a photocurrent given by

$$\begin{aligned} i_{Nk}(t) &= \mathcal{R}|u_D(t)|^2 \qquad (4.32) \\ &= \mathcal{R}P_L\alpha_{\Phi M}^2\alpha_{FBG,T} \sum_{\substack{p \\ (Np+q\neq k)}} \sum_{q} \sum_{\substack{r \\ (Nr+s\neq k)}} \sum_{s} J_p(m) J_q(m') J_r(m) J_s(m')\, e^{j[(p-r)\Omega+(q-s)\Omega']t}. \end{aligned}$$

For fundamental downconversion with optical carrier suppression, $(N, k) = (1, 0)$. Applying this constraint to Eq. (4.32) yields

$$i_{10}(t) = \mathcal{R}P_L\alpha_{\Phi M}^2\alpha_{FBG,T} \sum_{\substack{p \\ (p+q\neq 0)}} \sum_{q} \sum_{\substack{r \\ (r+s\neq 0)}} \sum_{s} J_p(m) J_q(m') J_r(m) J_s(m')\, e^{j[(p-r)\Omega+(q-s)\Omega']t}. \tag{4.33}$$

The restricted summation in Eq. (4.33) can be written as the difference of two

full summations

$$\begin{aligned} i_{10}(t) &= \mathcal{R}P_L\alpha_{\Phi M}^2\alpha_{FBG,T} \\ &\times \left\{\sum_p J_p(m)\, e^{jp\Omega t}\sum_q J_q(m')\, e^{jq\Omega' t}\sum_r J_r(m)\, e^{-jr\Omega t}\sum_s J_s(m')\, e^{-js\Omega' t}\right. \\ &- \left.\sum_p\sum_r J_p(m)J_{-p}(m')J_r(m)J_{-r}(m')\, e^{j(p-r)(\Omega-\Omega')t}\right\}. \end{aligned} \tag{4.34}$$

From Eq. (4.7), it is clear that the first term in Eq. (4.34) evaluates to unity. Thus, Eq. (4.34) can be simplified as

$$i_{10}(t) = \mathcal{R}P_L\alpha_{\Phi M}^2\alpha_{FBG,T}\left\{1 - \sum_p\sum_r J_p(m)J_{-p}(m')J_r(m)J_{-r}(m')\, e^{j[(p-r)(\Omega-\Omega')]t}\right\}. \tag{4.35}$$

The DC photocurrent component can be found by including only the terms in Eq. (4.35) where $p - r = 0$ as

$$I_{DC} = \mathcal{R}P_L\alpha_{\Phi M}^2\alpha_{FBG,T}\left[1 - \sum_p J_p^2(m)J_p^2(m')\right]. \tag{4.36}$$

Only the AC terms in Eq. (4.35) oscillating at $\Omega_{IF} = |\Omega - \Omega'|$ contribute to the downconversion current at the IF. This is equivalent to setting $p - r = \pm 1$ and neglecting any DC components. In this case,

$$\begin{aligned} i_{10}(t)|_{\Omega_{IF}} &= \mathcal{R}P_L\alpha_{\Phi M}^2\alpha_{FBG,T} \\ &\times \left[\sum_p J_p(m)J_{-p}(m')J_{p-1}(m)J_{1-p}(m')\, e^{j\Omega_{IF}t} + c.c.\right]. \end{aligned} \tag{4.37}$$

For small RF modulation depths ($m \ll 1$), Eq. (4.36) and Eq. (4.37) can be Taylor expanded using Eqs. (4.18)-(4.19). Expanding Eq. (4.36) and Eq. (4.37) to first-order in m yields

$$I_{DC} \approx \mathcal{R}P_L\alpha_{\Phi M}^2\alpha_{FBG,T}\left[1 - J_0^2(m')\right] \tag{4.38}$$

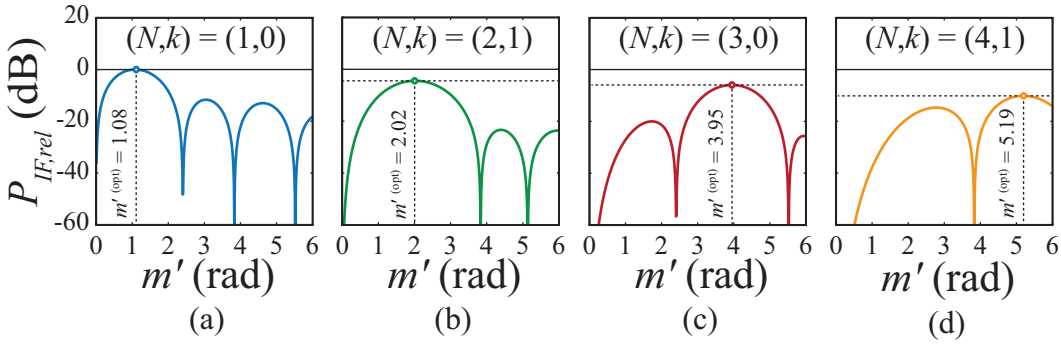

Figure 4.5: Calculated relative downconverted IF power as a function of LO modulation depth for the CΦM-OF link.

$$
\begin{aligned}
i_{10}(t)|_{\Omega_{IF}} &\approx 2\mathcal{R}P_L\alpha_{\Phi M}^2\alpha_{FBG,T}\, mJ_0(m')J_1(m')\cos\Omega_{IF}t \qquad (4.39)\\
&\approx \mathcal{R}P_L\alpha_{\Phi M}^2\alpha_{FBG,T}\, m\eta_{10}\cos\Omega_{IF}t
\end{aligned}
$$

where $\eta_{10} \equiv 2J_0(m')J_1(m')$ is defined here as the downconversion factor for $(N,k) = (1,0)$. To first-order in m, the time-averaged downconverted output power at the IF is given by

$$P_{IF} = 2\left[\mathcal{R}P_L\alpha_{\Phi M}^2\alpha_{FBG,T}mJ_0(m')J_1(m')\right]^2 Z_{out}. \qquad (4.40)$$

The time-averaged RF input power through an input impedance, Z_{in}, is given by Eq. (4.25). Taking the ratio of Eq. (4.40) to Eq. (4.25), the small-signal RF-to-IF downconversion gain of the link is

$$
\begin{aligned}
G_{RF-IF,C\Phi M-OF} &= \left[\frac{2\pi\mathcal{R}P_L\alpha_{\Phi M}^2\alpha_{FBG,T}J_0(m')J_1(m')}{V_\pi}\right]^2 Z_{out}Z_{in} \qquad (4.41)\\
&= \left[\frac{\pi\mathcal{R}P_L\alpha_{\Phi M}^2\alpha_{FBG,T}}{V_\pi}\right]^2 Z_{out}Z_{in}\times\eta_{10}^2.
\end{aligned}
$$

Following the preceding analysis beginning at Eq. (4.32), the harmonic downconversion gain for $N \in \{1,2,3,4\}$ and $k \in \{0,1\}$ were calculated. The IF power relative

to the $(N,k)=(1,0)$ case are plotted as a function of LO modulation depth, m', in Fig. 4.5.

The maximum harmonic downconversion gains relative to the $(N,k)=(1,0)$ case have been tabulated and are provided in Table 4.1. The gain of a non-downconverting, quadrature-biased MZM IM-DD link was given in Eq. (4.27). The downconverting CΦM-OF gain in Eq. (4.41) can be expressed in terms of the IM-DD gain in Eq. (4.27) as

$$G_{RF-IF,C\Phi M-OF} = 16J_0^2(m')J_1^2(m')\left(\frac{\alpha_{MZM}}{\alpha_{\Phi M}^2\alpha_{FBG,T}}\right)G_{RF,IM-DD}. \tag{4.42}$$

The maximum downconversion gain of the CΦM-OF link is achieved by choosing the LO modulation depth, m', to maximize the factor $\eta_{10}(m')$. This occurs at $m'=1.08$ and corresponds to a link gain that is 2.64 dB higher than that of a comparable MZM link, if the losses in the modulators and the FBG are ignored. Assuming typical values for modulator and FBG insertion losses (i.e. $10\log_{10}\alpha_{\Phi M} = 10\log_{10}\alpha_{MZM} =$ 3 dB and $10\log_{10}\alpha_{FBG,T} = 1$ dB), the gain of the downconverting CΦM-OF link is

Table 4.1: CΦM-OF optimal parameters.

N	k	η_{Nk}	$m'^{(opt)}$	$20\log_{10}\lvert\eta_{Nk}^{(opt)}/\eta_{10}^{(opt)}\rvert$
1	0	$2J_0J_1$	1.08	0
2	1	$J_1J_3+J_1^2$	2.02	-4.4
3	0	$2J_0J_3$	3.95	-5.9
4	1	$J_1J_3+J_1J_5$	5.19	-10.2

-1.36 lower than that of a comparable non-downconverting, quadrature-biased MZM IM-DD link.

If Eq. (4.35) is Taylor expanded to third-order in m, then it can be shown that the resulting photocurrent for the $(N,k)=(1,0)$ case evaluates to

$$\begin{aligned} i_{10}(t)|_{\Omega_{IF}} &\approx \mathcal{R}P_L\alpha_{\Phi M}^2\alpha_{FBG,T} \\ &\times \left\{2mJ_0(m')J_1(m') - \frac{m^3}{4}\left[3J_0(m')J_1(m') - J_1(m')J_2(m')\right]\right\}\cos\Omega_{IF}t. \end{aligned} \tag{4.43}$$

The third-order distortion (TOD) product near the downconverted signal can be eliminated by appropriately setting the LO modulation depth, m'. Based on Eq. (4.43) it is clear that the linearization condition is

$$3J_0(m')J_1(m') - J_1(m')J_2(m') = 0. \tag{4.44}$$

The smallest value of m' that solves Eq. (4.44) was numerically found to be $m' = 2.17$. Compared with the maximum gain case ($m' = 1.08$), the RF-to-IF downconversion gain is 13.8 dB lower. Although not explicitly analyzed here, it can be shown that satisfying this linearization condition also eliminates the third-order intermodulation distortion products at $2f_1 - f_2 - f'$ and $2f_2 - f_1 - f'$, where f_1 and f_2 are the frequencies of a two-tone input signal [8].

The CΦM-OF system is designed to accommodate a wide range of possible input frequencies. In this case, chromatic dispersion limits the bandwidth, transmission length, and RF-to-IF downconversion gain. The mathematical model presented can be extended to include the effect of dispersive fiber between the first phase-modulator and the second phase-modulator. If the two phase-modulators are

separated by a fiber of length L, then to first-order, the amplitude of the downconverted photocurrent in Eq. (4.39) can be extended as

$$i_{10}(t)|_{\Omega_{IF}} \approx 2\mathcal{R}P_L\alpha_{\Phi M}^2\alpha_{FBG,T}\, mJ_0(m')J_1(m')\cos\Omega_{IF}t \times \cos\left(\frac{\pi LD}{c}\lambda_L^2 f^2\right) \quad (4.45)$$

where D is the chromatic dispersion of the fiber expressed in units of ps/nm·km and f is the RF frequency.

According to Eq. (4.45), the downconverted signal will be completely extinguished when the dispersion and frequency satisfy the following relationship

$$\frac{2L|D|}{c}\lambda_L^2 f^2 = (2p+1) \quad (4.46)$$

where $p = 0, 1, 2, 3, ...$ For the case of $|D| = 17$ ps/nm·km, $\lambda_L = 1552.470$ nm, and $f = 20$ GHz, the first null occurs at a fiber length of $L = 9.15$ km, and the 3 dB point occurs at $L = 4.58$ km.

Conversely, for a given fiber length, chromatic dispersion limits the maximum frequency that can be transmitted through a dispersive fiber of length L. The RF-to-IF downconversion gain is reduced by 3 dB at a frequency of

$$f = \frac{1}{2\lambda_L}\sqrt{\frac{c}{L|D|}}. \quad (4.47)$$

The analytical downconverted power is shown in Fig. 4.6 for $m = 0.16$ rad, $m' = 1.08$ rad, and $\mathcal{R}P_L\alpha_{\Phi M}^2\alpha_{FBG,T} = 3.9$ mA. This choice of parameters was chosen as it corresponds to experimentally measured values. Note that in particular, the total dispersion is a function of the signal frequency, f, fiber length, L, and chromatic dispersion, D. The calculated behavior agrees with that reported in the literature for phase-modulated links [95–98].

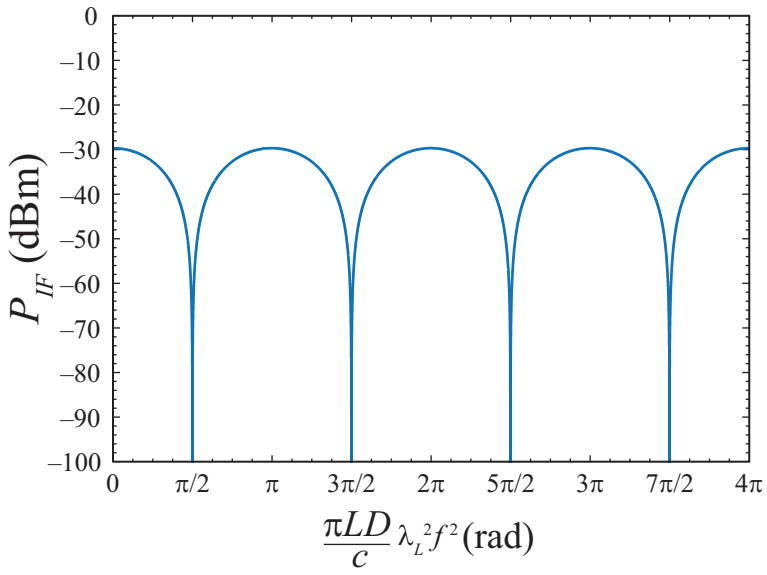

Figure 4.6: Calculated IF power dependence on fiber chromatic dispersion for fundamental downconversion using the CΦM-OF technique.

In Fig. 4.6, the effect of fiber loss is ignored. The effects of dispersion, loss, and dispersion plus loss on the normalized IF output power are plotted using common dispersion and loss parameters (i.e. $|D| = 17$ ps/nm·km and $\alpha_F = 0.2$ dB/km) for $\lambda_L = 1552.470$ nm and $f = 20$ GHz in Fig. 4.7. In this plot, a double-sideband (DSB) modulated signal was assumed. As is clear from Fig. 4.7, the loss due to ΦM-to-IM conversion can be eliminated by choosing an appropriate fiber length. For example, if the link length is $L = 27.5$ km, then an extra length of fiber of length $\Delta L = 8.3$ km can be added in order to access the next peak in transmission. However, the penalty in gain is 1.7 dB relative to a link of length $L = 27.5$ km without chromatic dispersion ΦM-to-IM conversion due to the added fiber loss.

Another configuration of interest is when the two phase-modulators are both

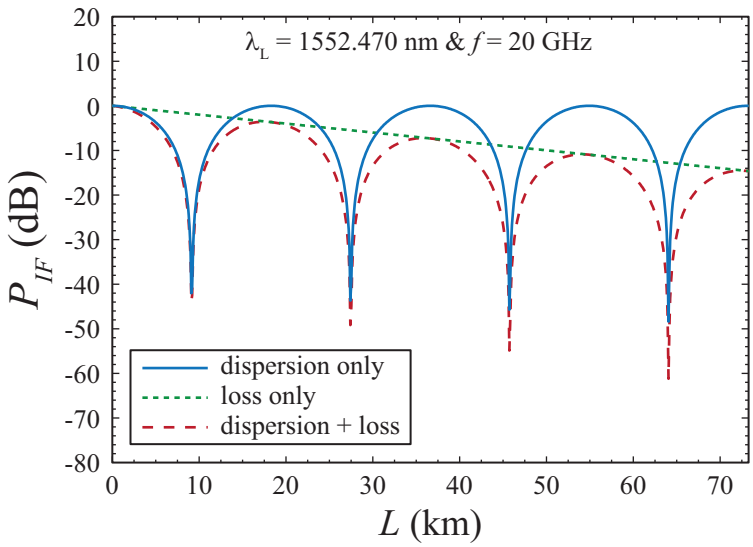

Figure 4.7: IF power dependence on loss and chromatic dispersion of a DSB optical signal over standard SMF.

co-located with the laser, which are then separated from the FBG and photodetector by a dispersive fiber. In this case, the analysis of the downconversion gain is slightly more complex [101]. Numerical simulations show, however, that although fading can occur under these conditions, the signal fading criterion is dictated primarily by the downconverted IF, at $f_{IF} = |f - f'|$.

In the case where $f = 20$ GHz, $f' = 19.6$ GHz, and $m' = 1.08$, we numerically calculate that the first null in transmission should occur at a length of $L \approx 200$ km. In this case, the optical fiber loss would be nearly 40 dB for standard single-mode fiber (SMF). Since the RF loss is twice the optical loss, the RF-to-IF gain would be reduced by nearly 80 dB.

The cascaded phase-modulation and optical filtering architecture shown in

Fig. 4.4 can be extended to perform vector demodulation [7, 10]. This can be accomplished by simply splitting the optical signal at point B and applying properly phased LO signals to the two LO phase-modulators as shown in Fig. 4.8.

The relative phase between the in-phase (I) and quadrature (Q) electrical LOs should be set to achieve $\theta = 90°/N$, where N is the harmonic downconversion number. An ideal 3 dB directional optical coupler reduces the photocurrent in each branch by a factor of $\epsilon = 1/2$. In addition, the coupler may have excess insertion losses. Thus, the preceding photocurrent results should be multiplied by a factor of $\alpha_{DOC}/2$.

For example, in the case of fundamental downconversion with OCS, $(N, k) =$

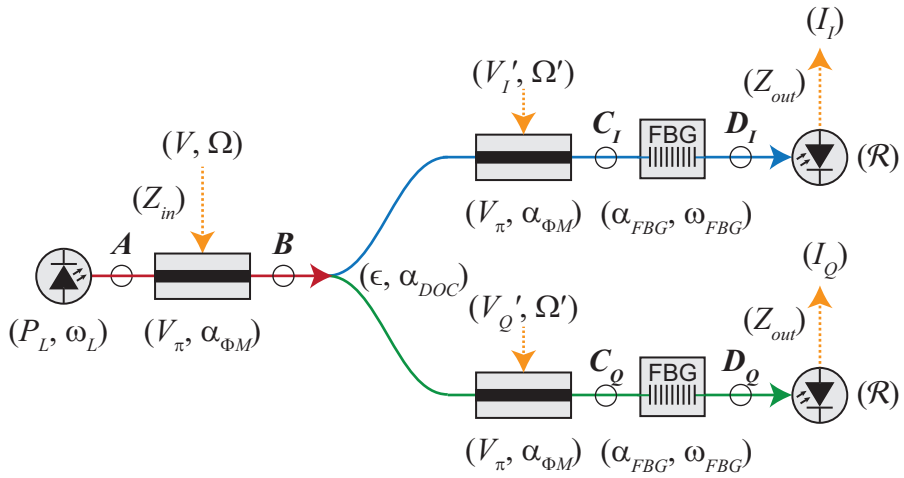

Figure 4.8: Mathematical model of the vector demodulating CΦM-OF with harmonic downconversion. After [7].

$(1,0)$, Eq. (4.39) becomes

$$i_{10,I}(t)|_{\Omega_{IF}} \approx \mathcal{R}P_L\alpha_{\Phi M}^2\alpha_{FBG,T}\alpha_{DOC}\, mJ_0(m')J_1(m')\cos\Omega_{IF}t \qquad (4.48)$$

$$i_{10,Q}(t)|_{\Omega_{IF}} \approx \mathcal{R}P_L\alpha_{\Phi M}^2\alpha_{FBG,T}\alpha_{DOC}\, mJ_0(m')J_1(m')\sin\Omega_{IF}t. \qquad (4.49)$$

For the results obtained in Eqs. (4.48)-(4.49), the relative phase difference between the I and Q LOs was set at $\theta = -90°$. As described previously, a harmonic of the LO can be used to achieve harmonic downconversion. Thus, harmonic vector demodulation can be achieved with this architecture.

Chapter 5

RF Photonic Receiver Results

In this chapter, the experimental results obtained with the two downconverting RF photonic receiver architectures analyzed in Chapter 4 are described. The two receivers utilize phase-modulation to encode the input signal onto an optical carrier. The first receiver is an extension of the work performed by Urick et al. on interferometric detection of phase-encoded optical signals. The second receiver is a continuation of the work performed by Haas et al. on phase-modulation to intensity modulation (ΦM-to-IM) conversion using optical carrier suppression (OCS) with a fiber Bragg grating (FBG).

5.1 Phase-Detection Using a MZI

The cascaded phase-modulation with interferometric detection (CΦM-ID) link shown in Fig. 4.2 was constructed using commercially available components. A narrow linewidth (< 3 kHz) fiber laser having a center wavelength of $\lambda_L = 1552.470$ nm and an output power of $P_L = 21$ dBm was used as the optical source. The output of the fiber laser was sent into two serially connected 40 GHz $LiNbO_3$ optical phase-modulators through short lengths of polarization maintaining fiber (PMF). The first phase-modulator had a measured V_π of 3.4 V at 7 GHz and the second phase-modulator had a measured V_π of 4.4 V at 6 GHz.

Two RF synthesizers were connected to the first phase-modulator through an RF hybrid to generate a pair of closely spaced microwave tones. Three-port ferrite circulators were inserted between the RF synthesizers and the hybrid in order to isolate the synthesizers and to mitigate RF reflections. A third RF synthesizer was used as the LO and was directly connected to the second phase-modulator.

The twice modulated optical signal was sent into an all-fiber, delay-line, asymmetric Mach-Zehnder interferometer (MZI) having a free-spectral range (FSR) of 12 GHz. The complementary outputs from the MZI were connected to a 20 GHz balanced photodetector having internal terminating resistors ($Z_{int} = Z_{out} = 50\ \Omega$). The electrical power at the intermediate frequency (IF) was measured using an electrical spectrum analyzer (ESA) and the DC photocurrents were monitored independently using two ammeters. The MZI bias phase, θ, was adjusted thermally through resistive heating.

For the first measurement, the first modulator was driven by a single microwave tone having a frequency of $f = 7.00$ GHz and producing a modulation depth of $m = 0.1$ rad. An electrical LO having a frequency of $f' = 6.00$ GHz was applied to the second phase-modulator. Prior to applying the RF and LO tones, the MZI differential delay was adjusted until all of the DC photocurrent was generated in one of the two photodiodes in the balanced photodetector.

The LO was then applied and the modulation depth, m', was adjusted such that the magnitudes of the current through the two photodiodes were equal ($m' \approx 1.2$ rad). The resulting electrical spectra is shown in Fig. 5.1. It should be noted that the magnitudes of the frequency components were not normalized to account

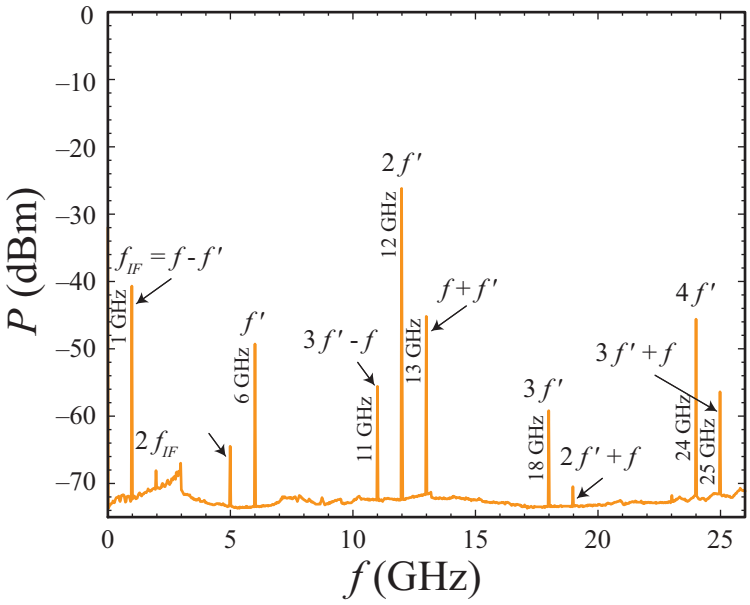

Figure 5.1: Measured electrical spectrum at the output of the CΦM-ID link for a single-tone input signal.

for photodetector roll-off or frequency dependent cable losses.

In the second experiment, the first modulator was driven with two closely spaced microwave tones having frequencies of $f_1 = 6.99$ GHz and $f_2 = 7.01$ GHz and the second modulator was driven by a microwave signal having frequency $f' = 6.00$ GHz. The same series of steps previously described were performed to bias the MZI. The downconverted signals at $f_1 - f' = 990$ MHz and $f_2 - f' = 1010$ MHz along with the third-order intermodulation distortion (IMD3) signals at $2f_1 - f_2 - f' = 970$ MHz and $2f_2 - f_1 - f' = 1030$ were measured with an electrical spectrum analyzer (ESA). The IF and IMD3 power per tone as functions of the input RF power per tone are shown in Fig. 5.2.

A simulation of this architecture was performed numerically in MATLAB® by

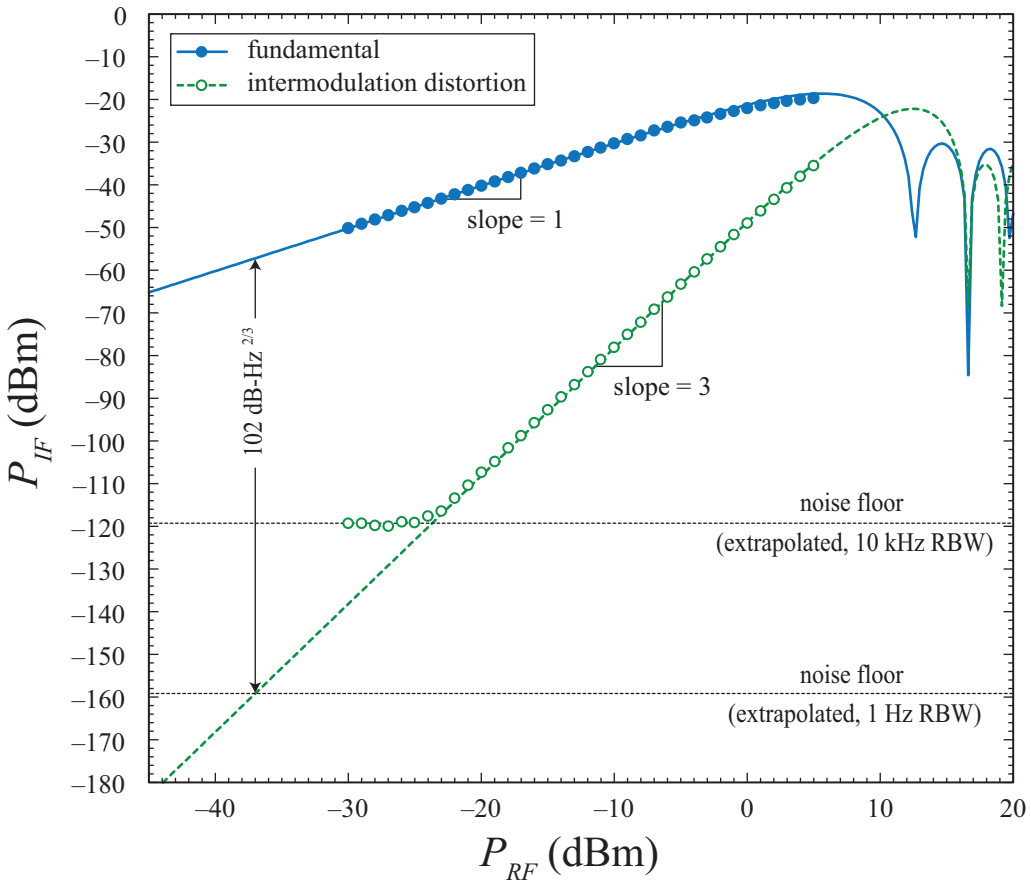

Figure 5.2: Measured (symbols) and simulated IF and IMD3 powers as functions of the RF power for a two-tone signal downconverted for the CΦM-ID link. After [6].

taking the fast Fourier transform (FFT) of the optical field at point C for the case of a two-tone input signal. In the frequency domain, the optical spectrum at $U_c(\omega)$ was multiplied by the frequency domain transfer functions of the MZI given by Eqs. (4.9)-(4.10). The magnitude squares of the inverse FFTs (IFFTs) of the filtered optical spectra, which correspond to $i_D(t)$ and $i_E(t)$, were then calculated. The difference photocurrent, $\Delta i(t)$, was evaluated as a function of the LO modulation depth, m', and then the IF and IMD3 powers were calculated. The analytical results are plotted along with the experimental results in Fig. 5.2.

5.2 Phase-Detection with Optical Filtering

Several experimental measurements based on the cascaded phase-modulation with optical filtering (CΦM-OF) architecture shown in Fig. 4.4 were performed. In the first set of experiments, the link was optically unamplified. A high-stability, narrow linewidth (< 3 kHz), fiber laser with a center wavelength of $\lambda_L = 1552.470$ nm was used as the optical source. The output of the laser was connected to the first phase-modulator through PMF. This phase-modulator was a 40 GHz, z-cut $LiNbO_3$ modulator with a measured V_π of 5.4 V at 20 GHz. The output of the first phase-modulator was connected to the input of the second phase-modulator through PMF. The second phase-modulator was nominally identical to the first, but it had a measured V_π of 4.1 V at 19.5 GHz.

The signal emerging from the second phase-modulator was sent through a FBG in transmission mode to suppress the optical carrier for fundamental down-

conversion, $(N, k) = (1, 0)$. The FBG was designed for add/ drop filtering of dense wavelength-division multiplexed (DWDM) channels with 25 GHz spacings. The filter suppressed the optical carrier by approximately 25 dB and had an out-of-band insertion loss of $\alpha_{FBG,T} = 2.5$ dB. The 3 dB bandwidth (BW) of the athermal FBG was measured to be approximately 14 GHz and the frequency offset between the optical carrier and the filter center frequency was less than 1 GHz. The optical output from the filter was connected to an InGaAs PIN photodiode having an internal termination resistor with $Z_{out} = Z_{int} = 50\ \Omega$ and a nominal 3 dB BW of 12 GHz.

Fig. 5.3 illustrates the downconversion process by showing the optical spectra measured at various points in the link. The optical spectra were captured using a high resolution Brillouin optical spectrum analyzer (BOSA) having a spectral resolution in the C-band of 80 fm (10 MHz). Readers interested in Brillouin scattering based optical spectrum analysis are referred to [140, 141]. The fiber laser spectrum is shown in Fig. 5.3(a) where P_L denotes the optical carrier power. The optical signal was modulated by a weak RF signal with power sufficient to produce a modulation depth of $m \approx 0.1$ rad. The process of phase-modulation produces spectral sidebands with intensities proportional to $J_p^2(m)$ at frequencies of $p \times f$ about the optical carrier where p is an integer as illustrated with the experimental results shown in Fig. 5.3(b). At the second phase-modulator, the optical signal is modulated by a strong microwave LO at $f' = 19.6$ GHz having sufficient power to produce a modulation depth of $m' \approx 1.08$. This generates additional optical sidebands with frequency spacings of $q \times f'$, where q is an integer, about each of the $p \times f$ frequency components previously generated. The resulting spectrum is shown in Fig. 5.3(c)

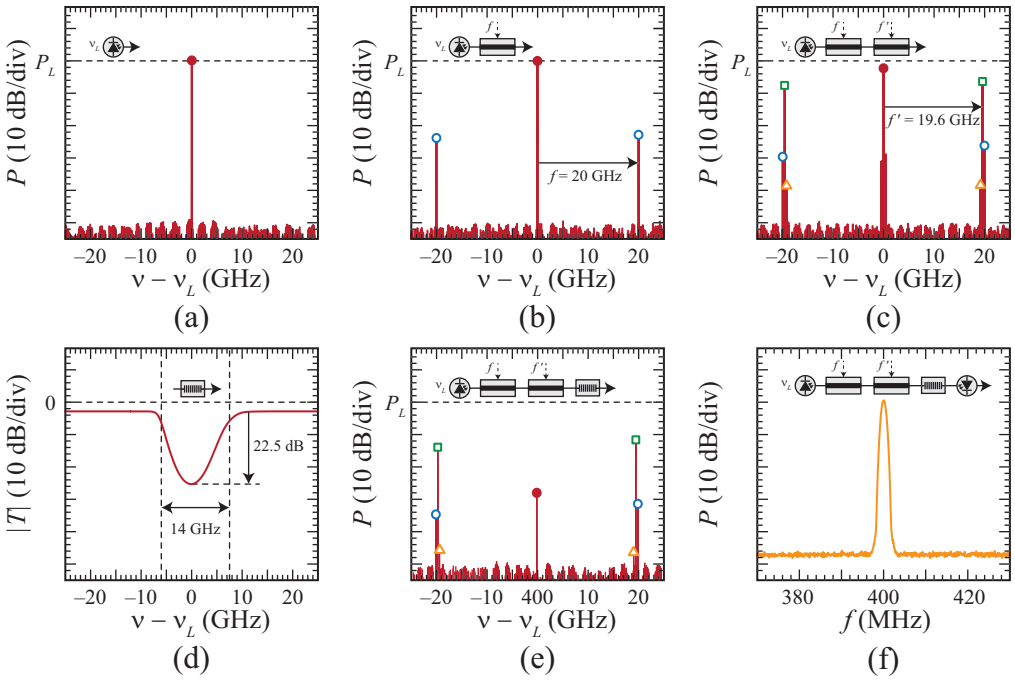

Figure 5.3: Experimental frequency domain characterization of the CΦM-OF link. (a)-(c) Optical spectra at points *A*-*C*, (d) FBG transmittance, (e) optical spectra at point *D*, and (f) IF power. After [8].

where each spectral component is proportional to $J_p^2(m)J_q^2(m')$.

The twice phase-modulated optical signal is then sent through a FBG configured in transmission mode with the optical transmittance shown in Fig. 5.3(d). The FBG suppressed the optical carrier for which $p + q = 0$ while allowing the optical sidebands to pass. The carrier suppressed optical spectrum is shown in Fig. 5.3(e). After optical notch filtering, the optical signal is detected by a square-law photodetector. The photocurrent contains terms at the downconverted IF of $\Omega_{IF} = |\Omega - \Omega'|$ that are proportional to the power of the RF input signal. Fig. 5.3(f) shows the measured electrical spectrum of the photodetected signal, which is clearly centered at the downconverted frequency of $f_{IF} = \Omega_{IF}/(2\pi) = 400$ MHz.

As discussed in Section 4.2, the downconverted signal power can be maximized by choosing $m' = 1.08$ rad. Ignoring the losses of the components, the maximum gain of the link is 2.6 dB higher than that of a non-downconverting IM-DD link based on a quadrature-biased MZM. If modulator insertion losses of $\alpha_{\Phi M} \approx \alpha_{MZM} \approx 3$ dB and a FBG insertion loss of $\alpha_{FBG} \approx 1$ dB are assumed, then the maximum gain of the link is -1.4 dB lower than a quadrature-biased IM-DD link. The analytical expressions for the DC photocurrent (I_{DC}), IF power (P_{IF}), and third-order IMD power (P_{IMD3}), along with experimental measurements (symbols) are shown in Fig. 5.4 for an input modulation depth of $m \approx 0.14$ rad.

Fig. 5.5(a) shows the electrical spectrum of the downconverted signal as measured for a LO modulation depth of $m' = 1.08$ rad, which corresponds to the maximum gain case. The IMD3 products are clearly visible at frequencies of $2f_1 - f_2 - f_0$ = 380 MHz and $2f_2 - f_1 - f_0 = 440$ MHz for a two-tone input signal consisting of

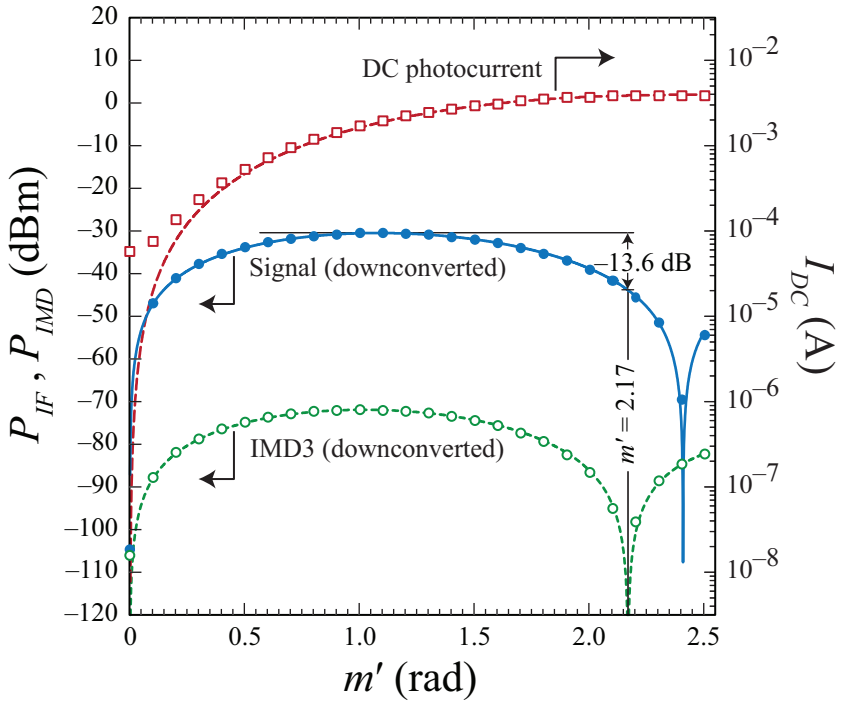

Figure 5.4: Measured (symbols) and theoretical DC photocurrent, IF power, and IMD3 power curves as functions of the LO modulation depth for the CΦM-OF link. After [8].

tones at $f_1 = 20.00$ GHz and $f_2 = 20.02$ GHz. The strengths of the two input tones were set equal and the LO frequency was set to $f' = 19.6$ GHz.

Alternatively, the link can be linearized by satisfying the condition given by Eq. (4.44). This corresponds to setting $m' = 2.17$ rad. The electrical spectrum for this case are shown in Fig. 5.5(b). The fundamental tones are experimentally reduced by 13.8 dB relative to their value shown in Fig. 5.5(a), which corresponds to the maximum gain case. This agrees quite well with the theoretical prediction of a 13.6 dB penalty in gain. In the linearized case, the IMD3 products fell below the noise floor of the ESA.

To demonstrate that the system was truly linearized, and not just simply attenuated, the input power per tone was increased by 13.8 dB to compensate for the penalty in gain. This case is shown in Fig. 5.5(c). It is clear from this figure that the IMD3 products are still suppressed below the noise floor of the ESA for the same output IF power as in Fig. 5.5(a). This confirms that, despite the penalty in gain, the linearization technique can in fact improve the dynamic range. When the IMD3 products are suppressed by setting $m' = 2.17$ rad, the residual sub-octave IMD products are expected to be dominated by fifth-order intermodulation distortion (IMD5). Thus, complete suppression of IMD products at $2f_1 - f_2 - f_0$ and $2f_2 - f_1 - f_0$ is not expected. However, the third-order dependence will be eliminated, reducing the total sub-octave IMD power and thereby increasing the spurious free dynamic range (SFDR). To verify this, the downconverted and IMD3 components were measured as functions of the input power.

Fig. 5.6 shows the output IF power per tone as a function of input RF power

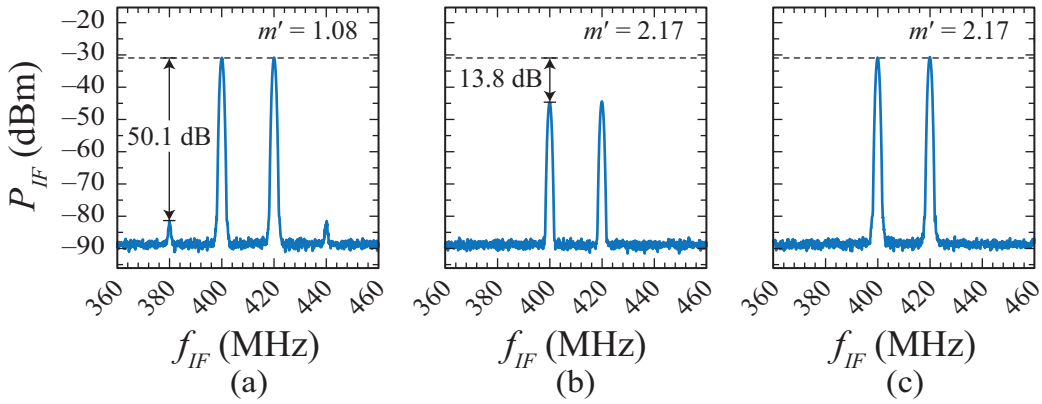

Figure 5.5: Measured downconverted electrical spectra illustrating third-order linearization of the CΦM-OF link. After [8].

per tone for microwave tones at $f_1 = 20.00$ GHz and $f_2 = 20.02$ GHz and a LO signal at $f' = 19.6$ GHz applied. For the simulated curves, the RF input power per tone was swept from P_{RF} = -40 dBm to +25 dBm. These curves were calculated by taking the FFT of Eq. (4.30) with a two-tone signal applied to the input (i.e. $v(t) = V(\sin\Omega_1 t + \sin\Omega_2 t)$). Then an ideal notch filter having a bandwidth of $BW_{FBG} = 10$ GHz centered at ω_L was multiplied by the FFT of Eq. (4.30). Finally, the IFFT of the resulting spectrum was calculated and the power at the IF and IMD3 frequencies were plotted. The parameter $\mathcal{R}P_L\alpha_{\Phi M}^2\alpha_{FBG,T}$ for the simulated curves was fit to the experimentally measured values, which are indicated by symbols in Fig. 5.6. The photodiodes had an internal terminating resistor, so the effective responsivity was $\mathcal{R} \to \mathcal{R}/2$.

The simulated and measured curves were obtained for two LO modulation depths, namely $m' = 1.08$ rad and $m' = 2.17$ rad. These LO modulation depths

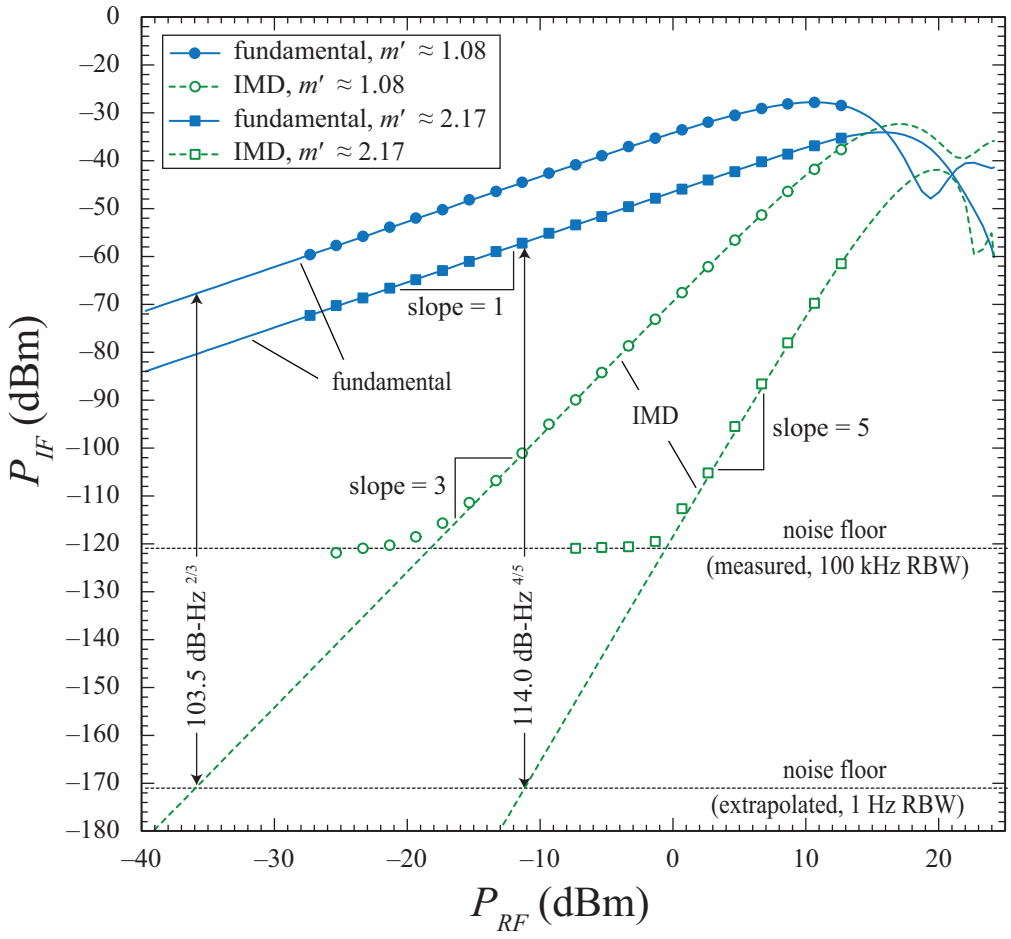

Figure 5.6: Measured (symbols) and simulated IF and IMD3 powers as functions of the RF power for a two-tone signal downconverted for the CΦM-ID link. After [8].

correspond to the maximum gain (circle symbols) and the linearized (square symbols) cases, respectively. In. Fig. 5.6, the curves corresponding to power at the IF are indicated by solid lines and the curves corresponding to power at the IMD3 frequencies are indicated by dashed lines.

All the measurements in Fig. 5.6 were taken with an ESA resolution bandwidth (RBW) of 100 kHz. The IMD3 products were measured using a low-noise IF preamplifier and a tunable RF bandpass filter at the output of the photodetector. The preamplifier was used to overcome the noise figure of the ESA and the filter was used to suppress the stronger fundamental tones from the weaker IMD tones for more accurate results. Despite the penalty in gain, the linearized SFDR was measured to be 114.0 dB-$Hz^{4/5}$, whereas the maximum gain SFDR was measured to be 103.5 dB-$Hz^{2/3}$. Thus, the SFDR has been increased by approximately 11 dB when extrapolated to a 1 Hz RBW and that the IMD products have been linearized to fifth-order, as indicated by the slope of the IMD products. This result confirms that the sub-octave IMD3 contributions have in fact been suppressed.

When calculating the RF-to-IF gain of the downconverting CΦM-OF link, an ideal notch filter that completely extinguished all of the terms in the vicinity of the carrier while fully transmitting all of the spectral sidebands was assumed. In practice, the bandwidth of the FBG used as the optical notch filter limits the lower frequency that can be relayed through the system. To experimentally investigate this effect, the downconversion gain was measured as a function of the input signal frequency.

The input RF tone was swept from 4 GHz to 34 GHz and the LO frequency was

simultaneously swept to maintain an output frequency of $f_{IF} = 400$ MHz. The LO modulation depth was set to achieve maximum RF-to-IF gain (i.e. $m' = 1.08$). Prior to performing the experiment, the half-wave voltages of the two phase-modulators were measured as functions of frequency so that the electrooptic conversion efficiency of the modulators could be factored out. Since the IF frequency was held constant, the frequency dependence of the photodetector was also eliminated. Thus, the bandwidth effects of the finite FBG width were isolated as shown in Fig. 5.7.

The gain was normalized relative to the reference value given by Eq. (4.27) for the lossless case where $\alpha_{MZM} = \alpha_{\Phi M} = \alpha_{FBG,T} = 1$. As before, the normalization was reduced by 6 dB ($\mathcal{R} \to \mathcal{R}/2$) to properly account for the presence of an internal $Z_{int} = Z_{out} = 50\ \Omega$ terminating resistor in the photodetector.

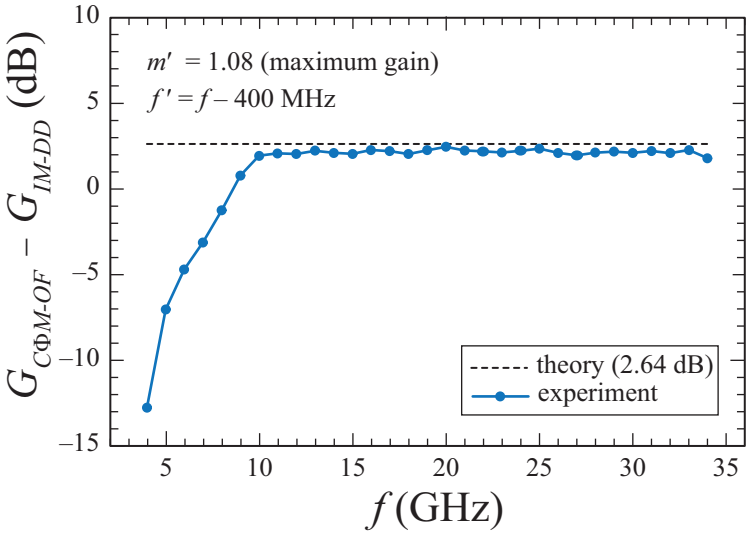

Figure 5.7: Measured and theoretical normalized downconversion gain curves as functions of RF frequency. After [8].

The dashed line in Fig. 5.7 shows the 2.64 dB downconversion gain of the CΦM-OF case as a function of the non-downconverting gain of an IM-DD link based on a quadrature-biased MZM. When the input signal frequency exceeded half the filter bandwidth, the experimentally measured gain closely approaches this theoretical value. As shown in Fig. 5.3(d), the FBG had a FWHM bandwidth of approximately 14 GHz. Therefore, when the input signal frequency fell below $f = 7$ GHz, the first-order optical sidebands were partially blocked by the filter, causing a reduction in RF-to-IF gain.

In the next set of experiments, harmonic downconversion at RF frequencies up to $f = 70$ GHz was demonstrated. The link was modified to include an Erbium-doped fiber amplifier (EDFA) as shown in Fig. 5.8.

A tunable CW laser with nominal output power of $P_L = 16$ dBm was used as the optical source. The output of the laser was connected to the first phase-modulator through PMF. The first phase-modulator was a 65 GHz, z-cut $LiNbO_3$ modulator with measured V_π s of 5.8 V at 20 GHz, 6.3 V at 40 GHz, and 7.6 V at 60

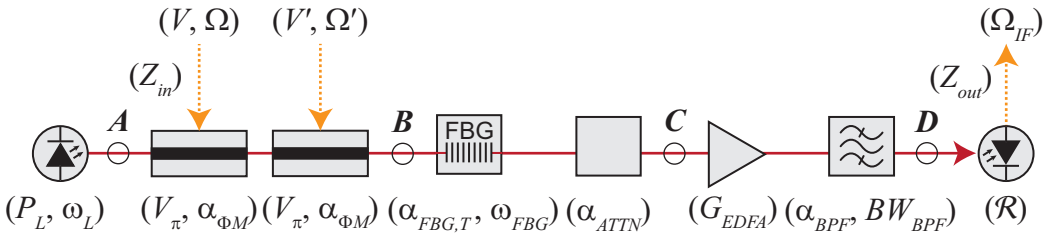

Figure 5.8: Mathematical model of the CΦM-OF link with optical amplification. After [9].

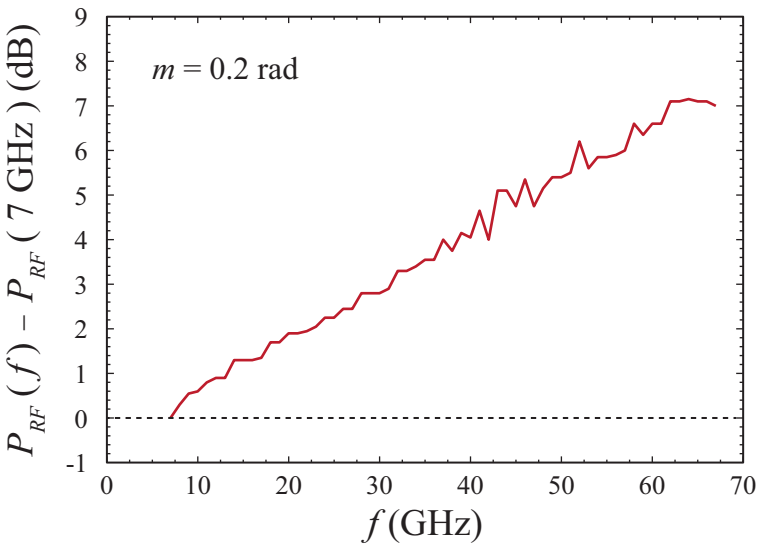

Figure 5.9: Measured relative RF power needed to achieve an RF modulation depth of $m = 0.2$ rad for the 65 GHz phase-modulator.

GHz and an optical insertion loss of $\alpha_{\Phi M} = 3.4$ dB. The relative RF power needed to achieve a modulation depth of $m = 0.2$ rad for this modulator is plotted as a function of frequency in Fig. 5.9. A modulation depth of $m = 0.2$ rad is equivalent to a carrier-to-sideband ratio (CSR) of 20 dB. In this figure, ΔP_{RF} was referenced to the power required to achieve a modulation depth of $m = 0.2$ rad at $f = 7$ GHz.

The second phase-modulator was connected to the first phase-modulator through PMF via a 3 dB coupler (not shown). The second phase-modulator was a 40 GHz, z-cut $LiNbO_3$ modulator with measured V_πs of 5.1 V at 10 GHz, 5.9 V at 20 GHz, and 6.7 V at 40 GHz and an optical insertion loss of $\alpha_{\Phi M} = 2.5$ dB. The output of the second phase-modulator was sent through single-mode fiber (SMF) into an

athermally packaged fiber FBG operating in transmission mode.

The FBG was designed to operate at $\lambda_{FBG} = 1552.520$ nm; however, due to fabrication tolerances, it had a center wavelength of $\lambda_{FBG} = 1552.552$ nm. The FBG transmission FWHM bandwidth was measured to be approximately 9.5 GHz and its out-of-band insertion loss was measured to be approximately $\alpha_{FBG,T} = 1.6$ dB. The FBG provided a maximum relative optical suppression of 13 dB at its center wavelength. After a variable optical delay line (not shown), the optical signal was sent into an EDFA operating in constant current mode.

The EDFA had a nominal gain of $G_{EDFA} = 35$ dB and a 1 dB compression output power of $P_{\text{1dB}} = 15$ dBm. The amplified optical signal was filtered using a tunable optical bandpass filter (BPF) to constrain the amplified spontaneous emission (ASE) noise bandwidth. Finally, the optical signal was sent into a photodetector having a bandwidth of $BW_{PD} = 23.5$ GHz, a responsivity of $\mathcal{R} = 0.8$ A/W, and a nominal 1 dB compression photocurrent $I_{\text{1dB}} = 16$ mA. An optical attenuator is shown to account for the power splitting ratio and excess insertion loss of a 3-dB optical coupler and the insertion loss of an optical delay line, which were omitted in Fig. 5.8. Although these components only serve as a source of optical loss in this set of experiments, their purpose will be clear in the next set of experiments.

Electrooptic downconversion of input signals having frequencies between 7 and 70 GHz was demonstrated using harmonics of a $f' = 20$ GHz LO. The powers at intermediate frequencies of $f_{IF} = |f - N\,f'|$ were measured using an ESA. Three IF power curves as functions of the RF frequency, which correspond to $(N, k) = \{(1, 0), (2, 1), (3, 0)\}$ were measured. The LO power was set to maximize the RF-to-

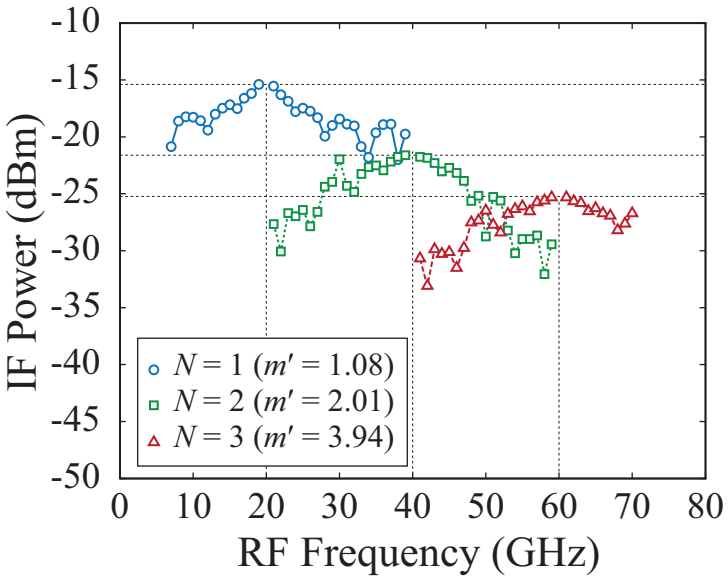

Figure 5.10: Measured normalized harmonic downconversion gain as a function of the RF frequency.

IF gain based on the values provided in Table 4.1. The laser was tuned such that either the $k = 0$ (carrier) or the $k = 1$ sideband was suppressed. This corresponded to tuning the laser to wavelengths of $\lambda_L = 1552.487$ nm ($k = 0$) and $\lambda_L = 1552.647$ nm ($k = 1$) as displayed by the laser control software. In this experiment the input modulation was maintained at $m = 0.1$ rad (CSR = 26 dB). The results of this measurement are shown in Fig. 5.10.

In Fig. 5.10, the frequency dependence of the photodetector and the coax cable between the photodetector and the ESA resulted in a measured frequency response resembling that of a bandpass filter. The measured difference in maximum gain between the $(N, k) = (1, 0)$ and $(N, k) = (2, 1)$ cases was -6.2 dB and the measured difference in maximum gain between the $(N, k) = (2, 1)$ and $(N, k) = (3, 0)$ cases

was −3.7 dB. From Table 4.1, these values were theoretically calculated to be −4.4 dB and −1.5 dB. Thus, there is a roughly a 2 dB difference in relative gain in the experimental measurements when compared to the theoretical predictions. This discrepancy could be due to EDFA saturation or optical filtering.

In the next set of experiments, harmonic vector demodulation was demonstrated. The system was configured as shown in Fig. 5.11. In this setup, the optical signal out of the first phase-modulator was split with a 3 dB beam splitter. The beam splitter was non-polarizing and the fiber pigtails were polarization maintaining. The two branches after the beam splitter were configured to be nominally identical. The top branch after the splitter in Fig. 5.15 is denoted as the in-phase (I) branch and the bottom as the quadrature (Q) branch. To demodulate a phase-encoded signal, the relative phase difference between the I and Q LOs was set to achieve $\theta = 90°/N$, where N is the harmonic downconversion number.

Although every reasonable attempt was made to keep the fiber lengths in each branch identical, variable optical delay lines (ODLs) were incorporated in the setup to correct the skew between the I and Q channels due to minor mismatches in fiber path lengths. The ODLs allowed for a temporal adjustment of 0 to 600 ps in each branch.

A data-encoded, millimeter-wave (mmW) signal at $f = 40$ GHz was synthesized using an arbitrary waveform generator (AWG), an RF hybrid, and an electrical upconverter. The upconverter was based on an electrical mixer. The amplified signal applied to the LO port of the electrical mixer had a center frequency of 35 GHz. A phase-shifter was incorporated between the LO synthesizer and the LO amplifier

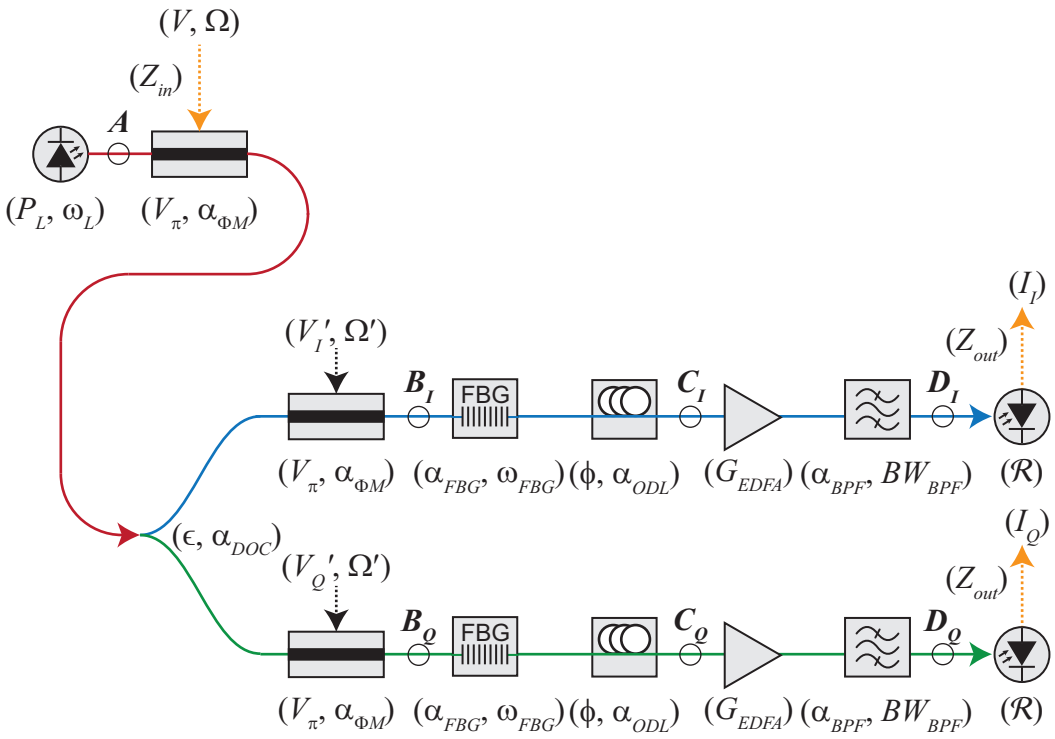

Figure 5.11: Diagram of the CΦM-OF link used to demonstrate harmonic downconversion and vector demodulation. After [10].

so that the overall phase of the baseband constellation measured on an oscilloscope could easily be adjusted.

The AWG had two 12-bit channels each having a maximum sample-rate of 12 GSa/s. The AWG was configured to generate either a 2.5 Gbps 4-quadrature amplitude modulated (4-QAM) or 5 Gbps 16-QAM signal with rectangular filtering at a center frequency of 5 GHz. The two channels from the AWG were combined in quadrature using a 90° RF hybrid and sent into the IF port of the electrical mixer. The output from the electrical mixer was high-pass filtered to suppress the IF and LO signals at 5 GHz and 35 GHz, respectively, while still passing the RF signal at 40 GHz. RF attenuators at the output of the amplifier were used to adjust the signal modulation depth. The electrical spectrum measured at the output of the RF hybrid is shown in Fig. 5.12(a) and the electrical spectrum measured at the output of the electrical upconverter is shown in Fig. 5.12(b).

The optical spectra measured at various points in the system for $(N, k) = (1, 0)$ are shown in Fig. 5.13. In Fig. 5.13(a), the optical spectrum out of the tunable laser is shown. In Fig. 5.13(b), the optical spectra in the I and Q branches are shown after the LO phase-modulators (points B_I and B_Q) in Fig. 5.11. In this case, the LO signals applied to the I and Q branch modulators produced a modulation depth of $m'_I \approx m'_Q \approx 1.08$ rad at a frequency of $f' = 40$ GHz. The RF signal shown in Fig. 5.12(b) was applied to the first phase-modulator.

The optical signals were then through two nominally identical FBGs that were designed to have a center wavelength of $\lambda_{FBG} = 1552.52$ nm, a reflectivity of $R = 99$ %, and a bandwidth of 80 pm. The transmittance of the FBGs were measured as a

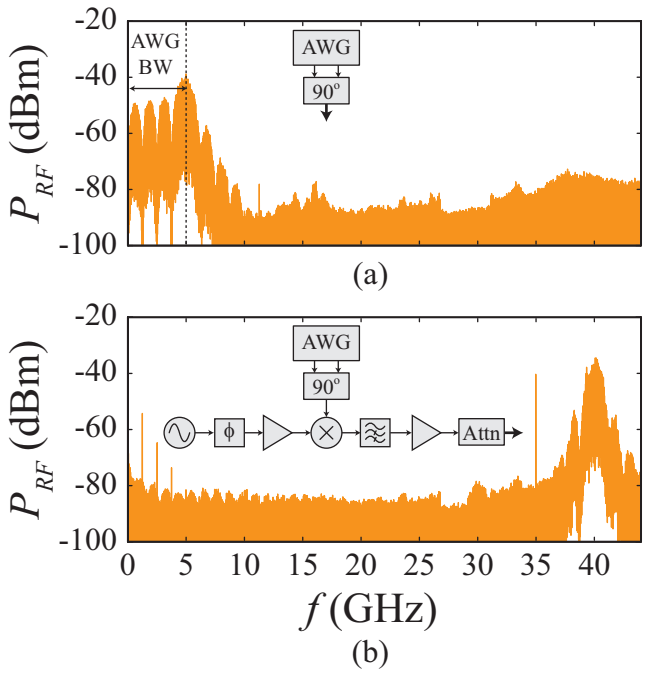

Figure 5.12: Measured electrical spectra of a 2.488 Gbps 4-QAM encoded signal at the outputs of (a) the AWG and (b) the electrical upconverter.

function of frequency with a lightwave measurement system. The transmittance as a function of frequency relative to the design frequency are shown in Fig. 5.14. The laser wavelength was set to simultaneously optimize the downconversion efficiency by suppressing the carrier in both channels as indicated by the shaded region in Fig. 5.14. The filtered optical signals were sent through 600 ps optical delay lines. The optical spectra after filtering (points C_I and C_Q) are shown in Fig. 5.12(c).

Prior to photodetection, the optical signals were amplified with EDFAs operating in constant current mode ($I_{EDFA} = 300$ mA) and filtered with 1.6 nm tunable optical BPFs. The filters were used to suppress the ASE noise by restricting the noise bandwidth. The amplified optical signals (points D_I and D_Q) are shown in

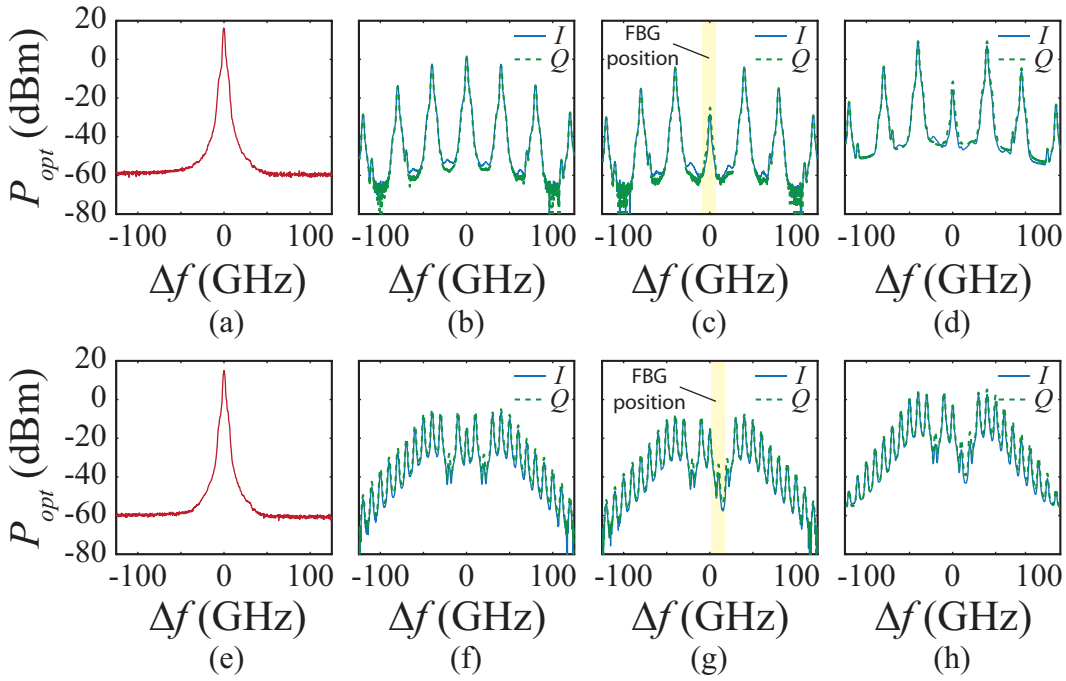

Figure 5.13: Measured optical spectra of a 2.488 Gbps 4-QAM encoded optical signal for (a)-(d) $N = 1$ and (e)-(h) $N = 4$.

Fig. 5.13(d).

The same series of experiments was performed for $(N, k) = (4, 1)$ as shown in Fig. 5.13(e)-(h). In this case, the LO signals applied to the I and Q modulators produced a modulation depth of $m'_I \approx m'_Q \approx 5.15$ rad at a frequency of $f' = 10$ GHz. Furthermore, the relative phase difference between I and Q LOs was set to $\theta = 90°/4 = 22.5°$.

Next, the 4-QAM and 16-QAM signals were demodulated and downconverted to produce baseband I and Q data-encoded waveforms. The baseband signals were amplified with electrical amplifiers having 3 dB bandwidths of 20 GHz and sent into a real-time oscilloscope (RTO) having a 1 GHz analog bandwidth and a sampling-

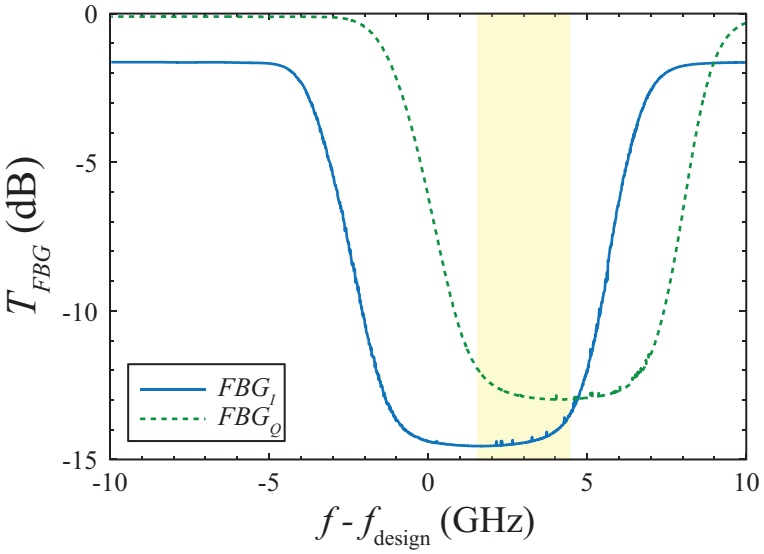

Figure 5.14: Measured optical transmittance curves of the FBGs relative to their design frequency.

rate of 10 GSa/s per channel. The sample mark out from the the AWG was used as the trigger signal for synchronization. The oscilloscope was set to 'peak detect' acquisition mode, which takes four samples within the time period of the sample rate and stores the minimum and maximum values. The sample rate was chosen to match the symbol rate $R_s = 1.25$ GBaud and the oscilloscope was synchronized via a 10 MHz reference. Using this mode allowed transition-free constellation diagrams to be displayed in real-time.

The channels were electronically de-skewed by 800 ps in the oscilloscope and fine adjustments were made using the variable optical delay lines. The two channels were captured and the histograms were plotted in MATLAB®. However, no digital signal processing (DSP) was implemented in MATLAB®. The results for $(N, k) =$

(1,0) and $(N, k) = (4,1)$ are shown in Fig. 5.15. The system operation was verified for $(N, k) = (2,1)$ with 2.5 Gbps 4-QAM and 5 Gbps 16-QAM data-encoded signals with a sub-optimal LO modulation of $m' = 1.85$ rad. A sub-optimal LO modulation was used as electrical amplifiers to produce the optimal modulation depth were not available at the time of the experiment. From Table 4.1, the optimal modulation depth for $(N, k) = (2,1)$ is $m' = 2.02$ rad. The system operation was also verified in part for $(N, k) = (3,0)$ with a 2.5 Gbps data-encoded signal with a sub-optimal LO modulation depth of $m' = 2.9$. From Table 4.1, the optical modulation depth for $(N, k) = (3,0)$ is $m' = 3.94$ rad. Demodulation of 5 Gbps 16-QAM signals could not be verified due to the availability of suitable electrical amplifiers in the laboratory at the time these experiments were performed.

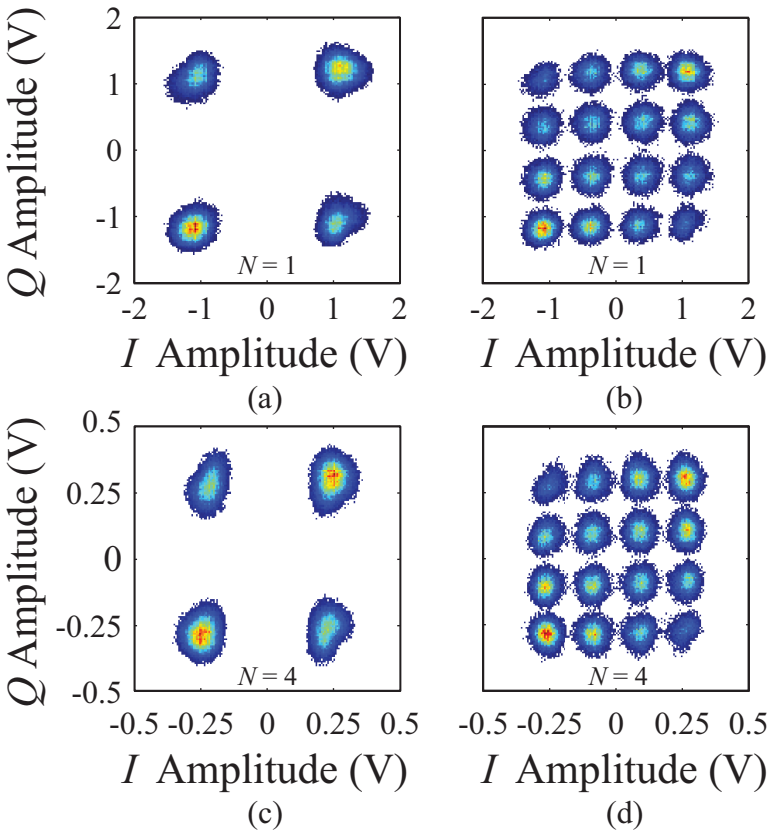

Figure 5.15: Measured demodulated 4-QAM and 16-QAM baseband constellations for (a)-(b) fundamental downconversion and (c)-(d) fourth-order harmonic downconversion.

Chapter 6

RF Photonic Transmitter Theory

In this chapter, the theory behind two upconverting RF photonic transmitter (TX) architectures is presented and analyzed. One of the transmitters uses a pair of electrooptic (EO) phase-modulators and an optical filter to impose a data-encoded signal onto an RF carrier. The other transmitter utilizes a dual-drive Mach-Zehnder modulator (DD-MZM). The DD-MZM transmitter architecture is extended to implement vector modulation. Upconversion using a harmonic of the electrical local oscillator (LO) is demonstrated with both transmitters.

6.1 RF Modulation Using Phase-Modulation

The phase of an RF signal can be encoded by using electrooptic phase-modulation and optical filtering arranged in an interferometric configuration [11, 13]. A similar technique was proposed and demonstrated for frequency conversion by Mast et al. in 2012 using intensity-modulation [43]. The concept of operation is to split an optical signal into two nominally identical branches using a directional optical coupler (DOC). In the upper branch, an RF or a data signal is encoded onto the phase of the optical signal. In the lower arm, a strong LO is modulated onto the optical phase. Phase-modulation generates a set of sidebands as shown in Fig. 3.8, so optical bandpass filtering is used to isolate the desired sideband. A narrow-bandwidth

optical bandpass filter (BPF) based on an optical circulator (OC) and a fiber Bragg grating (FBG) is shown in Fig. 3.14. In the configuration described by Mast et al., optical bandpass filtering was performed in both arms.

The two optical signals are recombined using a second optical coupler. An Erbium-doped fiber amplifier (EDFA) can be used to amplify the optical signal prior to square-law photodetection. A span of optical fiber can also be inserted between the EDFA and the photodetector if optical relay is required. The simplified schematic of the parallel phase-modulation with optical filtering (PΦM-OF) link is shown in Fig. 6.1.

An optical carrier with power P_L and angular frequency ω_L is split into two branches using a symmetric 2 x 2 polarization maintaining (PM) directional optical coupler (DOC). The field in the upper branch is phase-modulated by the input signal. Assuming that an RF signal having amplitude V and angular frequency Ω

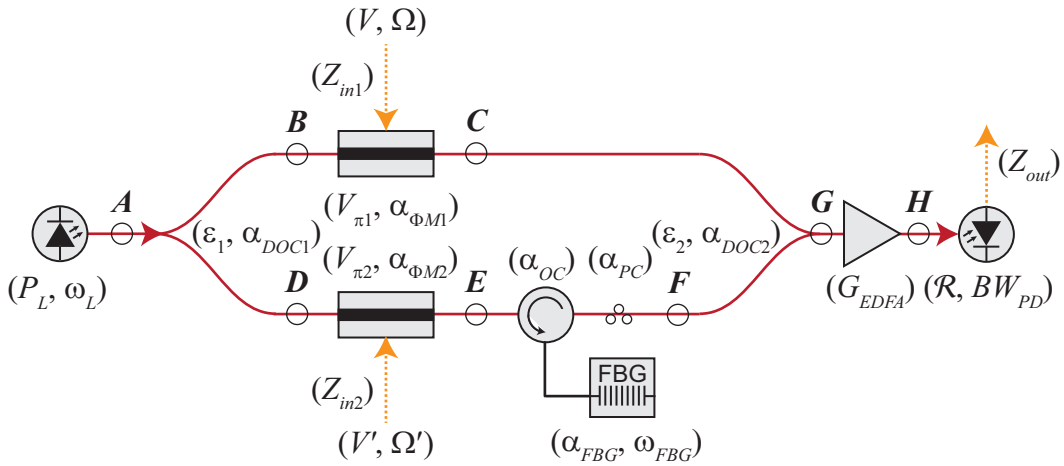

Figure 6.1: Mathematical model of the PΦM-OF link. After [11].

is applied, the optical field at point C can be written as

$$u_C(t) = \sqrt{P_L}\sqrt{\frac{\alpha_{DOC1}}{2}}\sqrt{\alpha_{\Phi M1}}\, e^{j\omega_L t} e^{jm\sin\Omega t} \tag{6.1}$$

where α_{DOC1} is the excess loss and $\epsilon_1 = 1/2$ is the power splitting ratio of the first directional optical coupler, $\alpha_{\Phi M1}$ is the insertion loss of the upper phase-modulator, and m is the modulation depth, in radians, defined as in Eq. (4.5). In the lower branch, the optical signal is phase-modulated by a strong electrical LO tone having amplitude V' and angular frequency Ω'. Thus, the optical field at point E can be expressed as

$$u_E(t) = j\sqrt{P_L}\sqrt{\frac{\alpha_{DOC1}}{2}}\sqrt{\alpha_{\Phi M2}}\, e^{j\omega_L t} e^{jm'\sin\Omega' t} \tag{6.2}$$

where $\alpha_{\Phi M2}$ is the insertion loss of the lower phase-modulator and m' is the modulation depth, in radians, again defined as in Eq. (4.5). Using the Jacobi-Anger expansion given by Eq. (4.7), the exponentiated sinusoid in Eq. (6.2) can be rewritten as

$$u_E(t) = j\sqrt{P_L}\sqrt{\frac{\alpha_{DOC1}}{2}}\sqrt{\alpha_{\Phi M2}}\, e^{j\omega_L t}\sum_{p=-\infty}^{\infty} J_p(m') e^{jp\Omega' t}. \tag{6.3}$$

An optical BPF implemented with an OC and an FBG can be used to select one of the LO sidebands generated by optical phase-modulation. The FBG center angular frequency was thermally tuned to $\omega_{FBG} = \omega_L + N\,\Omega'$ where N is a positive integer defined as the harmonic upconversion number. Assuming that the optical BPF provides complete suppression of out-of-band signals and uniform transmission of in-band signals with insertion loss of $\alpha_{BPF} = 2\alpha_{OC}\alpha_{FBG,R}$, where α_{OC} is the insertion loss of the optical coupler and $\alpha_{FBG,R}$ is the loss of the FBG in reflection,

the optical field at point F can be written as

$$u_F(t) = j\sqrt{P_L}\sqrt{\frac{\alpha_{DOC1}}{2}}\sqrt{\alpha_{\Phi M2}}\sqrt{\alpha_{BPF}}\sqrt{\alpha_{PC}}\, e^{j\omega_L t} J_N(m') e^{jN\Omega' t} \tag{6.4}$$

where α_{PC} is the insertion loss of the polarization controller (PC). The fields in the upper and lower branches are then combined using a 2x1 directional optical coupler having excess optical loss of α_{DOC2} and power splitting ratio of $\epsilon_2 = 1/2$ to produce a total optical field at point G given by

$$\begin{aligned} u_G(t) &= j\sqrt{P_L}\sqrt{\frac{\alpha_{DOC1}\alpha_{DOC2}}{4}} \\ &\times \left[\sqrt{\alpha_{\Phi M1}}\, e^{jm\sin\Omega t} + \sqrt{\alpha_{\Phi M2}}\sqrt{\alpha_{BPF}}\sqrt{\alpha_{PC}}\, J_N(m') e^{jN\Omega' t}\right] e^{j\omega_L t}. \end{aligned} \tag{6.5}$$

The signal incident on the photodetector is

$$\begin{aligned} u_H(t) &= j\sqrt{P_L}\sqrt{G_{EDFA}}\sqrt{\frac{\alpha_{DOC1}\alpha_{DOC2}}{4}} \\ &\times \left[\sqrt{\alpha_{\Phi M1}}\, e^{jm\sin\Omega t} + \sqrt{\alpha_{\Phi M2}}\sqrt{\alpha_{BPF}}\sqrt{\alpha_{PC}}\, J_N(m') e^{jN\Omega' t}\right] e^{j\omega_L t} \end{aligned} \tag{6.6}$$

where the EDFA is treated as an ideal linear amplifier with gain G_{EDFA}. Note that the effects of amplifier compression and noise are not considered here. The photocurrent generated by square-law detection is

$$\begin{aligned} i_H(t) &= \mathcal{R}|u_H(t)|^2 \\ &= \mathcal{R}P_L\frac{\alpha_{DOC1}\alpha_{DOC2}}{4}G_{EDFA} \\ &\times \left[\alpha_{\Phi M1} + \alpha_{\Phi M2}\alpha_{BPF}\alpha_{PC}J_N^2(m')\right. \\ &+ \left. 2\sqrt{\alpha_{\Phi M1}}\sqrt{\alpha_{\Phi M2}}\sqrt{\alpha_{BPF}}\sqrt{\alpha_{PC}}J_N(m')\cos\left(m\sin\Omega t - N\Omega' t\right)\right]. \end{aligned} \tag{6.7}$$

The DC component of the photocurrent is

$$I_{DC} = \frac{1}{4}\mathcal{R}P_L G_{EDFA}\alpha_{DOC1}\alpha_{DOC2}\left[\alpha_{\Phi M1} + \alpha_{\Phi M2}\alpha_{BPF}\alpha_{PC}J_N^2(m')\right] \tag{6.8}$$

and the AC components are given by

$$\begin{aligned} I_{AC}(t) &= \frac{1}{2}\mathcal{R}P_L G_{EDFA}\alpha_{DOC1}\alpha_{DOC2}\sqrt{\alpha_{\Phi M1}}\sqrt{\alpha_{\Phi M2}}\sqrt{\alpha_{BPF}}\sqrt{\alpha_{PC}} \\ &\times J_N(m')\left[\cos\left(m\sin\Omega t\right)\cos\left(N\Omega' t\right)+\sin\left(m\sin\Omega t\right)\sin\left(N\Omega' t\right)\right]. \end{aligned} \tag{6.9}$$

The sinusoids of sinusoids in Eq. (6.9) can be expanded as

$$\cos\left(z\sin\theta\right) = \sum_{p=-\infty}^{\infty} J_p(z)\cos\left(p\theta\right) \tag{6.10}$$

$$\sin\left(z\sin\theta\right) = \sum_{p=-\infty}^{\infty} J_p(z)\sin\left(p\theta\right). \tag{6.11}$$

Applying Eq. (6.9) in terms of Eqs. (6.10)-(6.11) yields

$$\begin{aligned} I_{AC}(t) &= \frac{1}{2}\mathcal{R}P_L G_{EDFA}\alpha_{DOC1}\alpha_{DOC2}\sqrt{\alpha_{\Phi M1}}\sqrt{\alpha_{\Phi M2}}\sqrt{\alpha_{BPF}}\sqrt{\alpha_{PC}}J_N(m') \\ &\times \left[\sum_{p=-\infty}^{\infty} J_p(m)\cos\left(p\Omega t\right)\cos\left(N\Omega' t\right)+\sum_{p=-\infty}^{\infty} J_p(m)\sin\left(p\Omega t\right)\sin\left(N\Omega' t\right)\right]. \end{aligned} \tag{6.12}$$

For small input modulation depths ($m \ll 1$), Eqs. (4.18)-(4.19) can be applied. Thus, Eq. (6.12) can be approximated as

$$\begin{aligned} I_{AC} &\approx \frac{1}{2}\mathcal{R}P_L G_{EDFA}\alpha_{DOC1}\alpha_{DOC2}\sqrt{\alpha_{\Phi M1}}\sqrt{\alpha_{\Phi M2}}\sqrt{\alpha_{BPF}}\sqrt{\alpha_{PC}} \\ &\times J_N(m')\left[\cos\left(N\Omega' t\right)+\frac{m}{2}\cos\left(N\,\Omega'-\Omega\right)t-\frac{m}{2}\cos\left(N\,\Omega'+\Omega\right)t\right]. \end{aligned} \tag{6.13}$$

Note that this technique generates a double-sideband RF signal. The signal oscillating at the upconverted frequency $\Omega_{RF} = N\,\Omega' + \Omega$ is

$$\begin{aligned} i(t)|_{\Omega_{RF}} &\approx -\frac{1}{4}\mathcal{R}P_L G_{EDFA}\alpha_{DOC1}\alpha_{DOC2}\sqrt{\alpha_{\Phi M1}}\sqrt{\alpha_{\Phi M2}}\sqrt{\alpha_{BPF}}\sqrt{\alpha_{PC}} \\ &\times J_N(m')m\cos\left(N\,\Omega'+\Omega\right)t. \end{aligned} \tag{6.14}$$

The expression given by Eq. (6.14) can be maximized for any arbitrary upconversion harmonic number, N, by maximizing the corresponding Bessel function of order

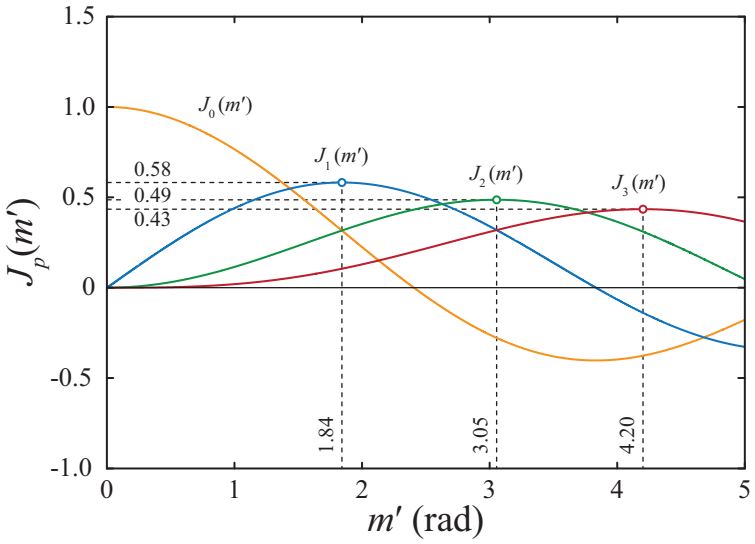

Figure 6.2: Calculated Bessel function amplitudes as functions of the LO modulation depth, m'.

$p = N$. The amplitudes of the Bessel functions of order $p \in \{0, 1, 2, 3\}$ as functions of the LO modulation depth, m', are plotted in Fig. 6.2.

Now if a baseband binary signal, $b(t)$, with bit-rate R_b is applied to the input of the upper phase-modulator, the photocurrent given in Eq. (6.7) can be modified as

$$\begin{aligned} i_H(t) &= \mathcal{R}P_L\frac{\alpha_{DOC1}\alpha_{DOC2}}{4}G_{EDFA} \\ &\times \left[\alpha_{\Phi M1} + \alpha_{\Phi M2}\alpha_{BPF}\alpha_{PC}J_N^2(m')\right. \\ &+ \left. 2\,2\sqrt{\alpha_{\Phi M1}}\sqrt{\alpha_{\Phi M2}}\sqrt{\alpha_{BPF}}\sqrt{\alpha_{PC}}J_N(m')\cos\left(m_b(t) - N\Omega' t\right)\right] \end{aligned} \tag{6.15}$$

where $m_b(t) = \pi V_b/V_\pi b(t)$ and $b(t) \in \{0, 1\}$. For efficient RF phase-modulation, the differential phase between $b(t) = 1$ and $b(t) = 0$ should be equal to π. That is,

$$V_b = V_\pi. \tag{6.16}$$

In this case,

$$I_{AC}(t) = \frac{1}{2}\mathcal{R}P_L G_{EDFA}\alpha_{DOC1}\alpha_{DOC2}\sqrt{\alpha_{\Phi M1}}\sqrt{\alpha_{\Phi M2}}\sqrt{\alpha_{BPF}}\sqrt{\alpha_{PC}} \quad (6.17)$$
$$\times \; J_N(m')\cos(\pi b(t))\cos(N\Omega' t)\,.$$

An illustrative example of binary phase-shift keyed (BPSK) modulation is shown in Fig. 6.3 for the case where R_b / 1 bit $= \pi N\Omega'/2$ and $V_b = V_\pi$.

6.2 RF Modulation Using Dual-Drive MZMs

The second approach presented in this dissertation utilizes a DD-MZM to electrooptically generate and modulate a mmW signal [12]. The technique can be extended to perform vector modulation by combining the optical signals out of two DD-MZMs, where appropriately phased LOs are used. To preclude the generation of heterodyne beat products, the frequency separation between the two unsynchronized

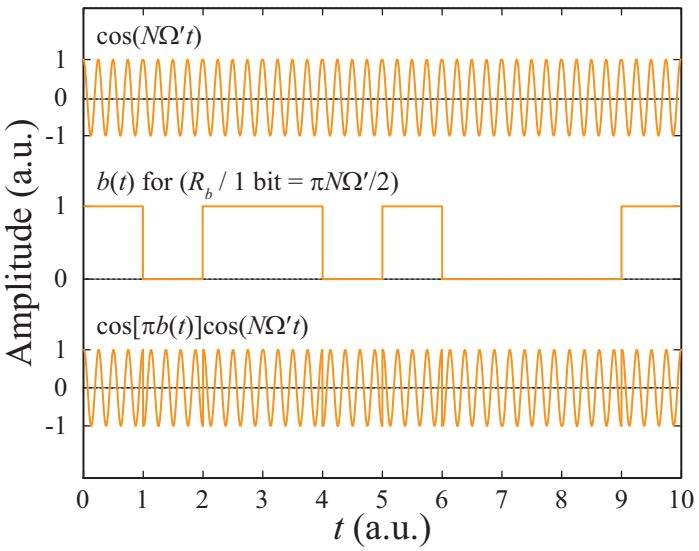

Figure 6.3: Illustrative example of encoding BPSK modulation onto an RF carrier.

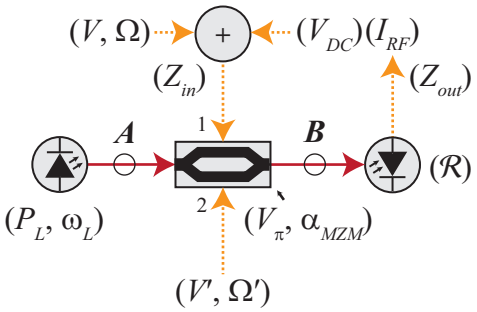

Figure 6.4: Mathematical model of the single DD-MZM link.

lasers can be chosen to be greater than the bandwidth of the photodetector.

First, the case with a single DD-MZM will be considered. The simplified schematic is given by Fig. 6.4. Note that DD-MZMs typically have three inputs, namely, two RF inputs and one DC input. For convenience, in this section it is assumed that the input signal and the DC signal were combined externally and applied to port 1 of the DD-MZM.

Based on the MZI analysis in Section 3.5 and the Intensity-Modulator analysis in Section 3.6.2, it can easily be shown that the complementary optical outputs emerging from a 1x2 DD-MZM can be expressed by

$$\begin{bmatrix} u_{B,1} \\ u_{B,2} \end{bmatrix} = j\sqrt{\alpha_{MZM}}e^{j\Sigma\phi(t)/2} \begin{bmatrix} \sin\Delta\phi(t)/2 \\ \cos\Delta\phi(t)/2 \end{bmatrix} u_A(t) \tag{6.18}$$

where

$$\begin{aligned} \Sigma\phi(t) &\equiv \phi_1(t) + \phi_2(t) \\ \Delta\phi(t) &\equiv \phi_1(t) - \phi_2(t) \end{aligned} \tag{6.19}$$

and α_{MZM} is the insertion loss of the DD-MZM modulator. Choosing $u_B(t) \equiv$

$u_{B,2}(t)$ results in

$$u_B(t) = j\sqrt{P_L}\sqrt{\alpha_{MZM}}\, e^{j\omega_L t} e^{j\Sigma\phi(t)/2} \cos\left[\phi(t)/2\right] \tag{6.20}$$

where the expression for $u_A(t)$ was given by Eq. (4.1). The photocurrent produced by square-law detection of Eq. (6.20) is

$$\begin{aligned} i_B(t) &= \mathcal{R}|u_B(t)|^2 \\ &= \frac{1}{2}\mathcal{R}P_L\alpha_{MZM}\left\{1 + \cos\left[\phi_1(t) - \phi_2(t)\right]\right\}. \end{aligned} \tag{6.21}$$

Using a difference-angle trigonometric identity, Eq. (6.21) can be rewritten as

$$\begin{aligned} i_B(t) &= \frac{1}{2}\mathcal{R}P_L\alpha_{MZM} \\ &\times \left\{1 + \cos\left[\phi_1(t)\right]\cos\left[\phi_2(t)\right] + \sin\left[\phi_1(t)\right]\sin\left[\phi_2(t)\right]\right\}. \end{aligned} \tag{6.22}$$

Now, assuming that the electrical LO is applied to port 2 of the DD-MZM, the time-varying phase, $\phi_2(t)$, can be defined as

$$\phi_2(t) = m' \sin \Omega' t \tag{6.23}$$

where the modulation depth, m' is defined analogously to that given in Eq. (4.5). Substituting Eq. (6.23) into Eq. (6.21) results in

$$i_B(t) = I_{DC}\left\{1 + \cos\left[\phi_1(t)\right]\cos\left(m' \sin \Omega' t\right) + \sin\left[\phi_1(t)\right]\sin\left(m' \sin \Omega' t\right)\right\} \tag{6.24}$$

where

$$I_{DC} = \frac{1}{2}\mathcal{R}P_L\alpha_{MZM}. \tag{6.25}$$

Applying the identities for the sinusoids of sinusoids given by Eqs. (6.10)-(6.11) to

Eq. (6.24) and rearranging yields

$$\begin{aligned} i_B(t) &= I_{DC}\left\{1 + J_0(m')\cos\left[\phi_1(t)\right]\right\} \\ &+ 2I_{DC}\sum_{p=1}^{\infty}\Big\{J_{(2p-1)}(m')\sin\left[\phi_1(t)\right]\sin\left[(2p-1)\Omega' t\right] \\ &+ J_{(2p)}(m')\cos\left[\phi_1(t)\right]\cos\left[(2p)\Omega' t\right]\Big\}. \end{aligned} \tag{6.26}$$

From Eq. (6.26) it is clear that the coefficient corresponding to an AC photocurrent term oscillating at $p\Omega'$ is proportional to the Bessel function of order p evaluated at the LO modulation depth m'. Thus, the power of the desired LO harmonic can be maximized by adjusting the LO strength. The Bessel functions of orders $p \in \{0, 1, 2, 3\}$ were previously plotted in Fig. 6.2. Furthermore, all components are simultaneously modulated by the signals applied to port 1 of the DD-MZM. Thus, frequency upconversion and modulation can be simultaneously performed electrooptically using a single DD-MZM.

Now, if an DC biased RF signal is applied to port 1 of the DD-MZM, then the time-dependent phase, $\phi_1(t)$, can be expressed as

$$\phi_1(t) = m\sin\Omega t + M_{DC} \tag{6.27}$$

where the modulation depths, m and M_{DC}, are defined analogously to that given in Eq. (4.5). Inserting Eq. (6.27) into Eq. (6.26), and applying the sum-angle trigono-

metric identities results in

$$\begin{aligned} i_B(t) &= I_{DC} \\ &+ I_{DC}J_0(m')\left[\cos\left(m\sin\Omega t\right)\cos\left(M_{DC}\right) - \sin\left(m\sin\Omega t\right)\sin\left(M_{DC}\right)\right] \\ &+ 2I_{DC}\left[\sin\left(m\sin\Omega t\right)\cos\left(M_{DC}\right) + \cos\left(m\sin\Omega t\right)\sin\left(M_{DC}\right)\right] \\ &\times \sum_{p=1}^{\infty} J_{(2p-1)}(m')\sin\left[(2p-1)\Omega' t\right] \\ &+ 2I_{DC}\left[\cos\left(m\sin\Omega t\right)\cos\left(M_{DC}\right) - \sin\left(m\sin\Omega t\right)\sin\left(M_{DC}\right)\right] \\ &\times \sum_{p=1}^{\infty} J_{(2p)}(m')\cos\left[(2p)\Omega' t\right]. \end{aligned} \tag{6.28}$$

Applying Eqs. (6.10)-(6.11) and Taylor expanding the resulting expression to first-order in m using Eqs. (4.18)-(4.19) yields

$$\begin{aligned} i_B(t) &= I_{DC} \\ &+ I_{DC}J_0(m')\left[\cos\left(M_{DC}\right) - m\sin\left(\Omega t\right)\sin\left(M_{DC}\right)\right] \\ &+ 2I_{DC}\left[m\sin\left(\Omega t\right)\cos\left(M_{DC}\right) + \sin\left(M_{DC}\right)\right] \\ &\times \sum_{p=1}^{\infty} J_{(2p-1)}(m')\sin\left[(2p-1)\,\Omega' t\right] \\ &+ 2I_{DC}\left[\cos\left(M_{DC}\right) - m\sin\left(\Omega t\right)\sin\left(M_{DC}\right)\right] \\ &\times \sum_{p=1}^{\infty} J_{(2p)}(m')\cos\left[(2p)\Omega' t\right]. \end{aligned} \tag{6.29}$$

For the cases where the DD-MZM is biased at a peak ($M_{DC} = 2q\pi$, where q is an integer) or at a null ($M_{DC} = (2q+1)\pi$), Eq. (6.29) simplifies to

$$\begin{aligned} i_B(t)_{pk,nl} &= I_{DC} \pm I_{DC}J_0(m') \\ &\pm 2I_{DC}m\sin\left(\Omega t\right) \times \sum_{p=1}^{\infty} J_{(2p-1)}(m')\sin\left[(2p-1)\,\Omega' t\right] \\ &\pm 2I_{DC} \times \sum_{p=1}^{\infty} J_{(2p)}(m')\cos\left[(2p)\Omega' t\right]. \end{aligned} \tag{6.30}$$

For the cases where the DD-MZM is biased at a negative quadrature point ($M_{DC} = \pi(4q+1)/2$) or at a positive quadrature point ($M_{DC} = \pi(4q+3)/2$), Eq. (6.29) simplifies to

$$\begin{aligned} i_B(t)_{\mp qd} &= I_{DC} \mp I_{DC} J_0(m') m \sin(\Omega t) \\ &\pm 2I_{DC} \times \sum_{p=1}^{\infty} J_{(2p-1)}(m') \sin\left[(2p-1)\,\Omega' t\right] \\ &\mp 2I_{DC} m \sin(\Omega t) \times \sum_{p=1}^{\infty} J_{(2p)}(m') \cos\left[(2p)\Omega' t\right]. \end{aligned} \tag{6.31}$$

The RF photonic transmitter can generate modulated RF components at even or odd multiples of the LO. This is a feature for multi-band distribution of signals [51]. For wireless backhaul, however, the antenna and the power amplifier will constrain the bandwidth of the transmitted signal in practice. A wide-bandwidth RF splitter (or diplexer) could be used to split the signal prior to distributing the RF signal into a bank of amplifiers and antennas. To comply with frequency allocation band plans, electrical filtering is still generally needed to reduce spurious emissions to acceptable levels.

A vector network analyzer (VNA) can be used to measure the S_{21} parameter, which is defined as the forward voltage gain. If the VNA is configured to operate in the zero-span mode, then the S_{21} parameter trace corresponds to a temporal measurement of the amplitude and phase of the signal into port 2 of the VNA as a function of the signal out of port 1 of the VNA. Assuming that the VNA port 1 drives port 2 of the DD-MZM and that the output from the photodetector is connected to port 2 of the VNA, then the complex forward voltage gain of the DD-MZM transmitter configuration can be measured as a function of the signal applied

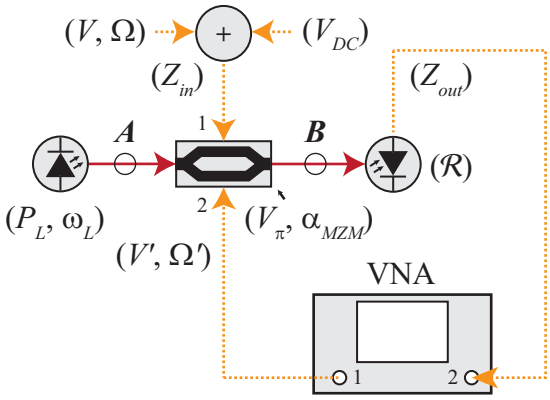

Figure 6.5: VNA configuration to demonstrate vector modulation.

to port 1 of the DD-MZM. This configuration is shown in Fig. 6.5.

As an illustrative example, consider Fig. 6.6. Here, the DD-MZM has a cosine-squared transfer function with no DC phase-offset. If the DD-MZM is biased at the peak, then only even order components will be generated. If the VNA zero span frequency is set at $f' = \Omega'/(2\pi)$, then the amplitude of the photocurrent oscillating at a frequency f' will be approximately zero. Thus, a point at the origin will be traced on the VNA display if the S_{21} parameter is plotted in the complex plane. This case is denoted by the Roman numeral I in Fig. 6.6.

If the DD-MZM is biased at the negative quadrature point, then only odd order components will be generated. So, if port 1 of the VNA again drives port 2 of the DD-MZM, then the output signal from the photodetector will be π rad out-of-phase from the input signal. Thus, a point at an angle of π rad will be displayed on the VNA if the S_{21} parameter is plotted in the complex plane. This case is denoted by the II in Fig. 6.6.

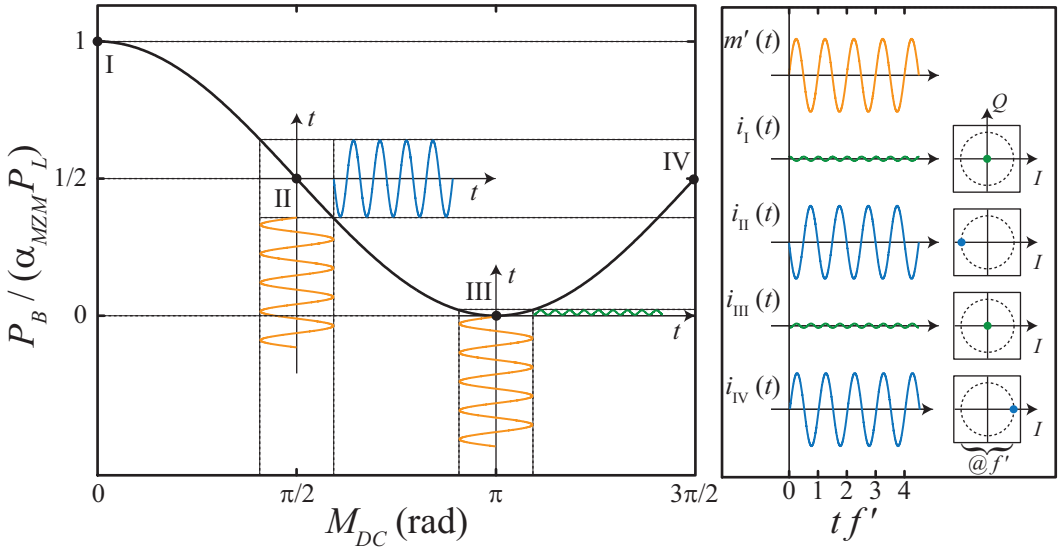

Figure 6.6: Illustrative example showing amplitude modulation of an RF carrier using a single DD-MZM.

Similar arguments can be made for cases where the DD-MZM is biased at the nulls or at the positive quadrature points. These cases are denoted by III and IV in Fig. 6.6. From this example it should be clear that the sign and amplitude of the generated signal can be controlled via the signal applied to port 1 of the DD-MZM.

Vector modulation can be achieved if the photocurrents from a pair of DD-MZMs are made to add in quadrature. One method for accomplishing this is to electrically combine the photocurrents in a 90° electrical hybrid. However, this approach would require that two high-speed photodetectors be utilized if mmW operation is desired. Alternatively, if the relative phase between the LO signals applied to the DD-MZMs is set properly, then the optical signals emerging from the two DD-MZMs can be optically combined and sent into a single photodetector

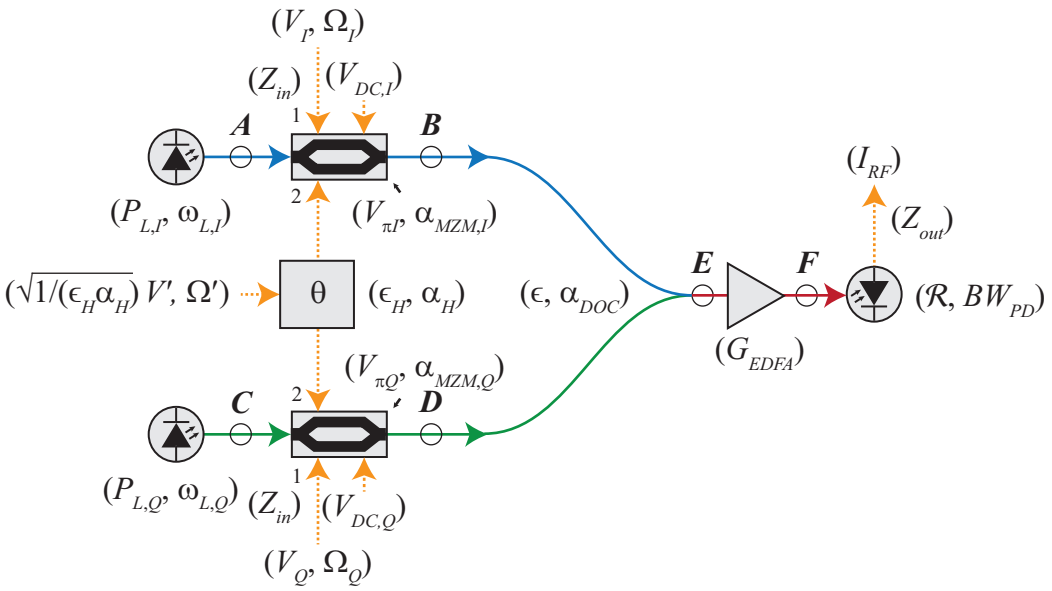

Figure 6.7: Mathematical model of vector modulation and upconversion based on a pair of DD-MZMs. After [12].

as shown in Fig. 6.7. Heterodyne mixing products can be ignored if the frequency separation between the two optical sources, $\Delta\nu = |\omega_{L,I} - \omega_{L,Q}|/(2\pi)$ is made much larger than the bandwidth of the photodetector, BW_{PD}.

For simplicity, in the following analysis, the EDFA is treated as an ideal linear gain element with gain of G_{EDFA}. Following from Eq. (6.28), the in-phase photocur-

rent can be expressed as

$$\begin{aligned} i_I(t) &= I_{DC,I} \\ &+ I_{DC,I} J_0(m') \left[\cos\left(m_I \sin \Omega_I t\right) \cos\left(M_{DC,I}\right) - \sin\left(m_I \sin \Omega_I t\right) \sin\left(M_{DC,I}\right)\right] \\ &+ 2I_{DC,I} \left[\sin\left(m_I \sin \Omega_I t\right) \cos\left(M_{DC,I}\right) + \cos\left(m_I \sin \Omega_I t\right) \sin\left(M_{DC,I}\right)\right] \\ &\times \sum_{p=1}^{\infty} J_{(2p-1)}(m') \sin\left[(2p-1)(\Omega' t + \theta)\right] \\ &+ 2I_{DC,I} \left[\cos\left(m_I \sin \Omega_I t\right) \cos\left(M_{DC,I}\right) - \sin\left(m_I \sin \Omega_I t\right) \sin\left(M_{DC,I}\right)\right] \\ &\times \sum_{p=1}^{\infty} J_{(2p)}(m') \cos\left[(2p)(\Omega' t + \theta)\right] \end{aligned} \tag{6.32}$$

and the quadrature photocurrent as

$$\begin{aligned} i_Q(t) &= I_{DC,Q} \\ &+ I_{DC,Q} J_0(m') \left[\cos\left(m_Q \sin \Omega_Q t\right) \cos\left(M_{DC,Q}\right) - \sin\left(m_Q \sin \Omega_Q t\right) \sin\left(M_{DC,Q}\right)\right] \\ &+ 2I_{DC,Q} \left[\sin\left(m_Q \sin \Omega_Q t\right) \cos\left(M_{DC,Q}\right) + \cos\left(m_Q \sin \Omega_Q t\right) \sin\left(M_{DC,Q}\right)\right] \\ &\times \sum_{p=1}^{\infty} J_{(2p-1)}(m') \sin\left[(2p-1)\Omega' t\right] \\ &+ 2I_{DC,Q} \left[\cos\left(m_Q \sin \Omega_Q t\right) \cos\left(M_{DC,Q}\right) - \sin\left(m_Q \sin \Omega_Q t\right) \sin\left(M_{DC,Q}\right)\right] \\ &\times \sum_{p=1}^{\infty} J_{(2p)}(m') \cos\left[(2p)\Omega' t\right] \end{aligned} \tag{6.33}$$

where θ is the relative phase difference between the I and Q LOs and $I_{DC,i}, i \in \{I, Q\}$ is defined as

$$I_{DC,i} = \frac{1}{4} \mathcal{R} P_{L,i} G_{EDFA} \alpha_{MZM,i} \alpha_{DOC}. \tag{6.34}$$

In Eq. (6.34), the directional optical coupler power splitting ratio was assumed to be $\epsilon = 1/2$ and the directional optical coupler insertion loss is denoted by α_{DOC}. Furthermore, the LO voltage has been scaled by $\sqrt{2/\alpha_H}$ in Fig. 6.7 to account for the splitting and insertion losses of the electrical hybrid.

Ideally, the optical powers from the two branches are nominally identical (i.e. $P_{L,I}\alpha_{MZM,I} = P_{L,Q}\alpha_{MZM,Q} = P_L\alpha_{MZM}$). In this case, $I_{DC,I} = I_{DC,Q} = I_{DC}$. Furthermore, if upconversion is desired, the DC and baseband contributions can be ignored. The total AC photocurrent ($N \geq 1$) can be expressed as

$$\begin{aligned}
I_{AC}(t) &= I_{AC,I}(t) + I_{AC,Q}(t) \qquad (6.35)\\
&= 2I_{DC}\sum_{p=1}^{\infty} J_{(2p-1)}(m')\\
&\times \{[\sin(m_I \sin\Omega_I t)\cos(M_{DC,I}) + \cos(m_I \sin\Omega_I t)\sin(M_{DC,I})]\\
&\times \sin[(2p-1)(\Omega' t + \theta)]\\
&+ [\sin(m_Q \sin\Omega_Q t)\cos(M_{DC,Q}) + \cos(m_Q \sin\Omega_Q t)\sin(M_{DC,Q})]\\
&\times \sin[(2p-1)\Omega' t]\}\\
&+ 2I_{DC}\sum_{p=1}^{\infty} J_{(2p)}(m')\\
&\times \{[\cos(m_I \sin\Omega_I t)\cos(M_{DC,I}) - \sin(m_I \sin\Omega_I t)\sin(M_{DC,I})]\\
&\times \cos[(2p)(\Omega' t + \theta)]\\
&+ [\cos(m_Q \sin\Omega_Q t)\cos(M_{DC,Q}) - \sin(m_Q \sin\Omega_Q t)\sin(M_{DC,Q})]\\
&\times \cos[(2p)\Omega' t]\}.
\end{aligned}$$

By examining Eq. (6.35), it can be observed that the N^{th} harmonic of the AC photocurrent can be set in quadrature if $\theta = 90°/N$. For small input modulation depths, ($m_I << 1$ and $m_Q << 1$) Eq. (6.35) can be Taylor expanded to first-order

in m_I and m_Q as

$$\begin{aligned} I_{AC}(t) &\approx 2I_{DC}\sum_{p=1}^{\infty} J_{(2p-1)}(m') \\ &\times \{[m_I \sin(\Omega_I t)\cos(M_{DC,I}) + \sin(M_{DC,I})]\sin[(2p-1)(\Omega' t+\theta)] \\ &+ [m_Q \sin(\Omega_Q t)\cos(M_{DC,Q}) + \sin(M_{DC,Q})]\sin[(2p-1)\Omega' t]\} \\ &+ 2I_{DC}\sum_{p=1}^{\infty} J_{(2p)}(m') \\ &\times \{[\cos(M_{DC,I}) - m_I \sin(\Omega_I t)\sin(M_{DC,I})]\cos[(2p)(\Omega' t+\theta)] \\ &+ [\cos(M_{DC,Q}) - m_Q \sin(\Omega_Q t)\sin(M_{DC,Q})]\cos[(2p)\Omega' t]\} \end{aligned} \tag{6.36}$$

where Eqs. (4.18)-(4.19) have been applied. For optimal RF upconversion, the DC biases should be set such that the two DD-MZMs are biased at either a transmission maximum (peak) or at a transmission minimum (null) for odd harmonics and at a quadrature point for even harmonics. For $N = 1$ (fundamental upconversion), Eq. (6.36) simplifies to

$$i(t)_{N=1} \approx 2I_{DC}J_1(m')\left[m_I \sin(\Omega_I t)\cos(\Omega' t) + m_Q \sin(\Omega_Q t)\sin(\Omega' t)\right] \tag{6.37}$$

which is clearly a vector modulated signal. A simple experiment that can be performed using the VNA is to connect port 1 of the VNA to the LO input prior to the electrical hybrid and port 2 of the VNA to the photodetector output.

If a sinusoidal signal is applied to port 1 of the I DD-MZM and a synchronized sinusoid signal at the same frequency but shifted by $\pi/2$ is applied to port 1 of the Q DD-MZM, then an ellipse will be traced in the complex plane if the S_{21} parameter is plotted in polar coordinates. If $m_I = m$ and $m_Q = 0$, then a line will be traced along the horizontal axis as shown in Fig. 6.8(a). If $m_I = 0$ and $m_Q = m$, then

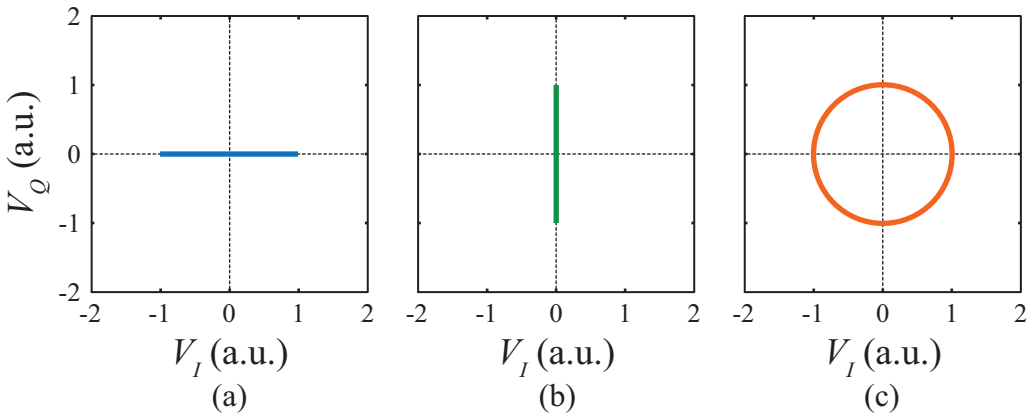

Figure 6.8: Example of vector modulation of sinusoidal signals using the VNA setup.

a line will be traced along the vertical axis as shown in Fig. 6.8(b). Finally, if $m_I = m_Q = m$, then a circle will be traced in the complex plane with angular frequency $\Omega_I = \Omega_Q = \Omega$ as shown in Fig. 6.8(c).

The previous analysis was performed assuming sinusoidal input signals. However, the system can also be used to modulate an arbitrary signal on the RF carrier. Suppose that Eq. (6.27) is generalized to

$$\phi_{1,i}(t) = m_i(t) + M_{DC} \tag{6.38}$$

where $i \in \{I, Q\}$, then Eq. (6.35) becomes

$$\begin{aligned} I_{AC}(t) &= I_{AC,I}(t) + I_{AC,Q}(t) \qquad (6.39) \\ &= 2I_{DC} \sum_{p=1}^{\infty} J_{(2p-1)}(m') \\ &\times \{\{\sin[m_I(t)]\cos(M_{DC,I}) + \cos[m_I(t)]\sin(M_{DC,I})\}\sin[(2p-1)(\Omega' t + \theta)] \\ &+ \{\sin[m_Q(t)]\cos(M_{DC,Q}) + \cos[m_Q(t)]\sin(M_{DC,Q})\}\sin[(2p-1)\Omega' t]\} \\ &+ 2I_{DC} \sum_{p=1}^{\infty} J_{(2p)}(m') \\ &\times \{\{\cos[m_I(t)]\cos(M_{DC,I}) - \sin[m_I(t)]\sin(M_{DC,I})\}\cos[(2p)(\Omega' t + \theta)] \\ &+ \{\cos[m_Q(t)]\cos(M_{DC,Q}) - \sin[m_Q(t)]\sin(M_{DC,Q})\}\cos[(2p)\Omega' t]\}. \end{aligned}$$

Assuming that $b_I(t)$ and $b_Q(t)$ are binary input signals, then modulation signals can be defined as

$$m_I(t) = m_I b_I(t) \qquad (6.40)$$

$$m_Q(t) = m_Q b_Q(t) \qquad (6.41)$$

where $b_i(t) \in \{0, 1\}$ for $i \in \{I, Q\}$. Parametric plots of Eq. (6.39) with $m_I = m_Q = 0$ for $N \in \{0, 1, 2, 3\}$ are plotted in Fig. 6.9. The maxima corresponding to the lowest values of M_{DC} and m' are indicated by circles.

From Fig. 6.2, the optimal DC bias points LO modulation depths for $N \in \{0, 1, 2, 3, 4\}$ were tabulated and are provided in Table 6.1 for q an integer.

The optimal peak-to-peak modulation depth for 4-QAM is π. However, smaller modulation depths should be used if analog input signals are to be relayed as transmitter has a sinusoidal transfer function.

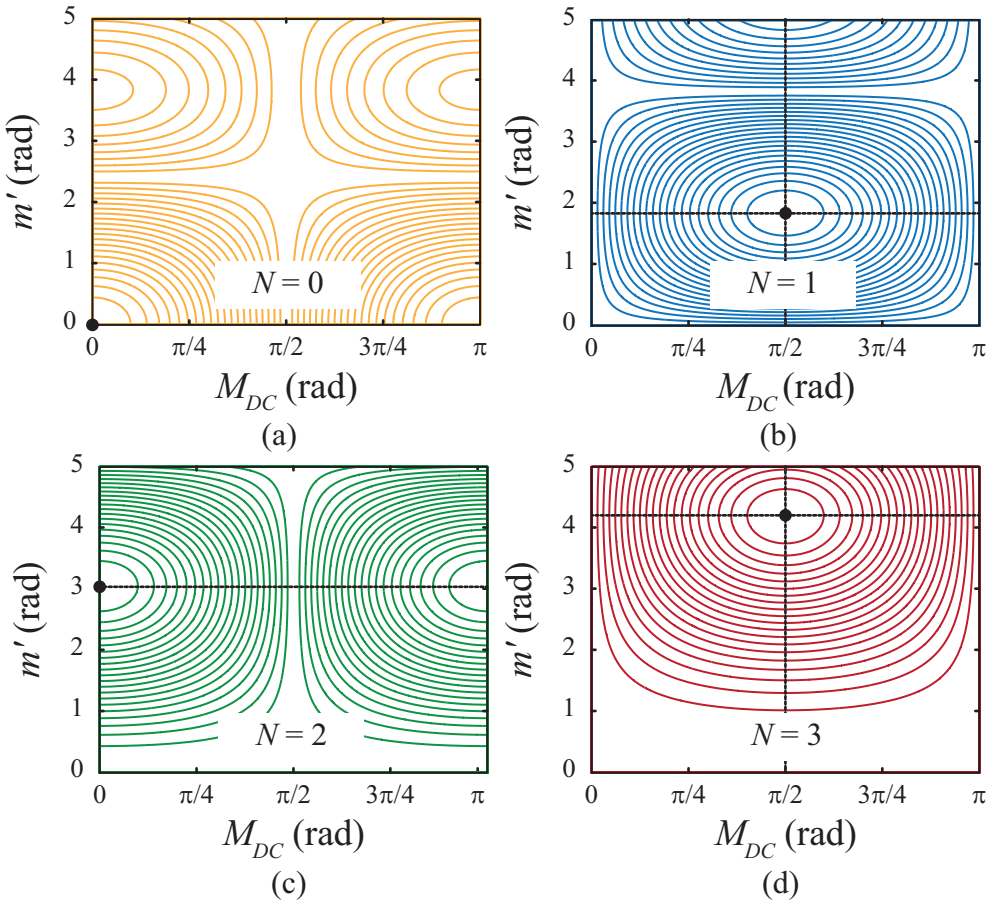

Figure 6.9: Calculated parametric plots of photocurrents as functions of the DC bias and the LO modulation depth.

Table 6.1: DD-MZM optimal parameters.

N	M_{DC} (rad)	m' (rad)	$20\log_{10}\lvert J_N(m')\rvert$
0	$\pi/2+q\pi$	0	-
1	$q\times\pi$	1.84	-4.7 dB
2	$\pi/2+q\pi$	3.05	-6.3 dB
3	$q\times\pi$	4.20	-7.2 dB
4	$\pi/2+q\pi$	5.31	-8.0 dB

Chapter 7

RF Photonic Transmitter Results

In this chapter, the experimental results obtained for the two upconverting RF photonic transmitter architectures analyzed in Chapter 6 are reported. The first transmitter, which is based on a fiber interferometer, can generate binary phase-shift keyed (BPSK) modulated RF signals. The second configuration, which employs a pair of dual-drive Mach-Zehnder modulators (DD-MZMs), can perform arbitrary vector modulation. Experimental results showing 4-quadrature amplitude modulation (4-QAM) and 16-QAM will be shown. Both transmitter architectures allow for harmonic upconversion of the electrical local oscillator (LO), allowing lower frequency devices to be utilized.

7.1 RF Modulation Using Phase-Modulation

In the transmitter, a binary phase-shift keyed (BPSK) signal was generated by optical heterodyne mixing of two optical tones followed by photodetection and electrical amplification. The continuous-wave (CW) signal produced by the laser had wavelength $\lambda_L = 1555.000$ nm and optical power $P_L = 21$ dBm was divided using a polarization maintaining (PM) 3 dB directional optical coupler (DOC) into two arms. The optical signal in the upper arm was phase-modulated by a non-return-to-zero (NRZ) $2^7 - 1$ pseudorandom binary sequence (PRBS) with a bit-rate

of $R_b = 0.5$ Gbps. The amplitude of the electrical PRBS signal was adjusted to achieve a peak-to-peak modulation depth close to π.

The optical signal in the lower arm was phase-modulated by a strong electrical LO having a frequency of $f' = 25$-35 GHz. The upper first-order sideband generated by phase-modulation was spectrally isolated using an optical bandpass filter (BPF) composed of a thermally tuned fiber Bragg grating (FBG) and an optical circulator (OC). As the optical filter was non-PM, an automatic polarization tracker module (PC) was used to maintain the state-of-polarization (SOP) along the slow axis of the fiber prior to mixing with the signal produced in the upper arm.

Although not shown in Fig. 6.1, variable optical attenuators were incorporated in the experimental setup to adjust the optical power in the two arms prior to combining the signals with a second PM 3 dB directional optical coupler. The optical signal was converted to a phase-encoded RF signal using a high-frequency photodetector (PD).

To downconvert the photonically generated data-encoded RF signal, a cascaded phase-modulation link with optical filtering ($k = 0$) was employed as the photonic receiver. The CΦM-OF link schematic was previously shown in Fig. 5.8. However, for this measurement, no optical amplification was used.

The CΦM-OF photonic receiver consisted of two cascaded EO phase-modulators followed by a FBG operating in transmission mode. The fiber Bragg grating (FBG) suppressed the optical carrier prior to photodetection. In the first modulator, a CW optical carrier having wavelength $\lambda_L = 1552.495$ nm and optical power $P_L = 21$ dBm was phase-modulated by a strong electrical LO with frequency f' equal to

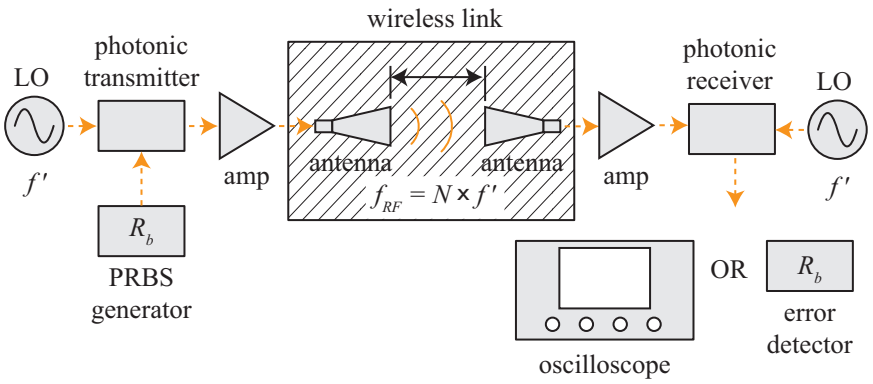

Figure 7.1: Experimental configuration of the PΦM-OF transmitter and CΦM-OF receiver.

the RF carrier frequency. The LO modulated optical signal was sent into a serially connected phase-modulator driven with the received RF signal. The FBG was thermally tuned to suppress the optical carrier, while transmitting the upper and lower sidebands.

The resulting carrier-suppressed, phase-modulated, optical signal was converted to a photocurrent using a square-law detector. The resulting RF signal was sent through a wireless link and the received RF signal was amplified and sent into the photonic receiver for demodulation and downconversion to baseband. The experimental configuration is shown in Fig. 7.1. Note that the wireless link section has patterned with diagonal lines. Although a wireless link was used to obtain the experimental results presented here, the details of wireless transmission will be deferred to Section 9.1. The output data signal from the photonic receiver was viewed using a real-time oscilloscope (RTO) having a 4 GHz analog bandwidth and a sampling frequency of 10 GSa/s. Fig. 7.2 shows the input NRZ electrical signal

measured at the transmitter input (back-to-back), together with three representative time-domain waveforms of the received signal at the output, each measured with a different phase offset ($\Delta\theta$). When the receiver LO was in-phase with the RF carrier (b), the data pattern was non-inverted. If the receiver LO phase was orthogonal to the RF carrier (c) the received signal was undetectable. Finally, if the receiver LO and RF carrier were out-of-phase (d), the polarity of the received signal was inverted as referenced to the transmitted signal. This phase-sensitive behavior is a characteristic of a coherent detection system.

A similar experimental setup was constructed to demonstrate frequency doubling of the LO ($N = 2$). In these experiments, the BPSK data-rate was also increased from $R_b = 0.5$ Gbps to $R_b = 6$ Gbps and the PRBS length was also increased from $2^7 - 1$ to $2^{31} - 1$. The PΦM-OF photonic transmitters used for the experiments were nominally identical with the exceptions that 1) the $N = 2$ sideband was selected to implement harmonic upconversion, 2) the polarization tracker module was removed, 3) the second PM DOC was replaced with a non-PM coupler, and 4) optical amplification was used prior to photodetection in the $R_b = 6$ Gbps cases. It should be noted that the use of a non-PM optical coupler reduced the stability of the setup as the beat product strength is a function of the SOP. Ideally, polarization-maintaining components would exclusively be used.

A functionally equivalent set of components was used to implement the CΦM-OF receiver. The main differences were 1) the receiver laser was a $P_L = 19$ dBm distributed feedback laser (DFB) having a center wavelength of $\lambda_L = 1548.45$ nm 2) optical amplification was used prior to the photodetector, and 3) the limiting

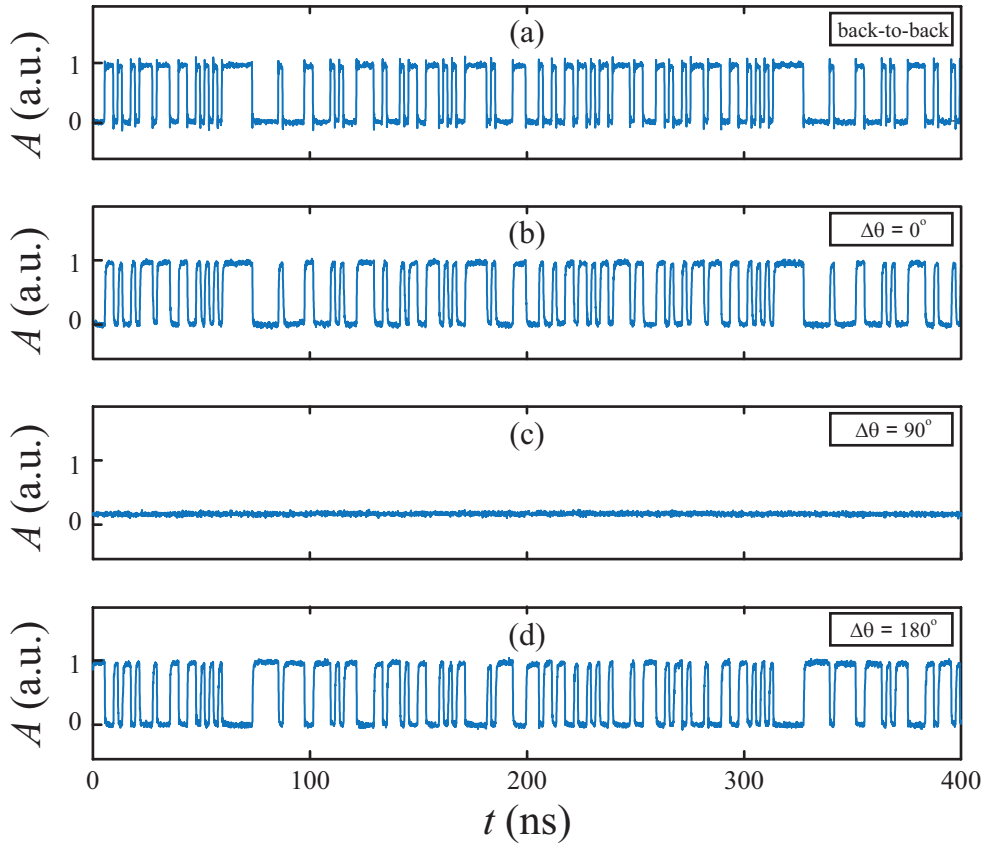

Figure 7.2: Measured data sequences for $R_b = 0.5$ Gbps with $f = 35$ GHz (a) input (back-to-back), output with (b) $\Delta\theta = 0°$, (c) $\Delta\theta = 90°$, and (d) $\Delta\theta = 180°$. After [13].

amplifier after the photodetector was replaced by a linear amplifier.

An additional difference in the setups was that spans of standard single-mode fiber (SMF), each of length $L = 200$ m, were placed in the transmitter and the receiver. The fiber was inserted between the Erbium-doped fiber amplifier (EDFA) and photodetector in the PΦM-OF transmitter and between the two phase-modulators in the CΦM-OF receiver. Since the SOP into the LO phase-modulator in the re-

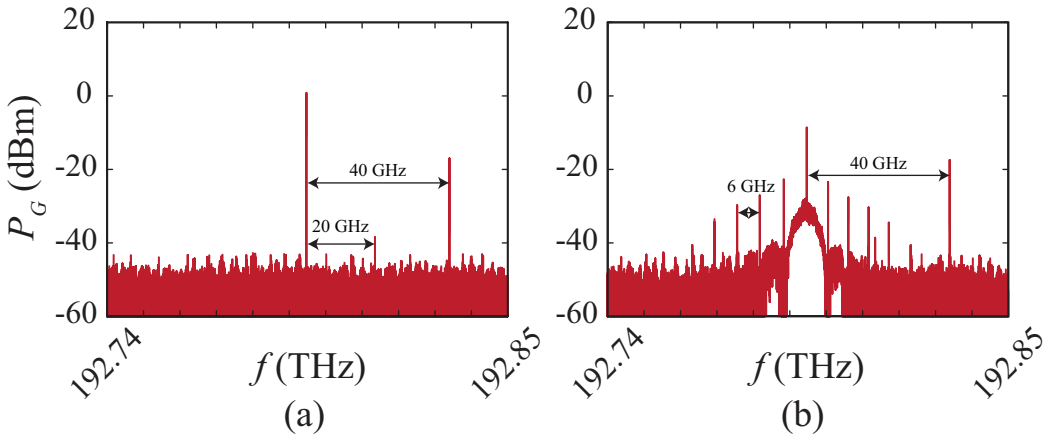

Figure 7.3: Measured optical spectra at point G in the PΦM-OF transmitter for $N = 2$ with (a) data 'off' and (b) 6 Gbps data 'on'. After [11].

ceiver varied randomly in time, a polarization tracker module was used. Finally, rather than using a real-time oscilloscope at the receiver to characterize the system performance, a digital sampling oscilloscope (DSO) and bit error tester (BERT) were used.

The optical spectra at point G in the PΦM-OF transmitter was measured with a Brillouin OSA (BOSA) The optical spectra with $f' = 20$ GHz is shown in Fig. 7.3 for the $N = 2$ case with and without a $R_b = 6$ Gbps on-off-keyed (OOK) signal applied. Since most of the measurements on this link were primarily conducted over a wireless link, further details on this configuration will be postponed to Section 9.1.

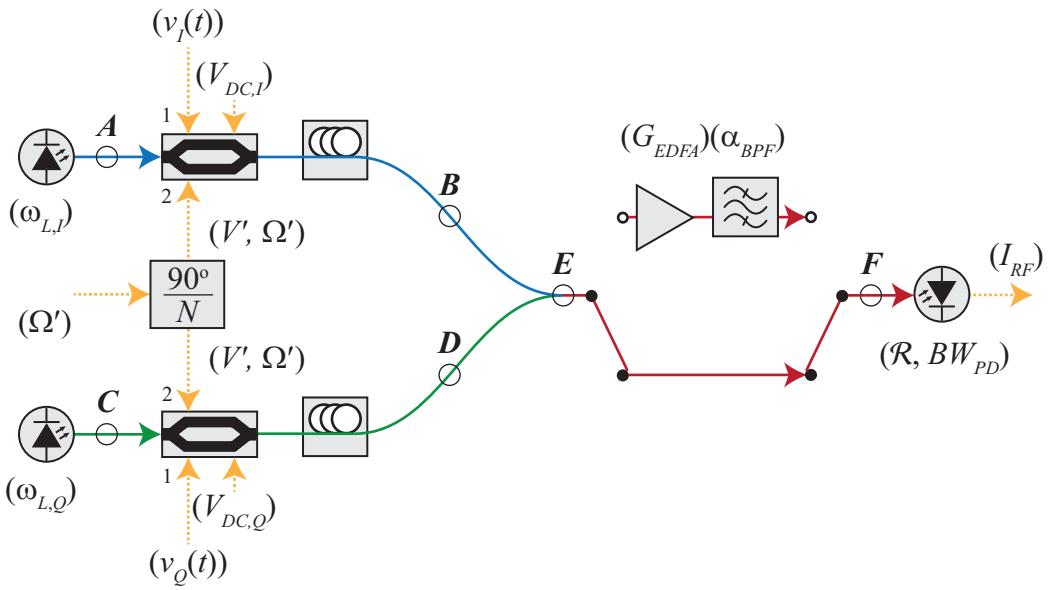

Figure 7.4: Simplified schematic of the DD-MZM based photonic vector modulation transmitter. After [12].

7.2 RF Modulation Using Dual-Drive MZMs

The experimental results for the RF photonic transmitter using dual-drive Mach-Zehnder modulators are described in this section. The electrooptic transmitter shown in Fig. 7.4 was constructed using commercially available components. The optical signals produced by two free-running external cavity, CW laser diodes were sent into two nominally identical 20 GHz lithium niobate ($LiNbO_3$) DD-MZMs through polarization maintaining fiber (PMF). The lasers had optical powers of approximately $P_L = 12 \pm 1$ dBm. The I branch laser had a wavelength of $\lambda_{L,I} = 1552.6$ nm and the Q branch laser had a wavelength of $\lambda_{L,Q} = 1554.94$ nm. The wavelength separation between the two lasers was approximately $\Delta\lambda_L = 2.3$ nm (291 GHz).

The DD-MZM in the I branch had an optical insertion loss of $\alpha_{MZM,I} \approx 2.4$ dB, RF half-wave voltages of $V_{\pi I,1} \approx V_{\pi I,2} \approx V_{\pi I} \approx 4.1$ V, and a DC bias half-wave voltage of $V_{\pi I,DC} \approx 6.0$ V. The DD-MZM in the Q branch was nominally identical to the DD-MZM in the I branch with the exception that the insertion loss was $\alpha_{MZM,Q} \approx 2.1$ dB. Both DD-MZMs had a 3 dB bandwidth of approximately 20 GHz.

The DD-MZM in the I branch was driven by an electrical LO and the DD-MZM in the Q was driven by an orthogonal electrical LO. The synchronized LOs were produced by splitting the amplified output from an analog signal generator with a 90° hybrid coupler. The electrical amplifier was either a 50 kHz to 20 GHz broadband amplifier or a 6-18 GHz power amplifier. The former was used for experiments performed at a fundamental frequency of $f_{RF} = f' = 20$ GHz while the power amplifier was used for harmonic upconversion experiments with $f_{RF} = N \times f' = 20$ GHz, $N \in \{2, 3\}$ and for $f_{RF} = 2\,f' = 36$ GHz. The DD-MZMs were also driven by electrical pseudorandom binary sequences. The data signal from the PRBS generator was amplified and applied to port 1 of the I branch DD-MZM and the data-bar signal, after being decorrelated by 38 bits, was amplified and applied to port 1 of the Q branch DD-MZM.

The modulated optical signals emerging from the DD-MZMs were sent into two variable optical delay lines (ODLs) prior to being coupled in a 50:50 (3 dB) directional optical coupler. The optical delay lines allowed minor path length mismatches between the I and the Q optical branches to be corrected. Since the optical delay lines only allowed adjustments of up to 600 ps in each branch, the maximum

single-mode fiber length that could be compensation for is approximately 120 mm at a wavelength of $\lambda_L = 1550$ nm.

For some measurements, the optical signal out of the single-mode coupler (point E) was amplified using a high-gain, low-noise EDFA that was set to operate in constant power mode. The amplified spontaneous emission (ASE) noise bandwidth was constrained using a 4 nm optical BPF. For convenience, a programmable optical filter was used to implement the rectangular BPF. The optical filter was based on liquid crystal on silicon (LCOS) wavelength selective switch (WSS) [142]. However, in principle, any suitable optical filter that allowed transmission of the two carriers and corresponding optical sidebands could be used. In Fig. 7.4, a switch is illustrated to denote that the EDFA + BPF combination can be manually connected between points E and F.

In some cases, the optical signal at point F was split with a 90:10 directional optical coupler. In these cases, the signal from the 10 % port was connected to an optical spectrum analyzer (OSA) while the signal from the 90 % was connected to a photodetector (PD). For simplicity, the 90:10 coupler is not shown in Fig. 7.4 as the optical insertion loss from the input to the 90 % output was only about 0.5 dB. Measurement results where the EDFA+BPF combination and/ or the 90:10 directional optical coupler were used will be noted in the text.

In the first set of measurements, a vector network analyzer (VNA) was used to characterize the photonic transmitter. For these experiments, no EDFA was used. The S_{21} scattering parameter was measured with port 1 of the VNA connected to the LO input and port 2 of the VNA connected to the photodetector output.

The in-phase (I) and quadrature (Q) voltage ratios were plotted in the complex plane. Since the frequency of the applied signals to ports 1 of the DD-MZMs were constrained by the narrow IF bandwidth of the VNA, a 3 dB RF power splitter was used to split the electrical LO and the relative phase between the I and the Q branches, θ, was adjusted optically using the optical delay lines. The experimental setup is shown in Fig. 7.5.

The generation of a vector modulated signal is demonstrated in the following experiment. First, the DD-MZMs were biased at their peaks. Next, a sinusoid having a period of $f = 20$ Hz and a peak amplitude of $V_I = 0.5$ V was applied to port 1 of the DD-MZM in the I branch. A nominally identical sinusoid with a 90° phase delay relative to the I channel input was applied to port 1 of the DD-MZM

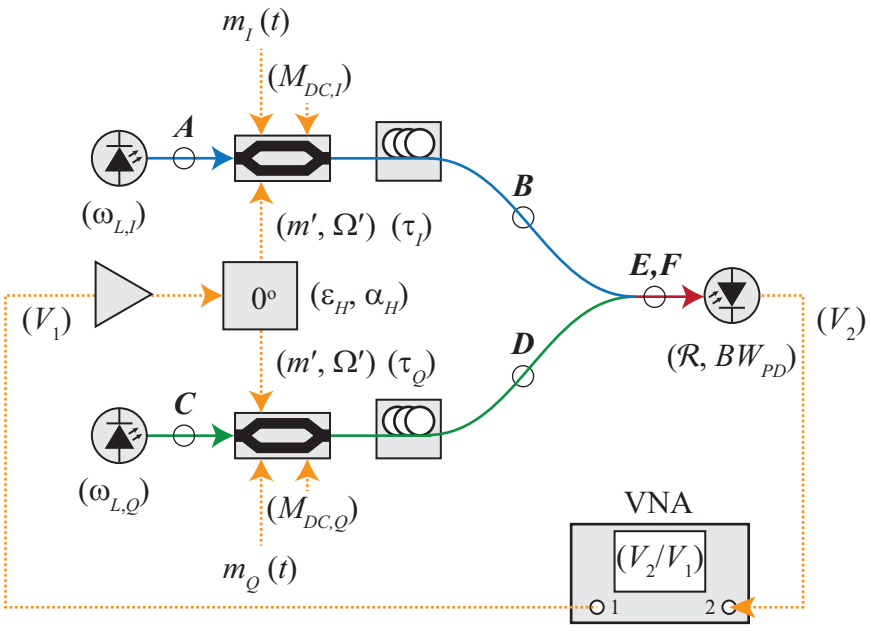

Figure 7.5: Experimental VNA setup to demonstrate vector modulation.

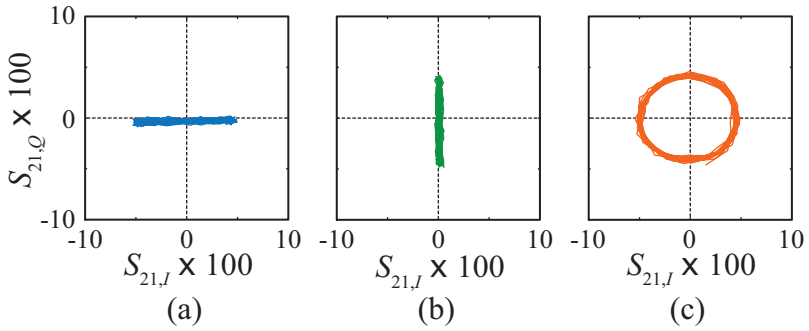

Figure 7.6: Measured plots of the S_{21} with the (a) I input 'on', (b) Q input 'on', and (c) I and Q inputs both 'on'.

in the Q branch. The modulation depths were approximately $m_I \approx m_Q \approx m \approx 0.4$ rad.

Note that these experimental results are qualitatively the same as the theoretical results shown in Fig. 6.8. Next, the input amplitude was varied from $V_i = 0.25$ V to $V_i = 1.0$ V, $i \in \{I, Q\}$. At small modulation depths, the output signal is linearly proportional to the input signal. This is expected as the transfer function between input modulation and output modulation is sinusoidal [143]. The Maclaurin series for $\sin z$ is

$$\sin m = \sum_{p=0}^{\infty} \frac{(-1)^p}{(2p+1)!} m^{2p+1}. \tag{7.1}$$

For small modulation depths ($m \ll 1$), Eq. (7.1) can be approximated as

$$\sin z \approx z \tag{7.2}$$

which is clearly linear. However, as the modulation depth is increased, higher order terms in the expansion given in Eq. (7.1) should be included. These higher order terms are nonlinear, which distort the signal. The S_{21} plots for $V_I = V_Q = V$

$\in \{0.25, 0.5, 1.0\}$ V are shown in Fig. 7.7. This range of voltages corresponds to input modulation depths of approximately $m = 0.2$ to 0.8 rad. The theoretical results are shown in Fig. 7.7(a) and the measurement results are shown in Fig. 7.7(b).

The electrooptic generation of 4-QAM/ quadrature phase-shift keyed (QPSK) signal encoded on an RF carrier is demonstrated in the following experiment. First, the DD-MZMs were biased at their peaks. Next, a square-wave having a period of $T = 0.1$ s and a peak amplitude of V_I was applied to port 1 of the DD-MZM in the I branch. A nominally identical square-wave with a time-delay of $T/4$ relative to the I channel input was applied to port 1 of the DD-MZM in the Q branch. The modulation depths were approximately $m_I \approx m_Q \approx m \approx 0.4$ rad. The signal out of port 1 of the VNA was amplified, split, and applied to ports 2 of the DD-MZMs. The LO modulation depths at a frequency of $f' = 18$ GHz were set at $m'_I \approx m'_Q \approx m' = 2.1$ rad. The in-phase and quadrature components of the S_{21} coefficient were plotted for four cases, as shown in Fig. 7.8.

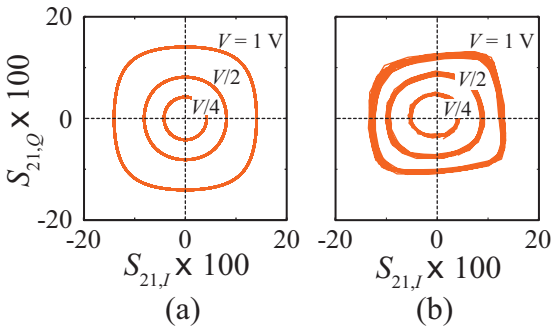

Figure 7.7: Plots of the S_{21} parameter as a function of modulation amplitude. (a) Theoretical results and (b) measurement results.

In Fig. 7.9(a), the two input signals were turned 'off'. Since the DD-MZMs were biased at their peaks, the odd-order harmonics of the LO were suppressed. Thus, a point at the origin was measured at a frequency of $f_{RF} = 1 \times f' = 18$ GHz. For Fig. 7.9(b)-(c), the I and Q input signals were independently applied, respectively. Finally, for Fig. 7.9(d), the I and Q input signals were simultaneously applied.

As discussed previously, the transfer function of the photonic transmitter is sinusoidal. For 4-QAM vector modulation, the optimal modulation peak-to-peak voltage swing is $V_{pp} = V_{\pi}$. This is equivalent to producing a quadrature phase-shift keyed (QPSK) signal for the case that the optical powers from the two arms are equal. If the DD-MZMs are biased at a peak/ null, this results in switching from the peak/ null to one of the quadrature points. Thus, the output will be switched between inverted/ non-inverted even harmonics, inverted odd harmonics, and non-inverted odd harmonics. An illustration was previously shown in Fig. 6.6. For the

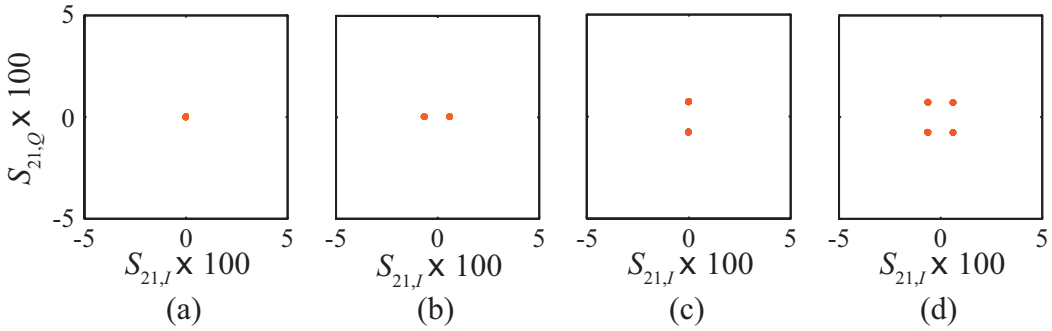

Figure 7.8: Measured plots of the S_{21} parameter illustrating 4-QAM generation. (a) I and Q 'off', (b) I 'on' and Q 'off', (c) I 'off' and Q 'on', and (d) I and Q 'on'.

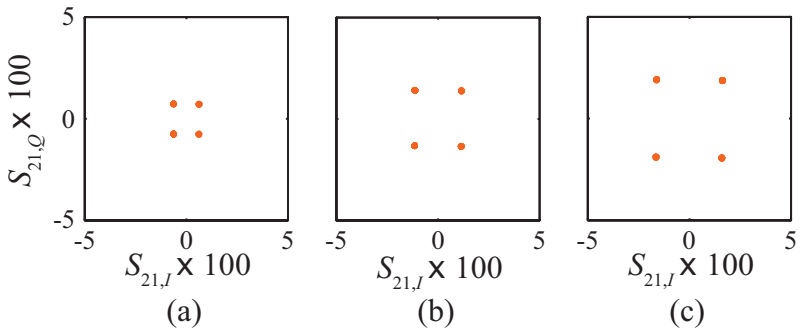

Figure 7.9: Measured plots of the S_{21} parameter demonstrating 4-QAM vector modulation for (a) $V = 0.5$ V, (b) $V = 1.0$ V, and (c) $V = 2.0$ V.

case where the LO modulation depth was chosen to maximize the $N = 1$ component, this amounts to primarily switching between inverted and non-inverted waveforms at the fundamental frequency ($f_{RF} = f'$). The measured S_{21} plots as a function of the input amplitude are shown in Fig. 7.9.

In Fig. 7.9, the symmetric bipolar peak amplitudes were $V_I = V_Q = V = \{0.5, 1.0, 2.0\}$ V corresponding to input modulation depths of approximately $m_I \approx m_Q \approx m \approx \{0.4, 0.8, 1.5\}$ rad. The half-wave voltage of the phase-modulators were approximately $V_{\pi,I} \approx V_{\pi,Q} \approx 4$ V. As indicated in Fig. 7.7, distortion is present when the input amplitude is large ($m \not\ll 1$). A look-up table could be used to correct for this distortion for complex modulation formats such as 16-QAM. However, analog vector modulated signals should not be driven as hard to avoid introducing distortion. The transfer function nonlinearity can be clearly visualized in Fig. 7.7.

To generate a 16-QAM constellations, 4-level waveforms were applied to the I and Q channels. The I channel input signal was created by adding a symmetric

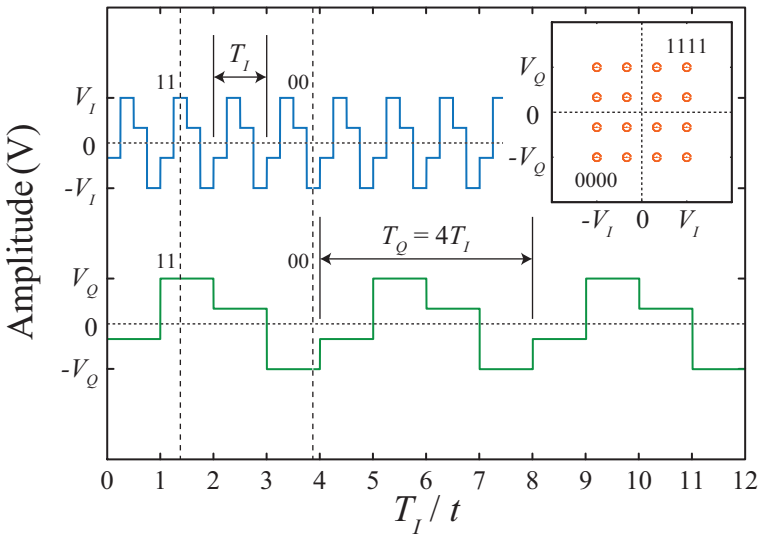

Figure 7.10: Qualitative illustration of 16-QAM signal generation via two periodic 4-level signals.

square wave with a period of T_I and amplitude A with a $T_I/4$ shifted symmetric square wave having an amplitude of $A/2$. The composite waveform was normalized by dividing the amplitude by $3A/2$. The repetition rate (RR) of the waveform applied to the I channel was set at $RR_I = 10$ Hz. The Q channel input signal was created in a similar fashion. The repetition rate of the waveform applied to the Q channel was set a $RR_Q = RR_I/4 = 2.5$ Hz. This created a set of waveforms with a baud rate of $1/RR_I = 10$ Baud ($R_b = 40$ bps). A qualitative example of generating I and Q 4-level waveforms is shown in Fig. 7.10.

Experimental measurements for the 16-QAM case are shown in Fig. 7.11. As in the 4-QAM case, the bipolar peak amplitudes were $V_I = V_Q = V = \{0.5, 1.0, 2.0\}$ V corresponding to input modulation depths of approximately $m_I \approx m_Q \approx m \approx$

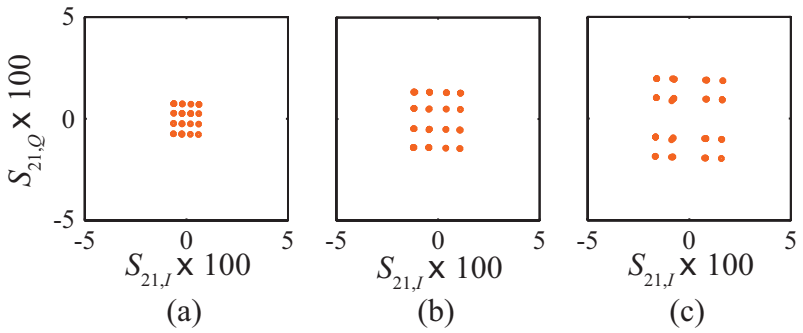

Figure 7.11: Measured plots of the S_{21} parameter demonstrating 16-QAM vector modulation for (a) $V = 0.5$ V, (b) $V = 1.0$ V, and (c) $V = 2.0$ V.

$\{0.4, 0.8, 1.5\}$ rad when the signals were at their maxima. From Fig. 7.11, it is evident that as the amplitude of the signals is increased, the constellation becomes distorted. Thus, unlike the 4-QAM case, the optimal peak-to-peak amplitudes are lower than $V_{pp} = V_\pi$. From Fig. 7.11, a maximum peak-to-peak amplitude of approximately $V_{pp} = V_\pi/2$ is a reasonable tradeoff between gain and distortion.

From Eq. (6.39), it was shown that vector modulation of harmonics of the LO can be achieved with the DD-MZM approach. This is demonstrated using vector network analysis with a frequency offset option. The source (port 1) and receiver (port 2) were configured as shown in Fig. 7.1. The input signals were synthesized with an arbitrary waveform generator (AWG) and had peak-to-peak amplitudes of $V_I = V_Q = V = 1$ V and frequencies of 5 Hz and 1.25 Hz, respectively. The LO frequency was set at $f' = 15$ GHz. The optimal modulation depths were previously calculated in Table 6.1 for $N \in \{1, 2, 3, 4\}$ to be $m' \in \{1.8, 3.1, 4.2, 5.3\}$ rad. In the experiment, the LO modulation depth was approximately $m' \in \{1.9, 3.1, 3.9, 3.9\}$ for

Table 7.1: VNA frequency offset settings.

	Mode	Sweep Type	Settings
Primary		CW Time	CW Freq f'
Source	Coupled	CW Time	CW Freq f'
Receiver	Coupled	CW Time	CW Freq $N \times f'$

$N \in \{1, 2, 3, 4\}$. The DD-MZMs were manually biased to appropriate bias points and the quadrature condition between the two channels was set with the optical delay lines. Unlike the results shown in Figs. 7.6, 7.8, 7.9, and 7.11, the constellations in Fig. 7.12(a)-(d) are scaled by different normalization constants. It should be noted that the LO modulation depth at $N = 4$ was far from optimal, resulting in a theoretical penalty in gain of 3.5 dB from the optimal value. Thus, the theoretical

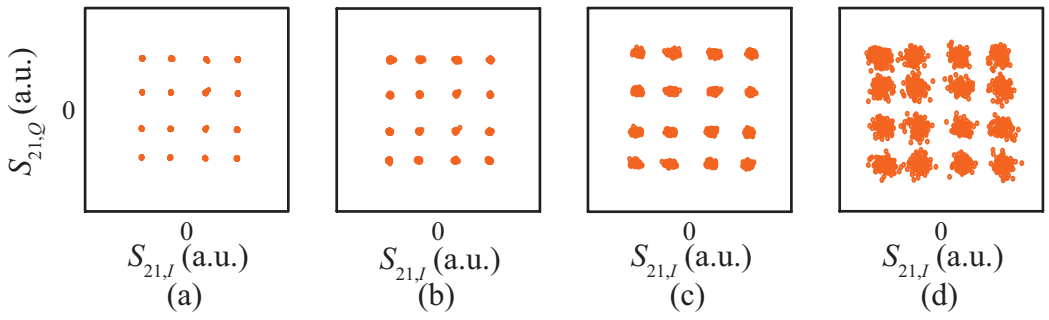

Figure 7.12: Measured plots of the S_{21} parameter demonstrating 16-QAM generation and harmonic upconversion for (a) $f_{RF} = 15$ GHz ($N = 1$), (b) $f_{RF} = 30$ GHz ($N = 2$), (c) $f_{RF} = 45$ GHz ($N = 3$), and (d) $f_{RF} = 60$ GHz ($N = 4$).

penalty in gain of the $N = 4$ case with $m' = 3.9$ rad relative to the $N = 1$ case with $m' = 1.8$ rad is 6.8 dB. This value does not include the increased cable losses or the lower photodetector responsivity, which decreased from $\mathcal{R} = 0.87$ A/W at f_{RF} = 15 GHz to $\mathcal{R} = 0.65$ A/W at $f_{RF} = 60$ GHz. Thus, it is not surprising that the signal-to-noise ratio (SNR) for the $N = 4$ case is lower than that of the SNR for the $N = 1$ case. The spread of the constellation points is indicative of a lower SNR. If the higher noise for the $N = 4$ case was due strictly to phase noise, the constellation points would be primarily be spread in the axial direction.

In the previous measurements, the power amplifier gain, G_A, and electrical hybrid power splitting ratio and excess loss, $\epsilon_H \alpha_H$, were not calibrated out of the VNA results. In one sense, the LO amplifier and splitter could be defined as part of the photonic transmitter. For completeness, the total small-signal gain of the amplifier/ electrical hybrid network was measured to be approximately $10 \log_{10} G_A \epsilon_H \alpha_{H,I} \alpha_C$ = 25.4 dB and $10 \log_{10} G_A \epsilon_H \alpha_{H,Q} \alpha_C = 24.5$ dB at $f' = 18$ GHz, where α_C is the coax insertion loss. The measurement results are shown in Fig. 7.13.

To perform the VNA measurements, the AWG was set in pulsed mode and was triggered by the VNA at the start of each zero-span trace. The AWG external reference input was connected to the VNA external reference to synchronize the sources.

In the next set of measurements, the optical signal at point E was amplified with the EDFA+BPF combination shown in Fig. 7.4. Furthermore, the 90:10 directional optical coupler was inserted at point F. The optical spectrum at the 10 % port of the coupler was measured with a standard grating based OSA or with a

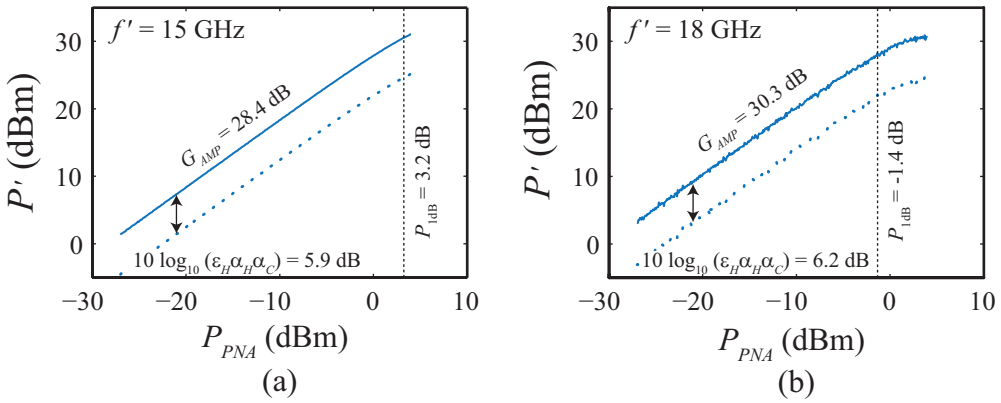

Figure 7.13: Measured RF amplifier and power splitter composite gain at (a) f = 15 GHz and (b) f = 18 GHz.

BOSA, the latter having a resolution bandwidth of RBW = 10 MHZ. The BOSA acquired optical spectrum of the two unmodulated lasers is shown in Fig. 7.14(a). As indicated in the figure, the frequency separation between the optical carriers was approximately 291 GHz, which is over a factor of 4× the bandwidth of any photodetector used in the measurements.

Two binary data signals, each having bit-rates of R_b = 1 Gbps, were applied to the DD-MZMs. The BOSA acquired modulated optical spectrum is shown in Fig. 7.14(b). The data signals were turned 'off' and orthogonal LOs having frequencies of f' = 20 GHz were applied to the DD-MZMs and the optical spectrum was acquired as shown in Fig. 7.14(c). Finally, the data signals and the LOs were applied to the DD-MZMs simultaneously. The resulting optical spectrum is shown in Fig. 7.14(d).

Two effects not predicted by the simply theory presented in Section 6.2 were

observed. The first was that asymmetry was observed in the optical spectrum. The analysis presented in Section 3.6.2 can be extended to account for RF phase differences between the arms, which can result in asymmetric spectra [124]. The second was thermal bias drift due to heating caused by the strong LO applied to one arm of the DD-MZM.

In the next set of experiments, vector modulation and upconversion was demonstrated. The output RF signal from the photodetector was amplified and high-pass filtered with an electrical filter having a 3 dB lower cutoff frequency of 18 GHz. After a short coaxial span, the RF signal was amplified again and sent into a 3 dB RF power splitter. One of the outputs was connected to an ESA. The other output was connected to an electrical receiver, which will be discussed shortly. The experimental setup is shown in Fig. 7.15.

The LO frequency was set at $Nf' = 20$ GHz for $N \in \{1, 2, 3\}$ and applied

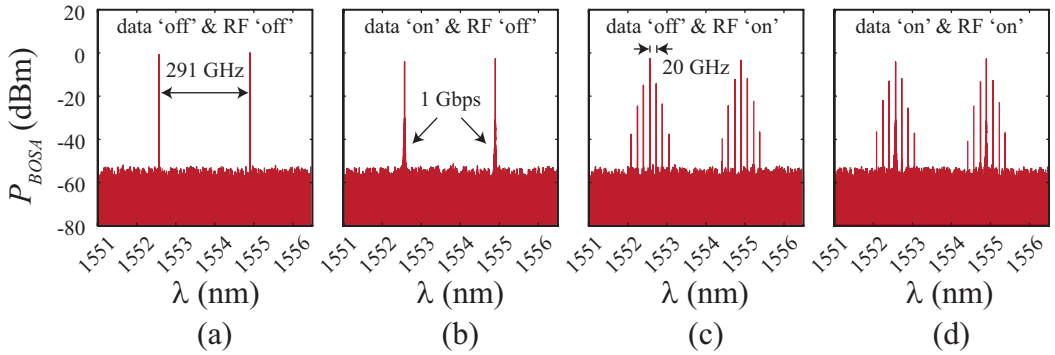

Figure 7.14: Measured optical spectra at point F in the vector DD-MZM transmitter. (a) Unmodulated, (b) modulated with data signals only, (c) modulated with LOs only, and (d) simultaneously modulated with data signals and LOs.

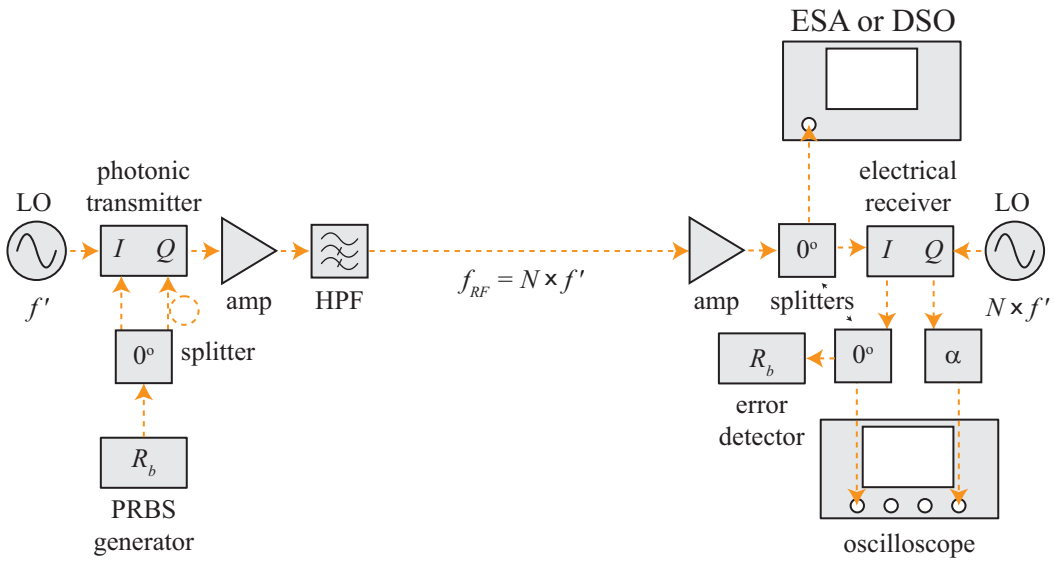

Figure 7.15: DD-MZM photonic transmitter and electrical receiver experimental setup.

to ports 2 of the DD-MZMs. The data applied to ports 1 of the DD-MZMs were two R_b = 1.24416 Gbps PRBS signals, decorrelated by 38 bits. Pattern lengths ranging from $2^7 - 1$ to $2^{23} - 1$ were applied, the latter being the longest pattern that the PRBS generator used in this experiment was capable of producing. For the measurement performed at the fundamental LO frequency, an RF signal at $f_{RF} = f'$ = 20 GHz was electrooptically modulated. For the frequency doubling measurement, the transmitter LO was electrooptically frequency doubled ($f_{RF} = 2 \times f' = 20$ GHz) and vector modulated. Likewise, for the frequency tripling experiment, the transmitter LO was electrooptically frequency tripled ($f_{RF} = 3 \times f' = 20$ GHz) and vector modulated. The vector modulated fundamental ($N = 1$), frequency doubled ($N = 2$), and frequency tripled ($N = 3$) electrical spectra are shown in

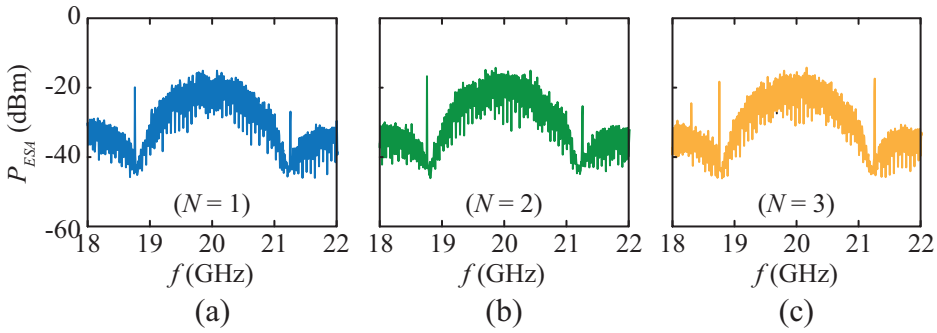

Figure 7.16: Measured 4-QAM modulated RF spectra. (a) Fundamental ($N = 1$), (b) frequency doubled ($N = 2$), and (c) frequency tripled ($N = 3$). After [12].

Fig. 7.16(a)-(c), respectively, for a PRBS pattern length of $2^{23} - 1$.

To characterize the performance of the photonic transmitter, an electrical coherent homodyne receiver was constructed as shown as Fig. 7.17. The electrical receiver consisted of an attenuator, an RF power splitter, two electrical mixers, a 90° RF hybrid network, and two electrical limiting amplifiers. Since an external amplifier was used prior to the electrical receiver, an attenuator (16 dB) was incorporated at the input of the receiver to prevent over-driving the electrical mixers. The outputs from the power splitter were sent into the RF ports of a pair of double-balanced electrical mixers.

The receiver LO was split with a RF 90° hybrid network, consisting of discrete RF components. After splitting the LO power with a 3 dB power splitter, the relative phase between the two LOs was set to 90° using a broadband phase shifter at one of the power splitter outputs. The orthogonal LOs were applied to the LO ports of the two electrical mixers. To account for the insertion loss of the phase shifter, a 3 dB

electrical attenuator placed at the other power splitter output. The downconverted signals emerging from the IF ports of the electrical mixers were amplified with electrical limiting amplifiers. Since phase tracking was not implemented in the receiver, a 10 MHz Rubidium (Rb) frequency standard was used to lock the TX and RX LOs along with the oscilloscope via their external 10 MHz reference inputs.

The vector modulated signals generated by the photonic transmitter were downconverted to baseband and demodulated using the electrical receiver. One of the baseband signals was split with an RF power splitter and the other was attenuated by 5 dB to account for splitting and excess losses. One of the outputs from the power splitter and the attenuated baseband signal was fed into a four channel digital oscilloscope. The digital oscilloscope had an analog bandwidth of 1 GHz and a maximum sample rate of 20 GSa/s. The other signal out of the power splitter was sent into a BERT error detector. The configuration with the I channel split and the Q channel attenuated was previously shown in Fig. 7.15.

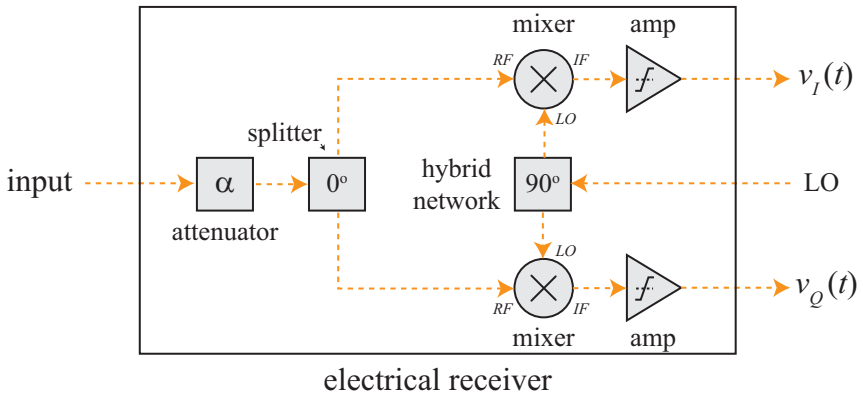

Figure 7.17: Simplified schematic of the electrical receiver. After [12].

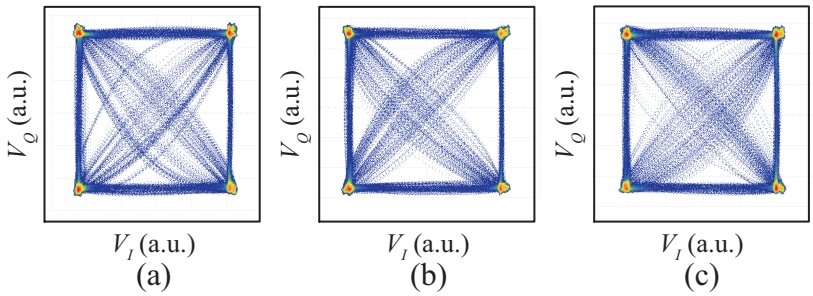

Figure 7.18: Measured 4-QAM baseband constellations after photonic generation followed by electrical detection. After [12].

In this configuration the baseband constellation and the BER for one channel were acquired. As soon as the BER measurement was complete, the channels were swapped and the measurement was performed again. No adjustments were made between complementary measurements. The baseband constellations corresponding to the electrical spectra shown in Fig. 7.16 are shown in Fig. 7.18. BERs of less than 1×10^{-9} were measured on both channels at $f_{RF} = 20$ GHz for $N \in \{1, 2, 3\}$ and $R_b = 1.24416$ Gbps.

The BERT used in the previous measurements was limited to a maximum bit-rate of 1.4 Gbps. To demonstrate transmitter operation at higher data-rates, a higher bit-rate PRBS source was employed. In the next set of measurements, the single channel bit-rate was changed from 1 Gbps to 4 Gbps. The optical spectra out of the 10 % port of the 90:10 optical coupler at point F of the transmitter with only the LO signal applied to the DD-MZM was measured using the BOSA. Next, the RF spectra out of the photodetector was measured using an ESA at the output of the 3 dB power splitter, as indicated in Fig. 7.15. The time domain signals were

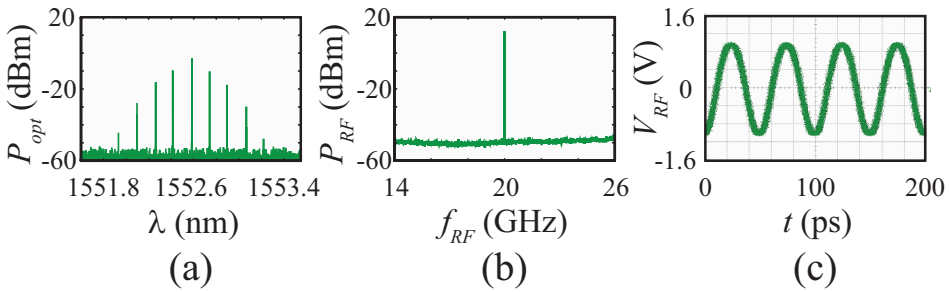

Figure 7.19: Measured (a) optical spectrum, (b) RF spectrum, and (c) RF waveform generated by the DD-MZM transmitter with no data applied (single channel).

also measured at the same point using a DSO with a 50 GHz electrical module. The results are shown in Fig. 7.19.

Finally, the data and LO signals were simultaneously applied to the DD-MZM. As in Fig. 7.19, the optical spectra, RF spectra, and RF waveforms are shown in Fig. 7.20(a)-(c). In addition, the electrically demodulated baseband signals are now shown in column (d). In Fig. 7.19, the rows correspond to the bit-rate, which was increased from $R_b = 1$ Gbps in row (i), to $R_b = 2$ Gbps in row (ii), and to $R_b = 4$ Gbps in row (iii).

The electrical mixers used in the electrical receiver had IF bandwidths of 3 GHz, limiting the maximum experimental bit-rate as evidenced in the electrically demodulated signals. The effect of the limited IF bandwidth on the baseband eye diagram is particularly pronounced in Fig. 7.20(iii,d).

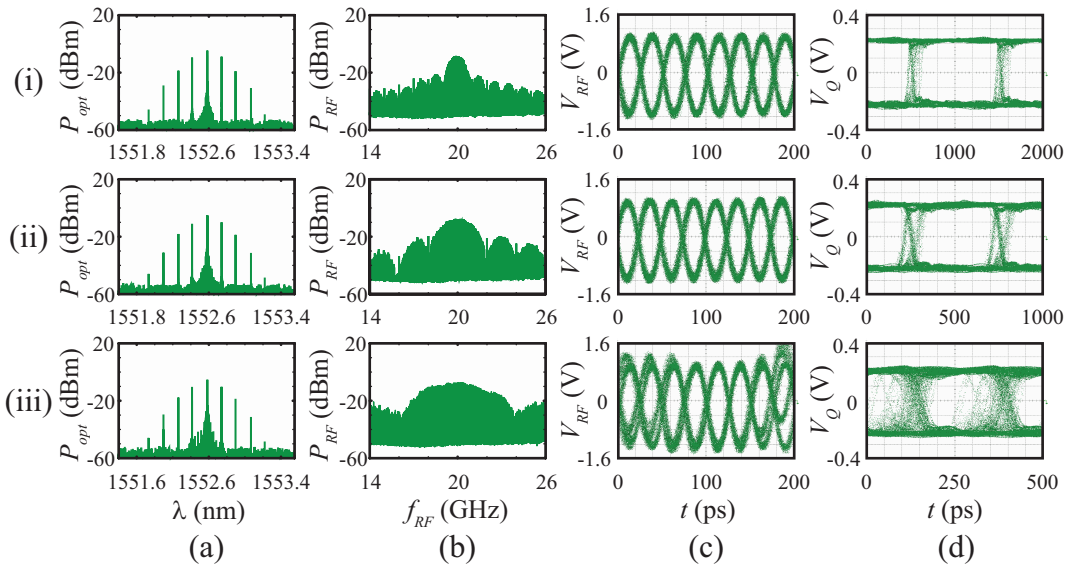

Figure 7.20: Measured (a) optical spectra, (b) RF spectra, (c) RF waveforms generated by the DD-MZM transmitter, and (d) electrically demodulated baseband waveforms with data applied (single channel).

Chapter 8

Wireless Transmission Theory

In general, a communication system consists of a transmitter, a channel, and a receiver [144]. In Chapters 4-5, the theory and experimental results for two photonic receivers were presented. Likewise, in Chapters 6-7, the theory and experimental results for two photonic transmitters were described. In this chapter, channel considerations for utilizing the RF photonic transmitter and receiver in a wireless communication system are addressed. Topics such line-of-sight (LOS) propagation, free-space path loss, and atmospheric absorption are considered. Furthermore, frequency and power emission regulations will be discussed for the 60 GHz and 70/80/90 GHz bands.

The channel is the path used to convey an information signal between the transmitter and receiver in a communication system. Physically, a channel could be a propagation channel or a wired channel, among others. In an ideal channel, the receive signal is equal to the transmit signal. However, nonidealities in the channel such as noise and interference, deterministic signal processing, and attenuation (static and time-varying) are present in practical systems [144]. The additive noise can be internal or external to the communication system. Internal noise is noise due the random motion and random production and annihilation of charge carriers. Thermal noise is an example. External additive noise, which includes atmospheric

noise, human generated noise, and solar and galactic noise, will not be considered here.

Wireless systems can be categorized according to the nature and placement of the users as point-to-point, point-to-multipoint, and multipoint-to-multipoint [3]. Communication directionality is an alternative way to categorize wireless systems. The main categories are simplex, half-duplex, and full duplex [3]. They can also be categorized by their operation frequency [3]. In this dissertation, point-to-point, simplex wireless systems are described.

8.1 Line-of-Sight Propagation

In general, an RF signal can take several paths between the source and the destination. The LOS path is the straight line path between the transmitter and receiver antennas. This path can be blocked by obstacles including buildings and mountains. At mmW frequencies, even small obstacles can block the LOS path.

Although the signal may propagate using the LOS path, it is also important to maintain clearance around this path to prevent phase-cancellation of the signal due to reflections from obstacles. The Fresnel zone is the boundary around the LOS path where a reflection would introduce an excess path length of $n\lambda/2$. In the case where a circular apertures are employed, the boundary can be described by an ellipsoid of revolution around the LOS path. The radius of the n^{th} Fresnel zone at a point a distance of d_{TX} from the transmitter and d_{RX} from the receiver can be

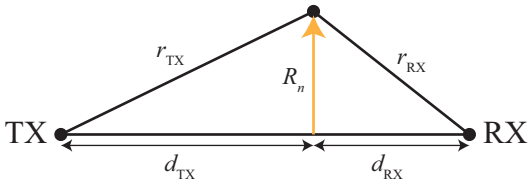

Figure 8.1: Geometry for Fresnel zone calculation. After [14].

expressed as [14]

$$R_n = \sqrt{\frac{n d_{TX} d_{RX} \lambda}{d}} \tag{8.1}$$

where λ is the wavelength of the radiation ($\lambda = c/f$) and $d = d_{TX} + d_{RX}$ is the LOS path length.

The maximum Fresnel zone radii, $R_{n,max}$ for $n \in \{1, 2, 3\}$ are calculated as a function of RF frequency for a LOS distance of $d = 1$ km and as a function of LOS distance for $f = 60$ GHz in Fig. 8.2. Of importance is that Fresnel zone radii scale as $1/\sqrt{f}$. Thus, maintaining clearance around the LOS path is particularly important at microwave frequencies and below and diminishes at mmW frequencies.

8.2 Non-Line-of-Sight Propagation

In addition to the LOS component, it is possible to relay non-LOS (NLOS) components through a channel. These components are due to a variety of phenomenon including reflection, refraction, and diffraction [145]. In some cases, NLOS signals are advantageous as they can provide connectivity when the LOS path is blocked. However, NLOS propagation can result in multiple copies of the transmitted signal to be received at the destination leading to interference and in some cases

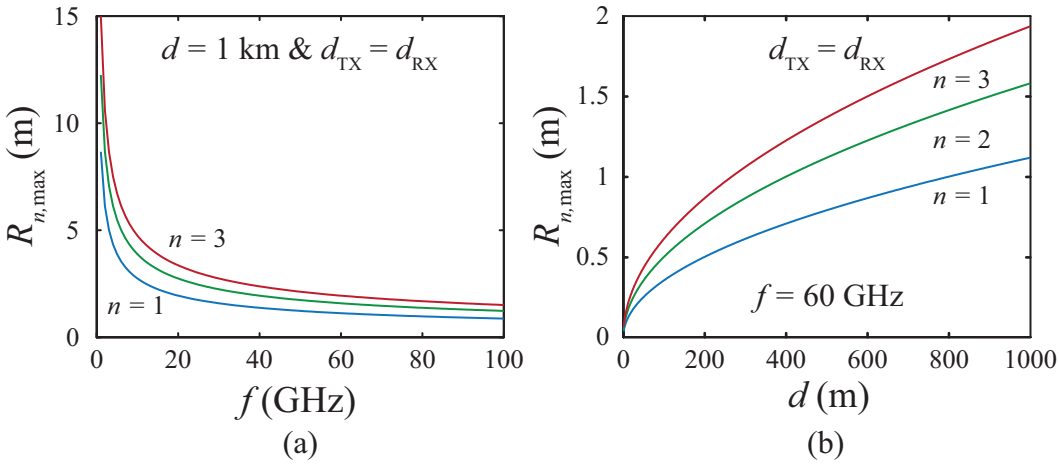

Figure 8.2: Calculated maximum Fresnel zone radii, $R_{n,\max}$, as functions of (a) the RF frequency and (b) the LOS distance.

multipath fading. This topic is of importance, particularly at frequencies in the ultra high frequency (UHF) band and below (i.e. $f \leq 3$ GHz). More information on fading is provided in [145].

Since the free-space path loss (described in the next section) increases as the square of the frequency, higher gain antennas are typically used at microwave and mmW frequencies. High gain antennas by definition have high directivities, so the LOS is the primary component for backhaul applications. Since this dissertation is primarily concerned with microwave and mmW backhaul using directional antennas, the theory behind multipath propagation and fading will not be addressed here and will simply be pointed-out. Modeling of LOS and NLOS channel capacities of 60 GHz indoor wireless communication systems is considered in [146].

8.3 Free-Space Path Loss

Free-space path loss (FSPL) is the loss incurred by the geometric spreading of the wavefront as a signal propagates in a medium. In logarithmic units, the FSPL, $L_{FS,\text{dB}}$, can be expressed as

$$L_{FS,\text{dB}} = 10n \log_{10}\left(\frac{4\pi f d}{c}\right) \tag{8.2}$$

where n is the path loss exponent. In isolation, the power density of the propagating signal decreases as the inverse-square of the propagation distance, thus $n = 2$. However, in practice, the average path loss exponent is typically greater than $n = 2$ and is empirically determined by measuring the path loss as a function of path length (e.g. see [147]).

In Fig. 8.3, Eq. (8.2) is plotted in terms of the RF frequency and in terms of normalized distance for $n = 2$. The normalized FSPL plotted in Fig. 8.3(b) is particularly helpful. Once the frequency dependence has been factored out and the normalized FSPL calculated, the incremental FSPL is identical for all frequencies. This is easy to observe by rewriting Eq. (8.2) as

$$L_{FS,\text{dB}} = 20 \log_{10}\left(\frac{4\pi f}{c}\right) + 20 \log_{10}(d) \tag{8.3}$$

and noting that the second term on the right hand side is zero at $d = 1$ m. Also, note that the path loss exponent has been set to $n = 2$ in Eq. (8.3). Based on Fig. 8.3(b), the normalized FSPL at $f_{RF} = 60$ GHz is $L_{FS,\text{dB}}(d_0 = 1\text{m}) = 68$ dB for $n = 2$. For comparison, the FSPL at the personal communication service (PCS) band ($f_{RF} =$ 1.9 GHz) is $L_{FS}(d_0 = 1\text{m}) = 38$ dB. As the frequency increases 10-fold, the FSPL

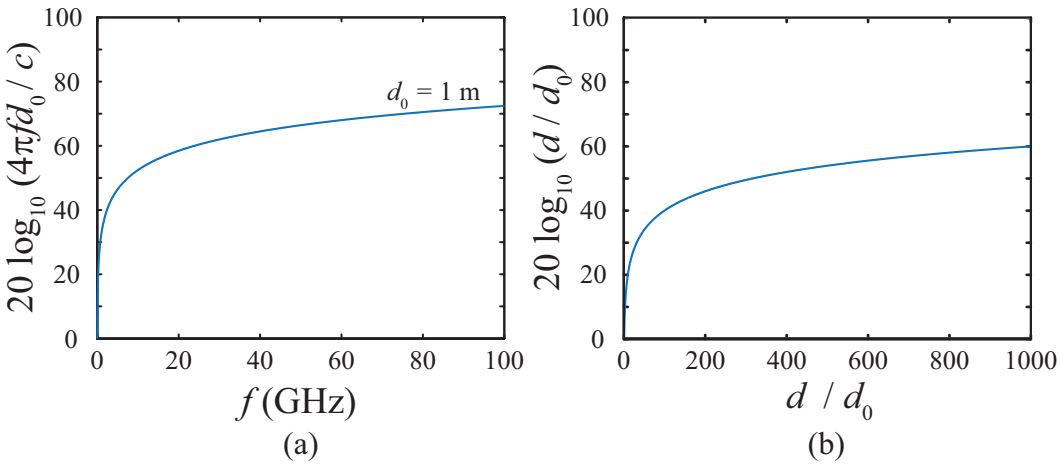

Figure 8.3: Calculated FSPL components as a function of (a) frequency and (b) normalized distance. The FSPL, $L_{FS,\mathrm{dB}}$, is the sum of (a) and (b).

increases by a factor of 100, or by 20 dB. Thus, high-gain, directional antennas are required at mmW frequencies [17].

8.4 Atmospheric Absorption

In addition to FSPL, other propagation loss factors that should be considered include atmospheric gaseous attenuation, precipitation attenuation, foliage blockage, scattering effects (diffused and specular), and diffraction [148]. Strong gaseous absorption peaks occur around 24 GHz and 60 GHz band due to water vapor (H_2O) and oxygen (O_2) mechanical resonances, respectively. Spectral windows where atmospheric losses are at a local minima occur at frequencies around 35 GHz, 94 GHz, 140 GHz, and 220 GHz [148]. The density and humidity of the atmosphere that the signal propagates through affects the attenuation strength. Clearly, higher

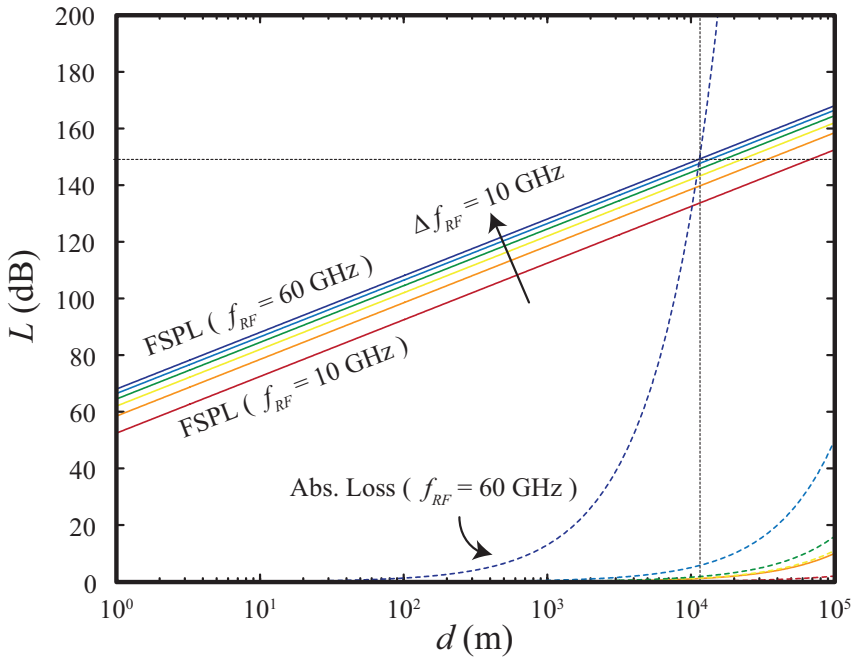

Figure 8.4: Calculated FSPL and absorption loss curves.

altitudes lead to lower atmospheric losses at microwave and mmW frequencies. Furthermore, the direction of propagation determines the degree of attenuation. Signals propagating at zenith will experience less atmospheric loss than those propagating horizontally [148].

An interesting point is that the absorption due to the oxygen resonance dominates the FSPL for distances greater than approximately 10 km at 60 GHz. This is one of the main reasons that the 60 GHz band is attractive for short distance links with high spectral reuse.

8.5 Noise

The main limitation to a wireless communication system is having the signal-to-interference-plus-noise ratio (SINR) fall to an unacceptable level. In many cases, such as mobile communications, the interference contribution dominates the noise contribution. However, in backhaul scenarios where highly directional antennas are utilized, noise is the dominant contribution to the interference-plus-noise level. Thus, the interference aspect will not be considered in this dissertation. As described in Appendix C, the signal-to-noise ratio (SNR) can never be improved in practice and will at best be preserved as the signal progresses through an element or a system.

The random motion of charge carriers in a lossy material generates thermal noise, also commonly referred to as Johnson-Nyquist noise. Generally, thermal noise power is expressed on a logarithmic scale as

$$P_{Nin,\mathrm{dBm}} = -174\mathrm{dBm} + 10\log_{10}\Delta f \tag{8.4}$$

where an input temperature of $T_{in} = 290$ K has been assumed (i.e. room-temperature) and Δf is the noise bandwidth. If the receiver adds noise, then the total noise at the receiver is

$$P_{NRX,\mathrm{dBm}} = P_{Nin,\mathrm{dBm}} + NF_{RX,\mathrm{dB}} \tag{8.5}$$

where $NF_{RX,\mathrm{dB}}$ is the noise figure of the receiver. From Eq. (8.5), the thermal noise level sets the lower bound on the minimum noise level. At the receiver, the noise power will at a minimum be equal to the input thermal noise power. Thus, propagation losses can lead to an effective degradation of SNR, which sets the fundamental

limit on the range of a link.

8.6 Friis Equation

A simple transmission formula was proposed by Friis [149] for determining the power received in a wireless link. Assuming the transmitting and receiving antennas have gains relative to an isotropic radiator of G_{TX} and G_{RX}, respectively, the received power, P_{RX} is given by

$$P_{RX} = \frac{G_{TX} G_{RX}}{L_{FS}} P_{TX} \tag{8.6}$$

where P_{TX} is the transmitted power and L_{FS} is the linear form of free space path loss given by Eq. (8.2) with $n = 2$. Commonly, the received power is expressed in units of decibels as

$$10 \log_{10} P_{RX} = 10 \log_{10} (P_{TX} G_{TX}) + 10 \log_{10} G_{RX} - 10 \log_{10} L_{FS} \tag{8.7}$$

where the product $P_{TX} G_{TX}$ is commonly denoted the equivalent isotropic radiated power (EIRP). Eq. (8.7) is valid at large propagation distances d satisfying

$$d \geq 2a^2 f / c \tag{8.8}$$

where a is the largest linear dimension of either of the antennas [149]. This condition is analogous to the Fraunhofer distance, which gives the condition for far-field radiation for the case of antennas having dimensions larger than half the wavelength of the RF signal.

8.7 Link Budget

Link budgets are helpful system level design tools to help to quantify whether a communication system design is feasible. In general, a link budget can be expressed in terms of the transmit power, P_{TX}, the receive power, P_{RX}, the gains in the system, G, and the losses in the system, L, as

$$P_{RX} = P_{TX} + \sum_{i=0}^{N_G} G_i - \sum_{i=0}^{N_L} L_i \tag{8.9}$$

where N_G is the number of gains in the system, N_L is the number of losses in the system. To close the link, the receive power, P_{RX}, must be greater than then receiver sensitivity. Propagation impediments that should be considered when calculating the link budget include attenuation (scattering and absorption), depolarization, noise emission, and scintillation among others [17, 148].

Other challenges in utilizing mmW frequencies for communication links include human shadowing, mutipath fading, Doppler shift (even at pedestrian velocities), and noise [17]. Additional details of propagation at mmW frequencies can be found in [26, 148].

In a wireless link, the tolerable path loss can be calculated as

$$\begin{aligned} L_{path,\mathrm{dB}} &= P_{TX,\mathrm{dBm}} + G_{TX,\mathrm{dBi}} + G_{RX,\mathrm{dBi}} + P_{Nin,\mathrm{dBm}} - SNR_{min,\mathrm{dB}} \\ &- M_{shad,\mathrm{dB}} - L_{EX,\mathrm{dB}} - L_{FS,\mathrm{dB}}(d = 1m) \end{aligned} \tag{8.10}$$

where $P_{TX,\mathrm{dBm}}$ is the transmit power, $G_{TX,\mathrm{dBi}}$ is the gain of the transmit antenna, $G_{RX,\mathrm{dBi}}$ is the gain of the receive antenna, $P_{Nin,\mathrm{dBm}}$ is the average noise power per bit as given by Eq. (8.4), $SNR_{min,\mathrm{dB}}$ is the minimum required SNR at the RX,

Table 8.1: Rain attenuation at 60 GHz. After [2].

Availability	Rate	Attenuation
99%	2 mm/h	1.3 dB/km
99.99%	25 mm/h	10.1 dB/km
99.999%	85 mm/h	32.5 dB/km

$M_{shad,\mathrm{dB}}$ is the shadowing link margin, $L_{EX,\mathrm{dB}}$ is the excess implementation loss, and $L_{FS,\mathrm{dB}}$ is the free-space path loss [17]. The atmospheric absorption at 60 GHz is commonly set at 15 dB/km [148]. For IEEE 802.15.3c, the shadowing margin is $M_{shad} = 1$ dB. It is also common to factor in margins for reflection losses and losses in the feeding network.

In addition to the atmospheric losses described in Section 8.4, precipitation can contribute to additional propagation losses. For example, commonly used values for rain attenuation margins for three availabilities at 60 GHz are provided in Table 8.7. Based on Eq. (8.10), the maximum operating range can be calculated to be

$$d = 10^{L_{path,\mathrm{dB}}/(10n)} \tag{8.11}$$

where n is the path loss exponent. The calculated link margin at 60 GHz for the availabilities given in Table 8.7 are calculated with a path loss exponent of $n = 2$. Thus, for carrier class links (availability = 99.999 %), the link margin is zero at a distance of $d = 1$ km.

In Eq. (8.10), the minimum SNR is a parameter. In many textbook, the SNR is given in terms of the energy per bit to the additive white Gaussian noise

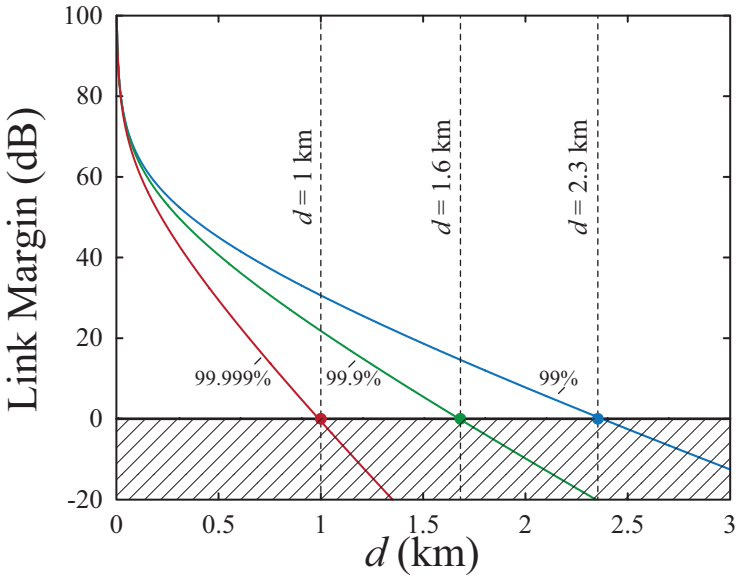

Figure 8.5: Calculated link margin for three availabilities based on the rain margins in Table 8.7.

(AWGN) power. The minimum SNR is depended on the modulation format and on the tolerable bit error rate (BER). The tolerable BER is often set by the forward error correction (FEC) code that is employed at the receiver. FECs require that additional symbols be encoded with the transmitted data symbols to perform error-correction. Common FECs are Reed-Solomon (RS), low-density parity-check (LDPC), Turbo, and convolutional codes, among others. However, the FEC requires sufficient computational power at the transmitter and the receiver and adds an overhead to the transmitted data. For example, a RS(255,223) code can correct 16 symbols in codeword of 255 symbols with an overhead of 7 %. Details on the theory of FEC are beyond the scope of this dissertation; however, many references are available on this topic [144].

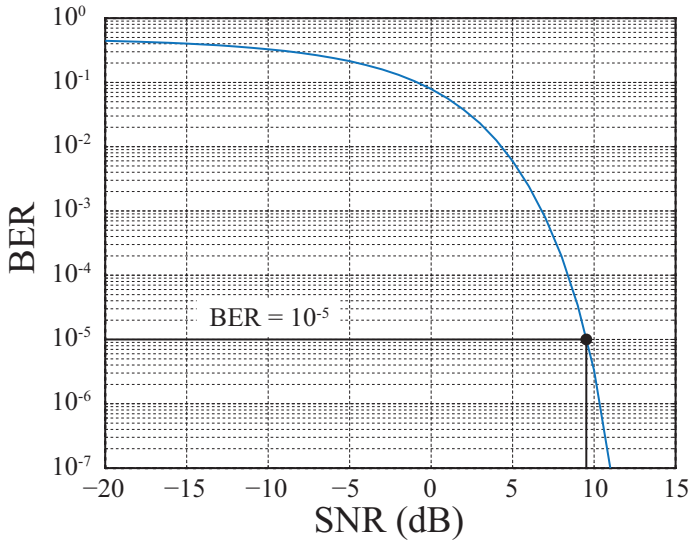

Figure 8.6: Calculated BER as a function of SNR for 4-QAM (QPSK) with AWGN.

Performing a numerical simulation, the BER as a function of SNR was calculated for 4-QAM assuming AWGN. The results are plotted in Fig. 8.6.

Assuming that the tolerable BER is arbitrarily set at 10^{-5}, then the minimum SNR, SNR_{min}, needed for various modulation formats is tabulated in Table 8.7. In Table 8.7, ASK is an abbreviation for amplitude-shift keying, FSK is an abbreviation for frequency-shift keying, PSK is an abbreviation for phase-shift keying, and QAM is an abbreviation for quadrature amplitude modulation. Also, often 2 symbol shift keying formats are referred to as 'binary' and 4-symbol shift keying formats are referred to as 'quadrature'. For example, 2-ASK is equivalent to binary ASK (BASK) and 4-PSK is equivalent to quadrature PSK (QPSK).

Table 8.2: SNR and bandwidth efficiency for various formats. After [3].

Modulation Format	SNR (dB) for $BER = 10^{-5}$	BW Efficiency (b/s/Hz)
2-ASK	15.6	1
2-FSK	12.6	1
2-PSK	9.6	1
4-PSK/4-QAM	9.6	2
8-PSK	13.0	3
16-PSK	18.7	4
16-QAM	13.4	4
64-QAM	17.8	6

8.8 Spectral Regulation

Electromagnetic emissions are regulated by governing bodies worldwide. In the USA, the Federal Communications Commission (FCC) manages frequency emissions up to 275 GHz (47 C.F.R. §2.106). Often, the maximum equivalent isotropically radiated power is specified. In addition to EIRP, the FCC regulates transmission parameters such as bandwidth, co-channel interference, adjacent interference, spurious emissions, among others.

In the 57-64 GHz band, the FCC limits the maximum in-building 60 GHz EIRP to 40 dBm. Recently, the maximum EIRP for outdoor links was increased if

high gain antennas are implemented. For the case where $G_{TX,\text{dBi}}$ is greater than or equal to 51 dBi, the maximum EIRP is 82 dBm with a 2 dB reduction in EIRP for every 1 dB that $G_{TX,\text{dBi}}$ is below 51 dBi (47 C.F.R. §15.255) [150].

In 2003, the FCC announced lightly licensed mmW spectrum for high-speed 'pencil beam' communications. In addition to licensing, 70/80/90 GHz band links must be coordinated with the National Telecommunications & Information Administration (NTIA) and registered with a Database Manager. The E-band spectrum is split between bands at 71-76 GHz, 81-86 GHz, 92-94 GHz, and 94.1-95 GHz.

The maximum transmitter EIRP for the 70/80 GHz bands is 85 dBm for fixed and mobile applications with a minimum antenna gain of 43 dBi and a maximum 3 dB beam width of 1.2° [151]. Similar to the 60 GHz band case, the maximum EIRP must be reduced by 2 dB for every 1 dB that the $G_{TX,\text{dBi}}$ is below 43 dBi. In addition, the FCC regulates the minimum BW efficiency at 71-76 GHz and 81-86 GHz to be 0.125 b/s/Hz. In the 92-94 GHz and 94.1-95 GHz bands, the minimum BW efficiency requirement is 1.0 b/s/Hz.

It is important to realize that in addition to meeting technical requirements, practical links must also adhere to regulations that manage the RF spectrum.

Chapter 9

RF Link Experimental Results

9.1 BPSK Wireless Transmission

A wireless link was constructed to transmit binary-phase shift keyed (BPSK) microwave/ mmW RF signals. The photonic transmitter was based on the PΦM-OF TX architecture analyzed in Section 6.1 and the photonic receiver was based on the CΦM-OF link analyzed in Section 4.2. Experimental measurements were performed at RF frequencies of f_{RF} = 25 GHz, 35 GHz, and 40 GHz and for data-rates of R_b = $\{0.5, 2, 4, 6\}$ Gbps. The basic experimental configuration is shown in Fig. 9.1.

For the first set of experiments, the photonic transmitter and the photonic receiver were optically unamplified. The PΦM-OF photonic transmitter described

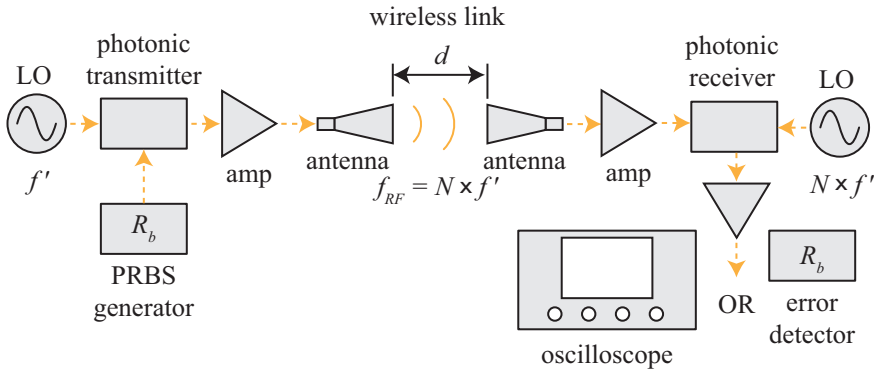

Figure 9.1: Experimental configuration of the PΦM-OF transmitter paired with the CΦM-OF receiver.

in Section 7.1 was paired with a photonic receiver that was nominally identical to the one described in Section 6.2. Based on a measurement of the optical spectrum at point H as referenced to Fig. 6.1, the optical power of the first sideband was approximately -9.5 dBm and the optical power of the carrier was approximately 4.4 dBm at an LO frequency of $f' = 25$ GHz. Based on Eq. (6.7), the optical power oscillating at $f_{RF} = f'$ is -18.2 dBm for an assumed responsivity of $\mathcal{R} = 0.7$ A/W and output impedance $Z_{out} = 50\ \Omega$. Since the photodetector contained an internal terminating resistor, the RF power from the photodetector is calculated to be approximately -24 dBm.

The RF signal was amplified with a 18-40 GHz amplifier having a nominal gain of $G = 30$ dB and a 1 dB compression point of $P_{1\text{dB}} = 17$ dBm. Thus, the calculated output power, ignoring feeding network losses, was $P_{TX} \approx 6$ dBm. The output from the amplifier was connected to a 26.5-40 GHz standard gain horn antenna with nominal gain of $G_{TX} = 20$ dBi. From measurements (not shown), the gain at a frequency of $f = 26$ GHz was found to be approximately 17.3 dBi. Thus, the effective isotropically radiated power (EIRP) at $f_{RF} = 25$ GHz was approximately 20 dBm.

At $f_{RF} = 25$ GHz, the free-space path loss over a distance of $d = 40$ cm was calculated to be $L_{FS,\text{dB}} = 52.4$ dB using Eq. (8.2) with $n = 2$. The antenna and amplifier used at the receive end were nominally identical to those used at the transmit end. Thus, the power applied to the input phase-modulator of the CΦM-OF receiver was approximately 15 dBm. From the manufacturer data-sheet, the half-wave voltage of the receiver input phase-modulator was approximately $V_\pi = 5$

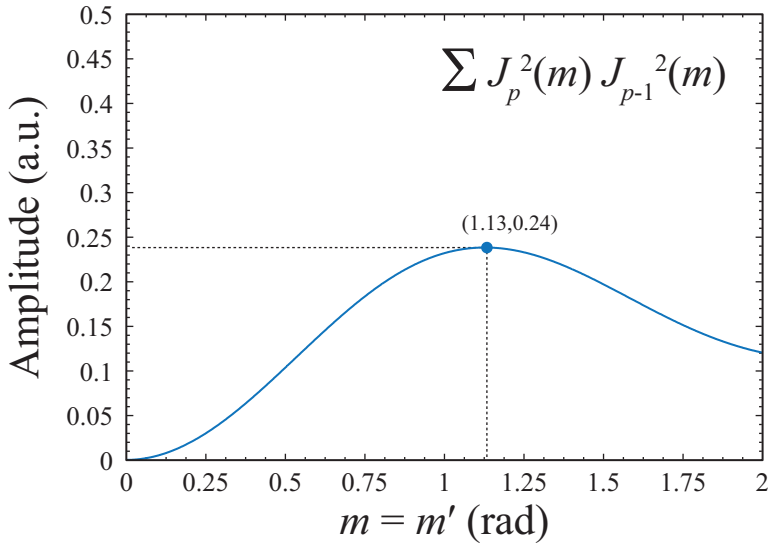

Figure 9.2: Numerical calculation of the optimal modulation depth for $m \approx m'$.

V at a frequency of $f = 25$ GHz. Based on the estimated received power, the RF input modulation depth, m, was estimated to be approximately 1 rad.

The RF power applied to the LO phase-modulator was on the order of 15 dBm. The LO phase-modulator was nominally identical to the signal phase-modulator. Thus, the LO modulation depth, m', was also on the order 1 rad. For the case where $m \approx m'$, Eq. (4.37) can be rewritten as

$$i_{10}(t)|_{\Omega_{IF}} \approx -2\mathcal{R}\alpha_{\Phi M}^2 \alpha_{FBG} \sum_p J_p^2(m) J_{p-1}^2(m) \cos \Omega_{IF} t. \tag{9.1}$$

The summation in Eq. (9.1) is plotted in Fig. 9.2.

From this figure, it is clear that the highest downconversion efficiency is achieved when $m = m' \approx 1.13$ rad. This is close to the estimated signal and LO modulation depths used in the experiment. The eye diagram prior to transmission and the eye diagram after photonic upconversion with the PΦM-OF transmitter,

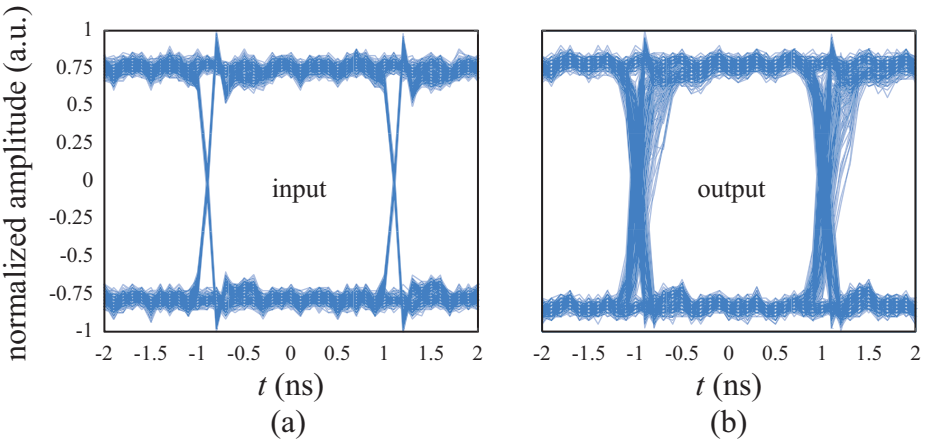

Figure 9.3: Measured eye diagrams at the (a) transmitter input and the (b) receiver output (after a limiting amplifier). After [13].

wireless relay, and downconversion with the CΦM-OF receiver are shown in Fig. 9.3. The measured eye diagrams were captured with $R_b = 0.5$ Gbps and $f_{RF} = f' = 25$ GHz. A similar experiment was performed with $f_{RF} = f' = 35$ GHz. The measured data sequences were previously shown in Fig. 7.2.

For the next set of experiments, the photonic transmitter and the photonic receiver were optically amplified. The main differences between this experiment and the last were that the $N = 2$ sideband was selected to implement harmonic upconversion at $f_{RF} = 2f' = 40$ GHz, the data-rate was increased from $R_b = 0.5$ Gbps to $R_b = 6$ Gbps, and optical amplification was used prior to photodetection in both the transmitter and receiver. In addition, the optical signal was relayed over $L = 200$ m of standard single-mode fiber (SMF) in the transmitter and in the receiver and the wireless transmission distance was increased from $d = 40$ cm to $d \approx 1$ m. At a mmW frequency of $f_{RF} = 40$ GHz, the free-space path loss increased to $L_{FS,\text{dB}}$

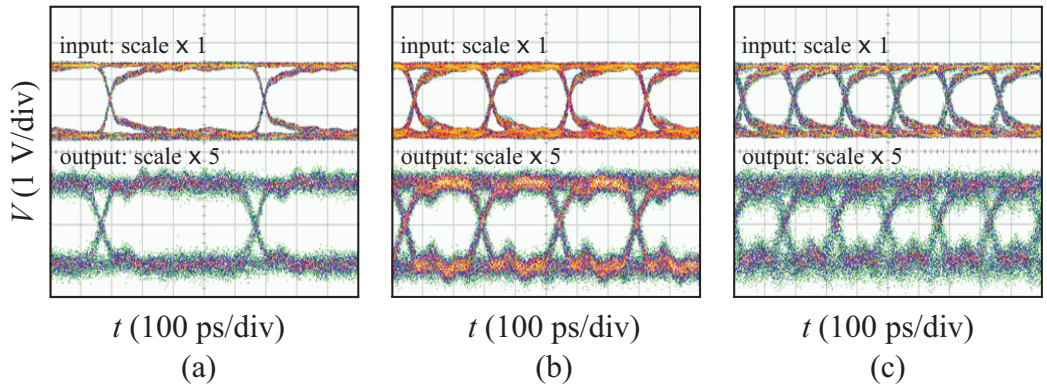

Figure 9.4: Measured eye diagrams at the input to the PΦM-OF transmitter and at the output of the CΦM-OF receiver for data-rates of (a) 2 Gbps, (b) 4 Gbps, and (c) 6 Gbps.

= 64 dB for $d = 1$ m.

To implement the the wireless link, the same pair of standard gain horn antennas as described previously was used. The gain was measured to be $G_{TX,\mathrm{dBi}} = G_{RX,\mathrm{dBi}} \approx 20$ dBi at $f_{RF} = 40$ GHz. A set of electrical amplifiers was used with measured gains of approximately 22.5 dB at 40 GHz. The received RF power was varied by changing the horn separation distance from approximately $d = 94$ cm to $d = 186$ cm. The input and output eye diagrams are shown in Fig. 9.4. The bit error rate (BER) was plotted as a function of received RF power, P_{RX}, out of the receive horn antenna as shown in Fig. 9.5.

In contrast to the first set of measurements, the received RF power was two orders of magnitude lower than the LO power. The signal modulation depth was estimated to be $m \approx 0.09$ rad assuming that the modulator V_π at 40 GHz is $\sqrt{2}$

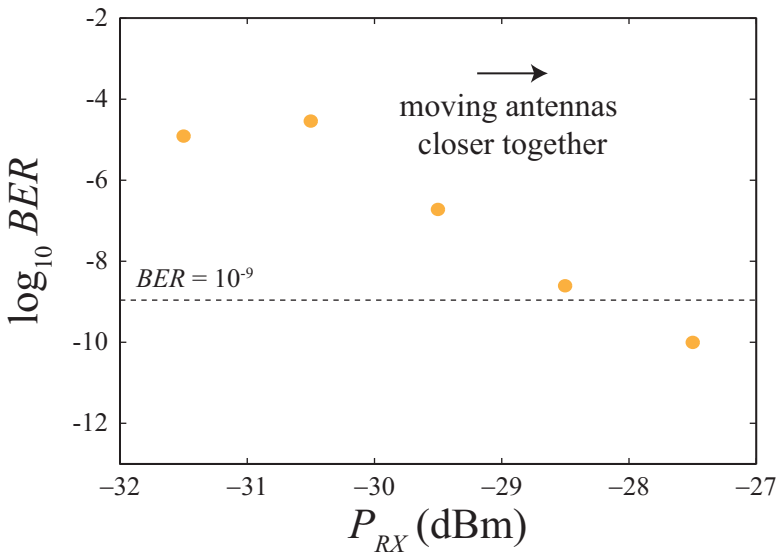

Figure 9.5: Measured BER as a function of received RF power for $f_{RF} = 40$ GHz and $R_b = 6$ Gbps for the PΦM-OF transmitter paired with the CΦM-OF receiver over a wireless link.

times higher than it is at 1 GHz. In this limit, the small-signal approximation given by Eq. (4.39) is valid and the optimal LO modulation depth is $m' = 1.08$ rad.

9.2 Wireless Transmission and RF Photonic Vector Demodulation

The vector demodulating CΦM-OF link shown in Fig. 5.11 was constructed as described in Section 5.2. To perform transmission measurements, an electrical receiver was constructed as shown in Fig. 9.6. The electrical transmitter consisted of a 90° hybrid followed by an electrical mixer. An electrical LO, having frequency $f' = 40$ GHz, was applied to the LO port of the mixer.

A $R_b = 200$ Mbps, 4-quadrature amplitude modulation (QAM) signal was

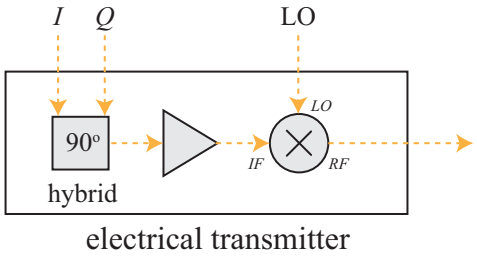

Figure 9.6: Simplified schematic of the vector modulation electrical transmitter.

generated by connecting the output from a two-channel arbitrary waveform generator (AWG) to the I and Q inputs of the electrical transmitter. As the AWG had balanced outputs and the I and Q inputs were unbalanced, a pair of phase-matched electrical baluns was used between the AWG and transmitter.

The output from the transmitter was amplified and sent into a $G_{TX,\mathrm{dBi}} = 20$ dBi standard gain horn antenna. At the receiver, a nominally identical $G_{RX,\mathrm{dBi}} = 20$ dBi standard gain horn antenna and amplifier were used. As the amplifiers had a bandwidth of 40 kHz to 38 GHz and the horn antennas had a bandwidth of 26.5 GHz to 40 GHz, only the lower upconverted signal at $f_{RF} = f_0 - f_1 = 36.4$ GHz was relayed to the vector demodulating CΦM-OF photonic receiver. The horn antennas were separated by $d \approx 1.1$ m resulting in a free-space path loss of $L_{FS,\mathrm{dB}} = 64.5$ dB.

The optical source in the photonic receiver was a fiber laser having a nominal optical power $P_L = 21$ dBm and center wavelength $\lambda_L = 1552.500$ nm. Since the fiber laser had a relative intensity noise (RIN) peak 1.6 MHz from the carrier, it was not possible to downconvert signals having bandwidths greater than approximately 1 MHz directly to baseband. A span of polarization maintaining fiber (PMF) was

inserted between the input and the polarization maintaining (PM) 3 dB directional optical coupler (DOC).

An electrical LO having frequency $f' = (f_{RF} - f_{IF})/2 = 18$ GHz was used to perform electrooptic harmonic downconversion. The two IF signals from the RF photonic receiver were electrically amplified and filtered and then digitized using with an oscilloscope having an analog bandwidth of 1 GHz. The experimental configuration is shown in Fig. 9.7. Representative digitized waveforms at an intermediate frequency (IF) of $f_{IF} = 400$ MHz are shown in Fig. 9.8.

Fig. 9.8(a) and (c) show the IF I/Q waveforms without data while Fig. 9.8(b) and (d) show the IF waveforms with $R_b = 200$ Mbps 4-QAM data. In the former case the AWG generated a sinusoidal tone at $f_1 = 3.6$ GHz. The digitized waveforms

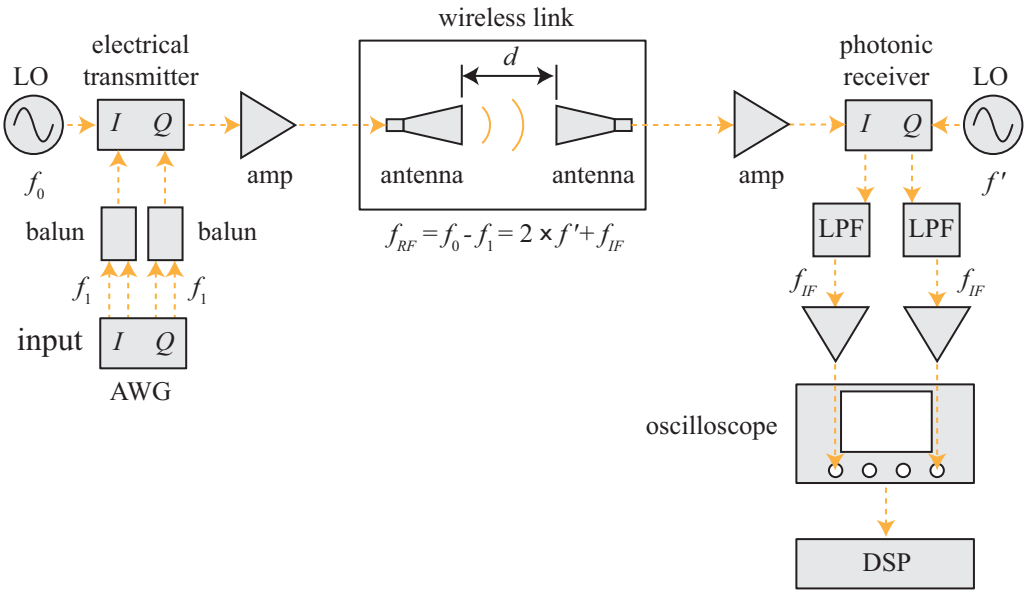

Figure 9.7: Experimental configuration of electrical vector modulation transmitter with photonic vector demodulating СΦМ-OF receiver.

were processed off-line in MATLAB®. The digital signal processing (DSP) algorithm simply instantiated frequency mixing with a common LO and low-pass filtering to recover the I/Q baseband signals as shown in Fig. 9.9.

It should be noted that in principle, only one IF channel is required to down-convert and demodulate the digitized signal to baseband. In DSP, a coherent receiver with orthogonal LOs could have been implemented. However, using only a single LO in the DSP algorithm illustrates that the two channels were in fact orthogonal,

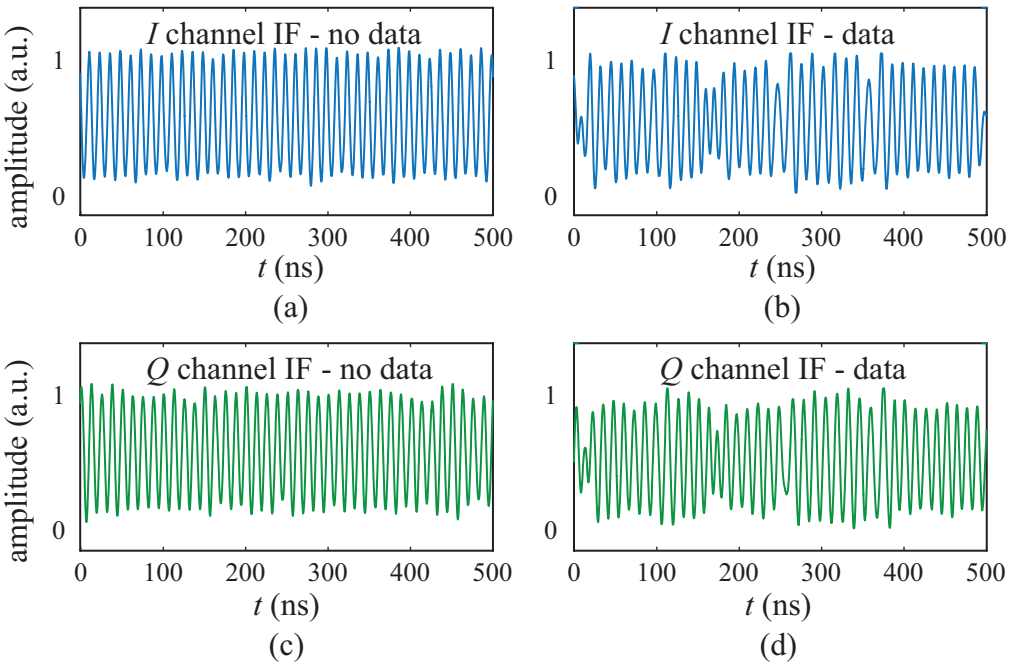

Figure 9.8: Measured digitized IF waveforms at the output of the vector CΦM-OF receiver for (a) I channel without data, (b) I channel with data, (c) Q channel without data, and (d) Q channel with data. After [10].

validating the proof-of-concept. The baseband input signals as generated by the AWG are shown in Fig. 9.9(a) and (c) and the DSP recovered baseband signals are shown in Fig. 9.9(b) and (d).

9.3 RF Photonic Vector Modulation and Wireless Transmission

The DD-MZM photonic vector modulating transmitter shown in Fig. 7.4 was used to generate and vector modulate a millimeter-wave RF signal. The resulting RF signal was sent through an 18-40 GHz electrical amplifier having nominal gain of $G = 30$ dB and noise figure of $NF = 5$ dB and then into an 18 GHz high-pass filter

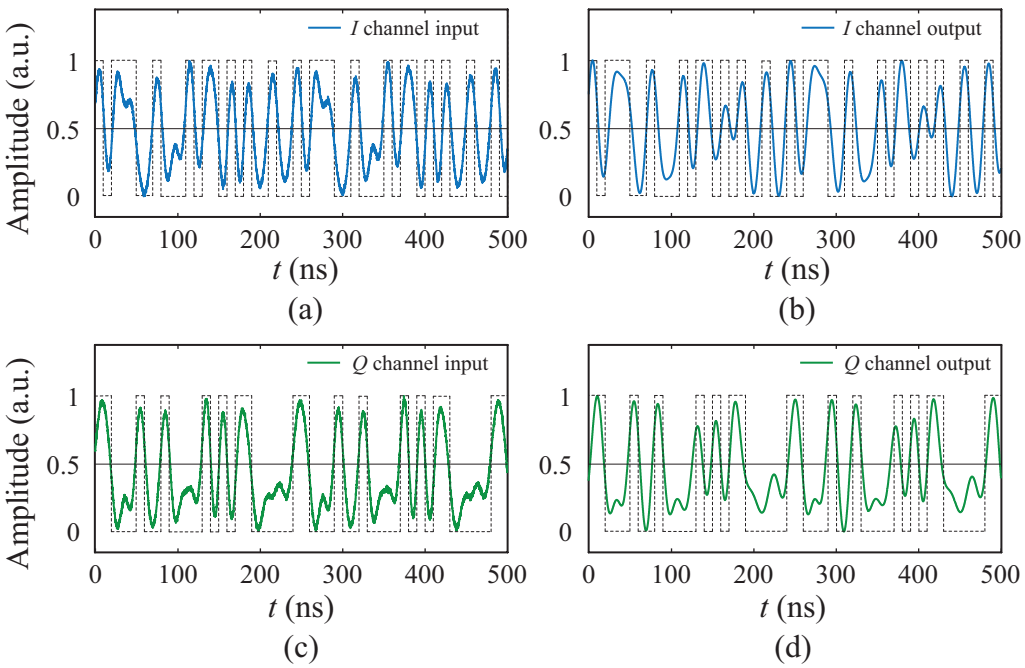

Figure 9.9: Time domain waveforms measured at the input of the vector DD-MZM transmitter (a) and (c) and at the output of the electrical receiver (b) and (d). After [10].

(HPF). The filter was used to ensure that any baseband signals were suppressed. The amplified RF signal was transmitted in free-space using a 26.5-40 GHz standard gain horn antenna with gain of $G_{TX,\mathrm{dBi}} = 20$ dBi. After propagating over a $d = 0.5$ m wireless link, a nominally identical horn antenna and amplifier were used at the receive end to collect the RF signal. At a mmW frequency of $f_{RF} = 36$ GHz, the free-space path loss over a distance $d = 0.5$ m was calculated to be $L_{FS,\mathrm{dB}} = 57.6$ dB using Eq. (8.2) with $n = 2$.

The photonic transmitter and electrical receiver configuration described in Section 7.2 were used with the exception that the transmitter LO frequency was set to $f' = 18$ GHz. Electrooptic harmonic frequency doubling of the LO was performed to generate an RF signal at $f_{RF} = 36$ GHz. At the electrical receiver, the LO frequency was set to $f' = 36$ GHz. The measurement setup is shown in Fig. 9.10.

As in Section 7.2, two pseudorandom binary sequence (PRBS) $2^{23} - 1$ non-return-to-zero (NRZ) data signals were applied to the photonic transmitter. The I and Q bit-rates were set at $R_{b,I} = R_{b,Q} = 1.24416$ Gbps and the Q channel was decorrelated from the I channel by 38 bits. This resulted in an aggregate bit-rate of $R_b = 2.48832$ Gbps. The data signals were vector modulated and upconverted to a frequency that was twice that of the applied LO.

Since the frequency range of the electrical spectrum analyzer (ESA) used in the experiment had a maximum bandwidth of 26.5 GHz, the electrical spectrum of the 36 GHz signal is not shown. However, no component at the transmitter LO frequency was observed at the receiver input. The baseband signals at the output

of the electrical receiver were measured to be error-free ($BER < 10^{-9}$) and the corresponding baseband constellation is shown in Fig. 9.11.

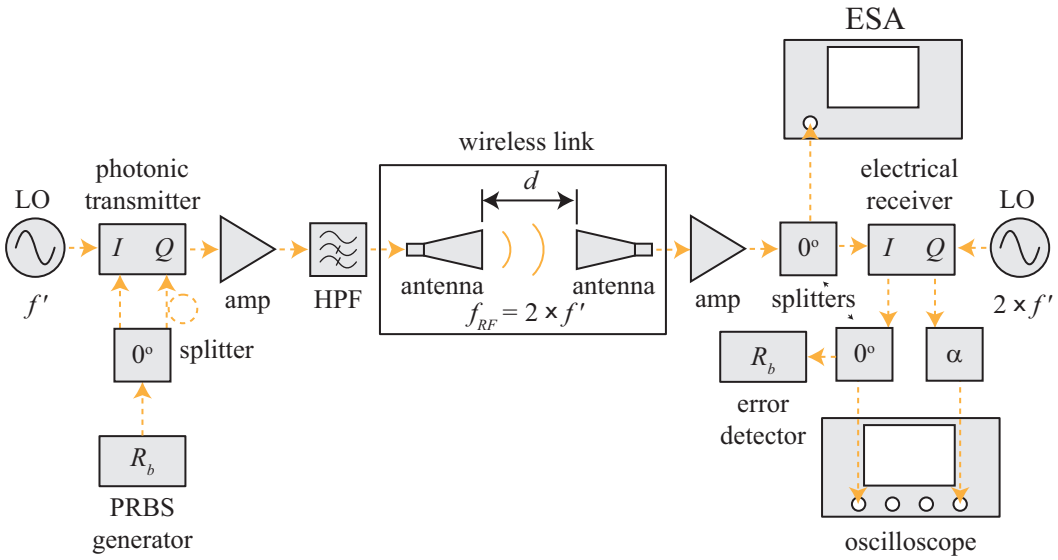

Figure 9.10: Experimental configuration of photonic vector modulation transmitter with electrical vector demodulation receiver. After [12].

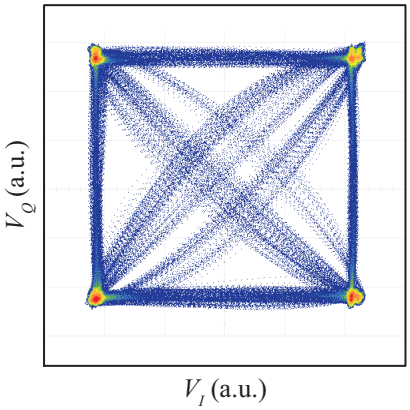

Figure 9.11: Measured baseband constellation after wireless transmission. After [12].

9.4 RF Photonic 4-QAM Link (Not Wireless)

The photonic vector modulating DD-MZM transmitter described in Section 9.4 was combined with the photonic vector demodulating CΦM-OF receiver described in Section 9.3. An electrical bandpass filter was used to emulate the wireless channel as a pair of horn antennas at the RF frequency were not available in the laboratory at the time that this experiment was conducted. The experimental configuration is shown in Fig. 9.12.

The photonic transmitter was configured to encode two $R_b = 1$ Gbps PRBS signals in quadrature onto a $f_{RF} = 15$ GHz microwave carrier. The modulated

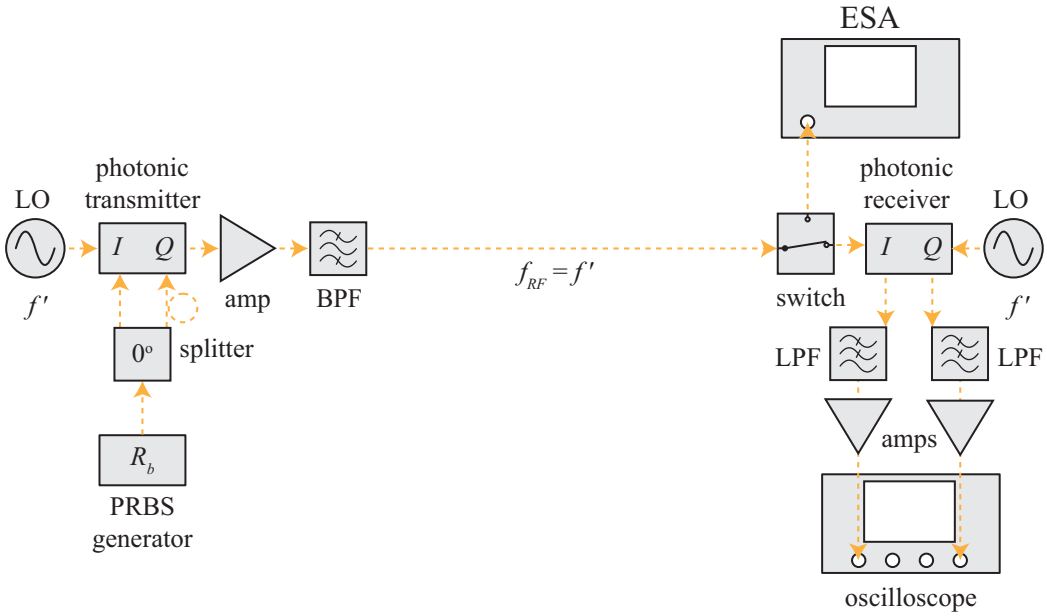

Figure 9.12: Experimental configuration of the photonic vector modulation transmitter with photonic vector demodulation receiver.

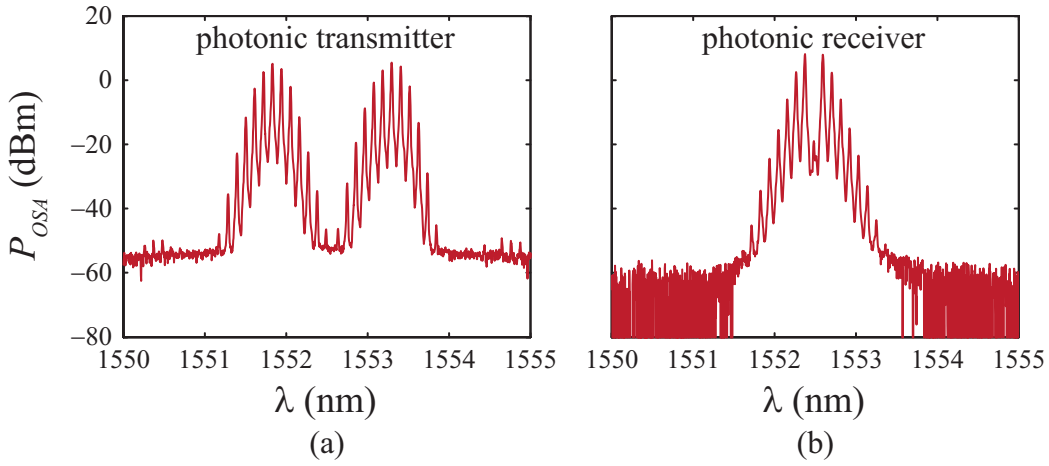

Figure 9.13: Measured optical spectra prior to photodetection in the (a) transmitter and (b) receiver.

microwave signal was amplified, filtered, and then applied to the input of the CΦM-OF photonic receiver. The receiver LO frequency was set at $f' = f_{RF} = 15$ GHz. The baseband outputs were low-pass filtered, amplified, and digitized.

One of the key differences in the photonic receiver implemented here was that the fiber laser used previously was replaced with a tunable (non-fiber) laser. This allowed higher data-rate signals to be demodulated without being swamped by laser RIN. The optical spectra prior to photodetection in both the transmitter and one branch of the receiver is shown in Fig. 9.13.

In both Fig. 9.13(a) and (b), the modulation sideband spacing is 15 GHz. The RF spectra at the output of the HPF was measured for the case where the data was 'off' and for the case where the data was 'on'. The results are shown in Fig. 9.14.

The electrical spectra at the outputs of the I and Q branches of the photonic

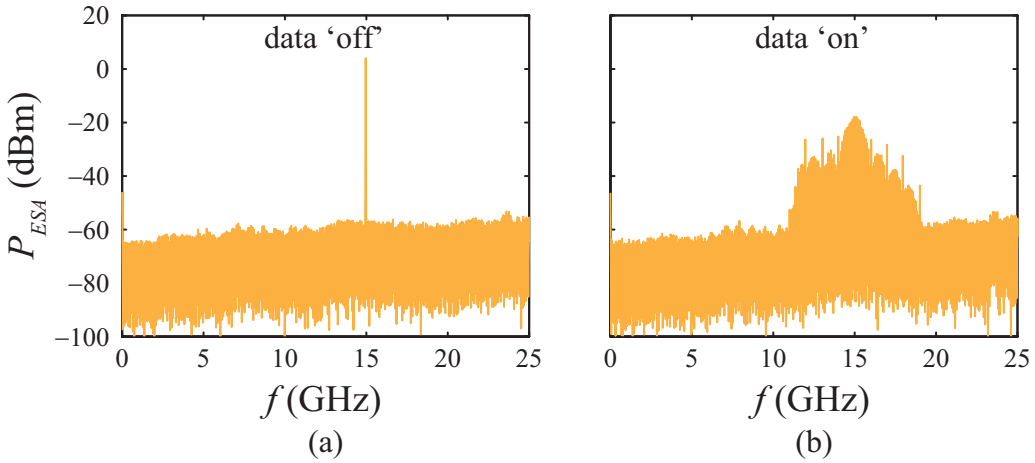

Figure 9.14: Measured electrical spectra into the photonic receiver phase-modulator with (a) data ‘off’ and (b) data ‘on’.

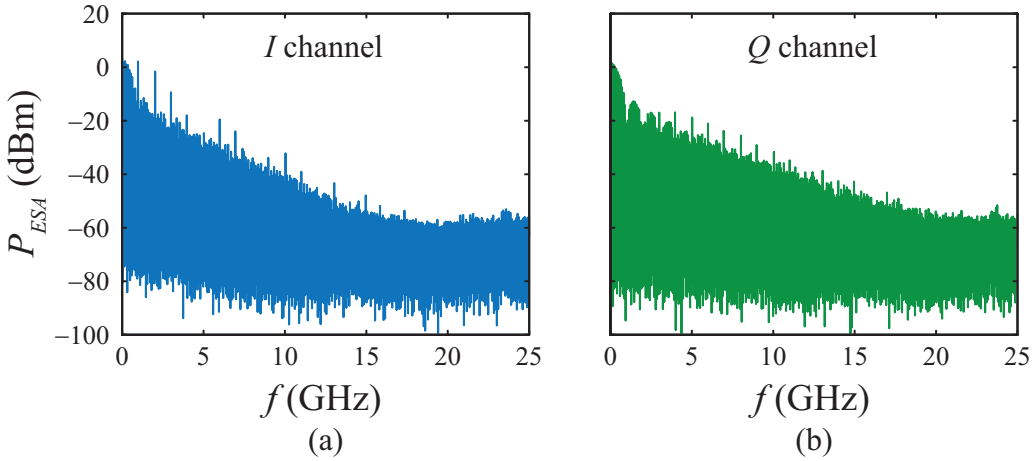

Figure 9.15: Measured downconverted electrical spectra at the output of the (a) I channel and (b) Q channel.

receiver are shown in Fig. 9.15. As evident from examining Fig. 9.15, the received baseband spectra are nominally identical, with the gain of the Q channel a little higher than that of the I channel. The transmitted and received baseband data

sequences are shown in Fig. 9.16.

Fig. 9.16(a) and (b) correspond to the input data sequences and Fig. 9.16(c) and (d) correspond to the recovered data sequences. Note that the shape of the output data sequences are nominally identical to the input data sequences. Furthermore, no significant filtering is observed. From these results, it can be inferred that higher data-rates are indeed possible. Furthermore, with the appropriate choice of electrical amplifiers and filters, the transmission frequency could in principle be increased. Thus, based on the results presented in this chapter, a vector modulated wireless link should be possible using the DD-MZM transmitter paired with the CΦM-OF receiver.

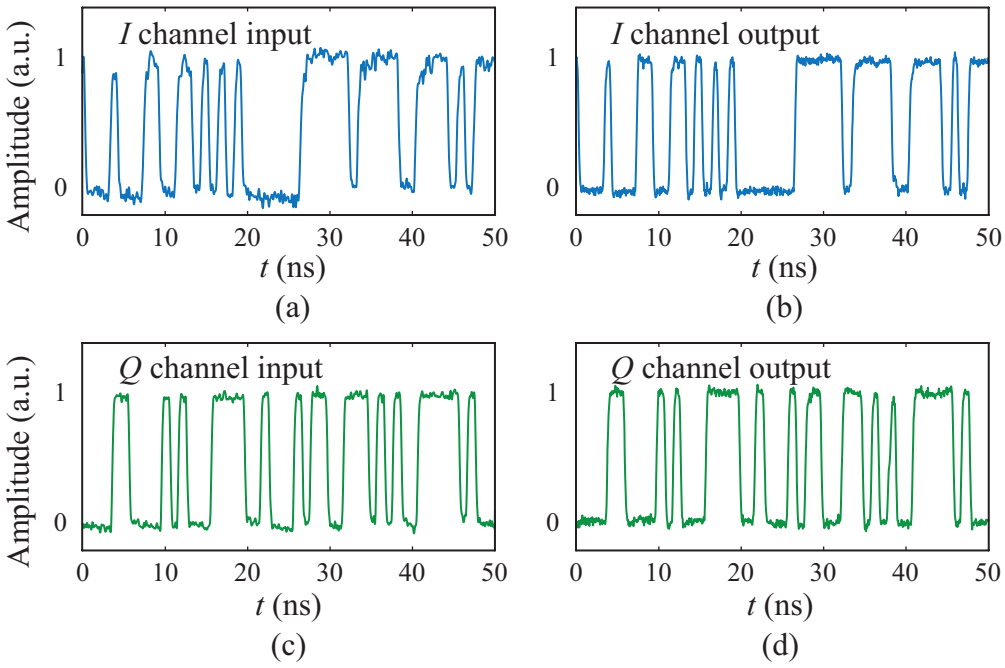

Figure 9.16: Measured baseband data sequences for (a) I channel input, (b) I channel output, (c) Q channel input, and (d) Q channel output.

Chapter 10

Conclusions

10.1 Summary

Several RF photonic techniques for modulating and demodulating signals on RF carriers are theoretically proposed and experimentally demonstrated at millimeter-wave (mmW) frequencies. Two demodulation techniques are reported, both allowing for electrooptic downconversion. The first approach utilized phase-modulation to intensity-modulation (ΦM-to-IM) conversion via an asymmetric delay line interferometer.

The advantage of this approach is the high gain that can be achieved relative to a standard quadrature-biased intensity-modulated link. However, the bandwidth is limited and electronic feedback is required in practice to maintain the bias point of the interferometer. The second approach utilized fiber Bragg gratings (FBGs) to selectively filter components of the phase-modulated signal. Experimental demonstrations from 7 to 70 GHz were presented and the technique was extended to perform vector demodulation and harmonic downconversion. The main features of this approach are that it is cost effective and a bias controller is not needed anywhere in the link, when an athermal FBG is utilized. The main disadvantage is that the FBG imposes bandwidth constraints. For example, for fundamental downconversion, the lowest frequency that can be downconverted efficiently has a frequency of half the

bandwidth of the FBG (5-10 GHz). In addition, the link has a slight penalty in gain when compared to the interferometric approach.

Two RF photonic techniques were presented to generate and modulate RF signals. Both techniques allow for harmonic upconversion of the electrical local oscillator (LO). The first-technique is based on phase-modulation and optical filtering. Gigabit data-rates were demonstrated; however instabilities in the fiber interferometer limited the performance to short duration laboratory measurements. Since the instabilities were thermal and acoustic in nature, it is possible in principle to stabilize the link using a feedback loop. However, stabilization was not investigated in this dissertation. A second technique for generating and modulating an RF carrier was presented based on a pair of dual-drive Mach-Zehnder modulators (DD-MZMs). Two optical sources having a spectral separation greater than the bandwidth were employed to preclude the generation of heterodyne mixing products in the photodetector. By properly phasing the arms, vector modulation of high-order modulation systems was demonstrated using a frequency quadrupled electrical LO. The main disadvantage of this approach is that bias controllers are needed to maintain the DD-MZM set-points.

Microwave and millimeter-wave links were demonstrated using the modulators and demodulators investigated in this work. A wireless link using the phase-modulation based transmitter and the phase-modulation with optical filtering receiver was demonstrated at a carrier frequency of 40 GHz. Furthermore, spans of 200 m of optical fiber were placed at both the transmit and receive ends to highlight the low-loss transport of millimeter-wave signals achievable in the optical domain.

Error-free wireless transmission was demonstrated at bit-rates of up to 6 Gbps. Wireless demonstrations were also performed by pairing an RF photonic transmitter with an electrical receiver, and vice versa. The main limitation to using electrical transmitter or receiver are the inherent bandwidth limitations of electrical mixing. Finally, a microwave link was demonstrated using the vector modulating RF photonic transmitter paired with the vector demodulating RF photonic receiver. Due to availability of appropriate filters, amplifiers, and antennas, the demonstration was constrained to a wired link. However, based on the results, wireless transmission at millimeter-wave frequencies appears feasible.

10.2 Future Work

The work presented in this dissertation sets the stage for a variety of future work on millimeter-wave wireless communication systems utilizing RF photonic vector modulators and demodulators. One of the areas that seems achievable in the near-term is millimeter-wave wireless transport of vector modulated Gigabit signals using components having microwave bandwidths. The only high frequency RF photonic components necessary are a high-speed photodetector at the transmit end and a high-speed phase-modulator at the receive end, both which are now commercially available at frequencies of at least 65 GHz.

A longer term goal is to integrate the photonic modulator and demodulator on-chip. At present the systems demonstrated in this dissertation are quite costly as they rely heavily on 'gold packaged' devices. Photonic integration could, in theory,

provide lower cost per unit if economies of scale can be leveraged. Furthermore, photonic integration could provide performance benefits. For example, if the BPSK transmitter reported in this work was integrated on chip, instability and polarization issues could have been greatly reduced. Another area of integration that could prove rewarding is on-chip integration of antennas with the transmitter photodetector and the receiver input modulator. Some work has been reported in the literature on these topics (e.g. [152,153]). In addition to enabling more compact transmitters and receivers, antenna integration eliminates the need to match all of the components to 50 Ω, which should allow for more efficient designs.

Appendix A

Intensity-Modulation Direct-Detection

Intensity-modulated, direct-detection (IM-DD) links are the most frequency studied externally modulated RF photonic configuration. The mathematical diagram of an IM-DD system based on a Mach-Zehnder modulator (MZM) is shown in Fig. A.1. Inserting Eq. (3.23) into Eq. (3.3) gives the photocurrent produced by the IM-DD system as

$$\begin{aligned} i(t) &= \mathcal{R}P_L\alpha_{MZM}\sin^2\left[\phi(t)/2\right] \qquad (A.1)\\ &= \frac{1}{2}\mathcal{R}P_L\alpha_{MZM}\left[1-\cos M_{DC}\cos\left(m\sin\Omega t\right)+\sin M_{DC}\sin\left(m\sin\Omega t\right)\right]. \end{aligned}$$

Generally, the MZM is biased at one of its quadrature points (i.e. $M_{DC} = (1+2n)\pi/2$ for n an integer) for optical relay. Assuming that one of the positive quadrature points is chosen (i.e. $M_{DC} = (1+4n)\pi/2$), Eq. (A.1) reduces to

$$i(t) = \frac{1}{2}\mathcal{R}P_L\alpha_{MZM}\left[1+\sin\left(m\sin\Omega t\right)\right]. \qquad (A.2)$$

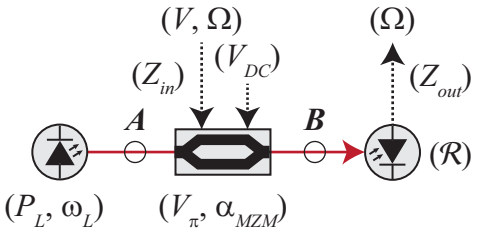

Figure A.1: Mathematical model of an electrooptic IM-DD link.

The sinusoid having sinusoidal argument in Eq. (A.2) can be expanded in terms of Bessel functions using the identity

$$\sin\left(z\sin\theta\right) = \sum_{p=-\infty}^{\infty} J_p(z)\sin p\theta. \tag{A.3}$$

Inserting Eq. (A.3) into Eq. (A.2) yields

$$i(t) = \frac{1}{2}\mathcal{R}P_L\alpha_{MZM}\left[1 + \sum_{p=-\infty}^{\infty} J_p(m)\sin p\Omega t\right]. \tag{A.4}$$

Expanding Eq. (A.4) to first-order in m yields

$$i(t) = \frac{1}{2}\mathcal{R}P_L\alpha_{MZM}\left(1 + m\sin\Omega t\right). \tag{A.5}$$

The DC photocurrent component of Eq. (A.5) is

$$I_{DC} = \frac{1}{2}\mathcal{R}P_L\alpha_{MZM} \tag{A.6}$$

and the AC photocurrent component of Eq. (A.5) is

$$i_{AC}(t) = \frac{1}{2}\mathcal{R}P_L\alpha_{MZM}m\sin\Omega t. \tag{A.7}$$

The average RF output power can be calculated to be

$$P_{out} = \frac{1}{2}\left(\frac{1}{2}\mathcal{R}P_L\alpha_{MZM}m\right)^2 Z_{out}. \tag{A.8}$$

Likewise, the average RF input power is

$$P_{in} = \frac{1}{2}\left(\frac{mV_\pi}{\pi}\right)^2 \frac{1}{Z_{in}}. \tag{A.9}$$

The small-signal gain of the (non-downconverting) IM-DD system can be found by taking the ratio of Eq. (A.8) to Eq. (A.9) to be

$$G_{IM-DD} = \left(\frac{\pi\mathcal{R}P_L\alpha_{MZM}}{2V_\pi}\right)^2 Z_{out}Z_{in}. \tag{A.10}$$

The gain of the IM-DD system is used as the baseline for comparison with the phase-modulation and detection schemes discussed in this dissertation.

Appendix B

Coherent-Detection

Phase-encoded information can be recovered using coherent-detection (CohD). In a conventional coherent-detection scheme, the encoded optical signal is mixed with an optical local oscillator (OLO) prior to photodetection [106]. Coherent-detection can also be used to detect intensity-modulated signals. The sensitivity of a coherent-detection can be much greater than the sensitivity of direct-detection as mixing with an OLO can amplify the input signal.

The mathematical model for coherent detection for the single phase-modulator case is shown in Fig. B.1. The mixing of the optical signal with an OLO allows both phase and amplitude information to be extracted. Assuming that the optical signals

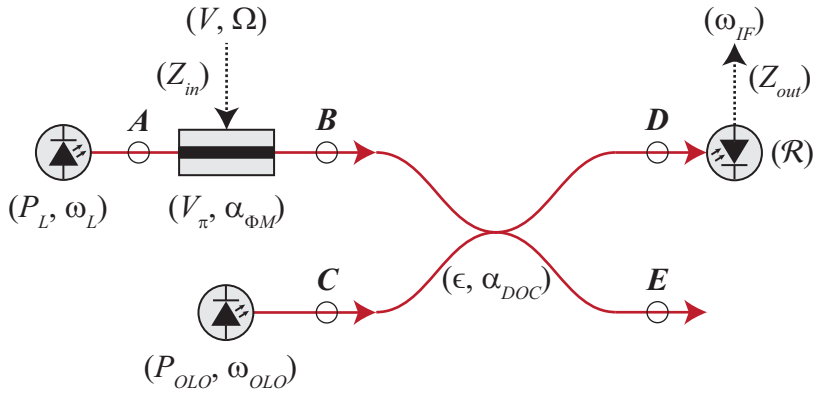

Figure B.1: Mathematical model of an electrooptic ΦM-CohD link.

$u_A(t)$ and $u_C(t)$ can be represented by

$$\begin{aligned} u_A(t) &= \sqrt{P_L}\, e^{j\omega_L t} \\ u_C(t) &= \sqrt{P_{OLO}}\, e^{j\omega_{OLO} t} \end{aligned} \tag{B.1}$$

the optical signal incident on the photodetector, $u_D(t)$, can be written as

$$u_D(t) = \left[\begin{array}{cc} \sqrt{\alpha_{DOC}} & 0 \end{array} \right] \left[\begin{array}{cc} \sqrt{1-\epsilon} & j\sqrt{\epsilon} \\ j\sqrt{\epsilon} & \sqrt{1-\epsilon} \end{array} \right] \left[\begin{array}{cc} \sqrt{\alpha_{\Phi M}}\, e^{jm\sin\Omega t} & 0 \\ 0 & e^{j\Delta\phi} \end{array} \right] \left[\begin{array}{c} u_A(t) \\ u_C(t) \end{array} \right] \tag{B.2}$$

where ϵ is the power-coupling coefficient and α_{DOC} is the excess optical loss of the directional optical coupler (DOC). For convenience, it is assumed that the state-of-polarization (SOP) of the encoded optical signal and the OLO are aligned to achieve maximum mixing efficiency. Furthermore, it is assumed that the relative phase difference between the optical signal and the OLO is static and has been referenced such that it is completely accounted for by $\Delta\phi$.

Under these assumptions, the photocurrent produced by square-law detection of the field described by Eq. (B.2) is

$$\begin{aligned} i(t) &= \mathcal{R}|u_D(t)|^2 \\ &= \mathcal{R}\alpha_{DOC} \\ &\times \left[(1-\epsilon)P_L\alpha_{\Phi M} + \epsilon P_{OLO}\right. \\ &+ \left. 2\sqrt{\epsilon(1-\epsilon)}\sqrt{P_L\alpha_{\Phi M}}\sqrt{P_{OLO}}\sin\left(\omega_{IF}t + m\sin\Omega t - \Delta\phi\right)\right] \end{aligned} \tag{B.3}$$

where $\omega_{IF} = |\omega_L - \omega_{OLO}|$ is the angular frequency difference between the optical carrier and the OLO.

In principle any intermediate frequency (IF) can be achieved, limited only by the bandwidth of the photodetector and the relative tunability of the optical sources. For practical applications, it is critical that the optical sources be stabilized with respect to each other in order to avoid frequency drift of the IF.

For the simplified case where $\epsilon = 1/2$ and $\Delta\phi = 0$, Eq. (B.3) reduces to

$$i(t) = \frac{1}{2}\mathcal{R}\alpha_{DOC}\left[P_L\alpha_{\Phi M} + P_{OLO} + 2\sqrt{P_L\alpha_{\Phi M}}\sqrt{P_{OLO}}\sin\left(\omega_{IF}t + m\sin\Omega t\right)\right]. \tag{B.4}$$

The DC contribution of the photocurrent is

$$I_{DC} = \frac{1}{2}\mathcal{R}\alpha_{DOC}\left[P_L\alpha_{\Phi M} + P_{OLO}\right] \tag{B.5}$$

and the AC contribution is

$$\begin{aligned} i_{AC}(t) &= \mathcal{R}\alpha_{DOC}\sqrt{P_L\alpha_{\Phi M}}\sqrt{P_{OLO}}\sin\left(\omega_{IF}t + m\sin\Omega t\right) \qquad \text{(B.6)} \\ &= \mathcal{R}\alpha_{DOC}\sqrt{P_{L\alpha_{\Phi M}}}\sqrt{P_{OLO}}\left[\sin\omega_{IF}t\cos\left(m\sin\Omega t\right) + \cos\omega_{IF}t\sin\left(m\sin\Omega t\right)\right]. \end{aligned}$$

The sinusoids having sinusoidal arguments in Eq. (B.6) can be expressed using Eqs. (6.10)-(6.11) and are reproduced below as

$$\cos\left(z\sin\theta\right) = \sum_{p=-\infty}^{\infty} J_p(z)\cos p\theta \tag{B.7}$$

$$\sin\left(z\sin\theta\right) = \sum_{p=-\infty}^{\infty} J_p(z)\sin p\theta. \tag{B.8}$$

In terms of Bessel functions, Eq. (B.6) becomes

$$\begin{aligned} i_{AC}(t) &= \mathcal{R}\alpha_{DOC}\sqrt{P_L\alpha_{\Phi M}}\sqrt{P_{OLO}} \qquad \text{(B.9)} \\ &\times \left[\sin\omega_{IF}t\sum_{p=-\infty}^{\infty} J_p(m)\cos p\Omega t + \cos\omega_{IF}t\sum_{p=-\infty}^{\infty} J_p(m)\sin p\Omega t\right]. \end{aligned}$$

Expanding Eq. (B.9) to first order in m gives

$$i_{AC}(t) = \mathcal{R}\alpha_{DOC}\sqrt{P_L\alpha_{\Phi M}}\sqrt{P_{OLO}}\left\{\sin\omega_{IF}t\left[1+\mathcal{O}(2)\right]+\cos\omega_{IF}t\left[m\sin\Omega t+\mathcal{O}(2)\right]\right\}. \tag{B.10}$$

Thus, the small-signal approximation of $i_{AC}(t)$ is

$$i_{AC}(t) \approx \mathcal{R}\alpha_{DOC}\sqrt{P_L\alpha_{\Phi M}}\sqrt{P_{OLO}}\left[\sin\omega_{IF}t+\cos\omega_{IF}t\left(m\sin\Omega t\right)\right]. \tag{B.11}$$

If the IF is non-zero, the system is operating in the heterodyne configuration while if the IF is zero, the system is operating in the homodyne configuration. For the homodyne case (i.e. $\omega_{IF}=0$), Eq. (B.11) reduces to

$$i_{AC}(t) \approx \mathcal{R}\alpha_{DOC}\sqrt{P_L\alpha_{\Phi M}}\sqrt{P_{OLO}}m\sin\Omega t \tag{B.12}$$

The average output RF power can be calculated to be

$$P_{out} = \frac{1}{2}\left(\mathcal{R}\alpha_{DOC}\sqrt{P_L\alpha_{\Phi M}}\sqrt{P_{OLO}}m\right)^2 Z_{out} \tag{B.13}$$

and the average RF input power is given by Eq. (A.9). The small-signal gain of the phase-modulation with coherent detection system can be found by taking the ratio of Eq. (B.13) to Eq. (A.9) to be

$$G = \left(\frac{\pi\mathcal{R}\alpha_{DOC}\sqrt{P_L\alpha_{\Phi M}}\sqrt{P_{OLO}}}{V_\pi}\right)^2 Z_{out}Z_{in} \tag{B.14}$$

Notice the similarity of the gain given by Eq. (B.14) for coherent detection of a phase-encoded signal with the gain given by Eq. (A.10) for the IM-DD system.

Unlike the IM-DD configuration, the gain of coherent-detection can be made arbitrarily large, limited only by the output power of the OLO and the maximum photocurrent that can be produced by the photodetector.

Appendix C

Noise

The key RF specifications of an RF photonic system are the noise figure (NF) and spurious free dynamic range (SFDR). In this appendix, noise power spectral densities (PSDs) commonly encountered in RF photonic systems and a general description of noise figures are considered.

C.1 Noise Power Spectral Density

Typical sources of noise in an optically amplified photonic link are thermal noise at the input and the output of the link, noise due to the relative intensity noise (RIN) of the laser, shot noise due to the discrete nature of photons and electrons at the detector, and noise associated with optical amplification using an Erbium-doped fiber amplifier (EDFA) [136]. Thermal noise is noise produced by thermally induced random motion of free electrons in a lossy medium that is directly proportional to the absolute temperature of the medium. The thermal noise present at the transmitter sets the fundamental limit on the achievable signal sensitivity. Written in terms of noise power spectral densities, the thermal noise input and output noise PSDs, S_{in} and S_{out}, are

$$S_{in} = k_B T_{in} \tag{C.1}$$

$$S_{out} = k_B T_{out} \tag{C.2}$$

where $k_B = 1.38 \times 10^{-23} J/K$ is the Boltzmann constant and T_{in} and T_{out} are the absolute temperatures at the input and output of the system in units of Kelvin.

To calculate the noise power, the noise PSD (which is in general frequency dependent), should be integrated over the relevant frequency range. That is,

$$P_{Ni} = \int_{f_1}^{f_2} S_i(f)\, df \tag{C.3}$$

where P_{Ni} is a generic noise power, f_1 is the lower frequency bound, f_2 is the upper frequency bound, and S_i is a generic frequency dependent noise PSD. At RF frequencies below 1 THz, the thermal noise PSD is constant over frequency or 'white' [3]. Thus, for a 'white' noise PSD, the integral given in Eq. (C.3) simplifies to

$$P_{Ni} = S_i \Delta f \tag{C.4}$$

where $\Delta f = f_2 - f_1$. At room temperature, $T = 290$ K, the thermal noise PSD is $S_{in} = 4.00 \times 10^{-21}$ W / Hz in linear units or $S_{in,\mathrm{dBm}}$ = -174 dB/Hz in logarithmic units. Thus, the corresponding noise power in logarithmic units in a bandwidth Δf is

$$P_{Nin,\mathrm{dBm}} = -174\mathrm{dBm} + 10 \log_{10} \Delta f. \tag{C.5}$$

Laser RIN is the normalized measure of the intensity noise to the optical power produced by a laser. In laser diodes, the intensity fluctuations are primarily due to spontaneous emission. The laser RIN is mathematically described as

$$RIN = \frac{S_{RIN,opt}(\omega)}{P_L^2} \tag{C.6}$$

where $S_{RIN,opt}$ is the optical RIN PSD and P_L is the optical power produced by the

laser. The RIN PSD is frequency dependent and peaks around the laser's relaxation oscillation frequency [106].

The electrical noise PSD at the output of the photodetector due to laser RIN is given by

$$S_{RIN} = I_{DC}^2 Z_{out} RIN \tag{C.7}$$

where I_{DC} is the average photocurrent, Z_{out} is the photodetector impedance, and RIN is given by Eq. (C.6).

The shot noise PSD is due to the quantum nature of photons and electrons. This contribution of noise is produced at the photodetector where photons are converted to electrons. In the case where a simple PIN photodetector is employed and the DC photocurrent is much larger than the dark current, the shot noise PSD is given by

$$S_{shot} = 2eI_{DC}Z_{out} \tag{C.8}$$

where $e = 1.602 \times 10^{-19}$ C is the elementary charge. The shot noise scales in proportion to the optical power incident on the photodetector. At a DC photocurrent of $I_{DC} \approx 0.25$ mA, the shot noise PSD has the same magnitude as the thermal noise PSD at $T_{out} = 290$ K in a $Z_{out} = 50\ \Omega$ impedance.

EDFAs are commonly employed to amplify optical signals in the C-band. In addition to amplifying the signal, they also add noise. In fact, unlike electrical amplifiers which are available with NFs less than 1 dB, the theoretical minimum NF of an EDFA is 3 dB [134, 135]. EDFAs work by optically exciting carriers in Erbium (Er^{3+}) ions to a meta-stable energy band at 1480-1550 nm [106]. C-band

photons traveling in the doped fiber cause stimulated emission of the excited carriers producing gain. The carrier can also relax through spontaneous emission, which is the main source of noise in EDFAs. The two types of spontaneous emission are signal-spontaneous (s-sp) and spontaneous-spontaneous (sp-sp). The corresponding noise PSDs are

$$S_{s-sp} = I_{DC}^2 Z_{out} \left(\frac{2h\nu F_{EDFA}}{P_{opt}} \right) \tag{C.9}$$

$$S_{sp-sp} = I_{DC}^2 Z_{out} \left(\frac{2h\nu F_{EDFA}}{P_{opt}} \right)^2 \Delta\nu \tag{C.10}$$

where $h = 6.62 \times 10^{-34}$ J-s is Planck's constant, ν is the optical frequency in Hz, F_{EDFA} is the noise factor of the EDFA in linear units, P_{opt} is the optical power into the EDFA in Watts (W), and $\Delta\nu$ is the optical bandwidth in Hz. Commonly an optical bandpass filter (BPF) is used to constrain the bandwidth of the amplified spontaneous emission (i.e. spontaneous-spontaneous emission) prior to photodetection.

For the case where the link is unamplified and the input and output temperatures are equal, the total noise PSD can be written as [154]

$$\begin{aligned} S_{tot} &= G S_{in} + S_{out} + S_{shot} + S_{RIN} \\ &= (1+G)\, k_B T + 2eI_{DC} Z_{out} + I_{DC}^2 Z_{out} RIN. \end{aligned} \tag{C.11}$$

Since the gain is typically less than unity for most unamplified RF photonic systems, it can be shown that the output noise will be dominated by shot and RIN noise contribution for photocurrents on order of $I_{DC} = 1$ mA at room temperature.

C.2 Noise Figure

The noise figure (NF) is the logarithmic form of the noise factor (F) and is an important figure of merit that describes the degradation of the signal-to-noise ratio (SNR) through an element. The noise factor can be expressed as

$$F = \frac{SNR_{in}}{SNR_{out}} \tag{C.12}$$

$$= \frac{P_{Sin}/P_{Nin}}{P_{Sout}/P_{Nout}} \tag{C.13}$$

where P_{Sin} is the input signal power, P_{Nin} is the input noise power, P_{Sout} is the output signal power, and P_{Nout} is the output noise power.

In this section, the noise factors will be derived for a hypothetical device, which is arbitrarily represented with the amplifier symbol in Fig. C.1. Note that the device could also represent a subsystem or a complete system.

In what follows, simplified notation will be used for convenience. That is, $P_N \rightarrow N$ represents noise power and $S_N \rightarrow S$ represents signal power. Furthermore, since the results will be extended to a cascaded system, Latin capital letters will be used to denote the signal and noise powers at various points in the link. Thus, in Fig. C.1, N_A denotes the input noise power and N_B denotes the output noise power.

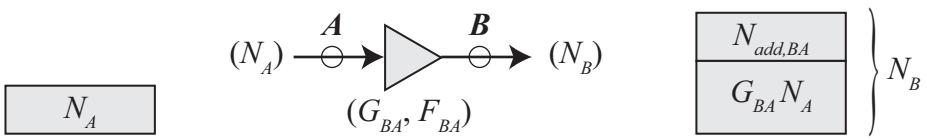

Figure C.1: Noise figure illustration.

The device amplifies the input signal and input noise with forward transmission gain G_{BA}. The noise factor of the device is denoted by F_{BA}. Specifying Eq. (C.12) to the diagram given by Fig. C.1 yields

$$\begin{aligned} F_{BA} &\equiv \frac{S_A/N_A}{S_B/N_B} \\ &= \frac{1}{G_{BA}}\frac{N_B}{N_A}. \end{aligned} \tag{C.14}$$

The noise at the output of the device is composed of amplified input noise, $G_{BA}N_A$, and added noise, $N_{add,BA}$. Thus,

$$N_B = N_{add,BA} + G_{BA}N_A \tag{C.15}$$

Substituting Eq. (C.15) into Eq. (C.14) yields

$$\begin{aligned} F_{BA} &= \frac{N_{add,BA} + G_{BA}N_A}{G_{BA}N_A} \\ &= 1 + \frac{1}{G_{BA}}\frac{N_{add,BA}}{N_A}. \end{aligned} \tag{C.16}$$

An ideal device adds no excess noise (i.e. $N_{add,BA} = 0$). In this limit, Eq. (C.16) reduces to

$$F_{BA}|_{\lim N_{add,BA}\to 0} = 1. \tag{C.17}$$

The result of Eq. (C.17) shows that the SNR can never be improved; that is, it is always degraded through an element.

The noise factor is related to the noise figure by

$$NF = 10\log_{10} F. \tag{C.18}$$

Thus, the noise figure for the element shown in Fig. C.1 is

$$NF_{BA} = 10\log_{10}\left(1 + \frac{1}{G_{BA}}\frac{N_{add,BA}}{N_A}\right). \tag{C.19}$$

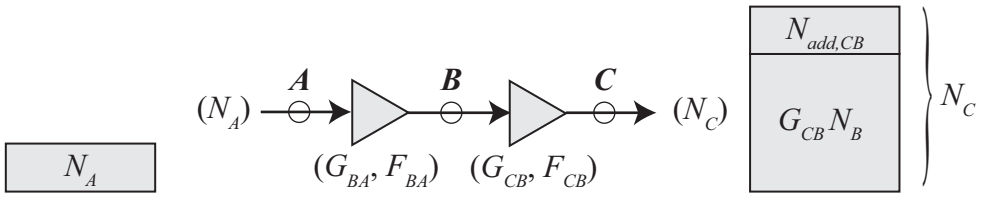

Figure C.2: Cascaded noise figure illustration.

The previous example can be extended to a cascade of devices. For example, consider the cascade of two elements shown in Fig. C.2. In this case, the output noise power is given by

$$N_C = N_{add,CB} + G_{CB}N_B \tag{C.20}$$

where G_{CB} is the gain and $N_{add,CB}$ is the added noise of the second element. Inserting the expression given by Eq. (C.15) into Eq. (C.20) yields

$$N_C = N_{add,CB} + G_{CB}\left(N_{add,BA} + G_{BA}N_A\right). \tag{C.21}$$

The composite noise factor of the two element network is given by

$$\begin{aligned} F_{CA} &= \frac{S_C/N_C}{S_A/N_A} \\ &= \frac{1}{G_{CB}G_{BA}}\frac{N_C}{N_A}. \end{aligned} \tag{C.22}$$

Substituting Eq. (C.21) into Eq. (C.22) yields

$$\begin{aligned} F_{CA} &= \frac{1}{G_{CB}G_{BA}}\frac{N_{add,CB} + G_{CB}N_{add,BA} + G_{CB}G_{BA}N_A}{N_A} \\ &= \left(1 + \frac{1}{G_{BA}}\frac{N_{add,BA}}{N_A}\right) + \frac{1}{G_{BA}}\left(\frac{1}{G_{CB}}\frac{N_{add,CB}}{N_A}\right) \end{aligned} \tag{C.23}$$

Using Eq. (C.16), Eq. (C.23) can be rewritten as

$$F_{CA} = F_{BA} + \frac{1}{G_{BA}}\left(F_{CB} - 1\right). \tag{C.24}$$

The result in Eq. (C.24) is significant. It states that the cascade noise figure is dominated by the gain and noise figure of the first device.

The most common methods for measuring the noise figure of a device are with a noise figure meter, using the gain method, or using the Y-factor method. Interested readers are referred to [155, 156] for more details on these measurement techniques.

Appendix D

Distortion

D.1 Dynamic Range

For sub-octave signals, the dynamic range (DR) of a nonlinear element is limited by third-order intermodulation distortion (IMD3). Intermodulation distortion (IMD) is associated with nonlinearities in the modulation and demodulation transfer functions. It should be noted that IMD is not limited to RF photonic elements. Electrical components often exhibit nonlinear transfer functions. For example, electrical amplifiers also generate third-order distortion (TOD) [157].

Commonly, the IMD3 products are measured with a two-tone test [158]. In this measurement, two closely spaced tones, with frequencies of f_1 and f_2, are applied to the device under test (DUT). In a linear element, the output can only contain frequency components that are applied to the input. However, in a nonlinear element, additional frequency components can be present. For the case where the element exhibits TOD, additional frequency components at $2f_1 - f_2$ and $2f_2 - f_1$ will be generated. Third-order IMD products are of particular concern because they occur close to the fundamental components and cannot simply be filtered out [159].

In the case where the DR is limited by TOD, the third-order intercept point (IP3) is a convenient parameter that describes the point where the extrapolated fundamental curve intersects the extrapolated IMD3 curve. When the IP3 point is

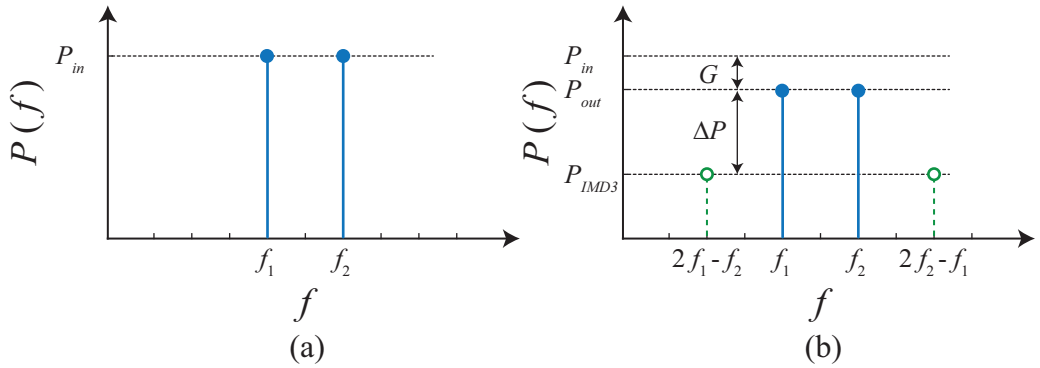

Figure D.1: Example spectra illustrating a two-tone test of a lossy element with TOD. (a) Input spectrum and (b) output spectrum.

referenced to the input, it is termed the input IP3 point (IIP3) and when the IP3 point is referenced to the output, it is termed the output IP3 point (OIP3).

D.2 Spurious Free Dynamic Range

The spurious free dynamic range (SFDR) is commonly used to quantify the performance of a nonlinear element. The SFDR describes the maximum dynamic range that can be achieved through a nonlinear element. The TOD limited SFDR, SFDR3, is defined as the maximum difference between the fundamental signal and noise floor. This occurs at the point where the IMD3 curve intersects the noise floor. Frequently, the fundamental and IMD3 output powers are plotted as functions of the input power for the case where the input is composed of two closely spaced tones having equal powers. An illustrative plot of output power as a function of input power is shown in Fig. D.2.

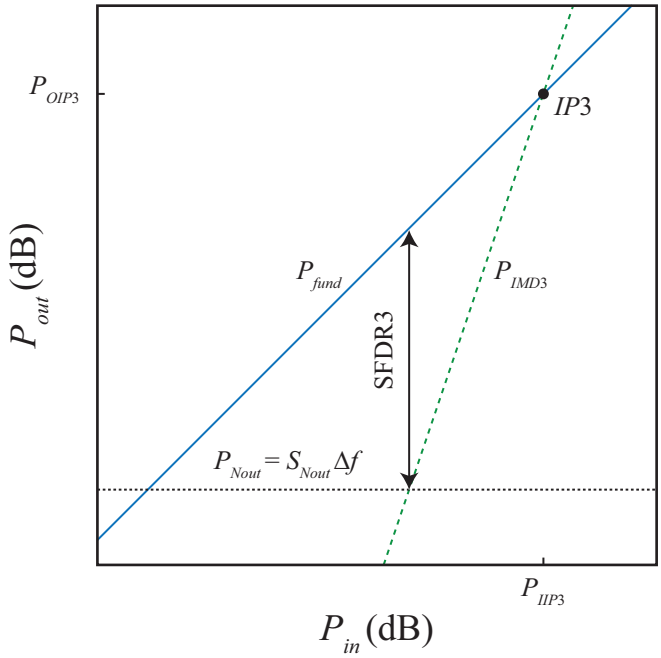

Figure D.2: Illustration of the output power per tone as a function of the the input power per tone for a hypothetical two-tone test.

In this appendix, a simple geometrical description of the third-order SFDR is presented. Since the two input tones are assumed to be closely spaced and of equal power, only one fundamental component and one IMD3 product need be plotted (e.g. f_1 and $2f_1 - f_2$). It is good practice to measure all four components to verify that the f_1 and f_2 curves are equal and the $2f_1 - f_2$ and $2f_2 - f_1$ curves are equal. In Fig. D.2, the fundamental curve is designated by the $P_{fund,\mathrm{dB}}$ label and the IMD3 curve is designated by the $P_{IMD3,\mathrm{dB}}$ label.

To derive the expression for the third-order SFDR, it is convenient to begin with case of a linear element. In this case, $P_{out,\mathrm{dB}} \equiv P_{fund,\mathrm{dB}}$. The general equation

of a straight line in (x,y) coordinates is well known and given by

$$y(x) = mx + b \tag{D.1}$$

where m is the slope and b is the y intercept. The small-signal gain of an element, G, in logarithmic units is given by

$$G_{\mathrm{dB}} = P_{fund,\mathrm{dB}} - P_{in,\mathrm{dB}}. \tag{D.2}$$

The small-signal gain can be rewritten in the form given by Eq. (D.1) as

$$P_{fund,\mathrm{dB}} = P_{in,\mathrm{dB}} + G_{\mathrm{dB}}. \tag{D.3}$$

In the case that the element exhibits TOD, the output spectrum will consist of fundamental and IMD3 components. The IMD3 curve can be expressed using Eq. (D.1) as

$$P_{IMD3,\mathrm{dB}} = m_3 P_{in,\mathrm{dB}} + b_3 \tag{D.4}$$

where m_3 and b_3 are the slope and $P_{out,\mathrm{dB}}$ intercept point of the IMD3 curve. TOD products are proportional to the cube of the input signal amplitude. Thus, the slope of the IMD3 power curve, when plotted in logarithmic units, is $m_3 = 3$. The third-order $P_{out,\mathrm{dB}}$ intercept point, b_3, can be defined in terms of the IP3 by equating Eq. (D.3) and Eq. (D.4) at an input power of $P_{in,\mathrm{dB}} = P_{IIP3}$. Performing the algebra, Eq. (D.4) can be rewritten as

$$P_{IMD3,\mathrm{dB}} = 3P_{in,\mathrm{dB}} + G_{\mathrm{dB}} - 2P_{IIP3,\mathrm{dB}}. \tag{D.5}$$

Per the definition above, the third-order SFDR is defined at the point where the power of the IMD3 products equal the power of the noise floor. Setting $P_{3,\mathrm{dB}} =$

$P_{Nout,\mathrm{dB}}$ and solving for $P_{in,\mathrm{dB}}$ yields

$$P_{in,\mathrm{dB}}\big|_{\left(P_{IMD3,\mathrm{dB}}=P_{Nout,\mathrm{dB}}\right)} = \frac{1}{3}\left(P_{Nout,\mathrm{dB}} - G_{\mathrm{dB}} + 2P_{IIP3,\mathrm{dB}}\right). \tag{D.6}$$

Substituting Eq. (D.6) into Eq. (D.3) gives

$$P_{fund,\mathrm{dB}}\big|_{\left(P_{IMD3,\mathrm{dB}}=P_{Nout,\mathrm{dB}}\right)} = \frac{1}{3}\left(P_{Nout,\mathrm{dB}} + 2G_{\mathrm{dB}} + 2P_{IIP3,\mathrm{dB}}\right). \tag{D.7}$$

Since the third-order SFDR is defined as the difference between the fundamental and the noise floor at the point where the third-order IMD products equal the noise floor,

$$\mathrm{SFDR3}_{\mathrm{dB\text{-}Hz^{2/3}}} = \frac{2}{3}\left[\left(P_{IIP3,\mathrm{dB}} + G_{\mathrm{dB}}\right) - P_{Nout,\mathrm{dB}}\right]. \tag{D.8}$$

The noise power is a function of bandwidth and can be expressed in terms of the noise power spectral density (PSD) as

$$P_{Nout,\mathrm{dB}}(f) = 10\log_{10}\int_{-\Delta f/2}^{\Delta f/2} S_{Nout,\mathrm{W/Hz}}(f)\,df. \tag{D.9}$$

Substituting Eq. (D.9) into Eq. (D.8) results in

$$\mathrm{SFDR3}_{\mathrm{dB\text{-}Hz^{2/3}}} = \frac{2}{3}\left[\left(P_{IIP3,\mathrm{dB}} + G_{\mathrm{dB}}\right) - 10\log_{10}\int_{-\Delta f/2}^{\Delta f/2} S_{Nout,\mathrm{W/Hz}}(f)\,df\right]. \tag{D.10}$$

From Eq. (D.10) it is clear that the third-order SFDR is a function of frequency, f, and bandwidth, Δf. The output noise PSD can be given in terms of the

$$S_{Nout}(f) = G(f)F(f)S_{in}(f) \tag{D.11}$$

where F is the noise factor and S_{in} is the input noise PSD (see Appendix C). Note that the frequency dependence of the gain, noise factor, and input noise PSD are in general functions of frequency. Assuming that the noise PSD is constant with

frequency, the integral in Eq. (D.10) can be replaced by the product of the noise PSD and the bandwidth. This assumption may or may not be valid for the device under test, so it is important to consider the frequency dependency of the output noise PSD contributions prior to proceeding. In many cases, the assumption can be made valid if the bandwidth is made small enough. In this case, Eq. (D.10) reduces to

$$\mathrm{SFDR3}_{\mathrm{dB\text{-}Hz^{2/3}}} = \frac{2}{3}\left[\left(P_{IIP3,\mathrm{dB}} + G_{\mathrm{dB}}\right) - 10\log_{10}\left(S_{Nout,\mathrm{W/Hz}}\Delta f\right)\right]. \tag{D.12}$$

Based on Eq. (D.11) and Eq. (D.12), a commonly used expression for SFDR3, assuming $T = 290$ K, is

$$\mathrm{SFDR3}_{\mathrm{dB\text{-}Hz^{2/3}}} = \frac{2}{3}\left[P_{IIP3,\mathrm{dB}} - (-174\mathrm{dBm} + NF_{\mathrm{dB}})\right] \tag{D.13}$$

The results in Eq. (D.13) can be extended to any order distortion using the same procedure presented in this appendix. For arbitrary order n, the spurious-free dynamic range is

$$\mathrm{SFDR}n_{\mathrm{dB\text{-}Hz^{(n-1)/n}}} = \frac{(n-1)}{n}\left[P_{IIPn,\mathrm{dB}} - (-174\mathrm{dBm} + NF_{\mathrm{dB}})\right] \tag{D.14}$$

where $P_{IIPn,\mathrm{dB}}$ is the input power corresponding to the n^{th}-order intercept point.

Measurements of the SFDR typically involve the use of an electrical spectrum analyzer (ESA). When an ESA is employed, the bandwidth that should be used in Eq. (D.10) is the resolution bandwidth (RBW) of the ESA. It is often a common practice to normalize the SFDR to a noise power bandwidth of $BW = 1$ Hz. In practice, the input noise power into a receiver is dominated by thermal noise. As

described in Appendix C, if the input noise power is thermal,

$$\begin{aligned} P_{Nin} &= 10\log_{10}(kT\Delta f) \\ &= 10\log_{10}(\Delta f) - 174\text{dBm} \end{aligned} \tag{D.15}$$

where an input temperature of $T = 290$ K has been assumed.

D.3 Linearization

For analog antenna remoting, the required SFDR is typically on the order of SFDR = 115 dB-Hz$^{2/3}$ [93]. The SFDR of a typical IM-DD link utilizing a quadrature biased MZM is $SDFR3 \approx 110$ dB-Hz$^{2/3}$ [44]. Thus, there are cases where the performance of the standard IM-DD RoF link does not meet the required performance specifications. Furthermore, if a pre-amplifier is used to lower the noise figure of the RF photonic link, the TOD from the amplifier is fed into the RoF link, potentially lowering the system SFDR performance. The calculation of cascade nonlinear devices is considered in [159].

There is a body of literature on linearizing RoF links that is well beyond the scope of this dissertation. The interested reader is referred to [154, 160–163] for the linearization of MZM links. By utilizing series or parallel networks of MZM and controlling the power splitting ratio of the RF signal applied to the MZMs, SFDRs of 126-130 dB-Hz$^{2/3}$ have been reported [34]. Electronic linearization can also be performed using an external linearization circuit [164] or predistortion [165].

Phase-modulation is a linear process (i.e. the optical phase-shift is a linear function of applied voltage). However, conventional optical-to-electrical schemes

such as coherent detection (CohD) introduce a sinusoidal nonlinearity. Linear phase detection can be performed with an photonic phase locked loop (PPLL), which is based on a CohD configuration with feedback. In this technique, the output from the photodetector is filtered and applied to a phase-modulator in-line with the optical local oscillator (OLO) [166]. Linear detection was reported with SFDRs greater than 120 dB-$Hz^{2/3}$ at frequencies around 140 kHz [167, 168]. However, the experimental results were limited to low frequencies due to the feedback loop delay. Lower loop delays are possible by integrating the receiver on-chip. For example, Bowers et al. demonstrated a SFDR3 of 125 dB-$Hz^{2/3}$ at 300 MHz based on an integrated PPLL with a loop bandwidth of 1.45 GHz [169, 170]. Other linear phase demodulation methods include demodulation using an optical hybrid and digital signal processing (DSP) [171].

Appendix E

UMD Publications and Presentations

E.1 Journal Articles

[J1] **V. R. Pagán** and T. E. Murphy. Electrooptic millimeter-wave harmonic downconversion and vector demodulation using cascaded phase-modulation and optical filtering. *Opt. Lett.* (accepted).

[J2] D. H. Park, **V. R. Pagán**, T. E. Murphy, J. Luo, A. K.-Y. Jen, and W. N. Herman. Free space millimeter wave-coupled electro-optic high speed nonlinear polymer phase modulator with in-plane slotted patch antennas. *Opt. Express*, 23(7):9464-9476, 2015

[J3] J. J. Wathen, **V. R. Pagán**, R. J. Suess, K. Y. Wang, A. C. Foster, and T. E. Murphy. Non-instantaneous optical linearity of an a-Si:H nanowire waveguide. *Opt. Express*, 22(19):22730-22742, 2014.

[J4] J. J. Wathen, **V. R. Pagán**, and T. E. Murphy. Simple method to characterize nonlinear refraction and loss in optical waveguides. *Opt. Lett.*, 37(22):4693-4695, 2012.

[J5] **V. R. Pagán**, B. M. Haas, and T. E. Murphy. Linearized electrooptic microwave downconversion using phase modulation and optical filtering. *Opt. Express*, 19(2):883-895, 2011.

E.2 Conference Proceedings

[CP1] D. H. Park, **V. R. Pagán**, T. E. Murphy, J. Luo, A. K.-Y. Jen, and W. N. Herman. Improved Carrier-to-Sideband Ratio for Free Space Millimeter Wave-Coupled Electro-Optic Polymer High Speed Phase Modulators. *Conference on Lasers and Electro-Optics* (accepted).

[CP2] **V. R. Pagán** and T. E. Murphy. Electrooptic Millimeter-Wave Downconversion and Vector Demodulation Using Phase-Modulation and Optical Filtering. In *IEEE Avionics Fiber-Optics and Photonics Conference*, 2014.

[CP3] **V. R. Pagán** and T. E. Murphy. Electrooptic Millimeter-Wave Generation and High-Speed Vector Modulation. In *IEEE International Topical Meeting on Microwave Photonics*, 2014.

[CP4] D. H. Park, **V. R. Pagán**, T. E. Murphy, J. Luo, A. K.-Y. Jen, and W. N. Herman. Free Space Millimeter Wave-Coupled Electro-Optic High Speed Phase Modulator Based on Nonlinear Optical Polymer In-Plane Waveguide Structure. In *Conference on Lasers and Electro-Optics*, 2014.

[CP5] **V. R. Pagán**, J. J. Wathen, K.-Y. Wang, A. C. Foster, and T. E. Murphy. Non-Instantaneous Optical Nonlinearities in a-Si:H Nanowire Waveguides. In *Conference on Lasers and Electro-Optics*, 2013.

[CP6] **V. R. Pagán** and T. E. Murphy. Phase-Modulated Radio-over-Fiber Systems. In *Optical Fiber Communication Conference*, 2013.

[CP7] **V. R. Pagán** and T. E. Murphy. Millimeter-Wave 6 Gb/s Wireless BPSK Electrooptic Link. In *IEEE International Topical Meeting on Microwave Photonics*, 2012.

[CP8] J. J. Wathen, **V. R. Pagán**, and T. E. Murphy. Simple Measurement of the Third-Order Nonlinear Loss Tangent in Optical Waveguides. In *Frontiers in Optics Conference*, 2012.

[CP9] **V. R. Pagán** and T. E. Murphy. Wireless BPSK Communication Using Electrooptic Modulation for Coherent Microwave Detection. In *Optical Fiber Communication Conference*, 2012.

[CP10] T. E. Murphy and **V. R. Pagán**. Phase modulated radio-over-fiber link with electro-optic downconversion using a delay-line interferometer. In *SPIE RF and Millimeter-Wave Photonics Conference Volume 7936*, 2011.

[CP11] **V. R. Pagán**, B. M. Haas, and T. E. Murphy. Phase modulated radio-over-fiber link with linearized electrooptic downconversion. In *IEEE International Topical Meeting on Microwave Photonics*, 2010.

Bibliography

[1] Cisco Visual Networking Index: Forecast and Methodology, 2013–2018. Technical report, Cisco, 2014.

[2] F. Giannetti, M. Luise, and R. Reggiannini. Mobile and Personal Communications in the 60 GHz Band: A Survey. *Wireless Pers. Commun.*, 10(2):207–243, 1999.

[3] D. M. Pozar. *Microwave and RF Design of Wireless Systems*. John Wiley & Sons, Inc., 2001.

[4] S. Chia, M. Gasparroni, and P. Brick. The Next Challenge for Cellular Networks: Backhaul. *IEEE Microw. Mag.*, 10(5):54–66, 2009.

[5] V. J. Urick, F. Bucholtz, P. S. Devgan, J. D. McKinney, and K. J. Williams. Phase Modulation With Interferometric Detection as an Alternative to Intensity Modulation With Direct Detection for Analog-Photonic Links. *IEEE Trans. Microw. Theory Tech.*, 55(9):1978–1985, 2007.

[6] T. E. Murphy and V. R. Pagán. Phase Modulated Radio-over-Fiber Link with Electrooptic Downconversion Using a Delay-Line Interferometer. In *Proc. SPIE*, volume 7936, 2011.

[7] V. R. Pagán and T. E. Murphy. Phase-Modulated Radio-over-Fiber Systems. In *Optical Fiber Communication Conference/National Fiber Optic Engineers Conference*, 2013.

[8] V. R. Pagán, B. M. Haas, and T. E. Murphy. Linearized electrooptic microwave downconversion using phase modulation and optical filtering. *Opt. Express*, 19(2):883–895, 2011.

[9] B. M. Haas and T. E. Murphy. A carrier-suppressed phase-modulated fiber optic link with IF downconversion of 30GHz 64-QAM signals. In *International Topical Meeting on Microwave Photonics*, 2009.

[10] V. R. Pagán and T. E. Murphy. Electrooptic Millimeter-Wave Downconversion and Vector Demodulation Using Phase-Modulation and Optical Filtering. In *IEEE Avionics, Fiber-Optics and Photonics Technology Conference*, 2014.

[11] V. R. Pagán and T. E. Murphy. Millimeter-Wave 6Gb/s Wireless BPSK Electrooptic Link. In *IEEE International Topical Meeting on Microwave Photonics*, 2012.

[12] V. R. Pagán and T. E. Murphy. Electrooptic Millimeter-Wave Generation and High-Speed Vector Modulation. In *IEEE International Topical Meeting on Microwave Photonics*, 2014.

[13] V. R. Pagán and T. E. Murphy. Wireless BPSK Communication Using Electrooptic Modulation for Coherent Microwave Detection. In *National Fiber Optic Engineers Conference*, 2012.

[14] C. Levis, J. T. Johnson, and F. L. Teixeira. *Radiowave Propagation*. John Wiley & Sons, 2010.

[15] M. Weiss, A. Stöhr, F. Lecoche, and B. Charbonnier. 27 Gbit/s Photonic Wireless 60 GHz Transmission System using 16-QAM OFDM. In *IEEE International Topical Meeting on Microwave Photonics*, 2009.

[16] A. Stöhr. Photonic Millimeter-Wave Generation and its Application in High Data Rate Wireless Access. In *IEEE International Topical Meeting on Microwave Photonics*, 2010.

[17] K.-C. Huang and Z. Wang. *Millimeter Wave Communication Systems*. John Wiley & Sons, Inc., 2011.

[18] Cisco Visual Networking Index: Global Mobile Data Traffic Forecast Update, 2014–2019. Technical report, Cisco, 2015.

[19] WiGig Alliance. Wireless Gigabit Alliance. http://www.wirelessgigabitalliance.org/, Jul. 2010.

[20] Wi-Fi Alliance. Unification with WiGig Alliance. http://www.wi-fi.org/, Jul. 2013.

[21] S. Bloom and W. S. Hartley. The Last-Mile Solution: Hybrid FSO Radio. Technical report, AirFiber, 2002.

[22] J. M. Kahn and J. R. Barry. Wireless Infrared Communications. *Proc. IEEE*, 85(2):265–298, 1997.

[23] R. W. Ridgway, D. W. Nippa, and S. Yen. Data transmission using phase-shift keying on a 92 GHz carrier. In *International Topical Meeting on Microwave Photonics*, 2009.

[24] M. Al Naboulsi, H. Sizun, and F. de Fornel. Fog attenuation prediction for optical and infrared waves. *Opt. Eng.*, 43(2):319–329, 2004.

[25] F. Nadeem, V. Kvicera, M. S. Awan, E. Leitgeb, S. Muhammad, and G. Kandus. Weather effects on hybrid FSO/RF communication link. *IEEE J. Select. Areas Commun.*, 27(9):1687–1697, 2009.

[26] Z. Pi and F. Khan. An Introduction to Millimeter-Wave Mobile Broadband Systems. *IEEE Commun. Mag.*, 49(6):101–107, 2011.

[27] T. S. Rappaport, S. Sun, R. Mayzus, H. Zhao, Y. Azar, K. Wang, G. N. Wong, J. K. Schulz, M. Samimi, and F. Gutierrez. Millimeter Wave Mobile Communications for 5G Cellular: It Will Work! *IEEE Access*, 1:335–349, 2013.

[28] L. Cheng, C. Liu, Z. Dong, J. Yu, and G.-K. Chang. 60-GHz and 100-GHz Wireless Transmission of High-Definition Video Services in Converged Radio-over-Fiber Systems. In *Conference on Lasers and Electro-Optics*, 2013.

[29] I. G. Insua, D. Plettemeter, and C. G. Sch affer. Broadband radio-over-fiber-based wireless access with 10 Gbits/s data rates. *J. Opt. Netw.*, 8(1):77–83, 2009.

[30] M. Weiβ, M. Huchard, A. St ohr, B. Charbonnier, S. Fedderwitz, and D. S. J ager. 60-GHz Photonic Millimeter-Wave Link for Short- to Medium-Range Wireless Transmission Up to 12.5 Gb/s. *J. Lightwave Technol.*, 26(15):2424–2429, 2008.

[31] C.-T. Lin, P.-T. Shih, Y.-H. Chen, W.-J. Jiang, J. Chen, and S. Chi. Experimental Demonstration of 10-Gb/s OFDM-QPSK Signal at 60 GHz Using Frequency-Doubling and Tandem SSB Modulation. In *Optical Fiber Communication Conference*, 2009.

[32] R. Sambaraju, V. Polo, J. L. Corral, and J. Marti. Ten gigabits per second 16-level quadrature amplitude modulated millimeter-wave carrier generation using dual-drive Mach-Zehnder modulators incorporated photonic-vector modulator. *Opt. Lett.*, 33(16):1833–1835, 2008.

[33] G. E. Betts, L. M. Johnson, C. H. Cox III, and S. D. Lowney. High-Performance Optical Analog Link Using External Modulator. *IEEE Photon. Technol. Lett.*, 1(11):404–406, 1989.

[34] C. Cox III. *Analog Optical Links: Theory and Practice*. Cambridge University Press, 2004.

[35] V. J. Urick, F. Bucholtz, J. D. McKinney, P. S. Devgan, A. L. Campillo, J. L. Dexter, and K. J. Williams. Long-Haul Analog Photonics. *J. Lightwave Technol.*, 29(8):1182–1205, 2011.

[36] S. Yegnanarayanan, P. D. Trinh, and B. Jalali. Recirculating photonic filter: a wavelength-selective time delay for phased-array antennas and wavelength code-division multiple access. *Opt. Lett.*, 21(10):740–742, 1996.

[37] J. Wang, F. Zeng, and J. Yao. All-optical microwave bandpass filters implemented in a radio-over-fiber link. *IEEE Photon. Technol. Lett*, 17(8):1737–1739, 2005.

[38] X. Xue, X. Zheng, H. Zhang, and B. Zhou. Wideband Photonic Radiofrequency Beamforming Network Employing a Broadband Optical Source Sliced by a Wavelength Selective Switch. In *Conference on Lasers and Electro-Optics*, 2013.

[39] J. Capmany, D. Pastor, and B. Ortega. New and flexible fiber-optic delay-line filters using chirped Bragg gratings and laser arrays. *IEEE Trans. Microwave Theory Tech.*, 47(7):1321–1326, 1999.

[40] J. Capmany, B. Ortega, and D. Pastor. A Tutorial on Microwave Photonic Filters. *J. Lightwave Technol.*, 24(1):201–229, 2006.

[41] E. Hamidi, D. E. Leaird, and A. M. Weiner. Tunable Programmable Microwave Photonic Filters Based on an Optical Frequency Comb. *IEEE Trans. Microwave Theory Tech.*, 58(11):3269–3278, 2010.

[42] X. Pang, Y. Zhao, L. Deng, X. Yu, and I. T. Monroy. A novel reconfigurable ultra-broadband millimeter-wave photonic harmonic down-converter. In *International Topical Conference on Microwave Photonics*, 2011.

[43] A. Mast, C. Middleton, S. Meredith, and R. DeSalvo. Extending Frequency and Bandwidth through the Use of Agile, High Dynamic Range Photonic Converters. In *IEEE Aerospace Conference*, 2012.

[44] G. Betts. Linearized modulator for suboctave-bandpass optical analog links. *IEEE Trans. Microw. Theory Tech.*, 42(12):2642–2649, 1994.

[45] J. Capmany and D. Novak. Microwave photonics combines two worlds. *Nature Photon.*, 1(6):319–330, 2007.

[46] A. J. Seeds and K. J. Williams. Microwave Photonics. *J. Lightwave Technol.*, 24(12):4628–4641, 2006.

[47] Y.-T. Hsueh, Z. Jia, H.-C. Chien, A. Chowdhury, J. Yu, and G.-K. Chang. Multiband 60-GHz Wireless Over Fiber Access System With High Dispersion Tolerance Using Frequency Tripling Technique. *J. Lightwave Technol.*, 29(8):1105–1111, 2011.

[48] A. H. M. R. Islam, M. Bakaul, and A. Nirmalathas. Multi-level ASK Demonstrations in Millimeter-wave Radio-over-fiber System using Free-running Lasers and RF Self-homodyning. In *IEEE International Topical Meeting on Microwave Photonics*, 2012.

[49] R. W. Ridgway and D. W. Nippa. Generation and Modulation of a 94-GHz Signal Using Electrooptic Modulators. *IEEE Photon. Technol. Lett.*, 20(8):653–655, 2008.

[50] R. Sambaraju, M. Á. Piqueras, V. Polo, J. L. Corral, and J. Martí. Generation of Multi-Gigabit-per-Second MQAM/MPSK-Modulated Millimeter-Wave Carriers Employing Photonic Vector Modulator Techniques. *J. Lightwave Technol.*, 25(11):3350–3357, 2007.

[51] L. Zhang, C. Ye, X. Hu, Z. Li, S.-H. Fan, Y.-T. Hsueh, Q. Chang, Y. Su, and G.-K. Chang. Generation of Multiband Signals in a Bidirectional Wireless Over Fiber System With High Scalability Using Heterodyne Mixing Technique. *IEEE Photon. Technol. Lett.*, 24(18):1621–1624, 2012.

[52] L. Zhang, M. Zhu, C. Ye, S.-H. Fan, C. L., X. H., P. C., Q. Chang, Y. Su, and G.-K. Chang. Generation and transmission of multiband and multi-gigabit 60-GHz MMW signals in an RoF system with frequency quintupling technique. *Opt. Express*, 21(8):9899–9905, 2013.

[53] A. Hirata, T. Kosugi, H. Takahashi, R. Yamaguchi, F. Nakajima, T. Furuta, H. Ito, H. Sugahara, Y. Sato, and T. Nagatsuma. 120-GHz-Band Millimeter-Wave Photonic Wireless Link for 10-Gb/s Data Transmission. *IEEE Trans. Microw. Theory Tech.*, 54(5):1937–1944, 2006.

[54] A. Stöhr, A. Akrout, R. Buβ, B. Charbonnier, F. van Dijk, A. Enard, S. Fedderwitz, D. Jäger, M. Huchard, F. Lecoche, J. Marti, R. Sambaraju, A. Steffan, A. Umbach, and M. Weiβ. 60 GHz radio-over-fiber technologies for broadband wireless services. *J. Opt. Netw.*, 8(5):471–487, 2009.

[55] R. Sambaraju, J. Palaci, R. Alemany, V. Polo, and J. L. Corral. Photonic vector demodulation of 2.5 Gbit/s QAM modulated wireless signals. In *International Topical Meeting on Microwave Photonics/Asia-Pacific Microwave Photonics Conference*, 2008.

[56] P. D. Biernacki, L. T. Nichols, D. G. Enders, K. J. Williams, and R. D. Esman. A two-channel optical downconverter for phase detection. *IEEE Trans. Microw. Theory Tech.*, 46(11):1784–1787, 1998.

[57] A. J. Seeds. Microwave Photonics. *IEEE Trans. Microw. Theory Tech.*, 50(3):877–887, 2002.

[58] T. E. Darcie and G. E. Bodeep. Lightwave subcarrier CATV transmission systems. *IEEE Trans. Microwave Theory Tech.*, 38(5):524–533, 1990.

[59] C. Cox III, E. Ackerman, R. Helkey, and G. Betts. Direct-detection analog optical links. *IEEE Trans. Microwave Theory Tech.*, 45(8):1375–1383, 1997.

[60] R. D. Esman, M. Y. Frankel, J. L. Dexter, L. Goldberg, M. G. Parent, D. Stilwell, and D. G. Cooper. Fiber-optic prism true time-delay antenna feed. *IEEE Photon. Technol. Lett.*, 5(11):1347–1349, 1993.

[61] T. R. Clark and R. Waterhouse. Photonics for RF Front Ends. *IEEE Microw. Mag.*, 12(3):87–95, 2011.

[62] E. Rouvalis, F. N. Baynes, X. Xie, K. Li, Q. Zhou, F. Quinlan, T. M. Fortier, S. A. Diddams, A. G. Steffan, A. Beling, and J. C. Campbell. High-Power and High-Linearity Photodetector Modules for Microwave Photonic Applications. *J. Lightwave Technol.*, 32(20):3810–3816, 2014.

[63] X. Xie, K. Li, Q. Zhou, A. Beling, and J. C. Campbell. High-Gain, Low-Noise-Figure, and High-Linearity Analog Photonic Link Based on a High-Performance Photodetector. *J. Lightwave Technol.*, 32(21):4187–4192, 2014.

[64] T. Sakamoto and T. Kawanishi M. Izutsu. Widely wavelength-tunable ultra-flat frequency comb generation using conventional dual-drive Mach-Zehnder modulator. *Electron. Lett.*, 43(19):1039–1040, 2007.

[65] H. Wen, W. Ye, X. Zheng, H. Zhang, and B. Zhou. Optical dual-pulse sampling for direct detection of vector modulated radio frequency signal. In *Conference on Lasers and Electro-Optics*, 2013.

[66] P. W. Juodawlkis, J. J. Hargreaves, R. D. Younger, G. W. Titi, and J. C. Twichell. Optical Down-Sampling of Wide-Band Microwave Signals. *J. Lightwave Technol.*, 21(12):3116–3124, 2003.

[67] G. C. Valley. Photonic analog-to-digital converters. *Opt. Express*, 15(5):1955–1982, 2007.

[68] P. R. Herczfeld. The Application of Lightwave Technology to Microwaves. In *European Microwave Conference*, volume 1, 1990.

[69] F. Devaux, Y. Sorel, and J. F. Kerdiles. Simple Measurement of Fiber Dispersion and of Chirp Parameter of Intensity Modulated Light Emitter. *J. Lightwave Technol.*, 11(12):1937–1940, 1993.

[70] E. I. Ackerman and A. S. Daryoush. Broad-band external modulation fiber-optic links for antenna-remoting applications. *IEEE Trans. Microw. Theory Tech.*, 45(8):1436–1442, 1997.

[71] C. Spiegelberg, J. Geng, Y. Hu, Y. Kaneda, S. J., and N. Peyghambarian. Low-Noise Narrow-Linewidth Fiber Laser at 1550 nm. *J. Lightwave Technol.*, 22(1):57–62, 2004.

[72] H. Huang, S. R. Nuccio, Y. Yue, J. Yang, Y. Ren, C. Wei, G. Yu, R. Dinu, D. Parekh, C. J. Chang-Hasnain, and A. E. Willner. Broadband Modulation Performance of 100-GHz EO Polymer MZMs. *J. Lightwave Technol.*, 30(23):3647–3652, 2012.

[73] J. Macario, P. Yao, S. Shi, A. Zablocki, C. Harrity, R. D. Martin, C. A. Schuetz, and D. W. Prather. Full spectrum millimeter-wave modulation. *Opt. Express*, 20(21):23623–23629, 2012.

[74] D. Zibar, X. Yu, C. Peucheret, P. Jeppesen, and I. T. Monroy. Digital Coherent Receiver for Phase-Modulated Radio-Over-Fiber Optical Links. *IEEE Photon. Technol. Lett.*, 21(3):155–157, 2009.

[75] C. H. Cox III, E. I. Ackerman, G. Betts, and J. L. Prince. Limits on the performance of RF-over-fiber links and their impact on device design. *IEEE Trans. Microwave Theory Tech.*, 54(2):906–920, 2006.

[76] W. E. Stephens and T. R. Joseph. System Characteristics of Direct Modulated and Externally Modulated RF Fiber-Optic Links. *J. Lightwave Technol.*, LT-5(3):380–387, 1987.

[77] C. E. Shannon. Communication in the Presence of Noise. *Proc. IRE*, 37(1):10–21, 1949.

[78] M. Hossein-Zadeh and A. F. J. Levi. Photonic microwave down-conversion based on linear modulation and filtering. In *Proceedings of PHO*, 2011.

[79] T. S. Tan, R. L. Jungerman, and S. S. Elliott. Optical Receiver and Modulator Frequency Response Measurement with a Nd:YAG Ring Laser Heterodyne Technique. *IEEE Trans. Microw. Theory Tech.*, 37(8):1217–1222, 1989.

[80] A. K. M. Lam, M. Fairburn, and N. A. F. Jaeger. Wide-Band Electrooptic Intensity Modulator Frequency Response Measurement Using an Optical Heterodyne Down-Conversion Technique. *IEEE Trans. Microw. Theory Tech.*, 54(1):240–246, 2006.

[81] G. K. Gopalakrishnan, W. K. Burns, and C. H. Bulmer. Microwave-Optical Mixing in $LiNbO_3$ Modulators. *IEEE Trans. Microw. Theory Tech.*, 41(12):2383–2391, 1993.

[82] A. C. Lindsay, G. A. Knight, and S. T. Winnall. Photonic Mixers for Wide Bandwidth RF Receiver Applications. *IEEE Trans. Microw. Theory Tech.*, 43(9):2311–2317, 1995.

[83] C. K. Sun, R. J. Orazi, S. A. Pappert, and W. K. Burns. A Photonic-Link Millimeter Wave Mixer Using Cascaded Optical Modulators and Harmonic Carrier Generation. *IEEE Photon. Technol. Lett.*, 8(9):1166–1168, 1996.

[84] F. Zeng and J. Yao. All-Optical Microwave Mixing and Bandpass Filtering in a Radio-Over-Fiber Link. *IEEE Photon. Technol. Lett.*, 17(4):899–901, 2005.

[85] G. K. Gopalakrishnan, R. P. Moeller, M. M. Howerton, W. K. Burns, K. J. Williams, and R. D. Esman. A Low-Loss Downconverting Analog Fiber-Optic Link. *IEEE Trans. Microw. Theory Tech.*, 43(9):2318–2323, 1995.

[86] J. T. Gallo and J. K. Godshall. Comparison of Series and Parallel Optical Modulators for Microwave Down-Conversion. *IEEE Photon. Technol. Lett.*, 10(11):1623–1625, 1998.

[87] Z. Tang, F. Zhang, and S. Pan. Photonic microwave downconverter based on an optoelectronic oscillator using a single dual-drive Mach-Zehnder modulator. *Opt. Express*, 22(1):305–310, 2014.

[88] E. H. W. Chan and R. A. Minasian. Microwave Photonic Downconverter With High Conversion Efficiency. *J. Lightwave Technol.*, 30(23):3580–3585, 2012.

[89] R. A. Minasian. Photonic signal processing of microwave signals. *IEEE Trans. Microwave Theory Tech.*, 54(2):832–846, 2006.

[90] K. P. Jackson, S. A. Newton, B. Moslehi, M. Tur, C. C. Cutler, J. W. Goodman, and H. J. Shaw. Optical Fiber Delay-Line Signal Processing. *IEEE Trans. Microwave Theory Tech.*, 33(3):193–210, 1985.

[91] A. Loayssa and F. J. Lahoz. Broad-band RF photonic phase shifter based on stimulated Brillouin scattering and single-sideband modulation. *IEEE Photon. Technol. Lett.*, 18(1):208–210, 2006.

[92] E. Ip, A. P. T. Lau, D. J. F. Barros, and J. M. Kahn. Coherent detection in optical fiber systems. *Opt. Express*, 16(2):753–791, 2008.

[93] R. F. Kalman, J. C. Fan, and L. G. Kazovsky. Dynamic Range of Coherent Analog Fiber-Optic Links. *J. Lightwave Technol.*, 12(7):1263–1277, 1994.

[94] Y. Yamamoto and T. Kimura. Coherent optical fiber transmission systems. *IEEE J. Quantum Electron.*, QE-17(6):919–935, 1981.

[95] A. R. Chraplyvy, R. W. Tkach, L. L. Buhl, and R. C. Alferness. Phase Modulation to Amplitude Modulation Conversion of CW Laser Light in Optical Fibres. *Electron. Lett.*, 22(8):409–411, 1986.

[96] A. F. Elrefaie, R. E. Wagner, D. A. Atlas, and D. G. Daut. Chromatic Dispersion Limitations in Coherent Lightwave Transmission Systems. *J. Lightwave Technol.*, 6(5):704–709, 1988.

[97] U. Gliese, S. Norskov, and T. N. Nielsen. Chromatic Dispersion in Fiber-Optic Microwave and Millimeter-Wave Links. *IEEE Trans. Microw. Theory Tech.*, 44(10):1716–1724, 1996.

[98] G. H. Smith, D. Novak, and Z. Ahmed. Overcoming Chromatic-Dispersion Effects in Fiber-Wireless Systems Incorporating External Modulators. *IEEE Trans. Microw. Theory Tech.*, 45(8):1410–1415, 1997.

[99] A. R. Chraplyvy. Limitations on Lightwave Communications Imposed by Optical-Fiber Nonlinearities. *J. Lightwave Technol.*, 8(10):1548–1557, 1990.

[100] Y. Le Guennec, G. Maury, J. Yao, and B. Cabon. New Optical Microwave Up-Conversion Solution in Radio-Over-Fiber Networks for 60-GHz Wireless Applications. *J. Lightwave Technol.*, 24(3):1277–1282, 2006.

[101] H. Chi, X. Zou, and J. Yao. Analytical Models for Phase-Modulation-Based Microwave Photonic Systems With Phase Modulation to Intensity Modulation Conversion Using a Dispersive Device. *J. Lightwave Technol.*, 27(5):511–521, 2009.

[102] X. S. Yao. Phase-to-Amplitude Modulation Conversion Using Brillouin Selective Sideband Amplification. *IEEE Photon. Technol. Lett.*, 10(2):264–266, 1998.

[103] M. Hossein-Zadeh and A. F. J. Levi. Self-homodyne photonic microwave receiver architecture based on linear optical modulation and filtering. *Microw. Opt. Technol. Lett.*, 50(2):345–350, 2008.

[104] B. Chen, S. L. Zheng, X. M. Zhang, X. F. Jin, and H. Chi. Simultaneously Realizing PM-IM Conversion and Efficiency Improvement of Fiber-Optic Links Using FBG. *J. Electromagnet. Waves and Appl.*, 23:161–170, 2009.

[105] E. Ackerman, S. Wanuga, J. MacDonald, and J. Prince. Balanced Receiver External Modulation Fiber-Optic Link Architecture With Reduced Noise Figure. In *IEEE MTT-S International Microwave Symposium*, 1993.

[106] R. Hui and M. O'Sullivan. *Fiber Optic Measurement Techniques*. Academic Press, 2009.

[107] Z. Tang, F. Zhang, D. Zhu, X. Zou, and S. Pan. A photonic frequency downconverter based on a single dual-drive Mach-Zehnder modulator. In *International Topical Meeting on Microwave Photonics*, 2013.

[108] Optoplex. Optical Hybrid Enables Next-Generation Optical Communications. http://www.optoplex.com/, 2015.

[109] K.-P. Ho. *Phase-Modulated Optical Communication Systems*. Springer, 2005.

[110] B. M. Haas and T. E. Murphy. Linearized Downconverting Microwave Photonic Link Using Dual-Wavelength Phase Modulation and Optical Filtering. *IEEE Photon. J.*, 3(1):1–12, 2011.

[111] H.-C. Chien, Y.-T. Hsueh, A. Chowdhury, J. Yu, and G.-K. Chang. On Frequency-Doubled Optical Millimeter-Wave Generation Technique Without Carrier Suppression for In-Building Wireless Over Fiber Applications. *IEEE Photon. Technol. Lett.*, 22(3):182–184, 2010.

[112] S. Koenig, F. Boes, D. Lopez-Diaz, J. Antes, R. Henneberger, R. Schmogrow, D. Hillerkuss, R. Palmer, T. Zwick, C. Koos, W. Freude, O. Ambacher, I. Kallfass, and J. Leuthold. 100 Gbit/s Wireless Link with mm-Wave Photonics. In *Optical Fiber Communication Conference/National Fiber Optic Engineers Conference*, 2013.

[113] W.-J. Jiang, C.-T. Lin, C.-H. Ho, C.-C. Wei, P.-T. Shih, J. Chen, and S. Chi. Photonic vector signal generation employing a novel optical direct-detection in-phase/quadrature-phase upconversion. *Opt. Lett.*, 35(23):4069–4071, 2010.

[114] N. A. Al-Shareefi, S. I. S. Hassan, F. Malek, R. Ngah, and S. A. Abbas. Optical Generation of 60 GHz Downstream Data in Radio over Fiber Systems Based on Two Parallel Dual-Drive MZMs. *Int. J. Eng. Tech.*, 6(2):579–587, 2014.

[115] J. R. Barry and E. A. Lee. Performance of coherent optical receivers. *Proc. IEEE*, 78(8):1369–1394, 1990.

[116] C. C. Davis. *Lasers and Electro-Optics: Fundamentals and Engineering*. Cambridge University Press, 1996.

[117] P. W. Milonni and J. H. Eberly. *Laser Physics*. John Wiley & Sons, Inc., 2010.

[118] K. J. Williams, R. D. Esman, and M. Dagenais. Nonlinearities in p-i-n Microwave Photodetectors. *J. Lightwave Technol.*, 14(1):84–96, 1996.

[119] J. C. Palais. *Fiber Optic Communications, 5th Ed.* Pearson Prentice Hall, 2004.

[120] G. Ducournau O., Latry, and M. Kétata. Fiber-based Mach-Zehnder interferometric structures: principles and required characteristics for efficient modulation format conversion. In *Proc. SPIE*, volume 6019, 2005.

[121] M. Lawrence. Lithium niobate integrated optics. *Rep. Prog. Phys.*, pages 363–429, 1993.

[122] W. N. Herman, S. R. Flom, and S. H. Foulger III. *ACS Symposium Series 1039, Organic Thin Films for Photonic Applications*. Oxford University Press, 2010.

[123] Y. Li, R. Wang, A. Bhardwaj, S. Ristic, and J. Bowers. High Linearity InP-Based Phase Modulators Using a Shallow Quantum-Well Design. *IEEE Photon. Technol. Lett*, 22(18):1340–1342, 2010.

[124] F. Auracher and R. Keil. Method for measuring the rf modulation characteristics of Mach-Zehnder-type modulators. *Appl. Phys. Lett.*, 36(8):626–629, 1980.

[125] Z. Jia, J. Yu, G. Ellinas, and G.-K. Chang. Key Enabling Technologies for Optical-Wireless Networks: Optical Millimeter-Wave Generation, Wavelength Reuse, and Architecture. *J. Lightwave Technol.*, 25(11):3452–3471, 2007.

[126] P. Bravetti, G. Ghislotti, and S. Balsamo. Chirp-Inducing Mechanisms in Mach-Zehnder Modulators and Their Effect on 10 Gb/s NRZ Transmission Studied Using Tunable-Chrip Single Drive Devices. *J. Lightwave Technol.*, 22(2):605–611, 2004.

[127] H. Kim and A. H. Gnauck. Chirp Characteristics of a Dual-Drive Mach-Zehnder Modulator With a Finite DC Extinction Ratio. *IEEE Photon. Technol. Lett.*, 14(3):298–300, 2002.

[128] H. A. Haus and W. Huang. Coupled-Mode Theory. *Proc. IEEE*, 79(10):1505–1518, 1991.

[129] D. Sadot and E. Boimovich. Tunable optical filters for dense WDM networks. *IEEE Commun. Mag.*, 36(12):50–55, 1998.

[130] N. M. Litchinitser, B. J. Eggleton, and D. B. Patterson. Fiber Bragg Gratings for Dispersion Compensation in Transmission: Theoretical Model and Design Criteria for Nearly Ideal Pulse Recompression. *J. Lightwave Technol.*, 15(8):1303–1313, 1997.

[131] M. Attygalle, C. Lim, G. J. Pendock, A. Nirmalathas, and G. Edvell. Transmission Improvement in Fiber Wireless Links Using Fiber Bragg Gratings. *IEEE Photon. Technol. Lett.*, 17(1):190–192, 2005.

[132] L. Rao, C. Liu, M. Zhu, J. Wang, and G.-K. Chang. A Novel Full-Duplex 60-GHz Radio-over-Fiber Transmission System for Next-Generation Wireless Access Networks. In *Conference on Lasers and Electro-Optics*, 2013.

[133] P.-T. Shih, C.-T. Lin, W.-J. Jiang, Y.-H. Chen, J. Chen, and S. Chi. Full duplex 60-GHz RoF link employing tandem single sideband modulation scheme and high spectral efficiency modulation format. *Opt. Express*, 17(22):19501–19508, 2009.

[134] C. M. Caves. Quantum limits on noise in linear amplifiers. *Phys. Rev. D*, 26(8):1817–1839, 1982.

[135] G.-I. Kweon. Noise Figure of Optical Amplifiers. *J. Korean Phys. Soc.*, 41(5):617–628, 2002.

[136] V. J. Urick, M. S. Rogge, F. Bucholtz, and K. J. Williams. The Performance of Analog Photonic Links Employing Highly Compressed Erbium-Doped Fiber Amplifiers. *IEEE Trans. Microw. Theory Tech.*, 54(7):3141–3145, 2006.

[137] G. P. Agrawal. *Nonlinear Fiber Optics, 2nd Ed.* Academic Press, 1995.

[138] F. Bowman. *Introduction to Bessel Functions*. Dover Publications Inc., 1958.

[139] V. R. Pagán, B. M. Haas, and T. E. Murphy. Phase modulated radio-over-fiber link with linearized electrooptic downconversion. In *IEEE International Topical Meeting on Microwave Photonics*, 2010.

[140] L. Martínez, A. Villafranca, and R. Escorihuela. High Resolution and Complex Optical Spectrum Analysis. Technical report, Aragon Photonics, 2010.

[141] E. Pellejer, P. Blasco, and L. Martínez. BOSA high resolution optical spectrum analyzer for OSNR measurements. Technical report, Aragon Photonics, 2010.

[142] M. A. F. Roelens, S. Frisken, J. A. Bolger, D. Abakoumov, G. Baxter, S. Poole, and B. J. Eggleton. Dispersion Trimming in a Reconfigurable Wavelength Selective Switch. *J. Lightwave Technol.*, 26(1):73–78, 2008.

[143] B. H. Kolner and D. W. Dolfi. Intermodulation distortion and compression in an integrated electrooptic modulator. *Appl. Opt.*, 26(17):3676–3680, 1987.

[144] R. E. Ziemer and R. L. Peterson. *Introduction to Digital Communications, 2nd Ed.* Prentice Hall, 2001.

[145] D. P. Agrawal and Q.-A. Zeng. *Introduction to Wireless and Mobile Systems, 2nd Ed.* Thomson, 2006.

[146] D. Jie, J.-J. Wang, H. Zhang, and G.-Y. Wang. Channel Capacity of 60 GHz Wireless Communication Systems over Indoor Line-of-Sight and Non-Line-of-Sight Channels. In *IEEE International Conference on Wireless Communications Networking and Mobile Computing*, 2010.

[147] J. B. Andersen, T. S. Rappaport, and S. Yoshida. Propagation Measurements and Models for Wireless Communications Channels. *IEEE Commun. Mag.*, 33(1):42–49, 1995.

[148] Millimeter Wave Propagation: Spectrum Management Implications. Technical Report Bulletin Number 70, Federal Communications Commission - Office of Engineering and Technology, 1997.

[149] H. T. Friis. A Note on a Simple Transmission Formula. *Proc. IRE*, 34(5):254–256, 1946.

[150] Electronic Code of Federal Regulations. Technical Report Title 47 §15.255, Federal Communications Commission, 2014.

[151] Memorandum Opinion and Order - WT Docket No. 02-146. Technical Report FCC 05-45, Federal Communications Commission, 2005.

[152] A. Hirata, T. Kosugi, H. Takahashi, J. Takeuchi, H. Togo, M. Yaita, N. Kukutsu, K. Aihara, K. Murata, Y. Sato, T. Nagatsuma, and Y. Kado. 120-GHz-Band Wireless Link Technologies for Outdoor 10-Gbit/s Data Transmission. *IEEE Trans. Microw. Theory Tech.*, 60(3):881–895, 2012.

[153] D. H. Park, V. R. Pagán, T. E. Murphy, J. Luo, A. K.-Y. Jen, and W. N. Herman. Free space millimeter wave-coupled electro-optic high speed nonlinear polymer phase modulator with in-plane slotted patch antennas. *Opt. Express*, 23(27):9464–9476, 2015.

[154] W. B. Bridges and J. H. Schaffner. Distortion in Linearized Electrooptic Modulators. *IEEE Trans. Microw. Theory Tech.*, 43(9):2184–2197, 1995.

[155] Three Methods of Noise Figure Measurement. Technical Report Tutorial 2875, Maxim, 2003.

[156] Fundamentals of RF and Microwave Noise Figure Measurements. Technical Report Application Note 57-1, Agilent, 2010.

[157] J. H. Schaffner and W. B. Bridges. Intermodulation distortion in high dynamic range microwave fiber-optic links with linearized modulators. *J. Lightwave Technol.*, 11(1):3–6, 1993.

[158] K. Barkley. Two-tone IMD measurement techniques. *RF Design Mag.*, pages 36–52, 2001.

[159] N. G. Kanaglekar, R. E. McIntosh, and W. E. Bryant. Analysis to two-tone, third-order distortion in cascaded two-ports. *IEEE Trans. Microwave Theory Tech.*, 36(4):701–705, 1988.

[160] L. M. Johnson and H. V. Roussell. Reduction of intermodulation distortion in interferometric optical modulators. *Opt. Lett.*, 13(10):928–930, 1988.

[161] S. K. Korotky and R. M. de Ridder. Dual Parallel Modulation Schemes for Low-Distortion Analog Optical Transmission. *IEEE J. Select. Areas Commun.*, 8(7):1377–1381, 1990.

[162] J. L. Brooks and R. A. Becker. Implementation and Evaluation of a Dual Parallel Linearization System for AM-SCM Video Transmission. *J. Lightwave Technol.*, 11(1):34–41, 1993.

[163] E. I. Ackerman. Broad-Band Linearization of a Mach-Zehnder Electrooptic Modulator. *IEEE Trans. Microw. Theory Tech.*, 47(12):2271–2279, 1999.

[164] Y. Chiu, B. Jalali, S. Garner, and W. Steier. Broad-Band Electronic Linearizer for Externally Modulated Analog Fiber-Optic Links. *IEEE Photon. Technol. Lett.*, 11(1):48–50, 1999.

[165] A. Katz, W. Jemison, M. Kubak, and J. Dragone. Improved radio over fiber performance using predistortion linearization. In *Proc. IEEE MTT-S*, volume 2, 2003.

[166] Y. Li, D. Yoo, P. Herczfeld, A. Rosen, A. Madjar, and S. Goldwasser. Receiver for coherent fiber-optic link with high dynamic range and low noise figure. In *International Topical Meeting on Microwave Photonics*, 2005.

[167] G. E. Betts, W. Krzewick, S. Wu, and P. K. L. Yu. Experimental Demonstration of Linear Phase Detection. *IEEE Photon. Technol. Lett.*, 19(13):993–995, 2007.

[168] H.-F. Chou, A. Ramaswamy, D. Zibar, L. A. Johansson, J. E. Bowers, M. Rodwell, and L. A. Coldren. Highly Linear Coherent Receiver With Feedback. *IEEE Photon. Technol. Lett.*, 19(12):940–942, 2007.

[169] J. E. Bowers, A. Ramaswamy, L. A. Johansson, J. Klamkin, M. Sysak, D. Zibar, L. Coldren, and M. Rodwell. Linear Coherent Receiver based on a Broadband and Sampling Optical Phase-Locked Loop. In *IEEE International Topical Meeting on Microwave Photonics*, 2007.

[170] A. Ramaswamy, L. A. Johansson, J. Klamkin, H.-F. Chou, C. Sheldon, M. J. Rodwell, L. A. Coldren, and J. E. Bowers. Integrated Coherent Receivers for High-Linearity Microwave Photonic Links. *J. Lightwave Technol.*, 26(1):209–216, 2008.

[171] T. R. Clark and M. L. Dennis. Coherent Optical Phase-Modulation Link. *IEEE Photon. Technol. Lett.*, 19(16):1206–1208, 2007.